Conditional cell penetration of a masked CPP and optimization of multimeric CPP-delivery modules for intracellular cargo delivery

TECHNISCHE UNIVERSITÄT DARMSTADT

vom Fachbereich Chemie
der Technischen Universität Darmstadt

zur Erlangung des Grades
Doctor rerum naturalium
(Dr. rer. nat.)

Dissertation

von Sarah Hofmann, M. Sc.

Erstgutachter: Prof. Dr. Harald Kolmar

Zweitgutachter: Prof. Dr. Heinz Neumann

Darmstadt 2024

Hofmann, Sarah: Conditional cell penetration of a masked CPP and optimization of multimeric CPP-delivery modules for intracellular cargo delivery.

Darmstadt, Technische Universität Darmstadt
Jahr der Veröffentlichung der Dissertation auf Tuprints: 2024

Tag der Einreichung: 5. September 2024

Tag der mündlichen Prüfung: 21. Oktober 2024

Der experimentelle Teil der vorliegenden Arbeit wurde unter der Leitung von Herr Prof. Dr. Harald Kolmar am Clemens-Schöpf-Institut für Organische Chemie und Biochemie der Technischen Universität Darmstadt von November 2019 bis Juli 2024 angefertigt.

Publications derived from this work:

S. Hofmann*, C. Dombrowsky*, D. Happel, C. Dessin, E. Cermjani, M. Cica, O. Avrutina, N. Sewald, H. Neumann, H. Kolmar, Conditional cell penetration of masked CPPs by an ADEPT-like approach, *ACS chemical biology* **2024**, *19*, 1320.

*Authors contributed equally to this work.

Further publications during doctoral thesis:

C. S. Dombrowsky, D. Happel, J. Habermann, **S. Hofmann**, S. Otmi, B. Cohen, H. Kolmar, A conditionally activated cytosol-penetrating antibody for TME-dependent intracellular cargo delivery, *Antibodies (Basel, Switzerland)* **2024**, *13*.

J. Lins, Y. A. Miloslavina, S. C. Carrara, L. Rösler, **S. Hofmann**, K. Herr, F. Theiß, L. Wienands, O. Avrutina, H. Kolmar, G. Buntkowsky, Parahydrogen-induced polarization allows 2000-fold signal enhancement in biologically active derivatives of the peptide-based drug octreotide. *Scientific reports* **2023**, *13*, 6388.

Contributions to conferences:

S. Hofmann, C. S. Dombrowsky, D. Happel, O. Avrutina, H. Neumann, H. Kolmar, An ADEPT concept for the intracellular delivery of cargos via cell penetrating peptides, *16th German Peptide Symposium* (28.08.2023 – 30.08.2023)

Table of Contents

1 Abstract

1.1 Zusammenfassung

Die Entwicklung von Biotherapeutika hat sich von wenig spezifischen niedermolekularen Arzneimitteln hin zu gezielten Verabreichungssystemen mit rezeptorspezifischen Liganden entwickelt, wodurch die therapeutische Dosis gesenkt und *Off-Target*-Effekte verringert werden. Die meisten Proteintherapeutika werden für spezifische Proteine auf der Zelloberfläche entwickelt und modulieren zelluläre Signalwege, die der Zielbindung nachgeschaltet sind. Aufgrund ihrer Größe und hydrophilen Eigenschaft sind diese Therapeutika zumeist auf extrazelluläre Ziele beschränkt, da diese die Zellmembran nicht durchdringen können. Da jedoch viele onkogene Erkrankungen auf dysregulierte intrazelluläre Protein-Protein-Interaktionen zurückzuführen sind, ist die gezielte intrazelluläre Verabreichung von Biomolekülen für die therapeutische Wirksamkeit nach wie vor sehr wünschenswert. Zellpenetrierende Peptide (engl. cell penetrating peptides, CPPs) bieten eine vielversprechende Strategie, da sie sich selbst und verschiedene Biomoleküle durch die Zellmembran hindurch transportieren können. Allerdings erfolgt diese Internalisierung nicht zellspezifisch, weshalb CPPs von einer erhöhten Selektivität für Tumorzellen profitieren würden. Dies gilt auch für den intrazellulären Transport größerer Frachtmoleküle, welche eine Multimerisierung von CPPs auf einem Gerüst erfordert. Dadurch findet eine erhöhte multivalente Interaktion mit der Zellmembran statt, sodass eine Zellpenetration ermöglicht oder gesteigert werden kann.

In dieser Arbeit wird eine Reihe von Studien vorgestellt, die darauf abzielen konditional aktivierte CPPs für die zellgezielte intrazelluläre Verabreichung zu entwickeln und multimere CPP-Verabreichungsmodule zu optimieren.

Im ersten Teil wurde das kationische und amphiphile Peptid L17E als Modell-CPP verwendet, um ein aktivierbares CPP zu erzeugen und den konditionalen und selektiven intrazellulären Transport eines angehängten Frachtmoleküls (Cargo) zu demonstrieren. Die unter physiologischen Bedingungen positiv geladenen Lysinreste des L17E-Peptids wurden mit Schutzgruppen maskiert, um ihre Rolle bei der zellulären Aufnahme zu untersuchen. Anschließend wurde ein enzymatisches Spaltsystem entwickelt, um das Peptid konditional zu aktivieren. Der Schutz aller fünf Lysinreste des Peptids führte zu einer Beeinträchtigung der zellulären Aufnahme, während die enzymatische Spaltung der Schutzgruppen zu einer Reaktivierung des intrazellulären Transports führte. Anschließend wurde der konditionale und selektive intrazelluläre Transport eines Toxins mittels eines ADEPT-ähnlichen Verfahrens in einem zellbasierten Assay untersucht. Die Verwendung eines HER2-targetierenden Antikörper-

Enzym-Konjugats führte dabei zu einer verstärkten Zelltötung bei der HER2-positiven Zelllinie im Vergleich zur HER2-negativen Zelllinie.

Zweitens wurde das Konzept, motiviert durch die Ergebnisse der konditionalen Aktivierung des aktivierbaren L17E-Peptids, auf ein Dextrangerüst ausgeweitet, welches mehrere L17E-Peptide trägt. Der intrazelluläre Transport eines Fluorophors zeigte jedoch keine eindeutigen Ergebnisse und die Demaskierung der Schutzgruppen des L17E-Peptids auf das Dextrangerüst konnte nicht verifiziert werden.

Im dritten Teil wurde Streptavidin als Multimerisierungsplattform untersucht. Mit seinen vier Bindungsstellen dient es als Gerüst für die gleichzeitige Bindung von bis zu vier biotinylierten Komponenten. So müsste jedes Cargomolekül oder jedes Dextran-Konjugat, das CPPs, therapeutisch relevante Proteine, rezeptortargetierende Liganden oder andere Effektormoleküle trägt, nur biotinyliert werden, um an Streptavidin gebunden zu werden. Da frühere Untersuchungen mit L17E-Dextran-Konjugaten auf Streptavidin eine erhebliche Zytotoxizität zeigten, war eine Optimierung erforderlich. Die Anzahl der L17E-Peptide pro Dextranmolekül wurde optimiert und weitere CPPs wurden untersucht. Dazu gehörte eine Variante des L17E-Peptids, das L17E/Q21E-Peptid, das cyclische CPP ATSP-7041 und ein α-helikales Peptid apCC-Di-B. Aus diesen neuen CPPs wurden Dextran-CPP-Konjugate synthetisiert. Mindestens zwei L17E- oder L17E/Q21E-Dextran-Konjugate pro Streptavidinmolekül mit eGFP als Cargo waren nötig für die intrazellulären Aufnahme des Konstrukts. Zellproliferationassays mit den Streptavidin-Architekturen zeigen an, dass auch bei solchen multivalenten Konstrukten für eine erfolgreiche zelluläre Internalisierung eine gewisse Zytotoxizität in Kauf genommen werden muss.

1.2 Abstract

The development of biotherapeutics has evolved from less specific small molecule drugs to targeted delivery systems using receptor-specific ligands, lowering therapeutic doses and reducing off-target effects. Most protein therapeutics are developed to target specific proteins on the cell surface, modulating cellular pathways downstream of target binding. Due to their large size and hydrophilic nature, these therapeutics are often limited to extracellular targets, as they cannot permeate the cell membrane. However, since many oncogenic disorders result from dysregulated intracellular protein-protein interactions, targeted intracellular delivery of biomolecules remains a highly desired strategy for therapeutic efficiency. Cell-penetrating peptides (CPPs) are promising molecules for intracellular targeting, as they can translocate themselves and various cargos across cell membranes. However, CPPs would benefit from

increased selectivity for tumor cells. This also applies for the intracellular delivery of larger cargos which may require multimerization of CPPs on a scaffold to enhance their ability to interact with the cell membrane for efficient permeation of the cell membrane.

This doctoral thesis presents a series of studies aimed at developing conditionally activated CPPs for cell-targeted intracellular delivery and optimizing multimeric CPP delivery modules.

In the first part, the cationic and amphiphilic L17E peptide was used as model CPP to generate an activatable CPP and demonstrate the conditional and selective intracellular delivery an attached cargo. The under physiological conditions positively charged lysine residues of the L17E peptide were masked with protecting groups to investigate their role in cellular uptake. An enzymatic cleavage system was then developed to activate the peptide conditionally. Protecting all five lysine residues of the peptide showed impaired cellular uptake, while enzymatic cleavage of the protecting groups resulted in the reactivation of intracellular delivery. A following uptake assay by an ADEPT (Antibody Dependent Enzyme Prodrug Therapy)-like delivery procedure using a HER2-targeting antibody-enzyme conjugate demonstrated the selective delivery of a toxin with increased cell killing observed on the HER2-positive cell line compared to the HER2-negative cell line.

Secondly, encouraged by the results on the conditional delivery by the activatable L17E peptide, the concept was extended to a dextran scaffold carrying multiple L17E peptides. However, the delivery of a fluorophore showed ambiguous results and demasking of the protecting groups of the L17E peptide on dextran could not be verified.

The third part investigated streptavidin as a versatile multifaceted delivery platform. With its four binding sites, it serves as a scaffold for binding up to four biotinylated components simultaneously. For example, any cargo or dextran-conjugate carrying CPPs, therapeutic drugs, receptor-targeting ligands or any other effector molecule would only need to be biotinylated to be assembled on streptavidin. Since previous investigations using the L17E-dextran conjugates on streptavidin showed significant cytotoxicity, optimization was required. The number of L17E peptides per dextran molecule was optimized and further CPPs were investigated. These included a cell lytic attenuated variant of the L17E peptide, the L17E/Q21E peptide, a stapled peptide ATSP-7041 and an α-helical peptide apCC-Di-B. Of these new dextran-CPP conjugates, at least two L17E- and L17E/Q21E-dextran conjugates per streptavidin molecule with an eGFP as cargo was required for intracellular delivery of the architecture. Cellular proliferation assays of these streptavidin architectures indicated for successful cellular internalization some cytotoxicity needs to be accepted.

2 Introduction

From the earliest papyrus records dating back to 3000-1500 B.C. in ancient Egypt where abnormal cell growth was attributed to the negative will of deities, to Hippocrates naming this phenomenon “cancinoma” and identifying it as a biological disease, to first “cures” by radical surgery procedures, a series of significant milestones followed that represent a transformative journey on which our understanding and approach to treating cancer has been revolutionized.[1]

Beginning with Marie and Pierre Curie’s revelation that radioactive substances are harmful to cells in the late 1890s, the concept of radiotherapy as a promising avenue besides surgery for cancer treatment emerged.[1] Notwithstanding these achievements, these methods proved ineffective for cancer patients in advanced stages. It was several decades later during World War II, that the accidental discovery of a DNA-modifying chemical agent (nitrogen mustard) causing myeloid and lymphoid suppression,[2,3] led to a significant turning point in tumor treatment. Especially upon learning that cancer cells replicate at a higher rates than healthy cells and the elucidation of the double-helical structure of DNA by James Watson and Francis Crick in 1953, the oncology field saw an intensified surge for the discovery of additional DNA-modifying drugs.[4] In the 1960s and 1970s, successes in the combination of radio- and chemotherapy i.e. chemoradiation therapy were seen.[5] This allowed lower doses of individual drugs, ensured a broader spectrum of interaction with cancer cells and slowed down drug resistance, which is still used today, for example in the treatment of Hodgkin’s Lymphoma.[6,7]

Nonetheless, it is widely recognized that a significant limitation of chemotherapeutic agents is their lack of specificity for targeting tumor cells. Although formulated based on his experience in infectious diseases, but also applicable to cancer, Paul Ehrlich already recognized in the 1900s that “we have to learn to aim chemically” and introduced the concept of a “magic bullet”.[8] In particular, the generation of monoclonal antibodies (mAbs) to target tumor-associated antigens was a remarkable achievement, especially with the advances in genetic engineering enabling the humanization of these antibodies often of murine origin.[9,10] This led to the development of the first two U.S. Food and Drug Administration (FDA) approved mAbs: the chimeric anti-CD20 monoclonal antibody rituximab for non-Hodgkin’s lymphoma and the humanized anti-human epidermal growth factor receptor 2 (HER2) monoclonal antibody trastuzumab for HER2-positive breast cancer in 1997 and 1998, respectively.[1,11] Advancing further, the adjoining of tumor-targeting mAbs to cytotoxic drugs gave rise to a novel class of protein therapeutics known as antibody-drug-conjugates (ADCs).[12] The conjugation of the drug to the tumor targeting antibody transported the payload directly to the tumor site, thereby

enhancing precision in treatment.[13] For instance, the FDA approved drug Kadcyla® comprises trastuzumab linked to emtansine, a microtubule inhibitor which prevents cell division and ultimately leads to cell death for HER2-positive breast cancers.[14] Antibodies and their derivatives are the most well-known and extensively studied targeting moieties for various biomedical applications, but there are also other non-immunoglobulin based proteins and peptides, which offer different advantages and characteristics.[15] These are for example, designed ankyrin repeat proteins (DARPins),[16] monobodies,[17] or affibodies[18]. The exploration of a broader range of targeting agents contributes to the development of more versatile and effective strategies in targeted therapies and diagnostics.

The aforementioned molecules are primarily tumor-cell surface targeting, however, extending their application to intracellular targets would expand the druggable target space even further.[19] There are many instances where the malfunction of an intracellular protein is at the root of oncogenic disorders, degenerative disorders or autoimmune diseases.[20] The p53 protein, for example, is frequently mutated in many human cancers. For targeting this mutant p53 protein (mutp53), several drugs have been developed, which either reactivate mutp53 to its wild-type function, degrade mutp53 and eliminate it, or induce cell death by targeting essential pathways that have become vulnerable due to mutp53.[21,22] Proteins play a pivotal role in transmitting signals that regulate normal cellular function, but mutations or abnormal activity of the proteins can lead to cellular dysfunction, often occurring through unregulated protein-protein interactions (PPIs).[19,20,23] With a conservative estimate of 130.000 PPIs of human proteins,[24] the multitude of intracellular interactions sites presents a promising foundation for therapeutic intervention.[19]

2.1 Protein therapeutics, peptide therapeutics and small molecules

Protein and peptide therapeutics and small molecules have demonstrated their potential in many areas of medicine including oncology, immunology, metabolic disorders or infectious diseases.[12,25–27] In 2023, the FDA approved 55 new drugs which include 17 biologics (12 monoclonal antibodies and 5 proteins/enzymes), 9 TIDES (peptides and oligonucleotides) and 29 small molecules.[28] The surge in global therapeutic market is fueled by the expected rise in incidences of chronic diseases. Alone in 2022, 20 million new cases of cancer were reported and 9.7 million deaths from cancer were reported worldwide.[29] The protein therapeutic market valued at USD 318 billion in 2022 is expected to exceed USD 549 billion by the end of 2031 under a compound annual growth rate (CAGR) of 6.3 %.[30] This growth represents the increasing demand for innovative treatments targeting specific disease markers and their

mechanisms, including the development of biologics for personalized medicines and biotechnology advancements for large-scale production of complex protein-based pharmaceutics.[31,32] Also the development of peptide therapeutics with a market value of USD 43 billion has seen significant increase with a CAGR of 6.1 % from 2024 to 2030.[33] Small molecules are a cornerstone of drug development due to their oral bioavailability, ease of synthesis and ability to target a wide range of disease pathways. For example the drug sunitinib, approved in 2017, inhibits tyrosine kinase activities of several vascular endothelial growth factor (VEGF) receptors and platelet-derived growth factors (PEGFs) to combat pro-angiogenic activity of various types of tumors.[34] The significant number of newly FDA-approved small molecule drugs from 2016 to 2023, comprising nearly 45 % of all approved drugs in that period, underlines the ongoing significance of small molecules.[35]

Most protein therapeutics are developed to target specific proteins located on the cell surface, whereupon target binding a cellular pathway is modulated downstream.[12,36] Due to their large size and hydrophilic nature, their therapeutic application is often limited to extracellular targets. However, the root of most oncogenic disorders comes from dysregulated intracellular PPIs that are implicated in all stages of oncogenesis (cell proliferation, cell survival, inflammation, invasion and metathesis). Therefore, it is important to identify and intervene on these disease-relevant PPIs by extending therapeutic applications to intracellular targets.[37] Although small molecule drugs can usually permeate the cell membrane, off-target effects are an issue. Small molecules have low molecular weight and consequently limited size, which naturally restricts the number of chemical moieties available to engage their target. Because they can only cover protein areas of 300-1000 $Å^2$, they often have lower specificity.[38] This problem may be compensated for with larger protein or peptide molecules, including enzymes, genetic material and transcription factors.[39–41] Due to their larger size, they are naturally able to cover larger PPI areas, often 1500-3000 $Å^2$ in size. This allows for comprehensive engagement with specific interaction sites, enhancing the potential for potent modulation of PPIs. Due to this specificity, protein and peptide therapeutics can achieve higher therapeutic effects at lower concentrations compared to small molecule therapeutics, but they are in most cases non-cell permeable. Therefore, to fully exploit the potential of these therapeutics, their targeted intracellular delivery remains an important field of study for research and medical applications.[42–45]

2.2 Strategies for intracellular delivery

The development of effective strategies for enhancing the cytosolic delivery of therapeutic compounds has developed into a large field over the years. Figure 1 depicts several strategies including physical methods such as microinjection or electroporation, or biochemical delivery platforms which include viral-vectors,[46] cell-penetrating peptides (discussed further in the next sections), nanoparticles or proteins (supercharged proteins[47] or cell-penetrating antibodies[48]). Additionally, the combination of different methods such as CPPs with nanoparticles as synergistic strategy have been investigated.[49–51] Gaining access to intracellular sites is a difficult task, because of the highly selective hydrophobic barrier presented by the cell membrane.[19,52]

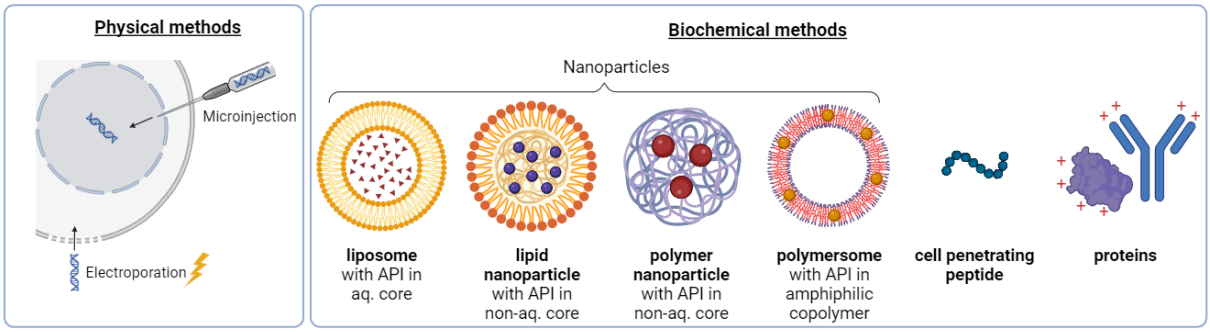

Figure 1| Physical and biochemical intracellular delivery platforms. API = active pharmaceutical ingredient. Created with Biorender.com.

2.2.1 The structure of the cell membrane

The cell membrane forms the boundary of a cell, creating a separation between the interior and exterior of an organism. It regulates the passages of substances, determining what can enter and leave the cell, usually permitting only small, non-charged molecules to diffuse through.[52,53] It is composed of a phospholipid bilayer with the fatty acid tails on the inside facing each other and flanked by hydrophilic head groups.[53] Figure 2 shows the general structure of the cell membrane, primarily comprised of three types of lipids: phospholipids, glycolipids and cholesterol. Phospholipids consists of two fatty acid chains connected to a glycerol molecule with a phosphate group attached to the glycerol.[53] With an additional choline, serine, ethanolamine or inositol attached to the phosphate head, they are collectively called glycerophospholipids i.e. phosphatidylcholine, phosphatidylserine, phosphatidylethanolamine, and phosphatidylinositol, respectively.[53] Phospholipids consisting of a sphingosine and fatty acid chain linked to a phosphate group are known as sphingophospholipids, that includes sphingomyelin.[53] While the choline-containing phospholipids sphingomyelin and phosphatidylcholine are primarily located on the outer leaflet, the amine-containing phospholipids phosphatidylethanolamine, phosphatidylinositol

and foremost phosphatidylserine are primarily enriched or fully localized in the cytosolic leaflet.[54,55] The fatty acid chains can be saturated or *cis*-unsaturated of varying lengths. *Cis*-unsaturated fatty acids are packed less tightly in the bilayer promoting fluidity in the membrane. It is the hydrophobic interior of the phospholipid bilayer, that renders the membrane impermeable to polar substances and many large biological molecules.[53]

The surface of the cell membrane also contains numerous proteins such as receptors, enzymes, transport or cell adhesion proteins. These proteins, as well as some phospholipids, are frequently glycosylated and accommodate carbohydrates that protrude from the cell surface. They play diverse roles in cell function, including structural support, the transport of molecules or electrons or cell signaling and communication with the outside environment.[52,56] Cholesterol is embedded within the cell membrane bilayer and plays a major role in membrane fluidity. It is characterized by a hydrophilic hydroxy group at its head and a four-ring steroid structure with a hydrophobic tail. The cell membrane is in a state of continuous motion, with the lipids moving laterally and, to a small degree, also vertically in a “flip-flop” motion.[56]

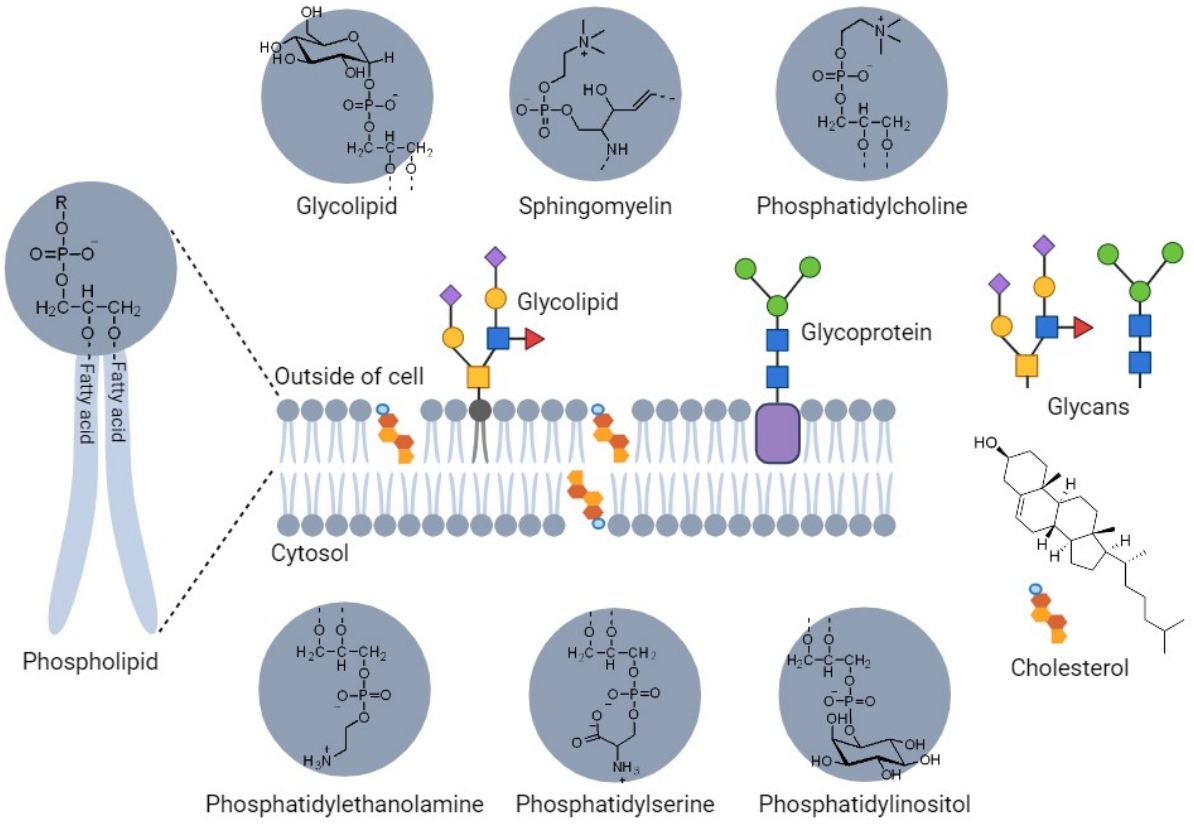

Figure 2| Components of the cell membrane. The cell membrane is composed of phospholipids, glycolipids, glycoproteins and cholesterol. Created with Biorender.com.

2.2.2 Cell penetrating peptides

Beginning with the discovery of the human immunodeficiency virus (HIV) trans-activator of transcription (TAT) protein's capability to penetrate cell membranes without causing damage,[57] numerous peptides of natural and synthetic origin with cell penetrating ability have been described of which their potential in research and therapeutic applications is highly recognized.[58] These peptides are known as cell penetrating peptides (CPPs) and possess the unique ability to not only translocate themselves, but also to facilitate the translocation of various cargos across the cell membrane. They have, for example, played a pivotal role in facilitating the intracellular delivery therapeutic drugs,[59] imaging agents, small interfering RNA (siRNA),[60] peptides[61–63] and proteins such as enzymes[64] and antibodies[65,66] or antibody fragments[67] which would otherwise not have access to the interior of the cell. Considering the physicochemical traits of CPPs, they are typically short, ranging from 5 to 30 amino acids in length and can exhibit both amphipathic (hydrophobic and hydrophilic) and cationic properties. Their positive charge at physiological pH is primarily attributed to multiple arginine or lysine residues, which interact with cell membranes and drive the internalization process. Frequently studied CPPs are the Pep-1 (KETWWETWWTEWSQPKKKRKV), penetratin (RQIKIWFQNRRMKWKKGG), nona-arginine (R9) and TAT peptides (GRKKRRQRRRPQ). They can be grouped into three main classes: primary amphiphatic, secondary amphiphatic and non-amphiphatic. While primary amphiphatic CPPs such as Pep-1 already exhibit segregated hydrophobic and cationic residues in their amino acid sequence, secondary amphiphatic peptides such as penetratin only reveal their hydrophobic and cationic segments in their folded state. In contrast, the TAT and R9 peptides are purely polycationic and unstructured.[68] CPPs do not only adopt various structural conformations, including α-helices and β-sheets, or random coils, but can interchange between structures, an example being penetratin which transitions from a random coil in water to α-helical or β-like conformations depending on its concentration and phospholipid composition.[69–72]

Cellular uptake mechanisms can be divided into energy-dependent or energy-independent pathways. The interaction of the positively charged CPP and negatively charged cell membrane destabilizes the cell membrane, creating multiple potential entry routes into the cell (Figure 3), which may not be limited to only one mechanism. For example, at lower concentrations, the arginine-rich TAT, antennapedia-homeodomain-derived antennapedia (Antp) and R9 peptides simultaneously use three endocytic pathways (clathrin-mediated endocytosis, caveolae-mediated endocytosis and macropinocytosis) on multiple cell lines, while at higher concentrations endocytosis-independent uptake mechanisms are preferred.[73]

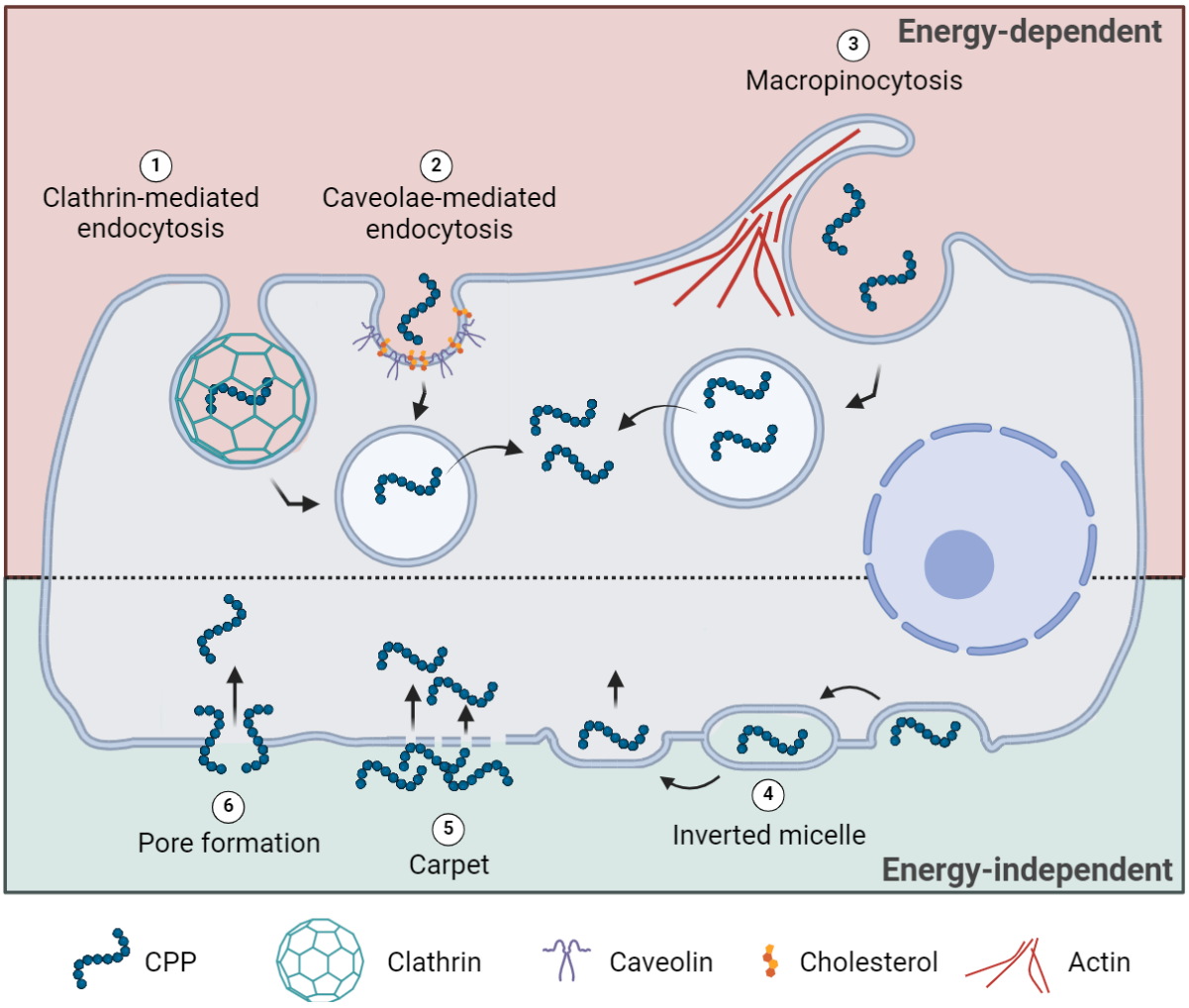

Figure 3| Illustration of energy-dependent and independent cellular uptake mechanisms. Created with Biorender.com.

Clathrin-mediated endocytosis, an energy-dependent pathway, involves the sequential formation of a clathrin-coated vesicle orchestrated by approximately 50 different proteins. Initiation occurs when adaptor proteins bind to plasma membrane lipids, recruiting clathrin and other coat-associated proteins to assemble into a lattice-like structure, forming a coat that induces membrane curvature and vesicle formation. The GTPase dynamin is subsequently recruited to the vesicle's neck, where it polymerizes and facilitates membrane scission through GTP hydrolysis.[74] Another internalization method is caveolae-mediated endocytosis, where the membrane coat is assembled by caveolin and integral proteins anchored to cholesterol in the cell membrane.[75] Macropinocytosis, on the other hand, which is the prevalent mechanism for the internalization of larger cargoes (greater than 30 kDa), involves the engulfment of substantial amounts of the surrounding fluid phase by the cell.[76,77] For energy-independent uptake, several models for direct penetration through the cell membrane have been proposed. The most common of these are the inverted micelle, carpet, and pore formation models

(including the toroidal/barrel stave model). In the inverted micelle model, the positive charge of the CPP interacts with the negatively charged phospholipid heads of the cell membrane, while the hydrophobic residues aid in reorganizing the lipid bilayer, allowing the CPP to insert itself into the membrane. In the pore formation model, CPPs form pores with the hydrophobic residues facing outward and the cationic hydrophilic residues facing inward. In the carpet model, multiple CPPs cover the cell membrane surface, leading to depolarization and destabilization of the membrane, ultimately resulting in direct permeation of the lipid bilayer.[78] Due to their heterogenous nature, and combined with a multitude of internalization mechanisms, it is complex, or even unfathomable, to strictly define the internalization pathway based on physicochemical and structural properties.[79] Cell penetration is also influenced by other factors such as the intrinsic physicochemical properties of the CPP itself and the cargo, the charge of the whole construct, which includes the ratio of CPPs to the cargo to be delivered, the working concentration, cell membrane composition i.e. cell type, temperature, and incubation time.[78,80]

Villaverde and coworkers showed that the uptake of green fluorescence protein (GFP) is positively influenced by the number of attached arginine residues and that different preferential uptake mechanisms prevail depending on the incubation time.[81] Regarding concentration, various publications showed that at low concentrations, uptake occurred primarily through endocytosis, which switched to direct penetration at higher concentrations ($>5\ \mu$M).[82,83] There have also been reports on cell penetration being dependent on the presence of heparan surface proteoglycans (HSPG) on the cell surface, which, with its negatively charged carboxyl and sulfate groups acts as an “electrostatic trap” for the CPP which is then internalized by adsorptive endocytosis.[82,84] On the contrary, this “electrostatic trap” has also shown to compromise cellular internalization , since the CPP remained largely adhered to the cell surface without internalization.[85] In a similar technology a thiol or maleimide-modified CPP is added in 2-5 fold excess to the CPP-cargo conjugate that temporarily anchors to the cell membrane by attaching to thiol-containing proteins or other macromolecules on the cell surface. This prolonged “lingering” of the peptide on the cell surface promotes the formation of nucleation zones and reduces membrane tension, preparing the cell membrane for permeation.[86,87] Furthermore, although cytosolic delivery of the peptides was not achieved, Tsien and coworkers revealed significant variability in the efficiency of cellular uptake into endosomes and lysosomes, influenced by factors such as CPP sequence, cyclization, and cell line.[88] A critical challenge that hinders CPP-based drug delivery is overcoming this endosomal entrapment. Therefore, understanding a CPPs physicochemical characteristics and internalization

mechanisms is an ongoing process and crucial for optimizing CPP-based strategies in drug delivery and cellular imaging applications.

The first and only FDA approved CPP-therapeutic to date is a RTP004-neurotoxin formulation developed by *Revance Therapeutics Inc.* (Nashville, Tennessee) for treatment of involuntary muscles spasms such as cervical dystonia or aesthetic treatment of glabellar lines in 2022.[89,90] RTP004 is a highly positively charged 35 amino acid peptide with 15 consecutive lysines in the core, flanked on both termini by a 9 amino acid TAT peptide with a single glycine residue as a spacer.[89] It attaches itself to the 150 kDa neurotoxin *DaxibotulinumtoxinA for Injection* (DAXI) by electrostatic interaction, and at the same time drives association to the negatively charged presynaptic nerve terminal. It is hypothesized that the prolonged lingering of the complex at the nerve terminal increases the likelihood that DAXI binds its synaptic vesicle glycoprotein 2 (SV2) target, and thus results in more internalized molecules.[91,92]

2.2.2.1 L17E peptide

CPPs found in nature often display a pattern of alternating cationic and hydrophobic amino acid residues in their sequence as previously mentioned. A notable example where hydrophobic and cationic residues face opposite sides is the L17E peptide, derived from the membrane lytic peptide M-lycotoxin in the venom of the wolf spider *Lycosa carolinensis*, discovered by Futaki and coworkers in 2017.[93] Substituting the leucine residue at position 17 of M-lycotoxin with a glutamic acid residue in the hydrophobic face of the α-helical amphiphilic peptide yielded the amino acid sequence IWLTALKFLGKHAAKHEAKQQLSKL (L17E) with attenuated lytic activity towards cell membranes. The reduced cytosolic delivery observed with the glutamic acid substitutions L6E and L9E in the L17E peptide highlights the importance of uncharged amino acids on the peptide's *N*-terminus for membrane interaction. Five lysine residues provide the peptide with a positive charge, aiding its interaction with negatively charged membranes. For instance, at a concentration of 40 μM, the L17E peptide has demonstrated its capability to efficiently transport bioactive proteins like the ribosome inactivation protein saporin, Cre recombinase, and antibodies (IgG) after 1 h incubation.[93,94] Initially, it was hypothesized that the L17E peptide enters cells via endocytosis with the negative charge from the glutamic acid residue preventing cell membrane lytic activity. As the peptide and coincubated cargo are endocytosed, the resulting pH decrease through endosomal maturation may protonate the glutamic acid residue. Consequently, the diminished negative charge results in an increased overall positive charge and a larger hydrophobic face of the L17E peptide. This would promote the disruption the endosomal membrane and release of its contents into the cytoplasm.[93] A follow up study however, proposed that uptake of the L17E peptide occurs differently. Rather,

it stimulates actin polymerization, resulting in the formation of permeable, ruffled cell membranes, which subsequently leads to macropinocytosis. However, before macropinocytosis is complete, these ruffled cell membranes are destabilized, such that the transient passage of biomacromolecules into the cytoplasm is enabled (Figure 4).[94]

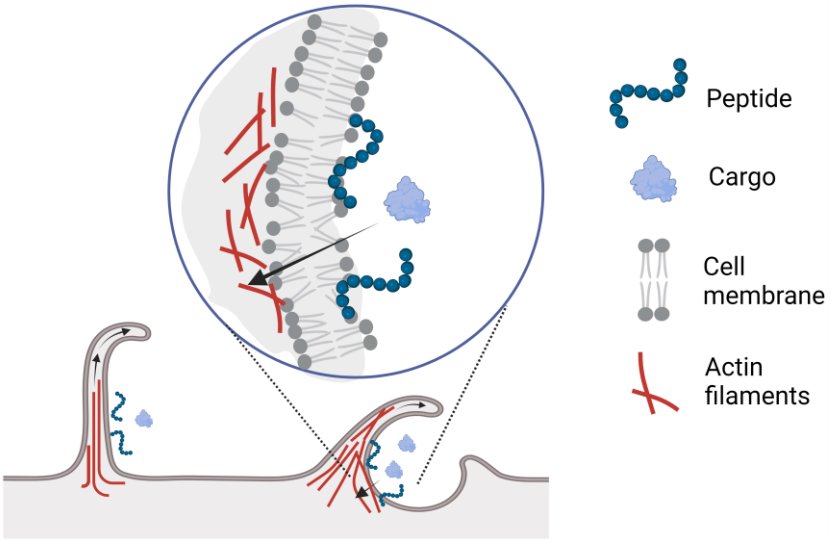

Figure 4| Schematic representation of the membrane ruffling process induced by L17E for the cytosolic delivery of co-incubated cargos. Adapted from Akishiba et al. [94] Created with Biorender.com.

2.2.2.2 L17E/Q21E peptide

Assuming the assembly of CPPs on the cell membrane is a crucial initiator for permeation of the cell membrane, dimerization of CPPs may lead to enhanced permeation. Dimerization of the L17E peptide however, resulted in significant cytotoxicity due to synergistic effects in cell membrane interaction. Already at concentrations as low as 1-2 μM, the L17E peptide dimer exhibited 80% cell viability only.[95] Furthermore, intracellular delivery of fluorescently labelled 10 kDa dextran at this concentration was considerably lower compared to the L17E peptide monomer at a concentration of 40 μM. Consequently, alongside the L17E peptide, Futaki and coworkers also developed the L17E/Q21E peptide which contained a second glutamic acid residue at position 21 instead of a glutamine residue (IWLTALKFLGKHAAKHEAKQELSKL). While the L17E/Q21E peptide exhibited inferior delivery efficiency in comparison to L17E, dimerization of the L17E/Q21E peptide by *N*-terminal fusion resulted in a comparable level of intracellular delivery to solitary L17E at a reduced peptide concentration (5 μM compared to 40 μM). This was evidenced by the diffuse cytosolic signals of fluorescently labelled 4 kDa and 70 Da dextran throughout the cytosol and successful delivery of an antibody targeting the nuclear pore complexes of the nuclear membrane.[95]

2.2.2.3 HAad peptide

Under consideration of the distinct compositions of cell and endosomal membranes, as well as the pH decrease within endosomes, Futaki and coworkers also engineered a lipid-sensitive and pH-responsive endosomal-lytic peptide, which they called HAad.[96] After uncovering the entry mechanism of the L17E peptide involving membrane ruffling and its transient passage into the cytosol during early stages of endocytosis, rather than the expected endosomal escape route, they aimed to design a peptide with enhanced endosomal escape capabilities as endocytosis remains a central uptake mechanism for large biomacromolecules. This was to using a peptide that becomes more hydrophobic under the slightly acidic conditions of the endosomes, typically around pH 5.0. Building upon the L17E peptide as foundation, much focus was directed towards the histidine and glutamic acid residues. For instance, the carboxyl moiety in the side chain of glutamic acid (pK_a 4.07) may not be fully protonated at endosomal pH and the minimal increase in hydrophobicity in the endosome possibly not sufficient for the peptide to exert its full lytic activity on the endosomal membrane. Therefore, as first consideration, glutamic acid was substituted for 2-aminoadipic acid (Aad) (pKa 4.21). The higher pKa value possibly results in protonation to higher proportion in endosomes and is therefore more hydrophobic at endosomal pH, leading to more favorable circumstances for endosomolysis. The second point they considered are the two histidine residues (pK_a 6.0) of the L17E peptide that are preferably protonated at endosomal pH, which, in this case, decreases hydrophobicity. Therefore, they replaced the histidine residues with uncharged alanine residues. However, due to significant toxicity observed with these substitutions in the L17E peptide, possibly due to an excess of hydrophobicity, the authors applied these alterations to the L17E/Q21E peptide, yielding the final peptide HAad (IWLTALKFLGKAAAKAXAKQXLSKL; X denotes Aad). This endosomolytic HAad peptide outperformed the L17E peptide in the intracellular delivery of an fluorescently labelled IgG and Cre recombinase which was demonstrated in a Cre-loxP recombination assay.[96]

2.2.2.4 ATSP-7041 peptide

The ATSP-7041 peptide is a stapled α-helical and amphiphilic peptide discovered by Sawyer and coworkers as a dual inhibitor of both mouse double minute 2 (MDM2) and MDMX (also called MDM4).[97] MDM2 and MDMX are negative regulators of the tumor suppressor p53, also referred to as “the guardian of the genome”. As a transcription factor that triggers cell cycle arrest upon activation in response to DNA damage and cellular stress, p53 safeguards cells from malignant transformation by facilitating DNA repair or promoting apoptosis.[98] Indeed, p53 mutations are most frequently observed in human cancers,[99] but also MDM2 and MDMX

overexpression in some cancers suppress wild-type p53 function. In the latter case, inhibition of MDM2 and MDMX could potentially restore p53-dependent cell cycle arrest, wherefore the ATSP-7041 peptide was first developed through iterative lead optimization of a phage display derived peptide. The ATSP-7041 peptide comprises a 17 amino acid sequence including an unnatural cyclobutyl alanine (Cba) amino acid and staple moiety under the *i*, *i+7* macrocyclization scheme, with favorable cell penetrating properties and stability under physiological conditions.[97] In a recent publication, more than 350 ATSP-7041 analogues were evaluated to gain insight into the favorable physicochemical properties of stapled peptides for cell penetration and on-target intracellular activity. While F3, W7 and Cba were critical for its inhibitory function against MDM2 in the single-digit nanomolar range, its α-helical conformation promoted through the *i*, *i+7* staple and its apolar face promoted cell penetration. The polar face together with hydrophilic sequences rescued the peptide from poor solubility and cell toxicity.[100]

2.2.2.5 apCC-Di-B peptide

The apCC-Di-B peptide is the basic, arginine-rich cell penetrating component of a rationally designed two-component antiparallel coiled-coil dimer by Woolfson and coworkers to examine and localize the exogenous delivery of cargos to intracellular proteins or organelles. Its binding partner, the acidic and complementary apCC-Di-A peptide, can be fused to an intracellularly localized component. This allows a fluorescently labelled apCC-Di-B peptide to seek and bind the complementary peptide, thereby effectively labelling the intracellular component.[101] In addition to a fluorescent label, the authors demonstrated the delivery of a functional “KinTag” sequence.[102] This sequence binds endogenous kinesin-1 light chains, which are associated with the kinesin-1 heavy chain motors responsible for driving the movement of, for example, organelles, vesicles or proteins, along microtubules. By fusion of the apCC-Di-A peptide and green fluorescent protein (GFP) to the lysosomal-associated membrane protein 1 (LAMP1) on late endosomes and lysosomes, internalized KinTag-apCC-Di-B and resulting apCC-Di-AB dimerization bridged the lysosomes to the kinesin heavy chain. Dispersion of the lysosomes from the perinuclear region and their accumulation at the cell periphery, indicated lysosomal transport by the kinesin heavy chain had occurred.[101]

2.2.3 Modular approaches and multimerization platforms

For CPPs fused to large protein therapeutics, it can be challenging to efficiently traverse the cell membrane and gain access to the cytosol. The prevailing cellular uptake mechanism of these larger CPP conjugates is endocytosis, requiring an endosomal escape step.[58] This only lands 1-7 % of the CPP-protein conjugate in the cytosol, depending on the cell line and cargo.[103–106]

In such instances, an approach fusing multiple CPPs to the cargo of interest can be chosen to increase the local concentration of the CPP. However, it is crucial to consider the biological activity of the cargo and where the CPP can be positioned, as the presence of the CPP may potentially impair its functionality.[107] Furthermore, a balance between CPP toxicity and uptake efficiency needs to be found.[108]

Several multivalent CPP strategies have been reported. In one strategy, protein oligomerization domains were attached to the CPPs. For instance, the amino acid residues 325-355 corresponding to the tetramerization domain of human p53 (hp53^{tet}) were covalently added at the *C*-terminus of decaarginine and decalysine. This domain self-assembled in solution in tetravalent form and thus a tetrameric CPP construct was obtained. Compared to the monovalent CPP, the tetravalent CPP delivered peptide nucleic acids (PNA) and DNA more efficiently into cells.[109,110] In another example, the fusion of at least seven arginine residues to an enhanced green fluorescent protein (eGFP) was required for its self-assembly to nanoparticles. This increase in positive charge, but also CPP-multivalency, positively influenced the amount of internalized protein.[81] Other multimerization platforms for peptides include adamantane[111] or tris-based scaffolds such as TREN (tris(2-aminoethyl)amine)[112], but also linear or branched peptide templates consisting of multiple lysines for peptide conjugation with spacers in between.[113,114] CPP multivalency can also be achieved purely by electrostatic interaction of the CPP to the cargo, as in the FDA-approved RTP004-neurotoxin CPP-therapeutic mentioned in chapter 2.2.2.[89] The specificity of antibodies is also a valuable feature to utilize, not only for binding extracellular targets, but for the binding of intracellular targets as well. Pringle et al. conjugated the TAT peptide in 1-5 copies to an antibody and saw enhancements in internalization with increasing TAT copies on the antibody.[115] While both cases showed enhanced cellular uptake of the antibody if the respective antigen of the antibody was also present on the cell surface, the examples implied multiple CPPs are necessary for delivering large cargos.

2.2.4 Dextran

Dextrans are polysaccharides primarily composed of α-(1,6)-linked D-glucose units with various branches including α-(1,2), α-(1,3) or α-(1,4) linkages (Figure 5). Derived from microbial sources, the pattern of branching depends on the microbial strain producing it and the cultivation conditions used during production.[116,117]

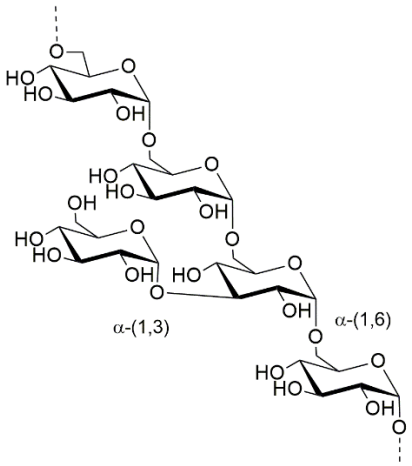

Figure 5| Structure of dextran with α-(1,6)-linked D-glucose units with α-(1,3)-branches.

Lactic acid bacteria (LAB) in their natural habitat produce lactic acid from carbohydrate fermentation, but for certain LAB such as the *Leuconostoc, Weissella* and *Streptococcus* species, the exposure to sucrose as carbon source in the medium results in dextran production. Dextran synthesis is performed by extracellular dextransucrase enzymes that are secreted by the LAB. While the presence of sucrose triggers the secretion of dextransucrase into the surrounding medium in the *Leuconostoc* and *Weissella* species, other species secrete the enzyme independently of sucrose.[118] In the process of dextran production, dextransucrase transfers D-glucopyranosyl units from sucrose to the reducing end of the growing dextran chain, thereby releasing fructose as byproduct (Figure 6).[116]

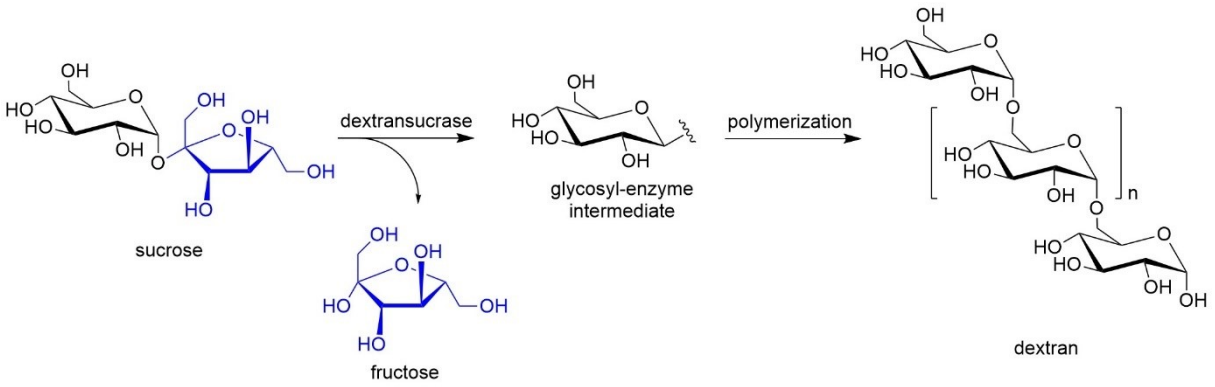

Figure 6| Synthesis of dextran by dextransucrase from sucrose in lactic acid bacteria.

The industry uses the bacterial strain *Leuconostoc mesenteroides* NRRL B-512F to produce dextran. Dextrans produced by fermentation using *L. mesenteroides* NRRL B-512F are FDA approved and find applications in various fields, such as in the health, cosmetic and food industry.[119] Commercial production is primarily performed in batches using a sucrose-rich medium by a process known as whole cell fermentation.[119,120] Native dextran has a high molecular weight (ranging from 9 MDa to 500 MDa) and high polydispersity. However, for

clinical applications such as blood substitutes, low molecular weight dextran with reduced polydispersity is preferred.[119] These can be obtained by acid or enzyme hydrolysis and subsequent fractionation of high molecular weight dextran.[121,122] Also cell-free cultures can be used to produce dextran using dextranase, but this requires steps to stabilize the enzyme.[123]

Dextran derived from *L. mesenteroides* NRRL B-512F is of particular interest due to its favorable properties. It exhibits a well-defined structure with minimal branching: 5 % are α-(1,3) branched, while 95 % are α-(1,6)-linked,[116] and is biocompatible and biodegradable, as it can be depolymerized by various dextranases that occur in the liver, spleen, kidney and colon.[124,125] Moreover, its low antigenicity and stability make it attractive for biological applications. Clinical grade dextrans with molecular weights of 40, 60 or 70 kDa (named dextran 40, 60 and 70) in 6-10 % aqueous solutions are used as plasma volume expanders to replace blood losses. Dextran 40 additionally improves blood flow, wherefore it is also used as a blood flow enhancer.[119] Apart from clinical applications, dextran is also an interesting polysaccharide for chemical modification, as various functionalities can be prepared by tuning and adjusting the functional groups introduced. In the food industry, dextran has been used as a hydrocolloid, for example in retaining moisture in bakery products, or improving textural properties, by serving as a thickening agent.[126] In the chemical industry, dextran is the principal component of matrices in size exclusion columns. Thereby, dextran is cross-linked using epichlorohydrin under alkaline conditions such that it becomes insoluble. Commercially this product is known as Sephadex®, a registered trademark of Cytiva.[127] Cross-linked dextran with additional charged groups are used as matrix in ion exchange columns. These include for example carboxymethyl Sephadex® and diethylaminoethyl Sephadex®.[128]

In the last decades, dextran has been extensively explored for drug delivery.[125] Its predominantly linear structure and numerous hydroxyl groups provide an appealing scaffold for conjugating imaging agents, drugs, proteins or antibodies. Especially for small compounds, the formulations with dextran or direct conjugations to dextran increases their molecular weight such that its half-life is extended due to reduced renal clearance. For instance, dextran hydrogel drug carriers developed have shown a slow and continuous release of drugs or antibiotics.[129,130] The antioxidant catalase with potential application in cancer therapy, demonstrated improved pharmacokinetics when conjugated to dextran.[131] Likewise, the anticancer agent doxorubicin (DOX) conjugated to dextran exhibited a prolonged half-life, reduced toxicity, high plasma concentrations and enhanced activity compared to free DOX.[132] Furthermore, Schneider et al. demonstrated high hydrophilicity and potency of an antibody-drug-dextran conjugates carrying up to 11 hydrophobic monomethyl auristatin E (MMAE)

toxins.[133] Hydrophilicity was also maintained for a tumor spheroid penetrating nanobody-dextran conjugate decorated with hydrophobic photosensitizer.[134]

Dextran has two orthogonal modification sites. The first site is the reducing end of the polysaccharide chain that is in equilibrium between the cyclic-closed chain and acyclic-open chain form as an aldehyde moiety. This aldehyde can undergo a variety of reactions with primary amines, hydrazides or aminooxy derivatives forming imines, hydrazones or oximes, to mention a few representable examples.[135] In the reaction with amines, the resulting imine can be subsequently stabilized by reduction to an amine using reducing agents such as sodium cyanoborohydride.[133] Also the introduction of spacers at the reducing end of dextran for further conjugation has been explored, for example with hexamethylenediamine, that enabled conjugation of catalase through carbodiimide activation of glutamic and aspartic acid residues on the protein´s surface, or pentamethylenediamine, that undergoes a microbial transglutaminase (mTG)-catalyzed transamidation reaction with a glutamine residue of an antibody.[133]

The second orthogonal modification site on dextran are the hydroxy groups of the repeating units. In general, there are many methods to react the hydroxyl groups of dextran: esterification, etherification, thiolation, silylation or amination amongst others.[119] Early amination methods made use of cyanogen bromide for activation of the hydroxy groups for subsequent coupling with an amine,[136] but apart from the high toxicity accompanied with cyanogen bromide, the dextran produced was highly heterogenous and unstable. Conversion of the hydroxyl groups to reactive aldehydes by periodate oxidation is a better method. Typically, the periodate ion causes bond breaking between the C_3-C_2 or C_3-C_4 positions, yielding two aldehyde groups.[137] For example, Curcio *et al.* used this method to attach DOX *via* an acid-labile imine bond to dextran, but also additionally used the unreacted hydroxyl groups of dextran in an esterification reaction with carboxylic moieties of lipoic acid (sensitive to glutathione), to generate a pH- and redox-sensitive, self-assembling prodrug polymer.[138] However, the dialdehyde intermediates resulting from periodate oxidation are highly reactive, such that they react with neighboring hydroxyl groups to form hemiacetal structures in the dextran chain. These unpredictable alterations to the dextran backbone changes solubility and viscosity, as well as decreased average molecular weight and increase in polydispersity.[137] A more reliable method to modify hydroxyl groups is perhaps carboxyethylation by alkylation of the hydroxyl groups with acrylamide with subsequent hydrolysis of the amide. This method was used to covalently attach pro-apoptotic BH3 peptides in multiple copies to the dextran backbone with well-defined manner. 2D-NMR analysis showed that carboxyethylation occurs exclusively on the C_2-position

of the glucose unit.[139] Besides spatial control, the number of carboxyl groups per dextran can be controlled stoichiometrically by the amount of acrylamide used, that governs the amount of drug loaded.[133] In our research group, the covalent attachment of multiple L17E peptides to dextran has demonstrated the efficient cytosolic delivery of biomolecular cargos.[140]

2.2.5 Streptavidin

Another possibility for multimerization is the use of streptavidin. Streptavidin (Figure 7) is a protein that is produced by the bacterium *Streptomyces avidinii*.[141]

Figure 7| Structure of streptavidin (pdb: 1SWB). The tetrameric structure is stabilized through can der Waals interactions that occur between the eight-stranded β-barrel subunits.

It is a 55 kDa tetramer, whereby the tetramer binds biotin with femtomolar affinity (4.0×10^{-14} M).[141] Similar affinity was observed for a monovalent streptavidin variant where three of the four subunits were mutated such that biotin could not bind.[141] The streptavidin subunits have a β-barrel structure formed by an eight-stranded, anti-parallel β-sheet with hydrogen-bonds to the adjacent strand in a staggered manner and hairpin loops. The *C*-terminus is extended out of the β-barrel that symmetrically pairs with a second subunit, forming an extended β-sheet. In turn, these dimers pair with another dimer to form the tetrameric structure that is stabilized by van der Waals interactions between the β-barrel interfaces that have complementary curvatures.[142] Monovalent streptavidin is therefore unstable and requires major reconstruction to exist in this form.[143]

Biotin binds to Ser^{45} in the loop connecting the β-strands 3 and 4 (L3/4) through a hydrogen bond to biotin upon binding, which closes over the binding pocket forming a lid.[144] Although there is no evidence for subunit cooperative activity upon biotin binding, the closing of the lid causes a slight flattening and wrapping that changes the β-barrel curvature. Consequently, the hydrogen-bond geometry and dimer-dimer interaction are altered. The tetramer adjusts to these changes to complement the new orientation by twisting slightly.[142]

Streptavidin is commonly used for immobilization and detection of biotinylated molecules, for example in protein binding studies, yet the utility of a stable non-covalent interaction with biotin was also recognized in drug delivery.[145] The recognition of streptavidin for clinical applications, efforts have been made to design streptavidin mutants with reduced immunogenicity.[146] Leveraging streptavidin's tetrameric structure, the four binding sites allows the assembly of up to four biotinylated components simultaneously,[141] including CPPs.

2.3 Strategies for targeted intracellular delivery

While CPP-multivalency can aid in the intracellular delivery of a cargo, CPPs do not show cell specificity. To utilize CPPs to their full potential, CPP-cargo delivery needs to be performed in a targeted manner, which is probably the greatest obstacle that needs to be overcome. Especially for *in vivo* application for drug delivery, it is important to protect healthy cells to reduce side-effects. Therefore, a handful of strategies such as CPPs with tumor-targeting moieties and tumor microenvironment responsive CPPs (activatable CPPs) have been devised, as illustrated Figure 8 and discussed in the next sections.

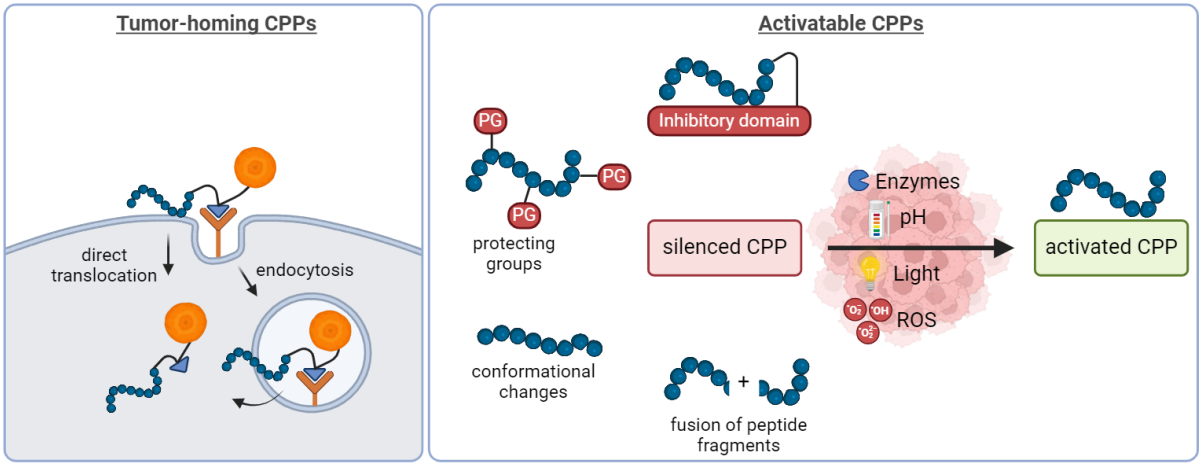

Figure 8| Strategies for targeted intracellular delivery using CPPs. Tumor-homing CPPs recognize receptors on the cell surface, which mediates cellular uptake. Activatable CPPs require reversion to their activated form triggered by conditions unique to the target site. Created with Biorender.com.

2.3.1 CPPs with tumor-targeting sequences

Tumor cells and tumor vasculature have unique markers on their cell surface that can be used as targets to direct the CPP to the tumor site.[147,148] Foremostly by phage display, tumor targeting amino acid sequences have been identified that, conjugated to CPPs, to act as tumor homing moieties, directing the CPP to its target cells. Two of these tumor homing peptides are the cyclic PEGA peptide that binds aminopeptidase P of malignant breast tissue[149] and the fibrin-binding linear CREKA peptide that binds fibrin, also frequented in malignant tumors.[150] Conjugation of a CPP-toxin to these tumor homing peptides saw increased delivery to the target

tumor cells.[150,151] Another tumor homing peptide is the RGD tripeptide, which is known to bind $\alpha_v\beta_3$ integrin protein highly expressed on endothelial cells in angiogenic vessels with high affinity.[152] The inhibition of endothelial cell proliferation deprives the tumor of vital nutrients necessary for growth. Following the failure of the highly anticipated cyclic RGD variant *cilengitide* in phase III clinical trials, research based on the RGD motif propelled, also in direction of CPPs.[153,154] The Neundorf group cyclized RGD using a diketopiperazine scaffold, generating the integrin ligand c(DKP-RGD)and conjugated it to a CPP-toxin. Using three cell lines with low, medium and high $\alpha_v\beta_3$ integrin expression, they described cellular uptake using a "kiss and run" model, wherein the interaction of the targeting ligand with the receptor prolongs the residing of the CPP such that internalization is mediated.[155] Prolonged retention and internalization at the target site is also advantageous for the delivery of imaging probes, which results in increased imaging contrast due to reduced washout.[156] Tumor-homing peptides have also been used to guide nanoparticle delivery vectors. For instance, an octaarginine (R8) CPP conjugated to a reverse RGD sequence (dGR), which binds both the $\alpha_v\beta_3$ integrin as well as neuropilin-1 receptors, was packaged into paclitaxel (PTX)-loaded liposomes. This PTX-R8-dGR liposomal formulation was preferentially internalized into glioma cells.[157]

In some cases, a tumor homing peptide can also have cell penetrating abilities. For example, Matsushita and coworkers first identified amino acid sequences as CPP candidates by mRNA display technology. Subsequently they screened for cell penetrating abilities on multiple cell lines to identify peptides with both cell penetrating and tumor-homing function.[158] Based on their identified peptides, Schmuck and coworkers used a tumor-homing CPP targeting MCF-7 breast cancer cells. By delivery of an anticancer drug, they showed preferential killing of MCF-7 cells compared to HeLa cells or healthy fibroblasts.[159]

While it is easier to modify tumor homing peptides with CPPs and drug cargo, tumor targeting moiety can take the form of an antibody. Gaston et al. conjugated various CPPs to a full-length tumor-targeting antibody. Antibody-CPP delivery could be achieved for ca. 5 % of the cells at 5 μM concentration and 24 h incubation, whereby only ca. 30 % of the cell population were available to produce a cellular response (due to transfection efficiency) with about 10 % of the applied dose internalized into the cells. Non-binding antibody-CPPs hardly produced any response in cellular uptake.[65]

2.3.2 Activatable CPPs

A solution to the non-specificity of CPPs is the generation of activatable CPPs (ACPPs). These CPPs are responsive to the altered conditions found in the tumor microenvironment, such as

the presence of tumor-associated enzymes and reactive oxygen species (ROS) or it´s lowered pH (~6.8) due to increased aerobic glycolysis compared to healthy tissue.[160] Also, external triggers for CPP activation such as light irradiation, can used to activate cellular uptake at the tumor site. There are a number of possibilities to generate activatable CPPs, for example by masking the positive charges of a cationic CPP by introducing inhibitory domains or protecting groups that are conjugated to the peptide by a trigger responsive linker.[161] This also serves as a solution to overcome the polycation dilemma in drug delivery, where cationic CPPs are impaired by electrostatic interactions with serum proteins, hindering *in vivo* application.[162] Other methods include inducing a conformational change of the CPP to activate cell penetrating ability, or the fusion (or polymerization) of peptide fragments to generate a CPP at the target site.[161]

2.3.2.1 Enzyme-activatable CPPs

Tsien and coworkers generated the first ACPP in 2004 by fusing a polyanionic domain (a polyglutamate sequence) to a cyanine5 (Cy5)-polyarginine CPP via matrix metalloprotease (MMP-2 and MMP-9, overexpressed in many tumor types)[163] sensitive PLGLAG linker. Clear contrast in fluorophore delivery could be observed between healthy tissue and MMP-expressing fibrosarcoma cells.[164] Intravenous injection of the ACPP demonstrated reduced toxicity and improved distribution to the target site, while remaining relatively non-adherent to healthy tissues.[165] However, optimization in the delivery to the cytosol is required, since the ACPP still remained largely entrapped in endosomes. In a follow up study, successful delivery of the ACPP into various tumor types validated the MMP-triggered CPP delivery method.[166] CPP activation by MMP cleavage has also been extended to ACPP decorated nanoparticles and micelles.[167,168] Apart from MMPs, the use of other exogenous proteases to cleave the masking polyanionic domain from the CPP has been shown. For example, neutrophil elastase that triggered the delivery of a Cy5 dye with five-fold contrast to tumor cells[169] or the serine protease thrombin where activation of the CPP served as a probe to detect thrombin activation.[170] Both these enzymes have been implicated in several cancers and diseases.[171] Also aminopeptidase N or dipeptidyl peptidase IV were used to cleave alanine or glycine-proline masking motifs on the lysine residues of the TAT CPP respectively that led to conditional cellular uptake.[172]

2.3.2.2 pH-activatable CPPs

ACPPs responsive to the acidic tumor microenvironment is a frequently used technique to target tumors. For instance, Han et al. used a low pH insertion peptide (pHLIP) that gains transmembrane activity due to conformational change to an α-helix under acidic tumor microenvironment conditions. pHLIP coated on magnetic nanoparticles with the

chemotherapeutic drug gemcitabine showed remarkable tumor growth inhibition in tumor mice models.[173] Zhang *et al.* modified an amphiphilic cationic peptide consisting of lysine and leucine residues to generate a pH-activatable CPP, by substitution of all lysine and two leucine residues with histidine residues. With a pKa of about 6.5, the histidine was protonated in the acidic tumor microenvironment such that cell penetrating activity was restored. Furthermore, the α-helical content of the CPP increased under acidic conditions, which also facilitates cell penetration.[174] Similarly Xiang et al. made use of the protonation of histidine for CPP activation. The ACPP was composed of the R8 CPP linked to a masking polyanionic domain comprised of glutamic acids with histidine residues, via an acid-labile linker (hydrazone). Under exposure to the lower pH in the tumor microenvironment, cleavage of the hydrazone linker and protonation of the histidine residues in the polyanionic domain promoted detachment of the polyanionic domain from the CPP and delivery of the payload into the cytoplasm.[175]

2.3.2.3 ROS-activatable CPPs

Reactive oxygen species (ROS)-activatable CPPs become activated at tumor cells that exhibit elevated levels of ROS, such as H_2O_2. For example, Tsien and coworkers designed a ROS-sensitive ACPP comprising of a FITC-labelled cationic R9 CPP and Cy5-labelled E9 polyanionic domain adjoined by a 4-boronic mandelic acid moiety. Reaction of the phenylboronic acid with H_2O_2 to phenol and release of CO_2 liberated the anionic domain that could be observed by fluorescence resonance energy transfer (FRET).[176]

2.3.2.4 Light-triggered-activatable CPPs

Light-sensitive ACPPs can be designed by introducing photoremovable protecting groups (PPGs), that are cleaved by irradiation with UV light. For example, lysine residues of the CPP penetratin were masked with the well-known o-nitrobenzyl photocage, that upon removal demonstrated enhanced intracellular delivery of a proapoptopic drug.[177] Another PPG is 7-diethylaminocoumarin (DEACM) that has been used in our research group to mask the L17E peptide. Uncaging was efficient, with over 95 % of the peptide in deprotected form by irradiation for 2 min, however the hydrophobic photocage compromised solubility of the peptide.[140] Alternatively, UV light irradiation has also been used to induce conformational changes of an azobenzene linker introduced within a CPP. This switches from a low-energy trans-conformation to a cis-conformation, controlled the secondary structure of a CPP to an active form.[178]

2.3.3 ADEPT

The antibody-directed enzyme prodrug therapy (ADEPT) is a two-step therapeutic strategy to cancer cell killing that aimed to improve the selectivity of small anticancer drug molecules. First, an enzyme that is conjugated to a tumor-targeting antibody is intravenously injected. The antibody component then binds to the antigen, delivering the enzyme directly to the tumor site. After allowing some time for clearance of the antibody-enzyme conjugate from the blood and healthy tissues, a nontoxic prodrug can then be administered. Only when the prodrug reaches the antibody-enzyme conjugate at the target site, can it be converted into a potent cytotoxic drug and exert its cytotoxic effects. This strategy inherently allows the accumulation of higher concentrations of active drug at the target site compared to an intravenously injected drug that is distributed around the body. Furthermore, one antibody-enzyme conjugate can catalyze the activation of many prodrugs at the site, which may also enable the killing of cells in the tumor microenvironment by bystander effect.[179]

The enzymes in ADEPT need to be carefully selected. Apart from being able to activate a prodrug, their catalytic properties should ideally be distinct from any other enzyme in systemic circulation to prevent pre-activation of the prodrug before it reaches the target site. Furthermore, it needs to be stable under physiological conditions and when conjugated to the antibody, must retain its enzymatic activity. As an enzyme located exclusively in the tumor microenvironment has not been found, the enzymes most commonly used for ADEPT were of non-mammalian origin with no mammalian homologue, such as carboxpeptidase G2 (CPG2), cytosine deaminase or β-lactamase.[179] Only the ADEPT system with CPG2 as enzyme reached clinical trials. It was conjugated to a non-internalizing murine anti-carcinoembryonic antigen monoclonal antibody A5B7 and used for the activation of a nitrogen mustard-based prodrug CMDA. Localization of the antibody-enzyme conjugate to the tumor could be observed. After 72h, the prodrug was administered. ADEPT showed partial responses, generating DNA inter-strand crosslinks in the tumor cell in the patients with advanced metastatic colorectal cancer, however the cancer cell was able to repair the damage within 24 h. Consequently, repeated ADEPT cycles were required, which could only be done with additional administration of cyclosporine to suppress immune responses.[180] Non-mammalian enzymes with a mammalian homologue and enzymes of mammalian origin were also investigated for reasons of reduced immunogenicity, but these were less efficient in converting the prodrug.[179]

The ADEPT concept gained attention 20 years ago, resulting in several publications, but interest has since then declined, likely due to failed clinical trials caused by immunogenic effects from non-human enzymes.[180] However, the ADEPT method may offer enhanced opportunities for

the activation of prodrugs and ACPPs, compared to the classical activation methods that utilize local enzymes, pH drop and ROS. These traditional systems can be too insensitive or too slow to achieve high accumulation of activated CPP at the tumor.[181] The ADEPT system does not rely on the natural conditions of the tumor microenvironment, but allows any external enzyme, to be brought specifically to the target site by the antibody. However, the enzyme must be chosen carefully; in addition to being compatible with prodrug activation, immunogenic effects need to be minimized, for example by humanization of bacterial enzymes or engineering a human enzyme with altered specificity to avoid off-target effects.[182]

2.3.4 Sirtuins

The enzymes used in this work for ACPP activation are derived from histone deacetylases (HDACs), also commonly referred to as lysine deacetylases (KDACs). Although the name implies that their primary function is the removal of acetyl residues, they have been implicated in catalyzing various deacylation reactions on different protein substrates, not only histones as originally thought. Unlike KDACs of the classes I, II and IV that are Zn^{2+} dependent, KDACs of class III are nicotinamide adenine dinucleotide (NAD)-dependent. These class III KDACs are also known as sirtuins (SIRTs), as they are structurally homologous to the yeast silent information regulator 2 (Sir2), which was first identified in *Saccharomyces cerevisiae* as a contributor to genomic stability. In humans, there are seven mammalian homologs of Sir2, named SirT1-7, that have been identified. While SirT1-7 share a conserved NAD binding domain and catalytic core, their *N*- and *C*-termini vary in length, chemical composition and post-translational modifications (PTMs), which determine their substrate specificity and subcellular localization. SIRTs form two globular domains: the larger Rossmann-fold domain, a structure consisting of a series of parallel β-strands interconnected by α-helices, and a Zn^{2+}-binding anti-parallel β-sheet, that consists of five α-helices and three β-strands on which a zinc ion is coordinated by four cysteine residues.[183] The SirT2 and SirT5 enzymes used in this work are briefly discussed in the following.

The SirT2 enzyme is predominantly located in the cytoplasm and has multiple roles, participating in inflammatory responses or in the regulation of metabolic activities by promoting gluconeogenesis, when necessary through its deacetylating activity. Moreover, SirT2 participates in the regulation of oxidative stress and in targeting apoptosis related proteins such as p53, however conflicting results on its role as an oncogene or tumor suppressor requires more studies on this enzyme. Although primarily located in the cytoplasm, it also shuttles into the nucleus during cell division in the G2/M phase to deacetylate the histone H4K16.[183]

SIRT deacetylation follows four main steps: the binding of NAD and acetyl lysine substrate, followed by glycosidic bond cleavage, acetyl transfer and finally the formation of the deacetylated lysine with O-acetyl-ADP ribose and nicotinamide as side products. A proposed mechanism based on bacterial SirT2[184] is shown in Figure 9.

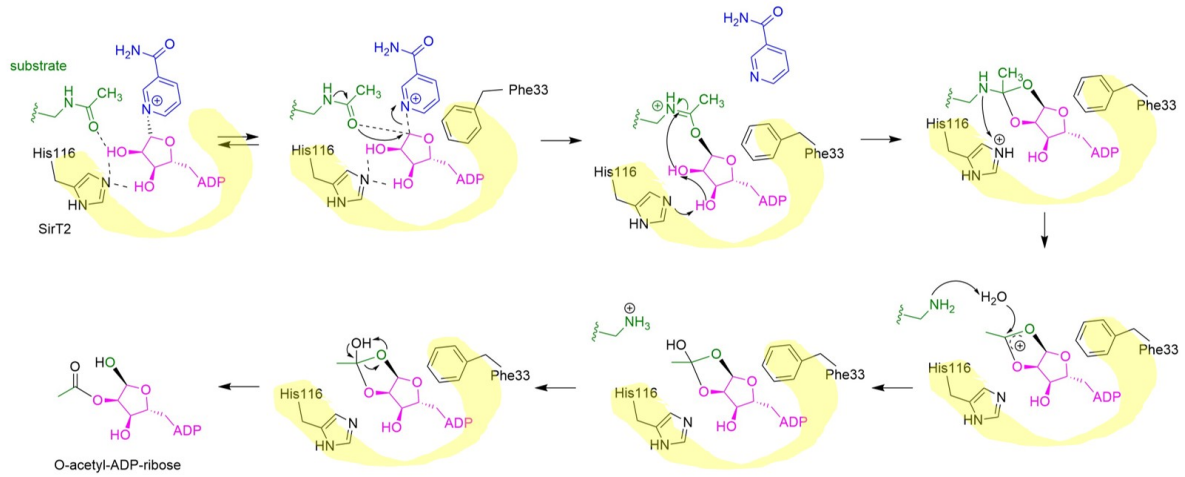

Figure 9| Proposed SirT2 deacetylation mechanism.[Adapted from [184]] Upon binding of SirT2 to NAD and acetylated lysine substrate, the nicotinamide ring is positioned into the hydrophobic pocket of the enzyme in an orientation that directs the α-face of the ribose towards the acetyl lysine. Cleavage of the N-glycosidic bond releases nicotinamide and draws the oxygen of the acetyl lysine to the electron-deficient C1' position, which forms an O-alkylamidate intermediate, stabilized by Phe33. His116 then abstracts a hydroxyl-proton, that promotes a nucleophilic attack of the hydroxyl-group on the C2' carbon atom to the lysine carbonyl, forming a cyclic amino-acetal intermediate, which H116 protonates under the release of the free amine. The remaining cyclic acyl-oxonium ion undergoes a water-mediated attack which after hydrogen transfer results in O-acetyl ADP ribose.

The SirT5 enzyme is primarily located in the mitochondria, but has also been found in the cytosol, peroxisomes and nucleus at low concentrations. As a mitochondrial enzyme, it regulates glucose metabolism, but is also involved in many other roles such as regulating autophagy, cell proliferation, migration and invasion. Similar to SirT2, they have demonstrated conflicting roles as oncogene or tumor suppressor, requiring further studies for deeper understanding of its function.[183,185] SirT5 is especially affine towards negatively charged acyl lysine residues and is primarily involved in the regulation of PTMs through lysine demalonylation, desuccinylation and deglutarylation. The presence of Ala86 (instead of Phe in SirT2), results in a larger binding pocket in the enzyme that is required for the entry of bulkier acyl-lysine residues.[185]

3 Objective

3.1 Conditional intracellular delivery *via* CPPs

As a major limitation of intracellular cargo delivery via CPPs is their lack of cell type specificity, the first part of this work aimed at addressing this issue. For many CPPs, the electrostatic interaction of their positive charges with negatively charged components of the cell membrane is a crucial first step for cellular uptake. Therefore, masking these positive charges would obstruct internalization. The masking of CPPs can take various forms, however, they all have in common a trigger-cleavable motif that de-masks i.e. activates the CPP under conditions ideally found only at the target site. With emphasis on "ideally", the reality shows these triggers are not localized exclusively at the target site or gradients at the target site are not high enough for efficient activation. Therefore, alternative activation conditions should be investigated.

The cationic and amphiphilic L17E peptide was used as model CPP for demonstration of conditional and selective delivery. Herein, the five lysine residues which affords the L17E peptide with its cationic character were masked by introduction of protecting groups. In the first investigations, the lysine residues at different positions of the L17E peptide were to be masked to determine the key lysine residues essential for cellular uptake. Next, a conditional activation system should be established through enzymatic cleavage of these protecting groups and finally, a set-up for selective delivery in form of an ADEPT-like procedure should be demonstrated in a proof of concept (Figure 10). By choosing a fluorophore as model cargo, it allows cellular uptake investigations to be visualized by confocal microscopy and measured by flow cytometry analysis. Supported by cell proliferation assays, the feasibility of this approach as a drug-delivery platform through the delivery of a toxin-cargo should be exemplified.

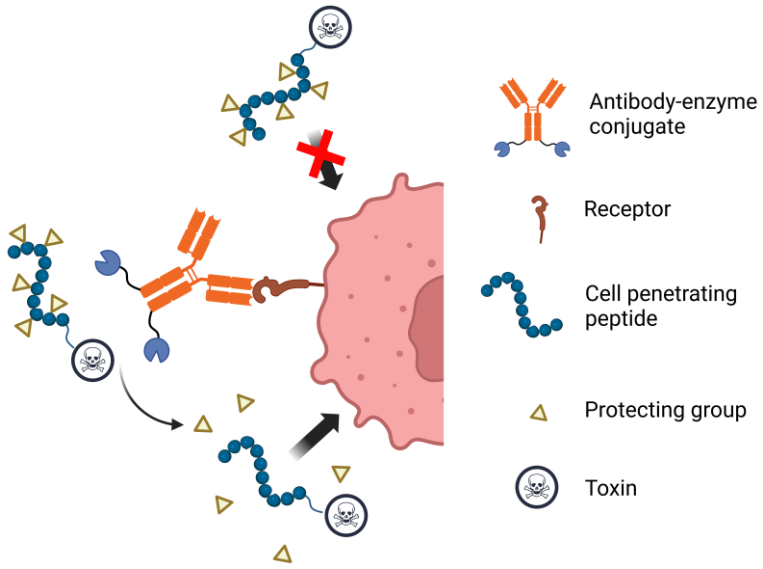

Figure 10| Schematic illustration of the conditional activation of a CPP by an ADEPT approach. Intracellular delivery of a masked CPP is impaired in absence of deprotecting enzyme. When an antibody-enzyme conjugate binds the target cells, the protecting groups on the CPP can be cleaved by the enzyme at the target site to reactivate cell penetrating activity.

3.2 Conditional delivery of dextran-ACPP conjugates

Larger cargos intended for intracellular deployment generally require multiple CPPs to be delivered into cells. For this reason, a number of delivery vehicles with multiple CPPs including nanoparticles, oligomerization domains, or branched or linear peptide scaffolds have been developed to improve cellular uptake.[186] Dr. Bastian Becker and Dr. Simon Englert had reported on a multivalent dextran hybrid containing L17E and cargo in multiple copies on the polymer with efficient cytoplasmic delivery at low concentration and negligible cytotoxicity.[140] This concept was to be expanded to a conditionally activated delivery platform by attachment of ACPPs to dextran (Figure 11).

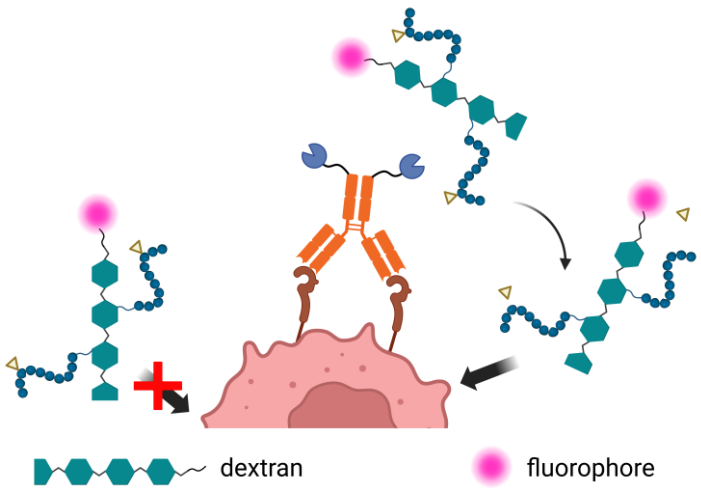

Figure 11| Schematic illustration of the conditional activation of a dextran-ACPP conjugate by an ADEPT approach.

3.3 Streptavidin modular delivery architectures

Considering the favorable physicochemical properties of dextran and promising foundation as multimerization platform for drugs and peptides, Dr. Simon Englert started to develop a modular system using streptavidin as centerpiece to simplify synthesis procedures and introduce a versatile multifaceted delivery platform. This approach leverages streptavidin's tetrameric structure that offers four biotin binding sites. Each streptavidin can serve as a scaffold for binding up to four biotinylated moieties simultaneously. For example, any cargo or dextran-conjugate carrying drugs, CPPs, receptor-targeting ligands or any other effector molecule would only need to be biotinylated to be assembled on streptavidin. The multiple combinatorial options reduce synthesis effort and allows for easy tailoring of the streptavidin-based architectures for different applications. Dr. Simon Englert showed successful intracellular delivery of eGFP by dextran-L17E-streptavidin architectures, however cellular uptake was accompanied with high toxicity, which limited the potential for further applications. Therefore, intracellular delivery through streptavidin-dextran architectures should be optimized.

The CPP choice should be expanded from the L17E peptide to include other CPPs, with the aim to find an improved delivery vehicle with at least the same delivery efficiency and reduced toxicity. Therefore, a cell lytic attenuated variant of the L17E peptide, the L17E/Q21E peptide, a stapled peptide ATSP-7041 and an α-helical peptide apCC-Di-B should be investigated for cellular uptake. Also, the number of CPPs per dextran and per dextran-streptavidin architecture were to be varied to find an optimal balance between cellular uptake and cytotoxicity. Furthermore, as proof of cytosolic uptake and to evaluate the potential of this method in modulation of cellular activities, split complementation assays should be performed and also a p53-sensitive assay modulated through the intracellular delivery of a peptide inhibitor.

4 Results and Discussion

4.1 Conditional and selective CPP intracellular delivery

4.1.1 The role of lysine residues of the L17E peptide for cellular uptake

4.1.1.1 Design and Synthesis

This project was aimed at improving the selectivity of CPPs in cargo delivery, which is especially important for therapeutic applications. Since the L17E peptide had proven to show effective cargo delivery in many cases, this peptide was selected as model CPP for generation of a tumor-specific activatable CPP. Cell penetrating peptides rely on their positive charge for cell penetrating activity, as has been demonstrated numerous times in the generation of activatable CPPs.[161] As the L17E peptide induces cargo delivery by destabilizing the cell membrane through interaction with negatively charged lipids on the cell surface,[93,94] it was assumed that the cell penetrating properties of the L17E peptide is associated to its positive charge derived from the five residing lysine residues. Therefore, the positive charge of the lysine residues was masked by protecting groups. As keeping the number of protecting groups at a minimum is advantageous for ease of deprotection and solubility,[140] protecting groups were introduced on different lysine residues in various combinations. Allyloxy carbonyl (alloc)-protecting groups were chosen as an uncharged protecting group, since Fmoc-Lys(Alloc)-OH building blocks were readily available and stable for peptide assembly in the microwave peptide synthesizer. Starting with the simultaneous protection of two lysine residues of L17E, the Alloc protecting group was positioned on the lysine residues at position K1+K2, K1+K3, K2+K4 and K3+K5, whereby the number denotes the lysine position in the L17E peptide in order from the *N*- to the *C*-terminus. A 5,6-TAMRA isomeric mixture was used as fluorogenic cargo, for evaluation of cellular uptake by confocal microscopy analysis. TAMRA was covalently attached by *N*-hydroxy succinimide coupling to an orthogonal lysine residue with N-[1-(4,4-dimethyl-2,6-dioxocyclohex-1-ylidene)ethyl] (Dde) protecting group added to the *C*-terminus of the peptide, as it is known that the *N*-terminus of the L17E peptide is essential for cellular uptake. The reaction is exemplary shown for the L17E peptide in Figure 12.

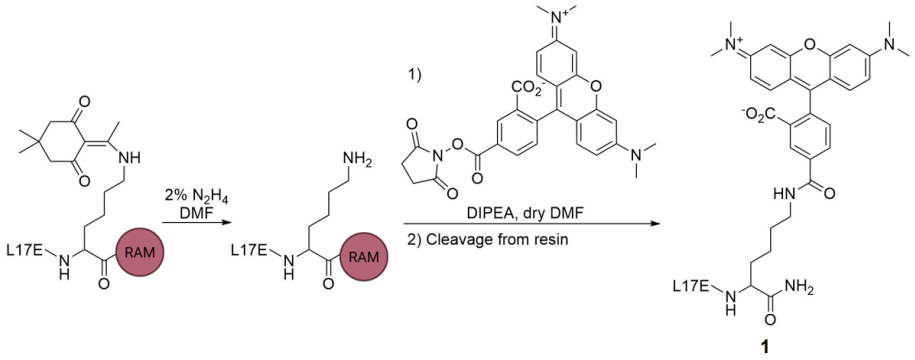

Figure 12| Reaction scheme of Dde deprotection and TAMRA attachment to L17E peptide through NHS ester coupling generating L17E-TAMRA **1**.

Figure 13 shows a summary of the L17E peptide variants assessed.

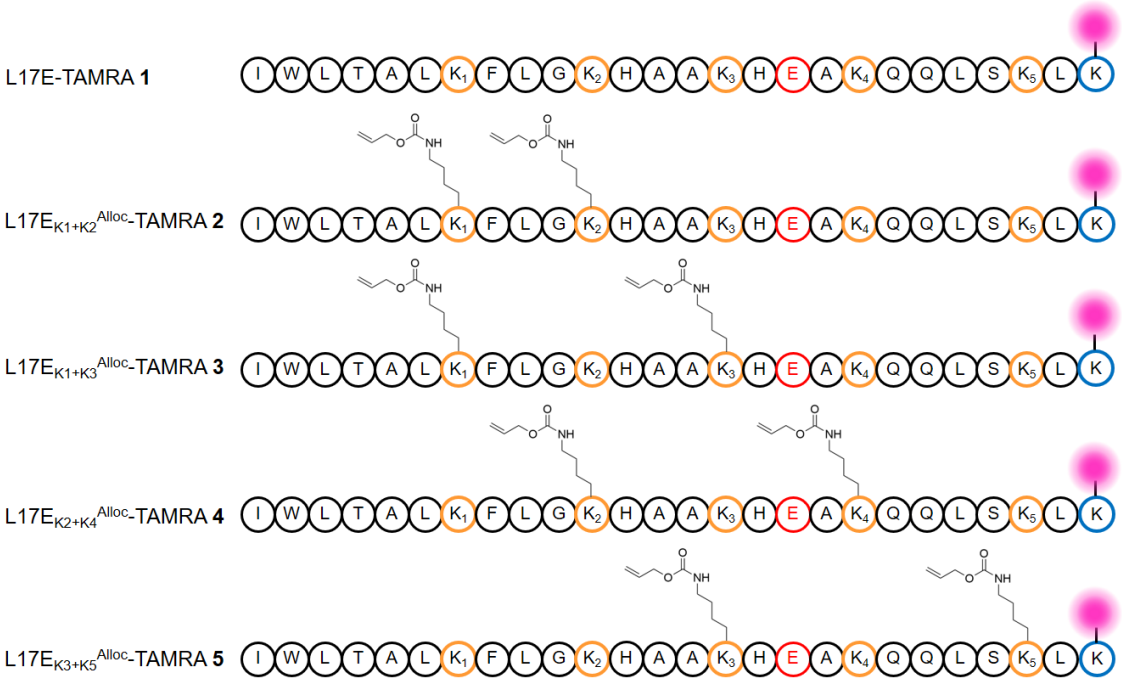

Figure 13| L17E peptide **1** and Alloc-L17E peptide variants **2** – **5** with 1 – 5 numbered lysine residues from *N*- to the *C*-terminus for evaluation of cellular uptake in orange and an orthogonal lysine in blue with a pink circle denoting 5,6-TAMRA.

4.1.1.2Cellular uptake assay of Alloc-protected L17E peptides

The cell penetrating activity of the TAMRA-labelled L17E peptides with Alloc-masked lysine residues on different positions was evaluated in a cellular uptake assay to determine the sites that hinder cellular uptake. Therefore, HeLa cells were incubated with 4 μM Alloc-L17E-TAMRA peptides in Dulbecco's Modified Eagle Medium (DMEM) containing 10 % FBS for 1 h and then incubated for another 3 h in medium only at 37 °C and 4 °C. Distribution of cellular fluorescence was observed by confocal microscopy under the same microscopy tuning parameters.

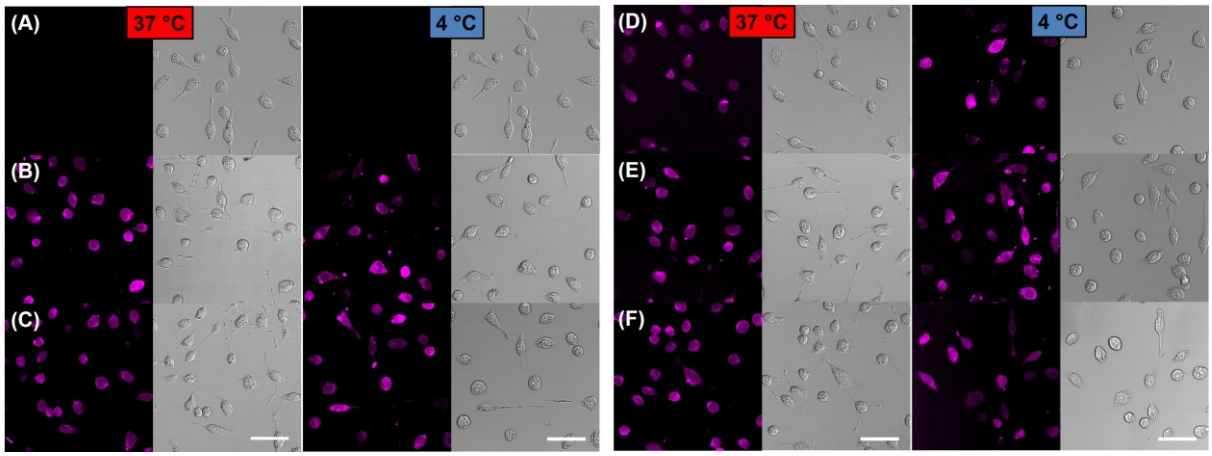

Figure 14| CLSM fluorescence and brightfield images of HeLa cells treated with 4 µM doubly masked Alloc-L17E-TAMRA peptides at 37 °C (left column) and 4 °C (right column) for 1 h. (A) cells only, (B) L17E-TAMRA **1**, (C) $L17E_{K1+K2}^{Alloc}$-TAMRA **2**, (D) $L17E_{K1+K3}^{Alloc}$-TAMRA **3**, (E) $L17E_{K2+K4}^{Alloc}$-TAMRA **4**, (F) $L17E_{K3+K5}^{Alloc}$-TAMRA **5**.[187]

The CLSM images in Figure 14 shows HeLa cells incubated with the various Alloc-L17E peptides. Contrary to expectations, all Alloc-masked L17E, independent of the masked lysine position, exhibited high intracellular fluorescence distributed throughout the cytosol showing that internalization had occurred. The fluorescence intensity of alloc-masked L17E peptide was comparable to that of the L17E peptide **1** without any masking groups. This was observed at 37 °C as well as at 4 °C, where cellular uptake by energy-dependent uptake mechanisms are suppressed.[188,189] Between these two temperatures, the cells treated at 4 °C show greater differences in fluorescence intensities between individual cells, which could be an indication for cellular internalization in multiple stages or a dual uptake mechanism, as has been similarly observed for other CPPs.[188,190] Although there is no defined secondary structure that is advantageous for cell penetration, the secondary structure individual to a CPP may promote cellular uptake,[191] which for the L17E peptide is an α-helical structure.[93] Furthermore, cellular uptake is influenced by the net charge of the cargo. Melvin an workers showed that positively charged cargos led to increased internalization, while negatively and uncharged cargos reduced internalization.[192] Since the fluorophore TAMRA used as delivery module is positively charged, it may have also facilitated cellular uptake to a greater extent than the inhibitory function of two masking groups. As internalization was not inhibited or even impaired by two masking groups on the L17E peptide **1**, it was chosen to fully mask all the lysine residues of the peptide. Due to solubility issues, which arose at higher concentrated stock solutions of the Alloc-L17E peptides, the protecting group was exchanged for the less hydrophobic acetyl-group. Furthermore, the acetyl group would allow a biologically compatible enzymatic deprotection step by a deacetylase for reactivation of the silenced CPP.

4.1.2 Conditional intracellular delivery of TAMRA by an acetylated-L17E peptide

4.1.2.1 Design and Synthesis

As the two alloc masking groups of the L17E peptide **2** – **5** had proven ineffective in impairing cellular uptake, it was decided to mask all the lysine side chains with acetyl units, which would allow for biocompatible deprotection with a deacetylase (Figure 15). As deacetylase, NAD-dependent SirT2 from the family of histone deacetylases was used. The plasmid for the enzyme was provided by Prof. Dr. Heinz Neumann (Hochschule Darmstadt) and produced by Carolin Dombrowsky. Synthesis of the five-time acetylated L17E peptide **6** was performed analogously to the Alloc-L17E peptides using Fmoc-Lys(Ac)-OH as building block. With TAMRA as fluorogenic cargo, intracellular delivery can be evaluated qualitatively by confocal microscopy and quantified by flow cytometry analysis.

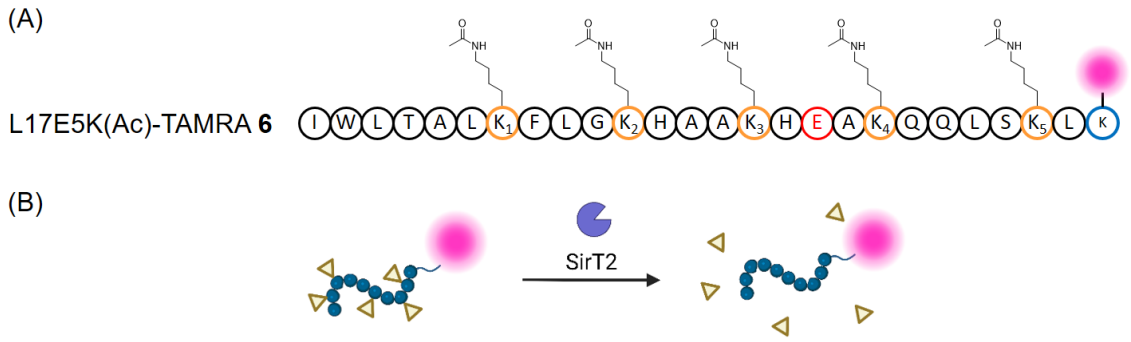

Figure 15| (A) Amino acid sequence of L17E5K(Ac)-TAMRA peptide **6** with five acetylated lysine residues shown in orange and an orthogonal lysine in blue with a pink circle denoting 5,6-TAMRA. (B) Schematic representation of the deacetylase SirT2 removing the acetyl protecting groups (yellow triangles) from the peptide.

4.1.2.2 Cellular uptake assays of acetylated-L17E-TAMRA peptide 6

The performance of the five acetyl protecting groups on the L17E peptide in blocking cellular uptake was first evaluated in a cellular uptake assay with subsequent confocal imaging. Therefore, HeLa cells were incubated with 5 μM TAMRA-labelled acetylated L17E peptide **6** or the unprotected L17E peptide **1** that served as control for 1 h at 30 °C. In addition, a sample containing HeLa cells treated with **6** and SirT2 in NAD-supplemented medium was prepared, to demonstrate re-activation of the CPP. After incubation, the cells were washed, fixed with 4 % paraformaldehyde and observed by CLSM. The confocal images are shown in Figure 16. This time round, the images display strongly reduced intracellular fluorescence for L17E5K(Ac)-TAMRA peptide **6** compared to the L17E-TAMRA peptide **1**, while the addition of SirT2 to **6**, resulted in recovery of intracellular fluorescence inside the cells.

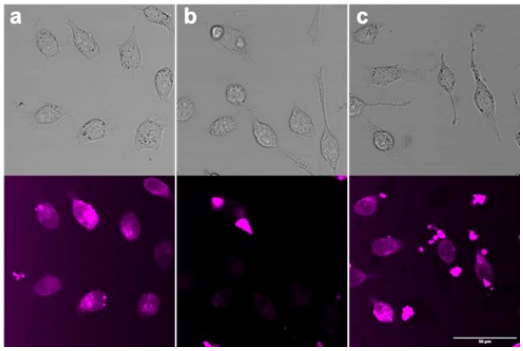

Figure 16| CLSM image brightfield (top) and fluorescence (bottom) of HeLa cells treated with a) 5 µM L17E-TAMRA **1**, b) L17E5K(Ac)-TAMRA **6** and c) 5 µM L17E5K(Ac)-TAMRA **6**, 1 µM SirT2 and 40 eq. NAD for 1 h at 30 °C. The scale bar denotes 50 µm.[187]

These results were a first indication that the cell penetrating activity can be impaired by masking all five lysine residues of the L17E peptide and that cell penetrating activity could be recovered through deacetylation by SirT2. It is important to note that the cellular uptake assay was performed at a reduced temperature of 30 °C, because the enzyme seemed to be unstable at 37 °C.

4.1.2.3 Quantification of the conditional activation of acetylated-L17E peptide 6

Following the encouraging results of the conditional activation of L17E5K(Ac)-TAMRA peptide **6** by SirT2, the intracellular fluorescence of the HeLa cells was quantified by flow cytometry analysis (Figure 17) and compared to the unmasked L17E-TAMRA peptide **1**. Therefore, after treatment of the HeLa cells with the constructs, the cells were trypsinized and their fluorescence was measured using a flow cytometer.

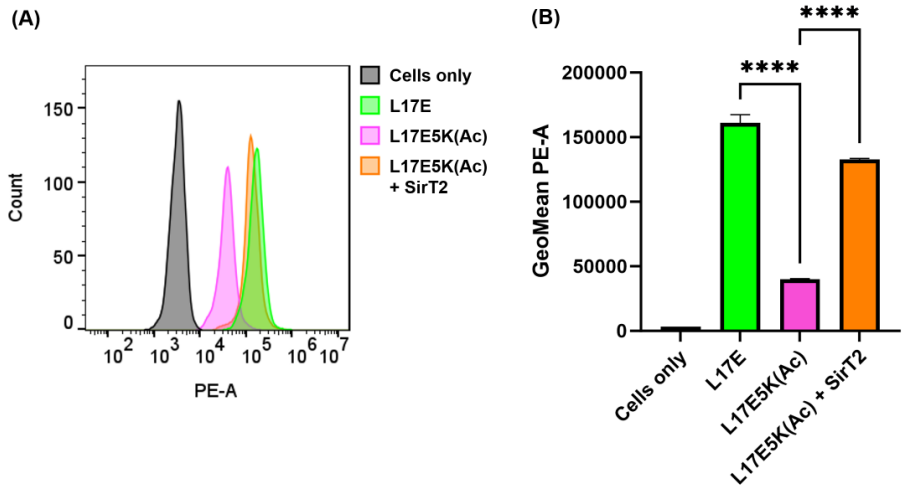

Figure 17| Flow cytometry analysis of the cellular uptake of 5 µM L17E-TAMRA **1**, L17E5K(Ac)-TAMRA **6** and SirT2-deacetylated L17E5K(Ac)-TAMRA **6** after 1 h incubation at 30 °C. (A) FACS plot of the count against fluorescence intensity (PE-channel), (B) Bar chart plot of mean fluorescence intensity for the different samples. Data represents mean ± SEM. One-way ANOVA followed by Tukey's test was used to analyze the data (0.1234 (ns), *p<0.0332, **p<0.0021, ***p<0.0002, ****p<0.0001). The data was plotted and analyzed using GraphPad Prism.[187]

The flow cytometry results reflected the results observed by confocal microscopy. The reduced fluorescence of cells treated with the L17E5K(Ac)-TAMRA peptide **6** indicates inhibition of cellular uptake, albeit not completely. The SirT2-treated L17E5K(Ac)-TAMRA peptide **6** showed recovery of cell penetration, reaching cellular fluorescence intensities comparable to the L17E-TAMRA peptide **1**.

To verify that cellular internalization was indeed due to cleavage of the acetyl groups on the lysine residues, the peptides L17E-Pra **7** and L17E5K(Ac)-Pra peptide **8**, were synthesized, whereby the propargylglycine (Pra) moiety was introduced for click reactions as described in section 4.3. L17E5K(Ac)-Pra peptide **8** was subjected to deprotection with SirT2 in PBS with NAD for 1 h at 30 °C. After removal of a large portion of SirT2 by thermal denaturation, the supernatant containing the peptide was analyzed by RP-HPLC (Figure 18 and Figure S 1) and LC-ESI-MS (Figure S 2). The RP-HPLC chromatogram in Figure 18 shows a shift of the deacetylated L17E5K(Ac) peptide **8** to the retention time of L17E peptide **7** (t_R = 17.6 min). The signal at t_R = 18.0 min, corresponded to the L17E peptide with one acetyl group according to the LC-ESI-MS. The signals at t_R = 1-7 min are presumed to be side products resulting from the cleavage of NAD[193] and any other residual deacetylase products not removed through denaturation. Comparing the areas under the peptide signals at t_R = 17.6 and 18.0 min, the L17E5K(Ac)-peptide is fully deprotected to approximately 66 %, while the remaining contained one acetyl group. It is unknown which acetylated lysine residue was not deprotected, but it may also not be restricted to only one lysine position either. Nevertheless, the one acetyl group on the peptide does not compromise cellular internalization, as the results in section 4.1.1.2 showed L17E with two protecting groups resulted in significant cellular uptake.

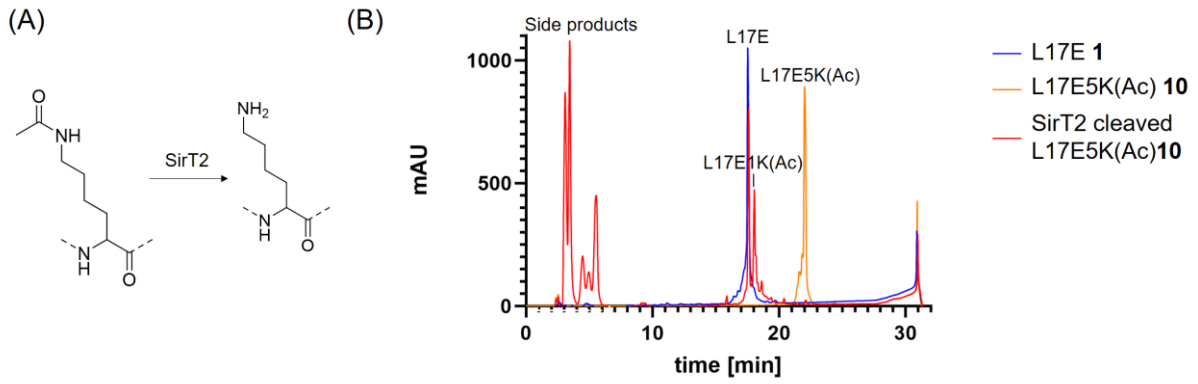

Figure 18| (A) Removal of the acetyl protecting group on a lysine residue by SirT2, (B) Overlaid RP-HPLC chromatograms of L17E-Pra **7**, L17E5K(Ac)-Pra **8** and SirT2 cleaved L17E-5K(Ac)-Pra **8** (gradient 0 to 60 % eluent B and 220 nm).[187] Plotted using GraphPad Prism.

The experiments established a conditional cellular uptake method, yet internalization would not be cell-specific. Therefore, the ADEPT approach, which utilizes a tumor-targeting antibody-enzyme conjugate for targeted delivery of the enzyme, was applied next.

4.1.3 Selective and conditional delivery of a fluorophore

4.1.3.1 Design

For the selective cellular uptake of the L17E5K(Ac)-TAMRA peptide **6**, the ADEPT method was employed using the in-house developed antibody anti-B7H3 that is known to bind the type 1 transmembrane glycoprotein B7H3 on HeLa cells at a K_D of 1 nM (Figure S 3, determined by Carolin Dombrowsky). The HER2-targeting antibody trastuzumab was chosen as negative control, that does not bind HeLa cells. For conjugation of the antibodies to the SirT2 deacetylase, the antibodies were engineered with a LPETGG recognition sequence at the C-terminus of the heavy chain and the SirT2 enzyme with a GGG extension on the N-terminus, that is recognized by the ligation enzyme sortase A. Coupling efficiencies of over 60 % were attained. (Figure S 4, performed by Carolin Dombrowsky).

For selective intracellular delivery, the ADEPT procedure was to be modelled in a cellular uptake assay. Therefore, HeLa cells are incubated with the antibody-SirT2 conjugate for 15 min at 30 °C to allow binding to the cell surface antigen. After the removal of unbound antibody-SirT2 and uncoupled SirT2 from the cells by a washing step, the peptide samples are incubated with the cells for 2 h at 30 °C and subsequently washed off. After an additional 3 h incubation at 37 °C, the cells can be fixed and observed by CLSM. The process is shown in Figure 19.

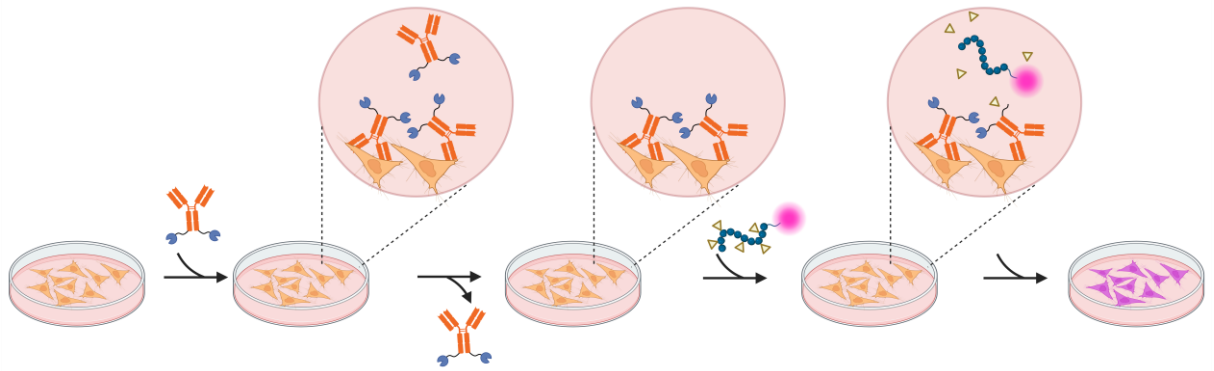

Figure 19| Schematic depiction of the ADEPT-like procedure in the cellular uptake assay of L17E5K(Ac)-TAMRA **6**. Image created with Biorender.com.

4.1.3.2 ADEPT-like cellular uptake assay: delivery of a fluorophore

Following the procedure depicted in Figure 19 using 5 μM peptide samples, confocal microscopy analysis revealed that HeLa cells treated with the acetylated L17E peptide **6** exhibited reduced fluorescence in the cytosol compared to those treated with the L17E peptide

1, that was recovered for cells that were treated with anti-B7H3-SirT2 antibody-enzyme conjugate, but not trastuzumab-SirT2 (Figure 20). As expected, anti-B7H3-SirT2 was not removed from the HeLa cells due to cell-surface antigen binding, and could deacetylate the peptide **6**. On the other hand, trastuzumab-SirT2 had been removed in the first washing step, since it did not bind the cells, and was not present to deacetylate the peptide **6** when it was added in the second step. However, although low, it should be mentioned that low fluorescence levels can be seen for HeLa cells treated with **6** only or also with Trastuzumab-SirT2, indicating some internalization had still occurred.

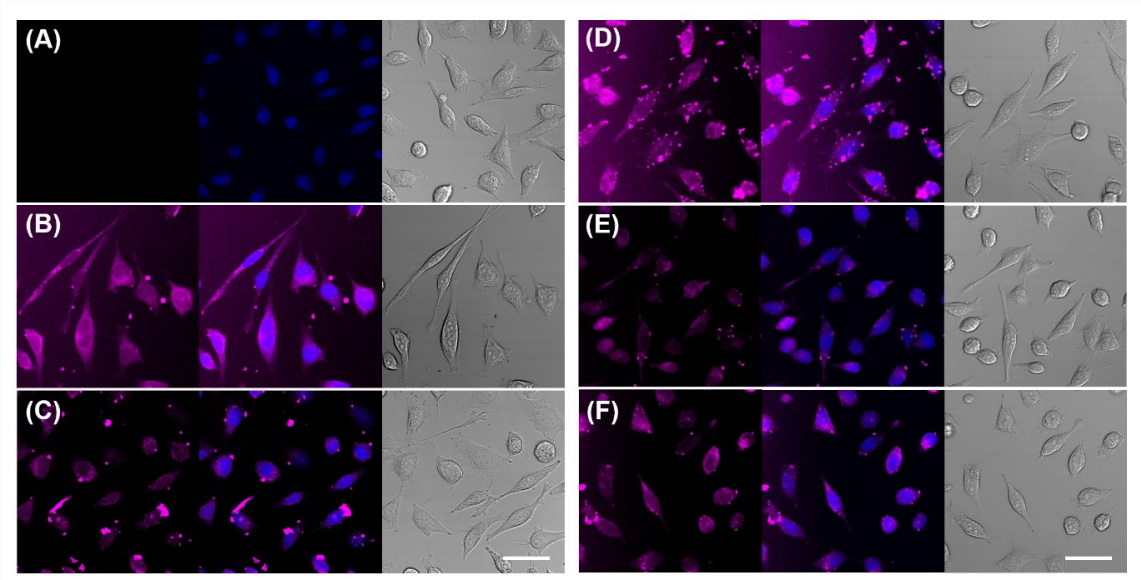

Figure 20| (A)-(F) CLSM microscopy images of HeLa cells treated with 5 µM peptide samples for 2 h at 30 °C in an ADEPT-like manner including controls. (A) Cells only, (B) L17E-TAMRA **1**, (C) L17E5K(Ac)-TAMRA **6**, (D) L17E5K(Ac)-TAMRA **6** with free SirT2, (E) 50 nM trastuzumab-SirT2 treated cells with L17E5K(Ac)-TAMRA **6**, (F) 50 nM anti-B7H3-SirT2 treated cells with L17E5K(Ac)-TAMRA **6**. Left: fluorescence channel, center: merge fluorescence with Hoechst channel (nuclear staining), right: brightfield channel. The scale bar denotes 50 µm. Images were taken under the same microscopy tuning parameters and processed with ImageJ.

4.1.4 Selective and conditional delivery of a toxin

4.1.4.1 Design

Thus far, selective intracellular delivery had only been evaluated qualitatively by CLSM analysis. While quantification can be done by flow cytometry, it has several limitations, for example, adhesion of the cargo to the outer membrane is also measured and, as the approach could also be interesting for the transport of drugs with cytosolic targets, the method also quantifies cargo entrapped in endosomes. Therefore, the delivery of a toxin with intracellular target is perhaps a better measure of delivery efficiency.

Continuing with the ADEPT-like concept, targeted delivery of a toxin using the L17E peptide was explored. Among various toxins, a molecule from the cryptophycin family was used (see

Figure S 5 for molecular structure and Figure S 13 for RP-HPLC chromatogram). Cryptophycins are reported to be cytotoxic in the picomolar range and inhibit microtubule polymerization in the G2/M phase of the cell cycle.[194] The cryptophycin 52 variant had progressed to phase II clinical studies in 2003 for treatment of non-small cell lung cancer (NSCLC), but was terminated due to adverse neurological toxicity effects.[195] Due to their high potency, cryptophycins featuring addressable functional groups are being explored to enable attachment to tumor-targeting moieties such as tumor-homing peptides or antibodies for targeted delivery.[196,197] The cryptophycin used in this work contained a maleimide functionality, which can be addressed with a thiol-containing peptide in a Michael addition reaction. To this end, the L17E and L17E5K(Ac) peptides were modified with an additional C-terminal cysteine, yielding L17E-Cys **9** and L17E5K(Ac)-Cys **10**. These were incubated with the maleimide-labelled cryptophycin in ammonium bicarbonate buffer pH 7.2 with DMSO for solubility, to obtain L17E-cryptophycin (cry) **11** (Figure 21) and L17E5K(Ac)-cry **12**. The cryptophycin also contained a valine-citrulline (Val-Cit) linker that is cleaved by cathepsin in endosomes to free the payload,[198] however this functionality is only used when the CPP-toxin is internalized by endocytosis.

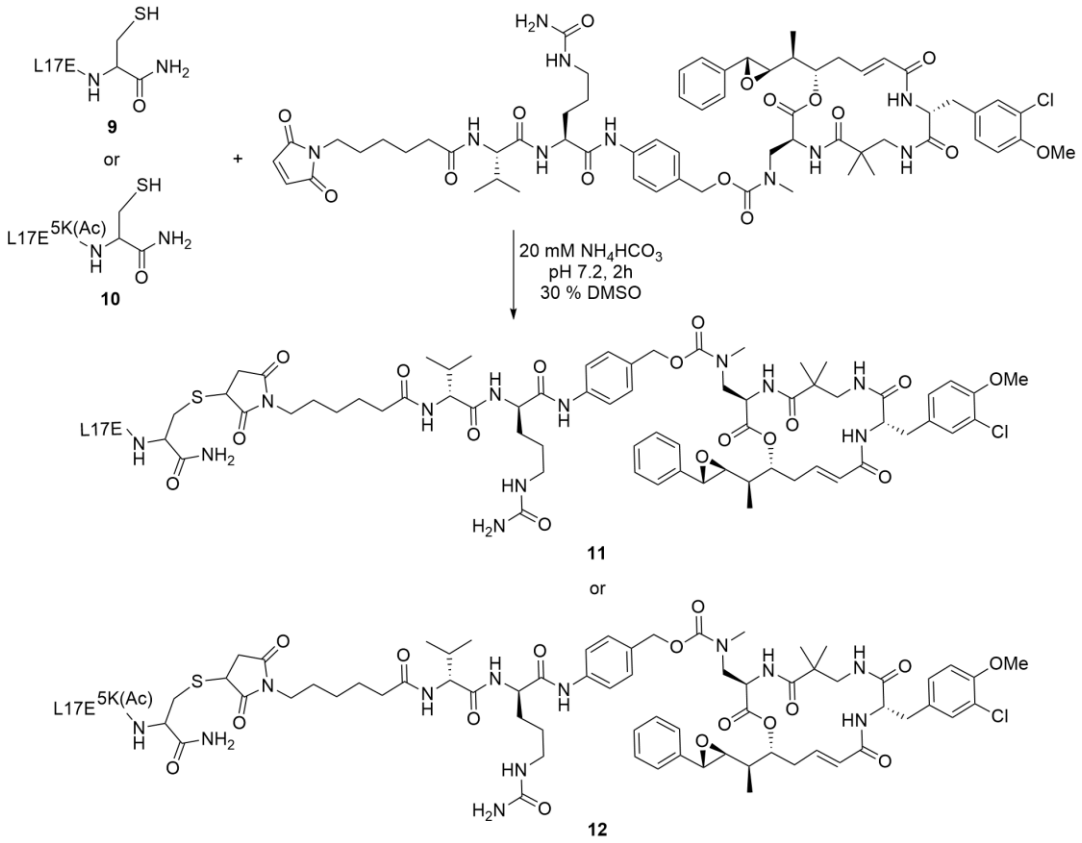

Figure 21| Reaction scheme for the conjugation of L17E-Cys **9** to maleimide-functionalized Val-Cit-PAB-cryptophycin in a Michael addition reaction to form L17E-cry **11**. L17E5K(Ac)-cry **12** was synthesized analogously from L17E5K(Ac)-Cys **10**.

The cellular uptake of the cryptophycin bearing peptides **11** and **12** was to be evaluated in a cell proliferation assay in an ADEPT-like approach using the antibody-enzyme conjugate trastuzumab-SirT2. Two breast cancer cell lines, SKBR3 (HER2+) and triple negative MDA-MB468 cells were chosen that represent positive and negative controls for the HER2 targeting antibody. Due to instability of the enzyme at 37 °C, a modified cell proliferation assay had to be performed that entailed incubation steps proceeding at 30 °C, similar to the delivery of TAMRA performed in section 4.1.3.2. Following the seeding and incubation of the cells overnight at 37 °C, the cells were acclimatized to 30 °C for 1 h. 50 nM Trastuzumab-SirT2 (or PBS) were incubated on the cells at the reduced temperature for 15 min to allow binding to the cells. Afterwards, unbound trastuzumab-SirT2 or free SirT2 was washed off and a dilution series of **12** was added and incubated on the cells for 2 h at 30 °C. In parallel, the cells were also treated with a dilution series of **11** as positive control. To observe SirT2 activity, a peptide sample **12** with free SirT2 in the mixture was also evaluated. The cells were washed again and incubated for another 72 h at 37 °C before measuring cell proliferation by the CellTiter96®Aqueous One solution cell proliferation assay. To emphasize, in this modified cell proliferation assay, the peptide samples are only given 2 h time to internalize into the cells, rather than the commonly practiced 72 h. All steps were performed in DMEM (w/ 10 % FBS and 1 % PS).

4.1.4.2 ADEPT-like cellular proliferation assay: delivery of a toxin

The results of the modified cell proliferation assay are displayed in Figure 22. For the cell lines SKBR3 and MDA-MB468, L17E-cry **11** killed the cells with EC_{50} values of 12.3 nM and 13.2 nM respectively, while L17E5K(Ac)-cry **12** killed the cells with higher EC_{50} values of 162.8 nM and 96.5 nM respectively. Pre-treatment of the cells with trastuzumab-SirT2 showed increased recovery of cell killing for HER2 positive SKBR3 cells as opposed to MDA-MB-468 cells, that are HER2 negative. While the EC_{50} value for SKBR3 cells treated with trastuzumab-SirT2 was similar to cells treated with free SirT2 (53.3 nM and 43.3 nM respectively), the EC_{50} value for trastuzumab-SirT2 treated MDA-MB468 cells (70.7 nM) remained largely unchanged compared to the masked L17E5K(Ac)-cry peptide **10**. MDA-MB468 cells treated with free SirT2 showed a lower EC_{50} value of 52.3 nM, but similarly for SKBR3 cells, the EC_{50} value of L17E-cry **9**, could not be attained. The lower concentrations used on the cells may have compromised the rate of deacetylation, as had been shown that SirT2 can efficiently deacetylate the peptide (Figure 18). Maximum cell killing (E_{max}) was in the range of 53-60 % for all samples, except for L17E5K(Ac)-cry **10** on MDA-MB468 cells, which showed a lower E_{max} of 41 %. Differences in performance of the peptides on the two cell lines underlines that, while CPPs are not cell type selective, the

cell type does influence the CPP uptake efficiency and needs to be examined on an individual basis.

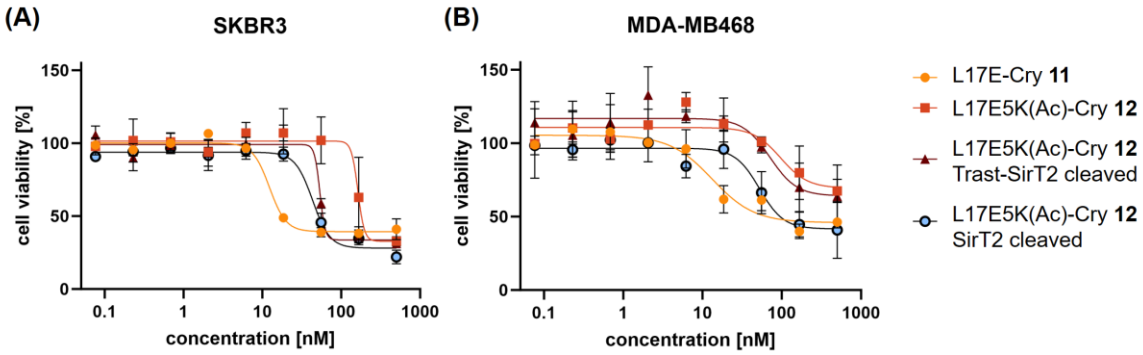

(C)

Sample	EC_{50}/ nM		E_{max}/ %	
	SKBR3	MDA-MB468	SKBR3	MDA-MB468
L17E-Cry **11**	12.3	13.2	61	60
L17E5K(Ac)-Cry **12**	162.8	96.5	68	41
L17E5K(Ac)-Cry **12** Trast-SirT2 cleaved	53.5	70.7	66	53
L17E5K(Ac)-Cry **12** SirT2 cleaved	43.3	52.3	66	55

Figure 22| Modified cell proliferation assays of (A) HER2 positive SKBR3 cells and (B) HER2 triple negative MDA-MB468 cells treated with L17E-cry **11** and L17E5K(Ac)-cry **12** in a concentration dilution series, with SirT2 treatment or trastuzumab-SirT2 pre-treatment. Peptide samples were incubated for 2 h on cells, removed, and incubated for another 72 h in medium only. (C) EC_{50} and maximum cell killing E_{max} values. Data was plotted and analyzed using GraphPad Prism.[187]

It should be emphasized that EC_{50} values in the nanomolar range were obtained in the cell proliferation assay, rather than picomolar values as is expected for cryptophycin. This is due to the short incubation time (2 h), done for reasons of enzyme stability, which may also influence the maximum cell killing values obtained. To clarify the potential performance of these peptides, a standard cell proliferation assay whereby L17E-cry **11** and L17E5K(Ac)-cry **12** are incubated for 72 h at 37 °C was performed using SKBR3 cells (Figure 23).

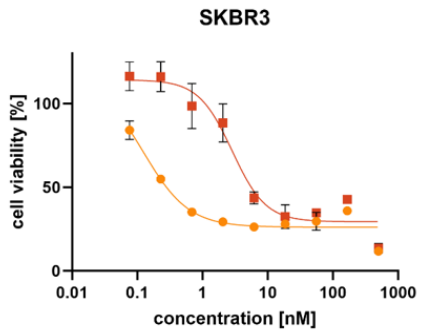

Sample	EC_{50}/ nM	E_{max}/ %
L17E-Cry **11**	0.13	89
L17E5K(Ac)-Cry **12**	2.85	84

Figure 23| Cell proliferation assay of L17E-cry **11** and L17E54K(Ac)-cry **12** on SKBR3 cells with EC_{50} and E_{max} values.[187]

In a standard cell proliferation assay, L17E-cry **12** showed the expected three-digit picomolar EC_{50} value (130 pM). L17E5K(Ac)-cry **12**, with an EC_{50} value of 2.85 nM, still showed considerable cytotoxicity, which may be attributed in part to the hydrophobic cryptophycin molecule itself. Therefore, it would be sensible to optimize the protecting group. However, the EC_{50} value fold difference between L17E-cry **11** and L17E5K(Ac)-cry **12** could be improved to a 22-fold difference, compared to the 13-fold difference before on SKBR3 cells. E_{max} for both samples was increased to 89 % and 84 %, indicating that efficiency of intracellular delivery was limited by the short incubation time. While it demonstrates the feasibility of the ADEPT-like approach, optimized conditions using a more stable enzyme and change of protecting group that is more effective in blocking cell penetration, are required. The strength of the ADEPT approach lies within its versatility to customize the combination of protecting group and deprotecting enzyme, that can be further optimized through engineering, and the choice of antibody to target specific cell surface antigens.

4.1.5 Optimization of the masking group on L17E

The acetyl-protected L17E peptide showed impaired cellular uptake compared to the L17E peptide in previous experiments, either with TAMRA or cryptophycin as cargo, but it was not completely blocked as was initially expected. Therefore, optimization involving a change of the masking group was investigated next.

4.1.5.1Design and synthesis

In alignment that negatively charged cargos are more difficult to traverse across the cell membrane than positively charged ones, we thought introducing negatively charged protecting groups on the L17E peptide would result in better blocking of cell penetration. For example, lysine succinylation is a post translational modification occurring in a wide range of proteins that induces a charge from +1 to -1 at physiological pH. Furthermore, staying in the family of sirtuins, SirT5 is a deacylase that had shown efficient deprotection of succinyl groups on lysines,[199] that could be used to remove the succinyl groups on the L17E peptide. Following this idea, L17E was synthesized with succinyl groups. The primary sequence was coupled on an automated platform using Fmoc-Lys(Dde)-OH building blocks for the lysine positions, where the succinyl group was to be placed, and Fmoc-Lys(Boc)-OH for the lysine residues that should remain amines. Subsequent Dde deprotection allowed the coupling of mono-tert-butyl succinate (Succ) to the free amine.

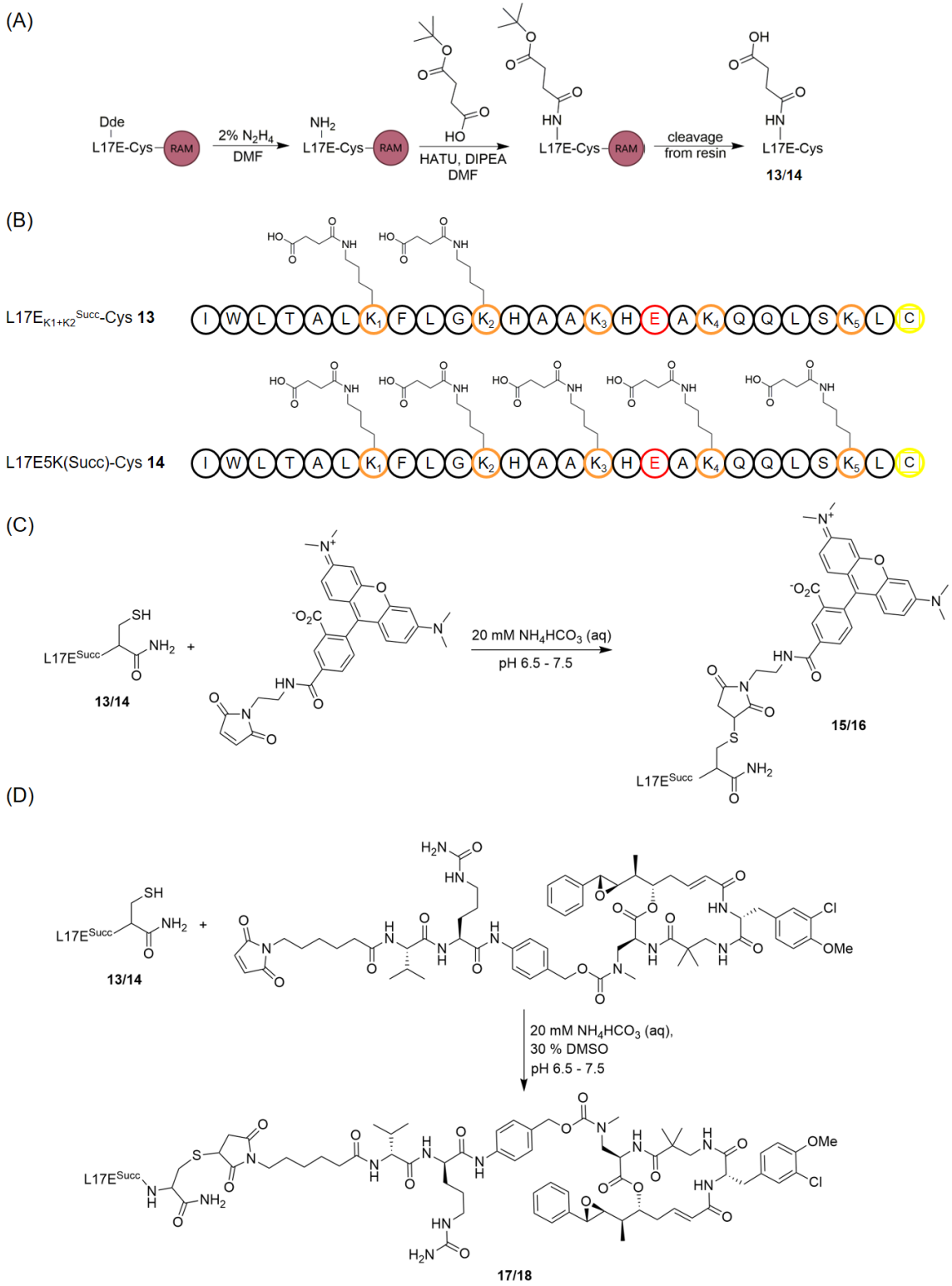

Figure 24| (A) Reaction scheme for the synthesis of L17E$_{K1+K2}^{Succ}$-Cys **13** and L17E5K(Succ)-Cys **14**. (B) Amino acid sequence of **13** and **14** with succinylated lysine residues and cysteine on the *C*-terminus. (C) TAMRA conjugation by thiol-maleimide reaction yields L17E$_{K1+K2}^{Succ}$-TAMRA **15** and L17E5K(Succ)-TAMRA **16**. (D) Synthesis of L17E$_{K1+K2}^{Succ}$-cry **17** and L17E5K(Succ)-cry **18** occurred analogously using maleimide-cryptophycin.

Figure 24 shows the synthesis of the succinylated L17E peptides L17E$_{K1+K2}^{Succ}$-Cys **13** and L17E5K(Succ)-Cys **14**. An additional cysteine on the *C*-terminus of the peptide allowed for conjugation of maleimide-TAMRA yielding L17E$_{K1+K2}^{Succ}$-TAMRA **15** and L17E5K(Succ)-TAMRA **16** or maleimide-cryptophycin yielding L17E$_{K1+K2}^{Succ}$-Cry **17** and L17E5K(Succ)-Cry **18** in a thiol-maleimide reaction. It should be noted that the synthesis of **15** and **16** could not be confirmed by LC-MS. The succinyl groups combined with the isomeric mixture of TAMRA, displayed a broad peak in chromatographic separation, such that the amount substance ionized in the MS at a given time may have been too little for detection. Nevertheless, since a pink solid was obtained after purification, it was assumed coupling was successful. Staying in line with the ADEPT-like delivery concept, the antibody enzyme conjugates αB7H3-SirT5 and trastuzumab-SirT5 were generated. This was performed by Carolin Dombrowsky analogously to the antibody-SirT2 conjugates used previously.

4.1.5.2 SirT5 desuccinylation of L17E5K(Succ) 14

Confirmation of peptide desuccinylation by SirT5 was performed in a solution containing the succinylated L17E peptide **14** with five succinyl groups, SirT5 and NAD in PBS and incubation for 1 h at 37 °C. The enzyme was removed by heat denaturation and the supernatant was analyzed by RP-HPLC (Figure 25).

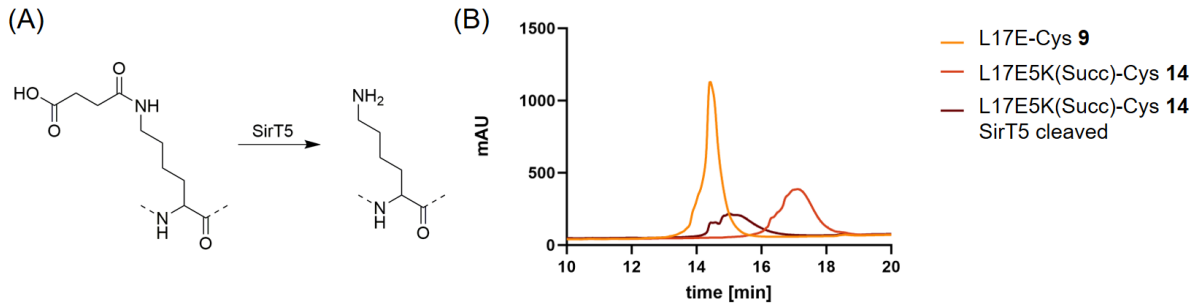

Figure 25| (A) Removal of the succinyl protecting group on a lysine residue by SirT5, (B) Overlaid RP-HPLC chromatograms from 10-20 min of L17E-Cys **9**, L17E5K(Succ)-Cys **14** and SirT5 cleaved **14** (gradient 0 to 100 % eluent B and 220 nm). Plotted using GraphPad Prism.

The RP-HPLC chromatogram shows a complete shift of the SirT5 cleaved L17E5K(Succ) **14** to the unprotected peptide **9**. LC-MS confirmed the mass of a fully deacetylated peptide (Figure S 7). Encouraged by these results, the conditional delivery of a fluorophore was investigated next.

4.1.5.3Cellular uptake assay: conditional intracellular delivery of a fluorophore

A cellular uptake assay using L17E$_{K1+K2}^{Succ}$-TAMRA **15** and L17E5K(Succ)-TAMRA **16** was performed similarly as described in section 4.1.1.2 and 4.1.2.2. Briefly, the succinylated peptides **15** and **16** were incubated for 2 h at 37 °C on HeLa cells, washed off, and the cells

were incubated another 3 h in medium only. For the ADEPT-like delivery method, the HeLa cells were pre-treated with αB7H3-SirT5 conjugates, that should bind the HeLa cells, or trastuzumab-SirT5, which served as negative control that should not bind HeLa cells. In addition, HeLa cells were treated with a mixture of **15** or **16** with SirT5 to observe desuccinylation function. The CLSM images are shown Figure 26.

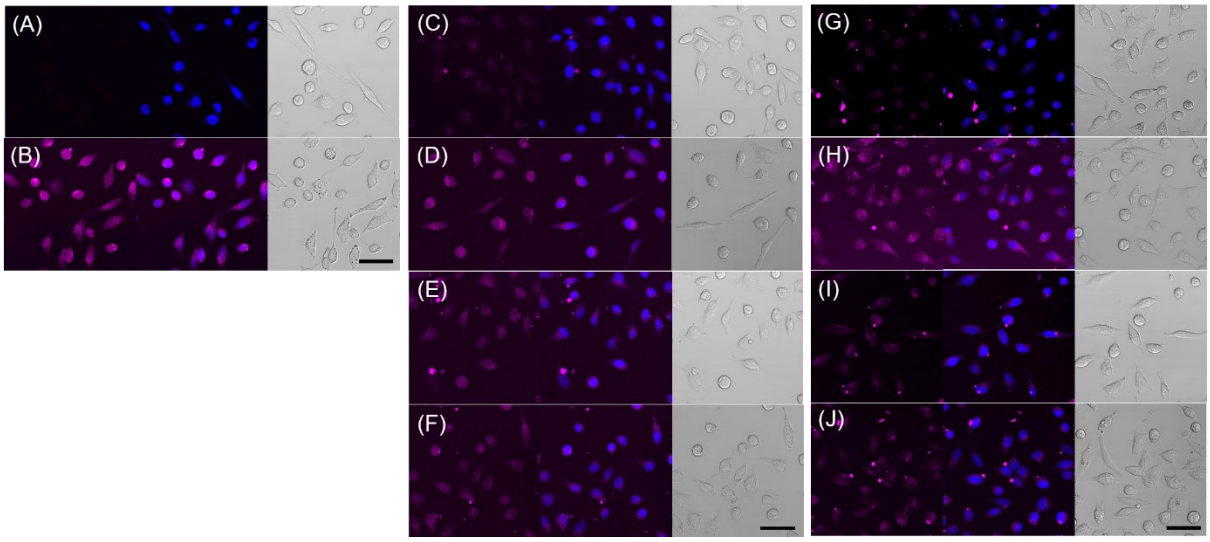

Figure 26| (A)-(J) CLSM images of HeLa cells treated with 5 µM peptide samples for 2 h at 37 °C including controls. (A) Cells only, (B) L17E-TAMRA **1**, (C) L17E$_{K1+K2}^{Succ}$-TAMRA **15**, (D) L17E$_{K1+K2}^{Succ}$-TAMRA **15** + SirT5, (E) 50 nM αB7H3-SirT5 treated cells with L17E$_{K1+K2}^{Succ}$-TAMRA **15**, (F) 50 nM trastuzumab-SirT5 treated cells with L17E$_{K1+K2}^{Succ}$-TAMRA **15**, (G) L17E-5K(Succ)-TAMRA **16**, (H) L17E-5K(Succ)-TAMRA **16** + SirT5, (I) 50 nM αB7H3-SirT5 treated cells with L17E5K(Succ)-TAMRA **16**, (J) 50 nM trastuzumab-SirT5 treated cells with L17E5K(Succ)-TAMRA **16**. Left: fluorescence channel, center: merge fluorescence with Hoechst channel (nuclear staining), right: brightfield channel. The scale bar denotes 50 µm. Images were taken under the same microscopy tuning parameters and processed with ImageJ.

The CLSM images showed strongly reduced intracellular fluorescence in HeLa cells treated with L17E$_{K1+K2}^{Succ}$-TAMRA **15** or L17E5K(Succ)-TAMRA **16**. Therefore, contrary to the L17E peptides with two alloc-protecting groups **2-5**, two succinyl groups on the L17E peptide were able to impair cellular uptake. This supports the claim that negative charges have a stronger effect in prohibiting internalization than with zero net charge. SirT5 treated peptides **15** and **16** resulted in recovery of intracellular fluorescence (Figure 26D and H respectively), with intracellular fluorescence intensities similar to the control L17E-TAMRA peptide **1** (Figure 26B). Contrary to expectations, HeLa cells pre-treated with αB7H3-SirT5 or trastuzumab-SirT5 both showed cytosolic intracellular fluorescence, indicating that the peptide had partly internalized, although this was only expected of αB7H3-treated cells. This was likely due to insufficient washing of the antibody-SirT5 conjugates, as a second experiment showed that both αB7H3-SirT5 and trastuzumab-SirT5 treated cells displayed an absence of intracellular fluorescence (Figure S 8), indicating that deprotection by the αB7H3-SirT5 conjugate had not occurred. This could be due

to the absence of αB7H3-binding to the HeLa cells, or impairment of SirT5 function for steric reasons, since it was conjugated to αB7H3. Therefore, optimization of the linker is required. Nevertheless, these results showed an improved blocking effect of the succinyl protecting group, compared to the acetyl protecting group. To further exemplify the performance of the negatively charged succinyl group on the L17E peptide, the TAMRA fluorophore was exchanged for a toxin and a cellular proliferation assay was conducted as described in the next section.

4.1.5.4Cellular proliferation assay: conditional intracellular delivery of a toxin

The recombinantly produced SirT5 enzyme showed enhanced stability compared to the SirT2 enzyme at 37 °C, which allowed a standard cellular proliferation assay to be performed. A dilution series of cryptophycin-labelled peptide samples was continuously incubated on the cells for 72 h at 37 °C. The number of viable cells was measured using the CellTiter96®Aqueous One solution cell proliferation assay. As the L17E$_{K1+K2}^{Succ}$-cry peptide **17**, still showed free cryptophycin in the sample after purification, which could falsify results due to cryptophycin's cell permeability, the cellular proliferation assay was only performed with L17E5K(Succ)-cry peptide **18**, shown in Figure 27.

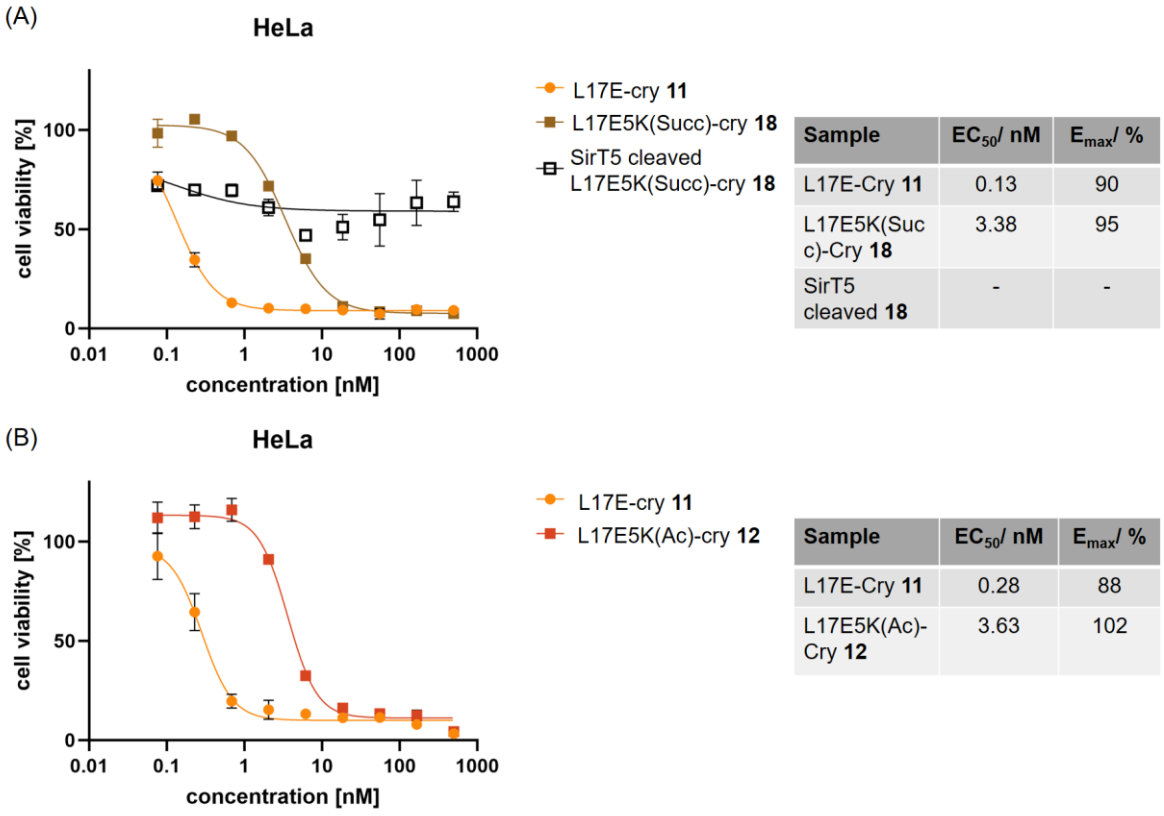

Sample	EC_{50}/ nM	E_{max}/ %
L17E-Cry **11**	0.13	90
L17E5K(Succ)-Cry **18**	3.38	95
SirT5 cleaved **18**	-	-

Sample	EC_{50}/ nM	E_{max}/ %
L17E-Cry **11**	0.28	88
L17E5K(Ac)-Cry **12**	3.63	102

Figure 27| Cell proliferation assays of L17E-cry **11** and (A) L17E5K(Succ)-cry **18** or (B) L17E5K(Ac)-cry **12** on HeLa cells with EC_{50} and E_{max} values.

As expected, the succinylated peptide **18** showed reduced cytotoxicity compared to the L17E-cry peptide **1**, with EC_{50} values of 0.13 nM and 3.38 nM, respectively, corresponding to a 26-fold difference. Unfortunately, activation of **18** using the SirT5 enzyme could not be observed, which may be linked to SirT5 instability and precipitation over 72 h, which may have falsified the absorbance measurements of the cell proliferation assay. Nevertheless, **18** still showed significant cytotoxicity, similar to the acetyl protected peptides, despite the blocking effects of the TAMRA-labelled succinyl-protected L17E peptides **15** and **16** observed in the previous section. For a direct comparison of performance of the succinyl and acetyl protecting groups, the cellular proliferation assay was repeated using L17E5K(Ac)-cry peptide **12** on HeLa cells (Figure 27B). It is noticeable that the EC_{50} values of the L17E peptides, whether masked five times with the succinyl or acetyl protecting group, display very similar values. Therefore, it is likely that the hydrophobicity of cryptophycin mediates internalization of the peptide conjugates to a greater extent than the protecting groups block it. This suggests that blocking the cellular internalization of a masked CPP is dependent on the cargo it is carrying. This observation aligns with the common consensus that the type of cargo influences cellular uptake efficiency. The cellular proliferation assay may therefore display different results for the masked L17E peptide conjugated to other toxins.

4.2 Dextran modification for the multimerization of CPPs

For the intracellular delivery of larger cargos, it can be necessary to use multiple CPPs to facilitate efficient delivery. Dextran is an attractive candidate as a scaffold for the multimerization of CPPs due to its high water solubility and clinical safety profile.

4.2.1 Design and synthesis of dextran

The modification of 10 kDa dextran from *L. mesenteroides* follows a well-established procedure in our working group. It first proceeds with a reductive amination step on the reducing end of dextran using cadaverine and the reducing agent sodium cyanoborohydride in alkaline conditions, generating *N*-Boc-cadaverine-dextran **19**. The next step, carboxyethylation, controls the desired number of CPPs to be conjugated to the dextran. In orientation to previous work by Dr.Bastian Becker and Dr. Simon Englert[140] it was initially chosen to couple around five CPPs to the dextran, whereby a balance between efficacy and cytotoxicity due to the CPP was prioritized. Carboxyethylation is performed in 1 M NaOH with acrylamide, whereby the amount of acrylamide controls the number of carboxyethyl (CE) groups per dextran. After hydrolysis of the amide, the resulting product *N*-Boc-cadaverine-dextran-CE **20** is modified with the azide linker *N*-(5-aminopentyl)-2-azidoacetamide **21**, that is synthesized from azido acetic acid and cadaverine on solid phase (2-chlorotrityl chloride (CTC) resin), yielding *N*-Boc-cadaverine-

dextran-N_3 **22**. Final removal of the Boc protecting group using TFA presents the product cadaverine-dextran-N_3 **23** with an amine moiety on the reducing end that serves as an orthogonal site for conjugation of a cargo. The steps for dextran modification are summarized in Figure 28. The intermediates were assessed by ^{1}H-NMR, whereby the signals were normalized to the 62 anomeric protons of the dextran molecule. This is the average number of glucose units per dextran with a molecular weight of 10 kDa, and since each glucose unit exhibits one anomeric proton that is significantly downfield shifted compared to the other signals, it can be clearly observed.

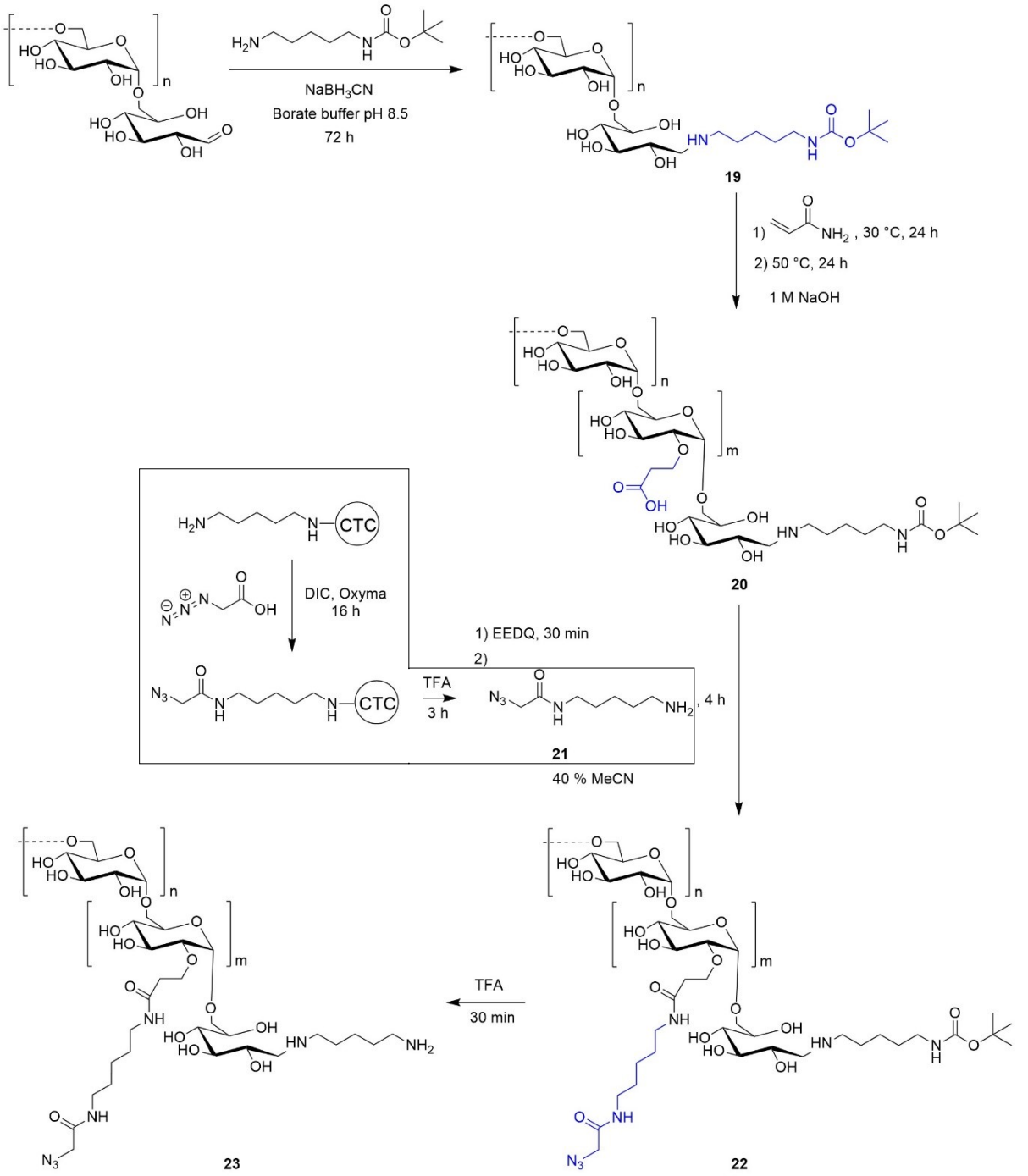

Figure 28| Synthesis route of the chemical modification of dextran, starting with reductive amination to *N*-Boc-cadaverine-dextran **19**, followed by carboxyethylation to obtain *N*-Boc-cadaverine-dextran-CE **20**. Attachment of *N*-(5-aminopentyl)-2-azidoacetamide **21**, synthesized on solid phase, to **20** yields *N*-Boc-cadaverine-dextran-N_3 **22** and after TFA treatment cadaverine dextran-N_3 **23**, with two orthogonal sites available for peptide and cargo conjugation.

Multiple dextran batches were synthesized for the following experiments. The details for the dextran modification procedure and the ^{1}H-NMR spectra are provided as an example for one batch. In the reductive amination step, the amine forms a Schiff base with the aldehyde of the terminal glucose unit in open-chain form, that is subsequently reduced by sodium

cyanoborohydride to form an irreversible bond between the two components. As the equilibrium of polysaccharides lies in favor of the closed-chain form,[200] the reaction is given a longer period of time to proceed (72 h) and occurs in the presence of a large excess of *N*-Boc-cadaverine in sodium borate buffer pH 8.5, for optimal conversion. After precipitation in methanol, purification by size exclusion chromatography and freeze-drying, the product *N*-Boc-cadaverine-dextran **19** (batch 1) was analyzed by ^{1}H-NMR (Figure 29). The signals of the aliphatic chain of *N*-Boc-cadaverine **2-6** and the singlet arising from the symmetry of the protons in the Boc-protecting group **7** respective to the 62 anomeric protons **1** was greater than expected (15 protons), which can be explained through unreacted *N*-Boc-cadaverine left in the sample despite SEC purification. This is likely, since the signal diminished after the carboxyethylation step that proceeded next.

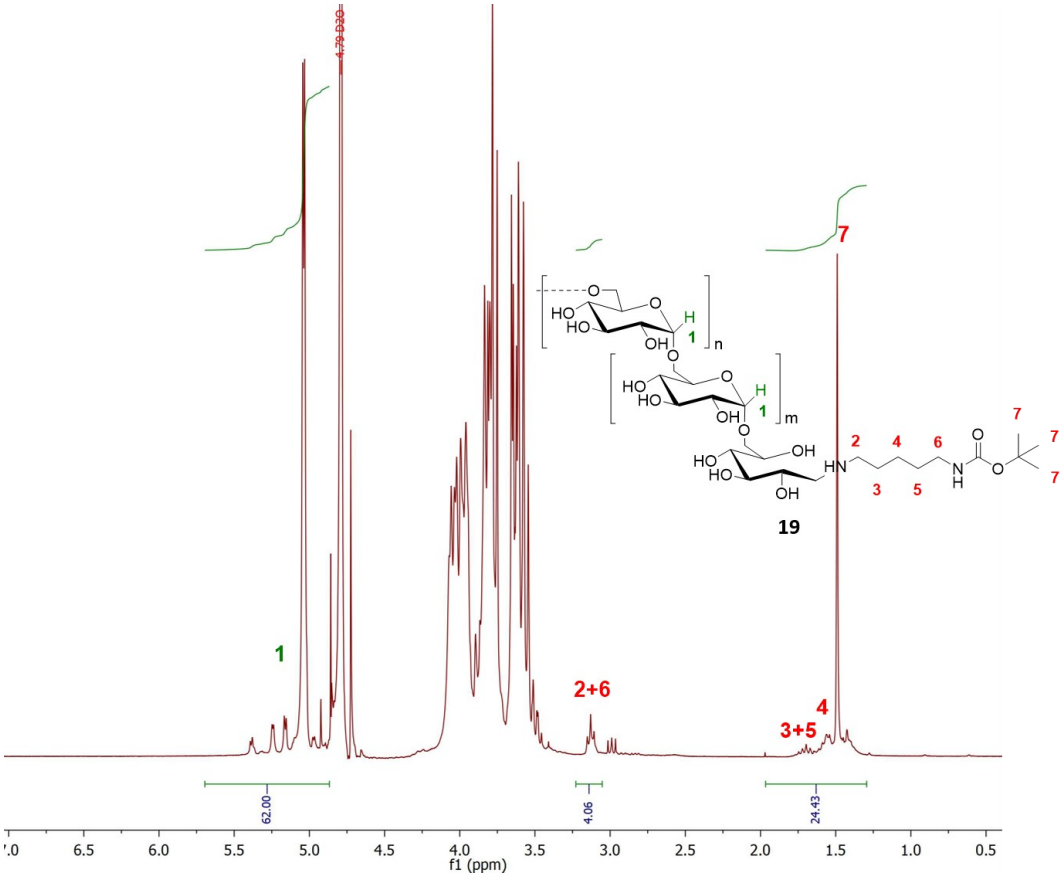

Figure 29| ^{1}H-NMR spectrum (300 MHz, D_2O) of *N*-Boc-cadaverine-dextran **19** (batch 1). The protons of *N*-Boc-cadaverine **2-7** are normalized to the anomeric protons **1** that are set to 62.

The product *N*-Boc-cadaverine-dextran **19** was subjected to carboxyethylation with acrylamide in basic aqueous solution at 30 °C for 24 h, whereby alkylation occurs exclusively on the C_2-glucose unit.[139] The reaction temperature was then raised to 50 °C to hydrolyze the amide. With approximately 2.5 eq. acrylamide necessary for one CE-group on dextran, the number of CE-groups can be controlled.[133] The product *N*-Boc-cadaverine-dextran-CE **20** was precipitated

in methanol, neutralized and purified by size exclusion chromatography. The ^{1}H-NMR spectrum of **20** obtained from from **19** (batch 1) is shown in Figure 30. The carboxyethylation step resulted in 5.6 CE-groups on average per dextran molecule (denoted *N*-Boc-cadaverine-dextran-CE(5.6) **20**, batch 1). This was calculated by halving the integral value of the new signal occurring at 2.5 ppm in the ^{1}H-NMR spectrum that corresponds to two protons of the CE-groups **8**. Furthermore, it is noticeable that that the value of the integral for *N*-Boc-cadaverine has reduced, although still higher than the expected value 15, indicating there was still unreacted *N*-Boc-cadaverine from the reductive amination step.

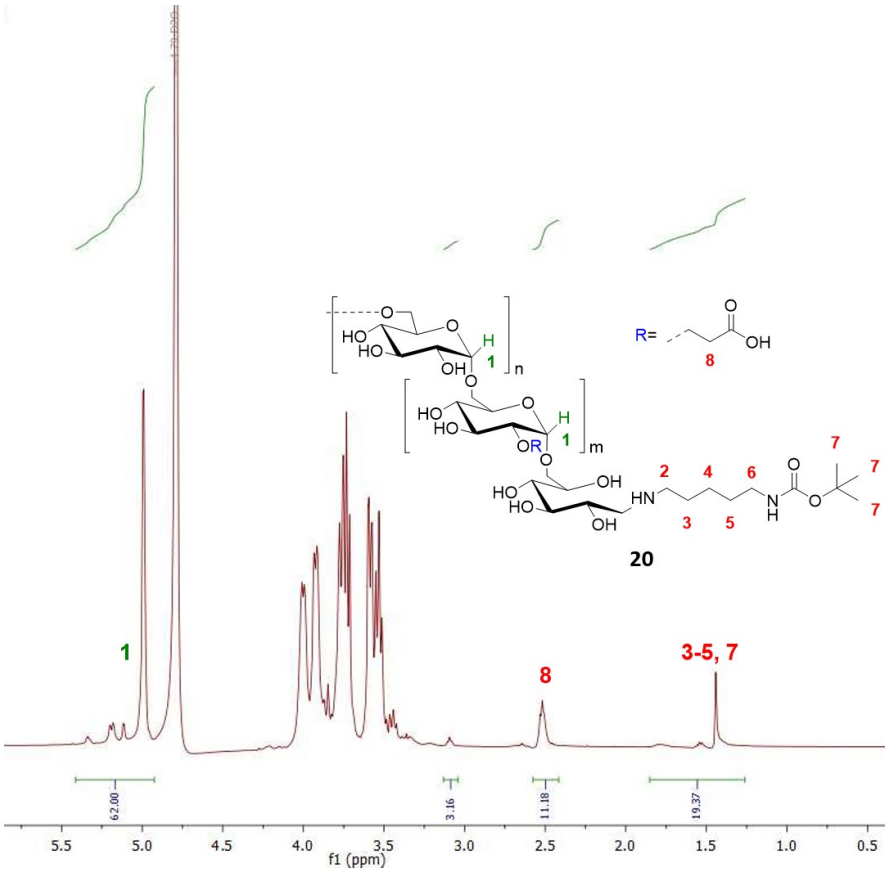

Figure 30| ^{1}H-NMR spectrum (300 MHz, D_2O) of *N*-Boc-cadaverine-dextran-CE **20** (batch 1) with 5.6 CE-groups/dextran.

The newly introduced carboxyl functionality was used for the attachment of a linker, bearing on one side an amine and on the other an azide group (*N*-(5-Aminopentyl)-2-azidoacetamide **21**, section 6.5.3) that can be used in a click reaction for conjugation of peptides to the scaffold. The carboxyl group was pre-activated for 30 minutes using EEDQ in 40 % acetonitrile and the linker was attached through formation of an amide bond. The product *N*-Boc-cadaverine-dextran-N_3 **22** (Figure 31) was isolated by precipitation in methanol and purified by size exclusion chromatography. In the last step, the Boc protecting group was cleaved by treatment with TFA for 30 min. After evaporation of the TFA, the product was dissolved in water and

lyophilized. Any remaining TFA in the product was neutralized and purified by size exclusion chromatography to yield the final product cadaverine-dextran-N_3 **23**, that resulted in the disappearance of the Boc-singlet protons **7** in the ^{1}H-NMR spectrum (Figure 31). The number of azide linkers attached per dextran molecule can be estimated from the integrals observed in spectrum using equation (1).[201,202] Thereby, an average over the signals from cadaverine on the reducing end and azide linker is formed.

$$\frac{N_3\ groups}{dextran} = \frac{\frac{(2+6)(total-red.end)}{4}+\frac{(8)}{2}+\frac{(3+5)(total-red.end)}{4}+\frac{(4)(total-red.end)}{2}}{4} \quad (1)$$

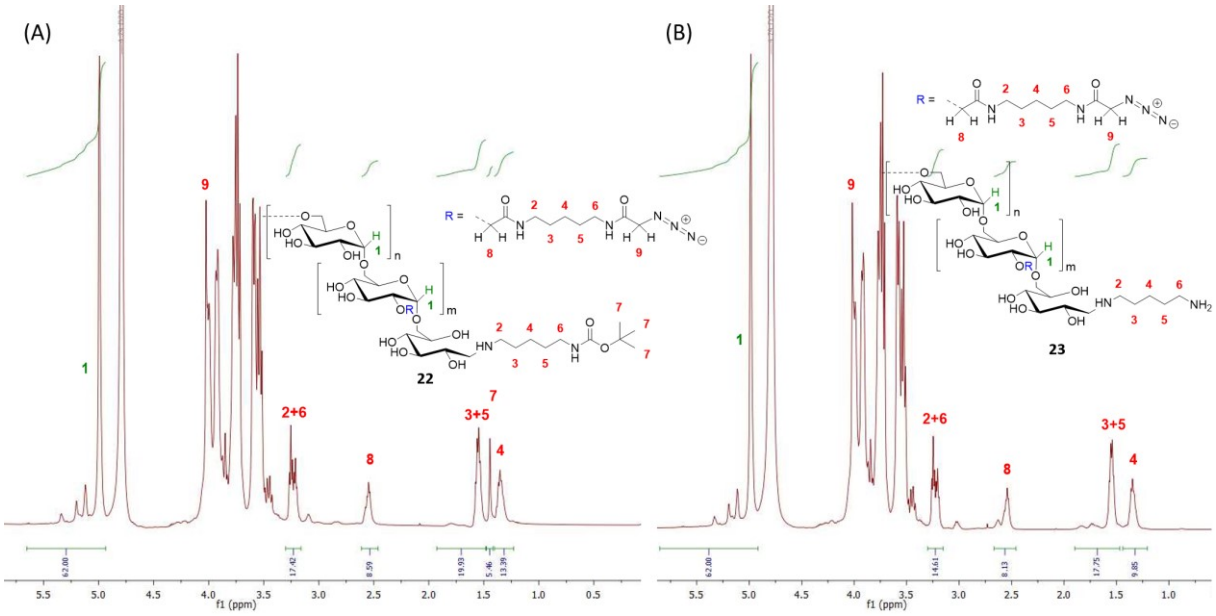

Figure 31| ^{1}H-NMR spectrum (300 MHz, D_2O) of (A) *N*-Boc-cadaverine-dextran-N_3 **22** (batch 1) with calculated 4.1 N_3-groups/dextran and (B) cadaverine-dextran-N_3 **23** (batch 1) with calculated 3.3 N_3-groups/dextran.

For cadaverine-dextran-N_3 **23** in Figure 31, it was assumed the reductive amination step had occurred quantitatively. Consequently, according to equation 1, cadaverine-dextran-N_3 **23** shows on average in Figure 31A before Boc deprotection 4.1 N_3-groups/dextran and Figure 31B after Boc deprotection 3.3 N_3-groups/dextran. This discrepancy is possibly due to baseline corrections leading to varying results, as it is noticeable, that all integrals after Boc deprotection are generally smaller in the spectrum. Table 1 shows a summary of all dextran batches synthesized in this work for the upcoming experiments with the number of CE-groups/dextran and number of N_3-groups/dextran determined before and after Boc deprotection as determined from the ^{1}H-NMR signals.

Table 1| Summary of all dextran batches synthesized in this work with the number of CE-groups/dextran and N_3-groups/dextran determined before and after Boc deprotection.

Dextran batch	No. of CE-groups	No. of N_3-groups before Boc removal	No. of N_3-groups after Boc removal
1	5.6	4.1	3.3
2	5.0	5.2	4.6
3	3.7	2.8	3.4
4	6.3	4.9	5.0

With the exception of batch 4, it is noticeable that the number of N_3-groups varies before and after Boc removal, which makes it difficult to precisely calculate the number of N_3-groups per dextran molecule. Furthermore, as the signals for the azide linkers in the ^{1}H-NMR overlap with those of the cadaverine moiety on the reducing end, the calculated number of N_3-groups depends on the integral of the cadaverine signals in the ^{1}H-NMR of the precursor products **19** or **20**. As was the case of the dextran batch shown, residual *N*-Boc-cadaverine that could not be removed after the reaction leads to falsely lowered average of N_3-groups per dextran. Therefore, as the attachment of the linker to the carboxyl groups of dextran is an amidation reaction, that is known to be highly efficient with yields over 90 %,[203] and especially because a large excess (8.5 eq.) azide linker were used per carboxyl group in the reaction, it may be more accurate to determine the number of N_3-groups by assuming 100 % conversion of the carboxylic acid groups, whose signals are distinct in the ^{1}H-NMR spectrum. For this reason, 100 % conversion of the CE-groups was assumed. Consequently, the cadaverine-dextran-N_3 shown in Figure 31 was denoted cadaverine-dextran-N_3(5.6), indicating the presence of 5.6 N_3-groups per dextran molecule. The same was applied for the other batches.

4.3 Conditional intracellular delivery of dextran-ACPP conjugates

Following the generation of activatable L17E peptides for conditional intracellular delivery, the concept was extended to dextran-L17E conjugates. Therefore, dextran-ACPP conjugates were generated next.

4.3.1 The role of masked L17E peptides on a dextran scaffold for conditional delivery

4.3.1.1 Design and synthesis

The amine on the reducing end of cadaverine-dextran-N_3(5.6) **23** was reacted with an NHS-ester of 5,6-TAMRA yielding TAMRA-dextran-N_3(5.6) **24** (Figure 32**)**. The fluorogenic cargo would allow cellular internalization to be observed by confocal microscopy. **24** was isolated by

precipitation in methanol and purified by size exclusion chromatography, whereby a pink solid was obtained.

Similar to section 4.1.1, as it is easier to deprotect fewer protecting groups, beginning with a minimal number of protecting groups on L17E would be advantageous. In parallel to the previously shown project, Alloc masking groups were investigated first. Even though two Alloc protecting groups on the solitary peptide had proven insufficient for intracellular delivery, it may perform differently when multimerized on a dextran scaffold due to the larger overall size of the carrier. For blocking cellular uptake, it was first considered that the *N*-terminus of L17E was important for cell penetration,[93] wherefore masking groups were introduced on the lysine positions K1 or K2. An alkyne functionality on the *C*-terminus was introduced by manual coupling of Fmoc-Pra-OH to the resin, while the peptide sequence was assembled using an automated peptide synthesizer. The peptide was cleaved from the resin and isolated by precipitation in cold diethyl ether. After purification of the peptide by preparative RP-HPLC, the resulting peptides L17E$_{K1}^{Alloc}$-Pra **25** and L17E$_{K2}^{Alloc}$-Pra **26** were conjugated to dextran in a copper-catalyzed azide-alkyne cycloaddition (CuAAC) click reaction that occurred at 30 °C for 3 h. The Cu^{I} catalyst was generated *in situ* from the reduction of $CuSO_4 \cdot 5H_2O$ by ascorbic acid in a mixture containing the prepared TAMRA-dextran-N_3(5.6) **24** and the Alloc-L17E peptides **25** or **26**. In the final step, the crude reaction mixture was purified by size exclusion chromatography and lyophilized. The reaction scheme is illustrated in Figure 32.

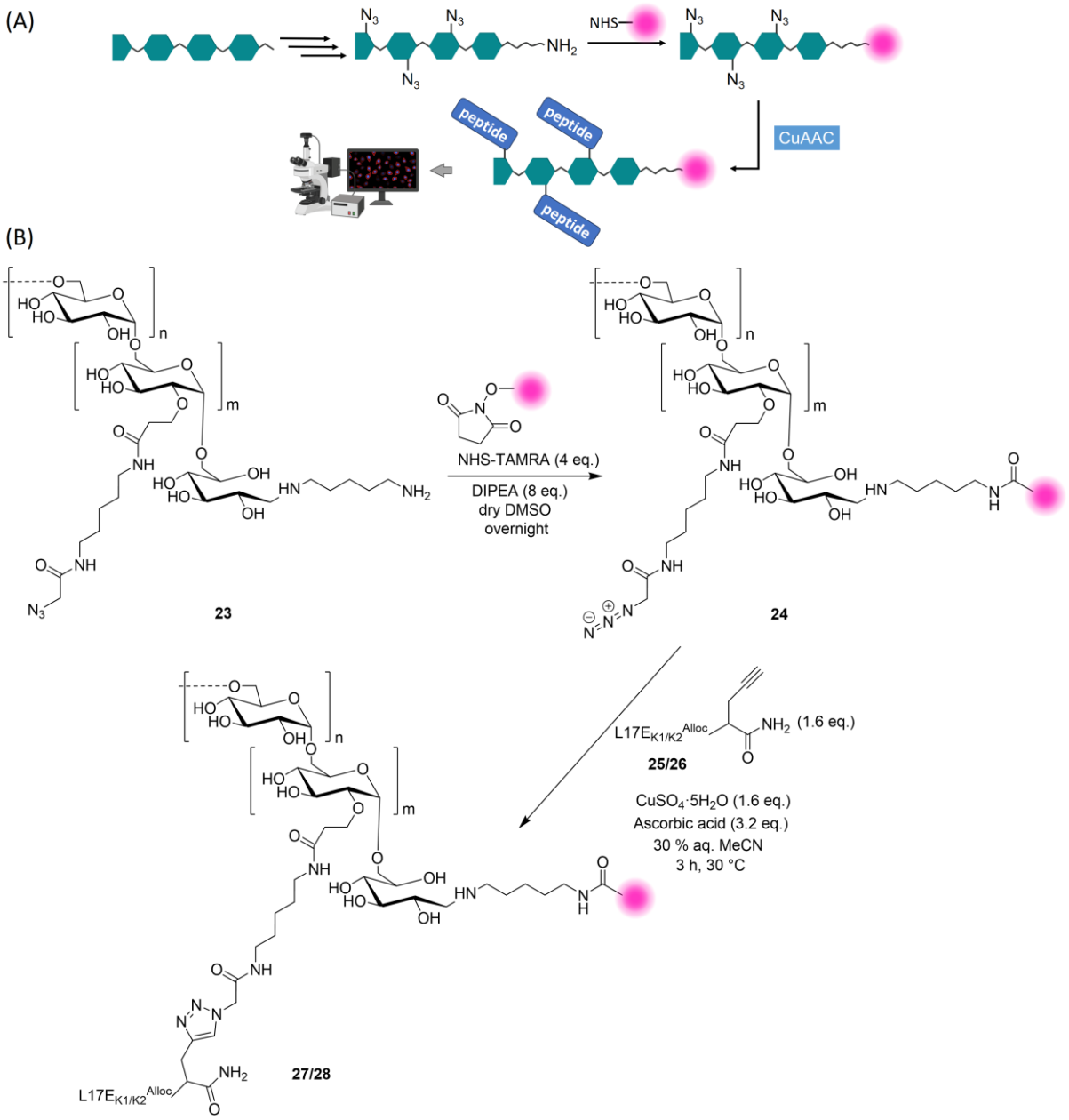

Figure 32| (A) Schematic illustration of dextran modification with TAMRA coupling and attachment of the peptide for confocal microscopy analysis. (B) Reaction scheme for the synthesis of TAMRA-dextran-N_3(5.6) **24** (batch 1) and following attachment of L17E$_{K1}^{Alloc}$-Pra **25** or L17E$_{K2}^{Alloc}$-Pra **26** by CuAAC to yield TAMRA-dextran-L17E$_{K1}^{Alloc}$(5.6) **27** or TAMRA-dextran-L17E$_{K2}^{Alloc}$(5.6) **28** respectively.

The attachment of the peptide to the dextran can be followed by observing the distinct asymmetric stretching vibrations of the azides upon excitation with infrared (IR) light that occurs at around 2124 cm^{-1},[204] and disappears with the attachment of the peptide upon conversion to a 1,2,3-triazole. Figure 33 shows the IR spectra before and after attachment of the peptide. Although a small band remains to be seen in the IR spectrum after CuAAC, for simplicity full conversion with the peptides **25** and **26** was assumed, yielding TAMRA-dextran-

L17E$_{K1}^{Alloc}$(5.6) **27** or TAMRA-dextran-L17E$_{K2}^{Alloc}$(5.6) **28**. The bracketed numbers suggest full conversion i.e. all N_3-groups were addressed by the peptide.

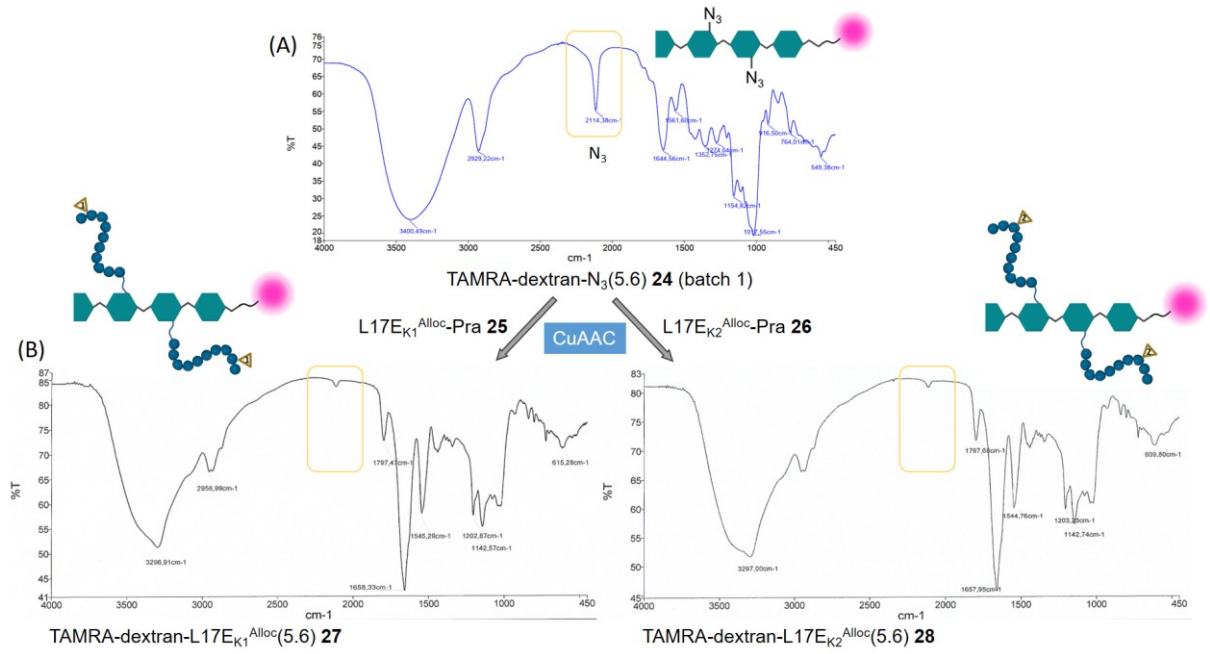

Figure 33| IR spectra of (A) TAMRA-dextran-N_3(5.6) **24** (batch 1) and (B) TAMRA-dextran-L17E$_{K1}^{Alloc}$(5.6) **27** and TAMRA-dextran-L17E$_{K2}^{Alloc}$(5.6) **28** after CuAAC. The N_3-vibrational band boxed in yellow has almost completely disappeared, indicating almost complete conversion.

As control for internalization, the unmasked L17E-Pra peptide **7** was also conjugated to TAMRA-dextran-N_3 **24** (a batch synthesized prior to this work with an average of 5 N_3-groups/dextran), to yield TAMRA-dextran-L17E(5) **29**. Conversion also occurred quantitatively (Figure 34).

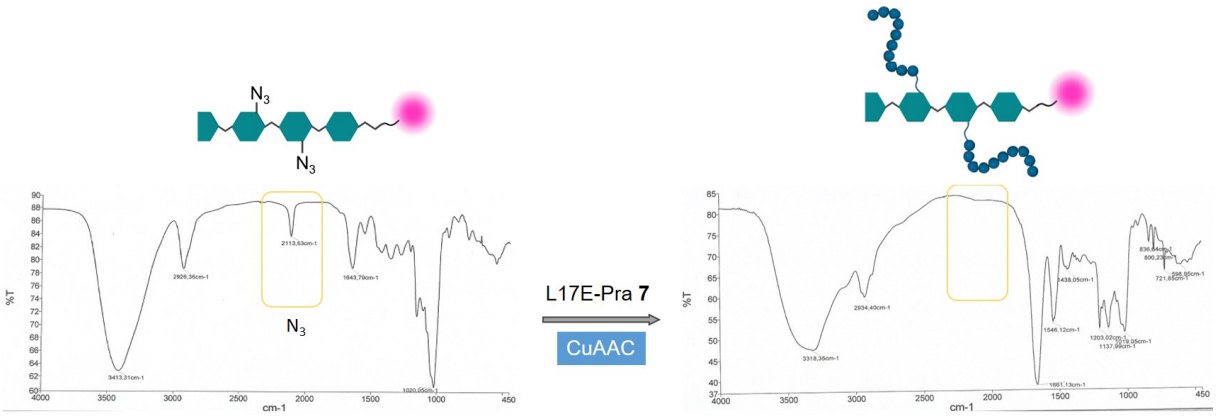

Figure 34| Scheme for CuAAC of L17E-Pra **7** to TAMRA-dextran-N_3(5) **24** (a batch synthesized prior to this work) and IR spectra of TAMRA-dextran-N_3(5) **24** (batch prior to this work) and TAMRA-dextran-L17E(5) **29** with N_3-vibrational band boxed in yellow.

As the TAMRA-dextran-L17E(1xAlloc) conjugates **27** and **28** unfortunately showed significant cellular uptake in internalization studies (see section 4.3.1.2), the number of alloc protecting

groups was increased to two. Multiple L17E(2xAlloc) peptides ($L17E_{K1+K2}^{Alloc}$-Pra **30**, $L17E_{K1+K3}^{Alloc}$-Pra **31**, $L17E_{K2+K4}^{Alloc}$-Pra **32** and $L17E_{K3+K5}^{Alloc}$-Pra **33**) with a propargyl glycine moiety on the *C*-terminus were synthesized, whereby the two alloc protecting groups were positioned as shown in Figure 13. TAMRA-dextran-L17E(2xAlloc) conjugates **34-37** were synthesized in the same manner as before by CuAAC and analyzed by IR spectroscopy (Figure 35). A small azide vibrational band can still be observed, indicating complete conversion was not achieved. Nevertheless, the vibrational band is small and for simplicity, complete conversion was assumed.

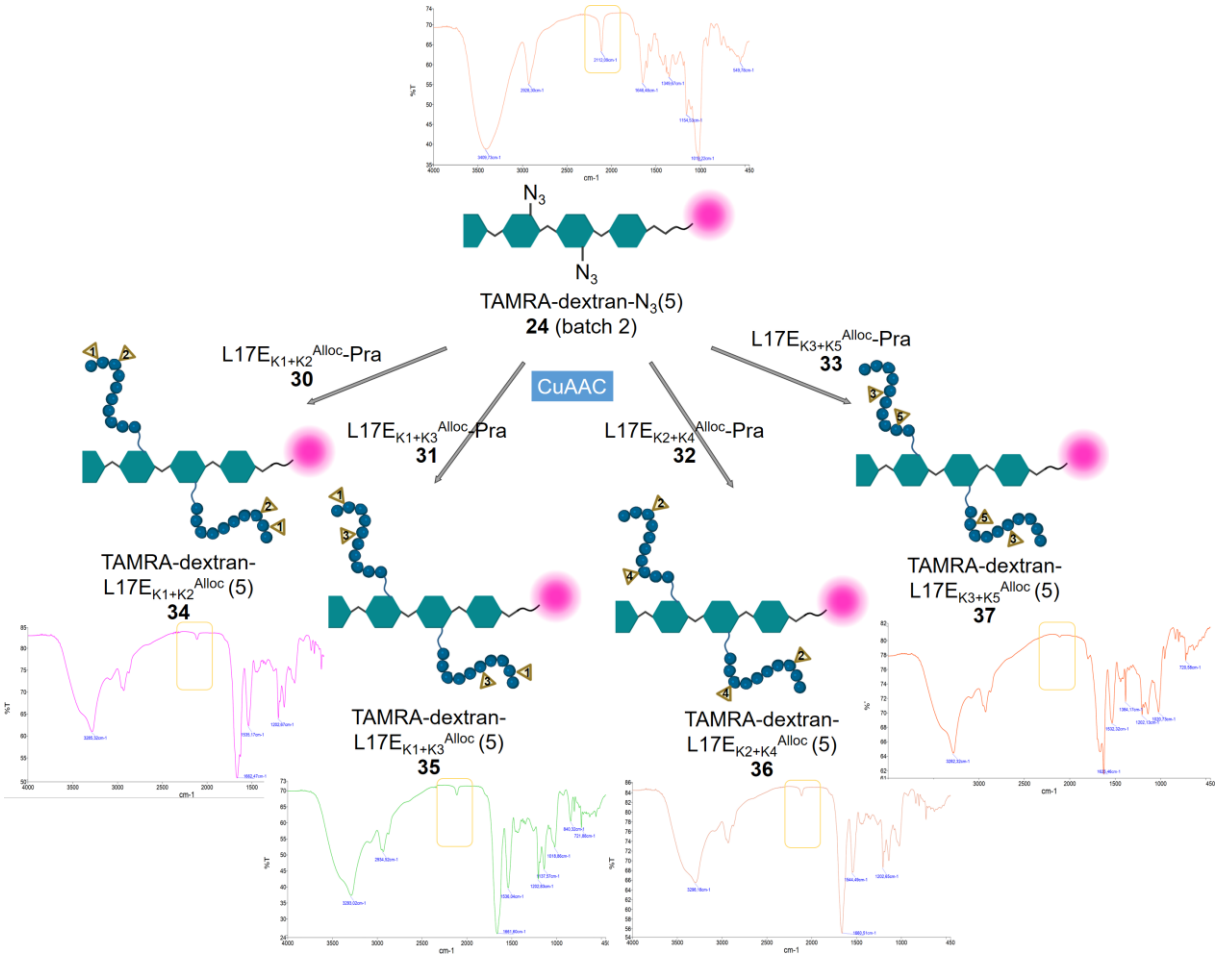

Figure 35| Scheme for CuAAC of L17E(2xAlloc) peptides **30-33** to TAMRA-dextran-N_3(5) **24** (batch 2) and corresponding IR spectra of TAMRA-dextran-L17E(2xAlloc)(5) conjugates **34-37** with N_3-vibrational band boxed in yellow.

4.3.1.2 Cellular uptake assay: intracellular delivery of TAMRA-dextran-L17E(1xAlloc) conjugates

The samples TAMRA-dextran-$L17E_{K1}^{Alloc}$(5.6) **27** and TAMRA-dextran-$L17E_{K2}^{Alloc}$(5.6) **28** were evaluated in a cellular uptake assay, with the expectation that the Alloc protecting group would impair internalization of the conjugate. HeLa cells were seeded in 8-well μ-slides and incubated with 5 μM of the dextran-L17E(1xAlloc) conjugates for 90 min at 37 °C in serum-containing

medium. The cells were fixed immediately afterwards and observed by CLSM. The control TAMRA-dextran-L17E(5) was incubated for 1 h only at the same conditions. The images are shown in Figure 36.

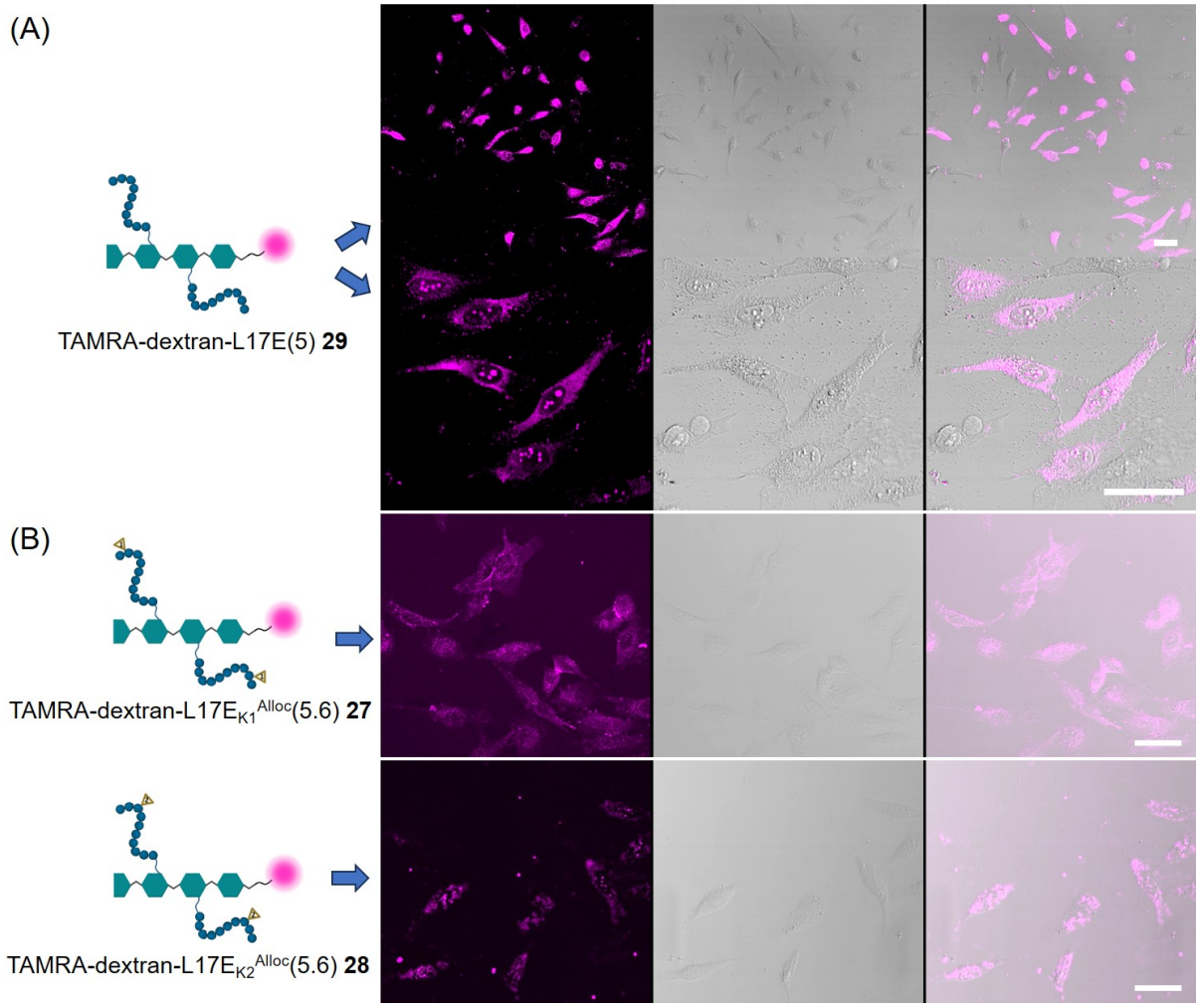

Figure 36| CLSM images of HeLa cells treated with (A) 5 µM TAMRA-dextran-L17E(5) **29** for 1 h and (B) 5 µM TAMRA-dextran-L17E(1xAlloc) conjugates **27** and **28** for 1.5 h at 37 °C. Left: fluorescence channel, center: brightfield channel, right: merge brightfield and fluorescence. The scale bar denotes 50 µm. Images were taken under the same microscopy tuning parameters and processed with ImageJ.

For TAMRA-dextran-L17E(5) bright intracellular fluorescence can be observed throughout the cytosol, indicating that cellular uptake had occurred. The presence of punctuate signals in the cell nucleus that are presumably nucleoli suggests that the conjugate also permeated the nuclear membrane. The nuclear envelope is interrupted by nuclear pore complexes (NPCs) that serve as an exclusive gateway for importing proteins into the nucleus and exporting RNA from the nucleus. In HeLa cells, the nuclear pore radius was estimated to be 4.9-5.7 nm in size, which easily allowed the passive diffusion of fluorescently labelled 20 kDa dextran and minimal diffusion of 40 kDa dextran, while 70 kDa dextran did not show signs of passive diffusion through the nuclear membrane.[205] The observed nuclear transport of TAMRA-dextran-L17E(5)

29 that has an approximate molecular weight of 26 kDa supports the data. For the TAMRA-dextran-L17E(1xAlloc) conjugates **27** and **28**, the CLSM images indicated through the presence of cytosolic fluorescence that cellular uptake still occurred despite introduction of one protecting group on the L17E peptide. The TAMRA-dextran-L17E$_{K2}^{Alloc}$(5.6) conjugate appeared to form punctuate signals, which may be an indication for uptake through an endocytic mechanism, with the conjugate entrapped in endosomes. The presence of a masking group at the lysine residue K2 may disrupt the positive charge sequence of the peptide, potentially hindering its ability to internalize through the direct penetration pathway. While the CLSM images were taken under the same microscopy tuning parameters, it should be mentioned that the dextran-conjugate **29** was derived from another TAMRA-dextran batch as **27** and **28**, that can have variability in TAMRA labelling and the actual number of peptides the dextran carries on average, as already suggested by the 5 and 5.6 N_3-groups per dextran. Nevertheless, it was assumed the influence of these factors is smaller than the impact it would have in a cellular uptake assay, where significant observable differences to **29** were expected. Herein, the results indicated that one protecting group on the L17E peptide does not efficiently block cellular uptake of the dextran-L17E conjugate. For the next experiments, the number of protecting groups was raised from one to two. The internalization of the TAMRA-dextran-L17E(2xAlloc) conjugates **34-37** is shown in the next section.

4.3.1.3 Cellular uptake assay: intracellular delivery of TAMRA-dextran-L17E(2xAlloc) conjugates 34-37

The cellular uptake assay of TAMRA-dextran-L17E(2xAlloc) conjugates **34-37** was performed as described in the previous section 4.3.1.2 at 4 μM concentration and incubation for 1 h at 37 °C or 4 °C in serum-containing medium.

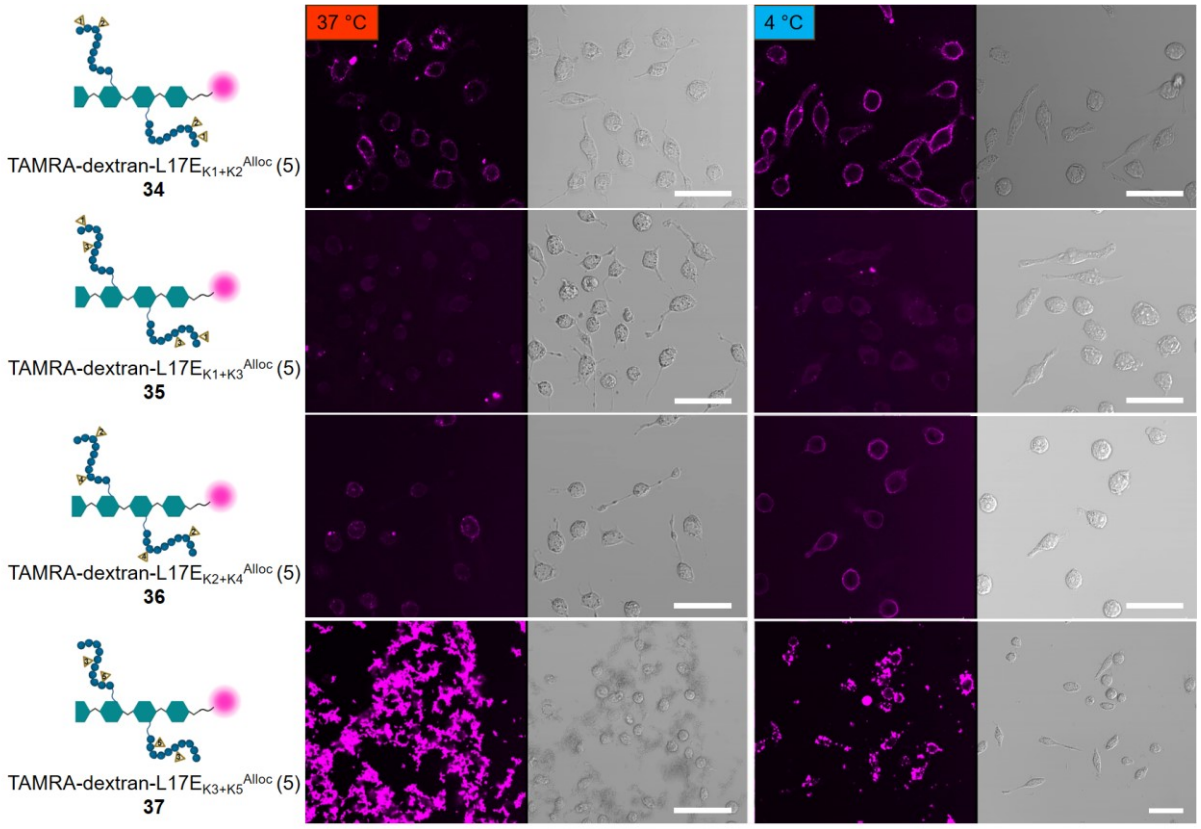

Figure 37| CLSM images of HeLa cells treated with 4 µM TAMRA-dextran-L17E(2xAlloc)(5) conjugates **34-37** for 1 h and at 37 °C or 4 °C. Left: fluorescence channel, right: brightfield channel. The scale bar denotes 50 µm. Images were taken under the same microscopy tuning parameters and processed with ImageJ.

Figure 37 shows the CLSM images of HeLa cells treated with the TAMRA-dextran-L17E(2xAlloc) conjugates **34-37**. Independent on the incubation temperature, masking the lysine residues K1+K2 or K2+K4 of the L17E peptide with Alloc groups on a dextran scaffold (**34** and **36**) primarily showed fluorescence outlining the cell membrane, rather than intracellular cytosolic fluorescence. This suggests the Alloc protecting group imparts stickiness to the conjugate, causing it to adsorb to the cell membrane. Some punctuate signals at the center of the cells can be seen for the K2+K4 masked dextran-L17E conjugate **36**, which may be the nucleoli, suggesting minimal cellular uptake occurred. This cannot be seen at 4 °C, suggesting uptake into the nucleus is energy dependent. However, since the unusual morphology of the cells at 37 °C is an indication for poor cell viability, this observation could be an artefact. When the lysine in K2 position is not masked, i.e. in the TAMRA-dextran-L17E$_{K1+K3}^{Alloc}$ conjugate **35**, adsorption to the outer membrane is strongly reduced, however some intracellular fluorescence can still be observed. This suggests the lysine in K2 position likely plays a significant role in cellular uptake. This is also supported by the internalization of TAMRA-dextran-L17E$_{K2}^{Alloc}$ conjugate **28** that seemed to follow another uptake mechanism compared to the unmasked peptide (Figure 36). Unfortunately, masking the lysines at positions K3+K5 of L17E on dextran

35 resulted in poor solubility of the construct, which is seen as precipitate in the images. In the next section, the alloc protecting groups were exchanged for acetyl protecting groups to enable deprotection by the SirT2 enzyme with the aim to reactivate intracellular delivery of the dextran conjugate.

4.3.2 Conditional activation of TAMRA-dextran-L17E(Ac) conjugates

4.3.2.1 Design

The cellular uptake assays from the previous section 4.3.1 suggested that lysine at the K2 position is central to cellular uptake. Therefore, new dextran-L17E conjugates were designed with acetyl protecting groups on the lysine at K2 position, but also the K1 positions as control. Although one alloc-protecting group on L17E multimerized on a dextran scaffold was not sufficient to inhibit its internalization, one acetyl protecting group, which although uncharged is also polar, could perform differently. Additionally, using one acetyl group per L17E peptide is advantageous because, particularly when multimerized on a dextran scaffold, it simplifies the deprotection process by reducing the number of protecting groups that need to be removed. The peptides L17E$_{K1}^{Ac}$-Pra **38** and L17E$_{K2}^{Ac}$-Pra **39** (section 6.6.12 and 6.6.13) were synthesized and conjugated to TAMRA-dextran-N$_3$(5) **24** by CuAAC, similarly to the previous section to yield the products TAMRA-dextran-L17E$_{K1}^{Ac}$(5) **40** and TAMRA-dextran-L17E$_{K2}^{Ac}$(5) **41** and analyzed by IR spectroscopy (Figure 38). Almost complete conversion was observed.

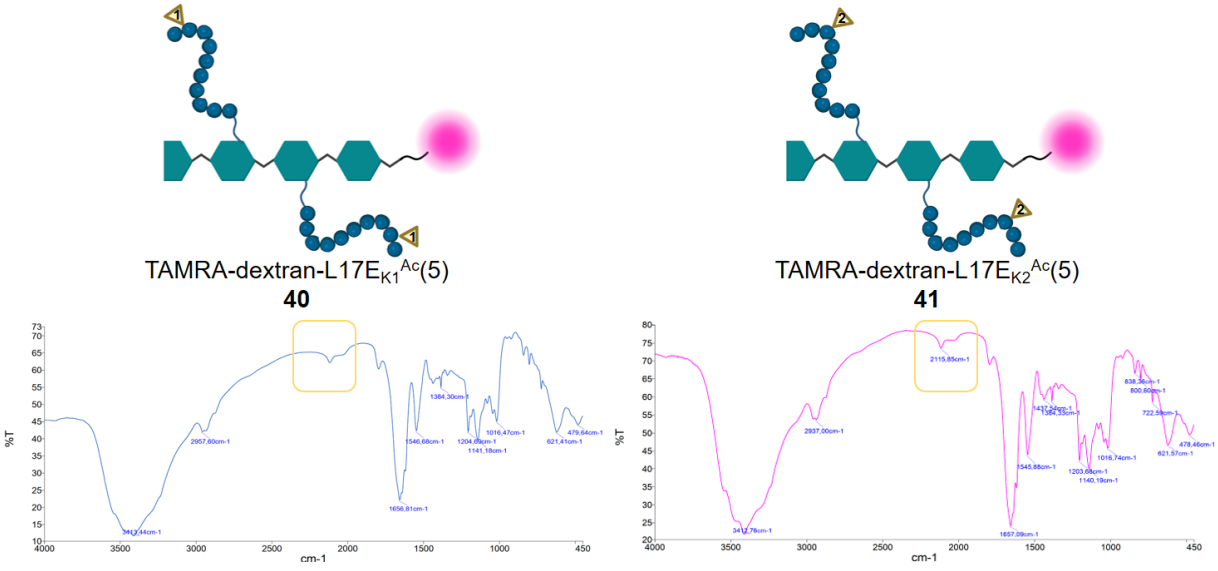

Figure 38| IR spectra of TAMRA-dextran-L17E^{Ac}(5) conjugates **40** and **41** with N$_3$-vibrational band boxed in yellow.

4.3.2.2 Conditional cellular uptake assay: intracellular delivery of TAMRA-dextran-L17E^{Ac} conjugates 40 and 41

The conditional reactivation of the intracellular delivery of TAMRA-dextran-L17E^{Ac} conjugates **40** and **41** was to be demonstrated through a cellular uptake assay, observed by intracellular

fluorescence by CLSM. Therefore, HeLa cells were treated with 5 μM **40** and **41**, and for the deprotection reactions additionally with 50 nM SirT2 and 400 μM NAD, in serum-containing medium. After incubation for 30 min, the sample was removed and incubated another 3 h in medium only. Due to the instability of the deacetylase SirT2 as mentioned in section 4.1.2, the cellular uptake assay was performed at 30 °C. The confocal microscopy images are shown in Figure 39.

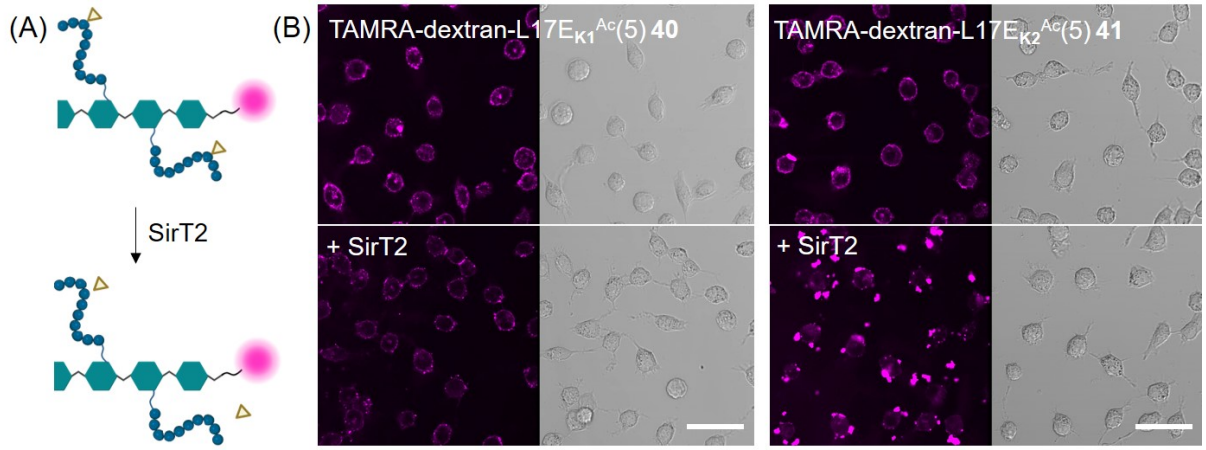

Figure 39| (A) Schematic illustration of the deprotection of dextran-ACPP conjugates. (B) CLSM images of HeLa cells treated with 5 µM TAMRA-dextran-L17E$_{K1}^{Ac}$(5) **40** and TAMRA-dextran-L17E$_{K2}^{Ac}$(5) **41**, without SirT2 incubation (top) and with 50 nM SirT2 and 400 µM NAD (bottom). Left: fluorescence channel, right: brightfield channel. The scale bar denotes 50 µm. Images were taken under the same microscopy tuning parameters and processed with ImageJ.

The CLSM images showed that one acetyl protecting group on L17E performed similarly to the L17E peptide containing two alloc protecting groups when multimerized on a dextran scaffold. Both **40** and **41** also accumulated around the cell membrane and were accompanied with some cytotoxicity, as indicated by the cell morphology. For the conjugate **40**, with lysine residue protected at the K1 position, fluorescence in the middle of the cell indicates some conjugate internalized, that is not seen for **41** with acetylated K2 position. The cellular uptake assay therefore suggested that the K2 position on L17E appears to more effectively impair cell penetration. Upon incubation of the dextran conjugates **40** and **41** with deacetylase, the expected strong intracellular fluorescence that extends throughout the cytosol of the cells was not observed. Conjugate **40** showed a similar fluorescence pattern outlining the cell membrane with SirT2 incubation, albeit at lower intensity. Conjugate **41** showed strongly reduced adsorption to the cell membrane and appeared to show weak intracellular fluorescence, which however is difficult to identify due to bright fluorescent spots that had appeared. These spots may be precipitation of the conjugate, or also conjugate co-precipitated with SirT2. Since these observations left ambiguous results, it was decided to verify whether SirT2 can indeed deacetylate the dextran-L17E^{Ac} conjugates.

4.3.2.3 Verification of SirT2 deacetylation of TAMRA-dextran-L17E$_{K2}^{Ac}$ conjugate 41

The TAMRA-dextran-L17E$_{K2}^{Ac}$ conjugate **41** was chosen for verification of SirT2 deacetylation, since the cellular uptake assay indicated that some internalization may have occurred. For this purpose, **41** was incubated in PBS with SirT2 and NAD for 1 h at 30 °C. Excess SirT2 was removed through heat denaturation and centrifugation. The supernatant was taken for further analysis.

Since the L17E^{Ac} peptides were conjugated to dextran, which has large weight distribution, deacetylation could not be simply proven by mass spectrometry. The polydispersity of the dextran polymer combined with the statistical conjugation of the peptide results in a non-uniform product, too polydisperse to yield conclusive results by MALDI analysis (Figure 40). Furthermore, TAMRA-dextran-L17E$_{K2}^{Ac}$(5) **41** has an average molecular weight of 26.7 kDa, whereupon deacetylation of one acetyl group, of which there are an average of five per dextran molecule due to the five L17E$_{K2}^{Ac}$ peptides, the resulting loss is only 0.2 kDa. This small change necessitates a highly sensitive method for proof of deacetylation.

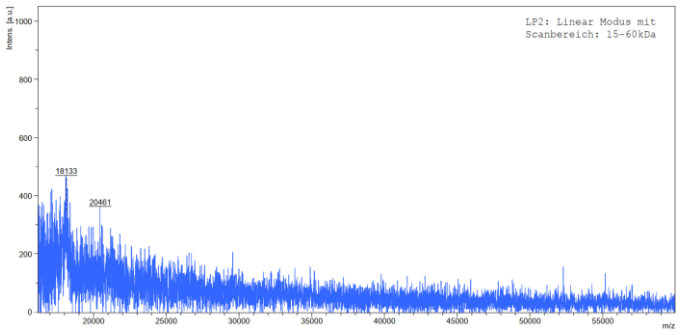

Figure 40| MALDI-TOF mass spectrum of SirT2 treated TAMRA-dextran-L17E$_{K2}^{Ac}$(5) **41** (average molecular weight 26.5 kDa). The heterogenous conjugate displays a high baseline in the spectrum.

Alternatively, instead of following a loss in molecular weight, SirT2 deprotection results in an increase in the number of primary amines as the lysine residues are deprotected. To accomplish this, the 2,4,6-trinitrobenzene sulfonic acid (TNBS) assay for determination of free amino groups was applied as second method in an attempt to verify deacetylation on the dextran conjugate **41**. TNBS is a sensitive reagent that reacts with primary amines to form a chromogenic derivative (*N*-(2,4,6-trinitrophenyl)amine) that can be measured at 335 nm. As the SirT2 enzyme also contains free amines and may not be fully removed in the denaturation step, a sample of **41** without the cofactor NAD was tested in parallel. In this sample, deacetylation should not occur. It was verified that NAD influence on the absorption signal at the concentration utilized (2 mM) is negligible (Figure S 8). Comparing SirT2 and NAD treated **41** to untreated **41**, the number of free primary amines should increase from 20 (resulting from

four primary amines per L17E peptide with each dextran molecule carrying five L17E peptides on average) to 25 (a total of five acetyl groups can be deprotected per dextran molecule). This corresponds to an increase in primary amine content by 25 %, which is expressed as a formula in equation (2). Samples were prepared in triplicates and measured using the *CLARIOStar®* microplate reader in three independent experiments. The results are shown in Table 2.

$$\frac{c(NH_2,\ SirT2+NAD+TAMRA\text{-}dextran\text{-}L17E_{K2}^{Ac}(5))}{c(NH_2,\ SirT2+TAMRA\text{-}dextran\text{-}L17E_{K2}^{Ac}(5))} \cdot 100\ \% = 125\ \% \qquad (2)$$

Table 2| TNBS assay results of SirT2 and NAD treated TAMRA-dextran-L17E$_{K2}^{Ac}$(5) **41** of three independent experiments measured in triplicates. High variability between individual experiments observed.

Exp.	TAMRA-dextran-L17E$_{K2}^{Ac}$(5) **41** A335 triplicates and mean value				$\frac{c(NH_2,SirT2+NAD+TAMRA-dextran-L17E_{K2}^{Ac}(5))}{c(NH_2,SirT2+TAMRA-dextran-L17E_{K2}^{Ac}(5))} \cdot 100\%$
	+2 mM NAD		0 mM NAD		
1	0.0727	$\bar{A}_{335}$ = 0.0950±0.0167	0.069667	$\bar{A}_{335}$ = 0.0737±0.0029	129 %
	0.0997		0.074667		
	0.1127		0.076667		
2	0.0227	$\bar{A}_{335}$ = 0.0337±0.0090	0.0307	$\bar{A}_{335}$ = 0.0420±0.0114	80 %
	0.0447		0.0377		
	0.0337		0.0577		
3	0.0833	$\bar{A}_{335}$ = 0.0797±0.0029	0.0203	$\bar{A}_{335}$ = 0.0243 ±0.0029	327 %
	0.0793		0.0253		
	0.0763		0.0273		

There was high variability between individual experiments comparing the amine content in conditions where deprotection should occur (samples with 2 mM NAD) and where it should not (samples without NAD). Therefore, it could not be determined whether SirT2 is able to deacetylate the L17E peptide on a dextran scaffold. As the amount of sample was limited, experiments were performed in small volumes of 30 μL, which can explain the high variability of the results. To minimize errors in the TNBS assay, it is recommended to use larger volumes.[206] Due to the high variability in the TNBS assay and the ambiguous results obtained from the CLSM images, the project was discontinued.

4.3.3 Optimization of the intracellular delivery of dextran-CPP conjugates

Experiments performed by Dr. Simon Englert indicated dextran-L17E conjugates had issues in toxicity at higher concentrations,[202] which was also suggested in some CLSM images of dextran-ACPP conjugates previously shown. Therefore, it was desirable to search for other CPPs, with at least comparable or even better cell penetrating properties, but with reduced cytotoxicity. Futaki and coworkers had reported several other L17E peptide variants with

attenuated cytotoxicity. Two of these L17E peptide variants, the L17E/Q21E and HAad peptides,[95,96] were chosen as candidates for dextran conjugation. The L17E/Q21E peptide in a dimeric format outperformed L17E as a solitary peptide,[95] making it interesting to investigate how multimerization of the peptides compares. The HAad peptide is a rationally designed endosomolytic peptide derived from the L17E/Q21E peptide with enhanced endosomal escape properties. With His-to-Ala substitutions that enlarge the hydrophobic face of the peptide and the substitution of glutamic acid residues for aminoadipic acid, it results in a peptide with more hydrophobic and less charged features in the endosomal compartment that may enhance interactions with endosomal membranes and endosomal escape. The HAad peptide may be beneficial for large dextran conjugates internalized through endocytosis – the prevalent mechanism for larger delivery vehicles.[58]

4.3.3.1 Design and synthesis of dextran-CPP conjugates

The L17E/Q21E and HAad peptides were modified with an additional *C*-terminal alkyne (**42** and **43** respectively) to enable a click reaction to an azide-modified dextran **24**, bearing a TAMRA molecule as payload to allow observation of internalization by confocal microscopy. The IR spectra of the products of the click reaction TAMRA-dextran-L17E/Q21E(5) **44** and TAMRA-dextran-HAad(5) **45** including sequence of the peptides are shown in Figure 41.

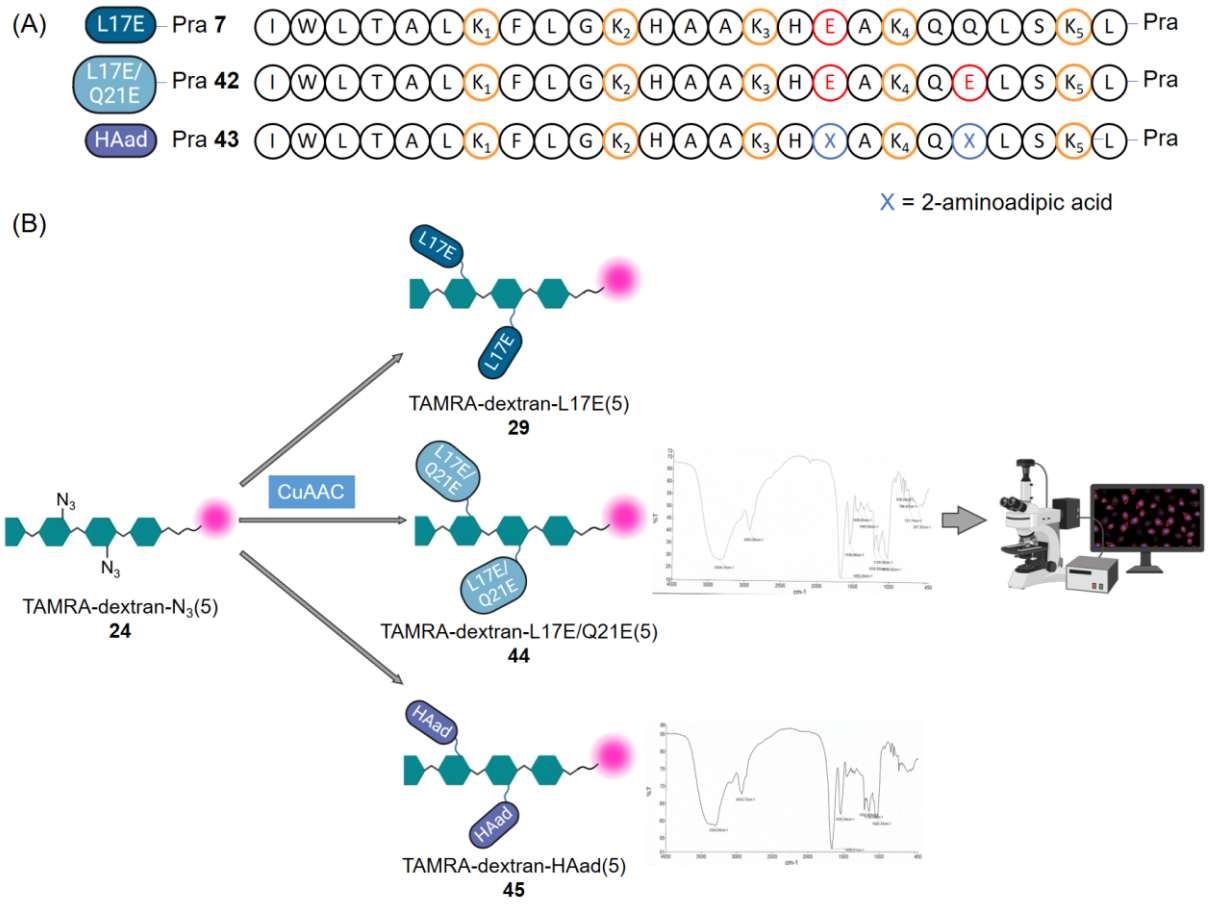

Figure 41| (A) Sequence of the peptides L17E-Pra 7, L17E/Q21E-Pra 42 and HAad-Pra 43. (B) Schematic illustration of the CuAAC reaction of these peptides to TAMRA-dextran-N_3(5) **24** yielding the conjugates TAMRA-dextran-L17E(5) **29**, TAMRA-dextran-L17E/Q21E(5) **44** and TAMRA-dextran-HAad(5) **45** including IR spectra for the new conjugates for confocal microscopy imaging.

4.3.3.2 Cellular uptake assay of alternative dextran-CPP conjugates

The performance of TAMRA-dextran-L17E(5) **29**, TAMRA-dextran-L17E/Q21E(5) **44** and TAMRA-dextran-HAad(5) **45** were evaluated in a cellular uptake assay. To accomplish this, 10 μM of the dextran conjugates **29**, **44** and **45** were incubated on HeLa cells in serum-containing medium for 1 h at 37 °C and then washed from the cells. After incubation of the cells for another 3 h in medium only, the cells were fixed and observed by CLSM (Figure 42).

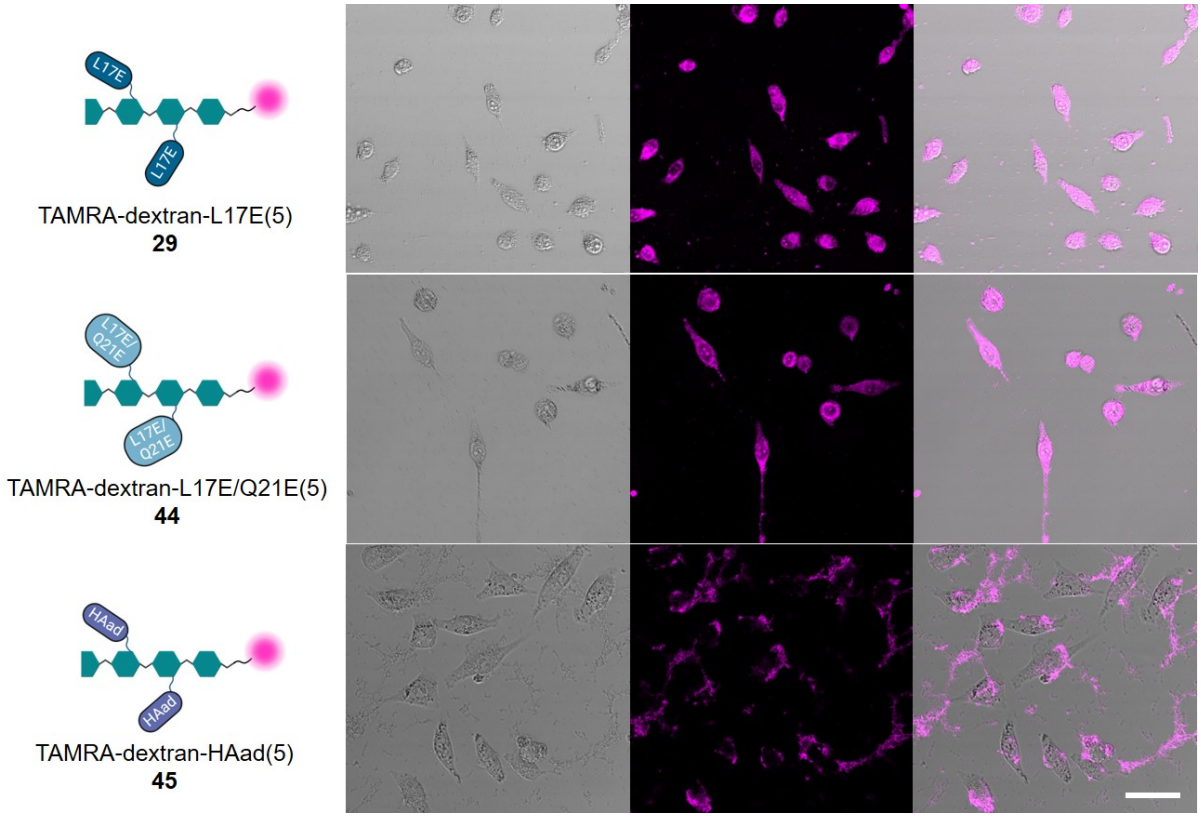

Figure 42| CLSM images of HeLa cells treated with 10 µM TAMRA-dextran-L17E(5) **29** (top), TAMRA-dextran-L17E/Q21E(5) **44** (middle) and TAMRA-dextran-HAad(5) **45** (bottom). Left: brightfield channel, center: fluorescence channel, right: overlay brightfield and fluorescence. The scale bar denotes 50 µm. Images were taken under the same microscopy tuning parameters and processed with ImageJ.

The CLSM images of HeLa cells treated with 10 μM TAMRA-dextran-L17E(5) **29** shown in Figure 42 are consistent with the results obtained with the construct at half the concentration in Figure 36. Fluorescence is evenly distributed throughout the cell cytoplasm and the nucleoli are labelled. The same could be observed for TAMRA-dextran-L17E/Q21E(5) **44**, without impairment in delivery compared to **29**, as indicated by the similar fluorescence intensities. On the contrary, the dextran conjugate with the endosomolytic peptide HAad **45** showed fluorescent debris outside of the cells, which could either be precipitation of the construct or remnants of destroyed cells or both. As the HAad peptide is more hydrophobic, it may have compromised solubility when multimerized. Furthermore, excess hydrophobicity has shown a tendency to lead to cell death.[96] Cells treated with TAMRA-dextran-N_3 **24** did not display fluorescence as expected (Figure S 10). As the L17E and L17E/Q21E peptides showed similar performance in cellular uptake, a cell proliferation assay was carried out to evaluate how the cytotoxicities of the two dextran conjugates **44** and **45** compare.

4.3.3.3 Cell proliferation assay of dextran-L17E 44 and dextran-L17E/Q21E 45 conjugates

For the cell proliferation assay, a concentration dilution series of TAMRA-dextran-L17E(5) **29** and TAMRA-dextran-L17E/Q21E(5) **44** were incubated on HeLa cells for 24 h. The result of the cell proliferation assay is depicted in Figure 43.

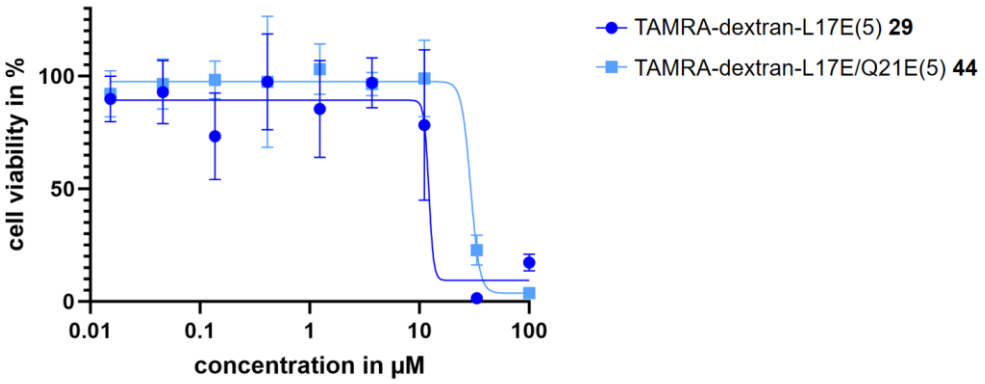

Figure 43| Cell proliferation assay of HeLa cells incubated with TAMRA-dextran-L17E(5) **29** and TAMRA-dextran-L17E/Q21E(5) **44** over 24 h. Image plotted using GraphPad Prism.

The mean lethal dose LD_{50} of the dextran-L17E conjugate **29** was determined to be 12 μM, which is comparable to the result obtained by Dr. Bastian Becker, who determined the LD_{50} value to be 10 μM for a dextran conjugate with an average of 4.8 L17E peptides per dextran (without TAMRA on the reducing end).[201] The dextran-L17E conjugate **29**, with an effective L17E concentration of 60 μM, showed increased toxicity compared to the solitary L17E peptide, for which no significant cytotoxicity could be observed up to 70 μM.[93,201] The dextran-L17E/Q21E conjugate **44** showed reduced cytotoxicity with an LD_{50} value of 31 μM. Combined with the cellular uptake, these preliminary results suggested that the L17E/Q21E conjugate was as efficient as the L17E peptide in intracellular delivery, while simultaneously exhibiting attenuated cytotoxicity. Therefore, the L17E/Q21E peptide could also be used to generate activatable dextran delivery modules for conditional intracellular delivery.

4.4 Streptavidin modular delivery architectures

4.4.1 Design and synthesis

It can be a long and tedious process to synthesize dextran conjugates with different CPPs and payloads for diverse applications. For this reason, a delivery module using streptavidin as a centerpiece building block was designed, that would allow up to four biotinylated components i.e. various combinations of dextran-CPP conjugate and payload, to be attached non-covalently in a mix-and-match approach by simple adjustment of stoichiometric ratios (Figure 44). Cell targeting moieties such as antibodies or peptides could be biotinylated and used for targeted

intracellular delivery. Dr. Simon Englert had showed the potential of these architectures for intracellular delivery, however the streptavidin-dextran-L17E architectures were always accompanied with significant cytotoxicity,[202] wherefore optimization was required. Given the finding that the L17E/Q21E dextran conjugate showed reduced cytotoxicity, the L17E/Q21E peptide was identified for further investigation along with the L17E peptide as a streptavidin delivery module. Furthermore, using streptavidin for tetramerization reduced synthesis effort such that two further CPPs, the stapled peptide ATSP-7041[97] and the α-helical rationally designed apCC-Di-B peptide[101] were investigated additionally for intracellular delivery.

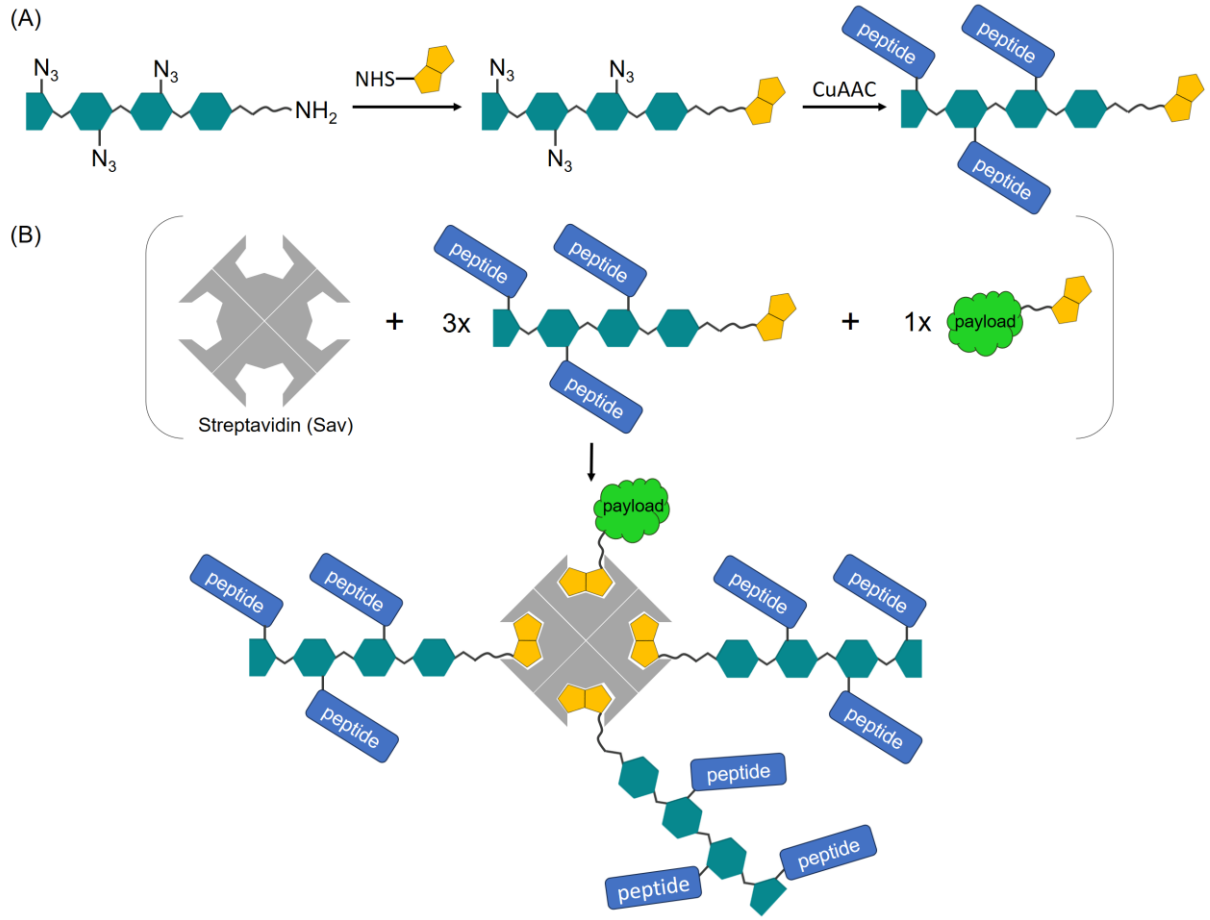

Figure 44| Schematic illustration of (A) biotinylation of dextran with subsequent CuAAC for attachment of peptides and (B) an example assembly of streptavidin-dextran conjugates with a dextran-CPP conjugate and payload in ratio 3:1.

Under consideration that Dr. Simon Englert observed cytotoxicity for streptavidin bearing two dextran-L17E conjugates (5.4 L17E peptides per dextran) at low micromolar concentrations, it would be practical to lower the number of L17E peptides per dextran conjugate to reduce overall cytotoxicity. Since the L17E/Q21E showed reduced toxicity, but needed dimerization to achieve at least the same delivery efficacy as the L17E peptide,[95] the number of L17E/Q21E per dextran could be increased. For the ATSP-7041 and apCC-Di-B peptides, it was chosen to

conjugate a lower number of these peptides, rather than a higher one to dextran due to their unknown toxicity profile. To do this, dextran was modified accordingly as described in section 4.2, resulting in dextran equipped with an average of 3.7 or 6.3 N_3-groups per molecule: cadaverine-dextran-N_3(3.7) **23** (batch 3) and cadaverine-dextran-N_3(6.3) **23** (batch 4) shown in Table 1. To enable binding of the dextran to streptavidin, the reducing end was biotinylated using NHS-biotin. Excess biotin was removed by size exclusion chromatography, resulting in the products biotin-dextran-N_3(3.7) **46** and biotin-dextran-N_3(6.3) **47**. The degree of labelling was not determined, coupling efficiencies were assumed to be comparable, so that the ratio of bound to unbound dextran conjugate to the streptavidin are similar and would be comparable in cellular uptake assays.

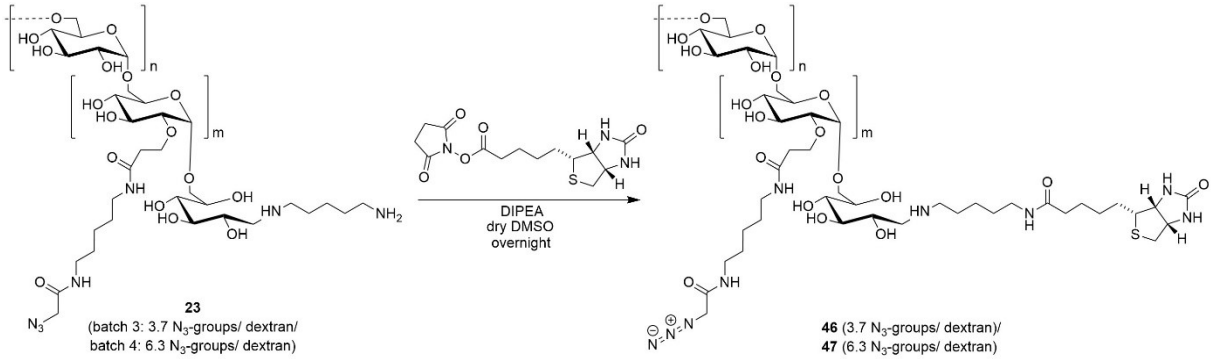

Figure 45| Reaction scheme for the biotinylation of cadaverine-dextran-N_3 **23** (batch 3 and 4) to yield biotin-dextran-N_3(3.7) **46** and biotin-dextran-N_3(6.3) **47**.

The L17E-Pra **7** and L17E/Q21E-Pra **42** peptides had been synthesized from the previous sections, therefore the project included the synthesis of the ATSP-7041 and apCC-Di-B peptides only. As these peptides had been used with fluorophores on the *N*-terminus in literature,[97,101] the alkyne moiety for the CuAAC reaction to dextran was also introduced on this terminus to ensure functionality of the peptide. Figure 46 shows the peptides alkyne-ATSP-7041 **48** and alkyne-apCC-Di-B **49**.

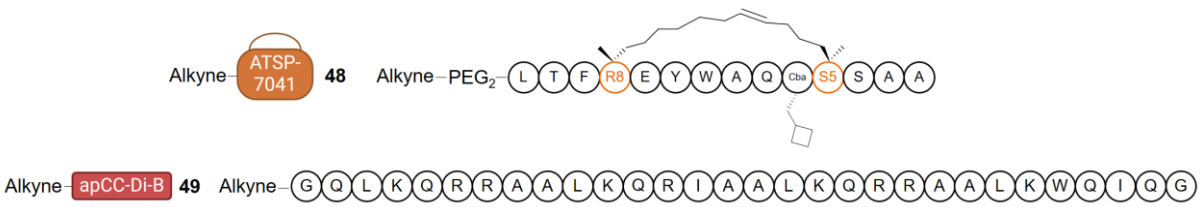

Figure 46| Sequences of the CPPs alkyne-ATSP-7041 **48** and alkyne-apCC-Di-B **49**.

The alkyne-ATSP-7041 peptide **48** was synthesized manually on solid support. After coupling the peptide sequence and polyethylene glycol (PEG) that served as a spacer to acquire distance to the dextran backbone when attached, ring closing metathesis (RCM) was performed between

the pentenyl and octenyl moiety in the peptide sequence with the 15 mol-% Grubbs Hoveyda 2nd Generation catalyst.[97] In the last step, the alkyne was introduced by coupling of 4-pentynoic acid. The synthesis of alkyne-ATSP-7041 **48** is illustrated in Figure 47.

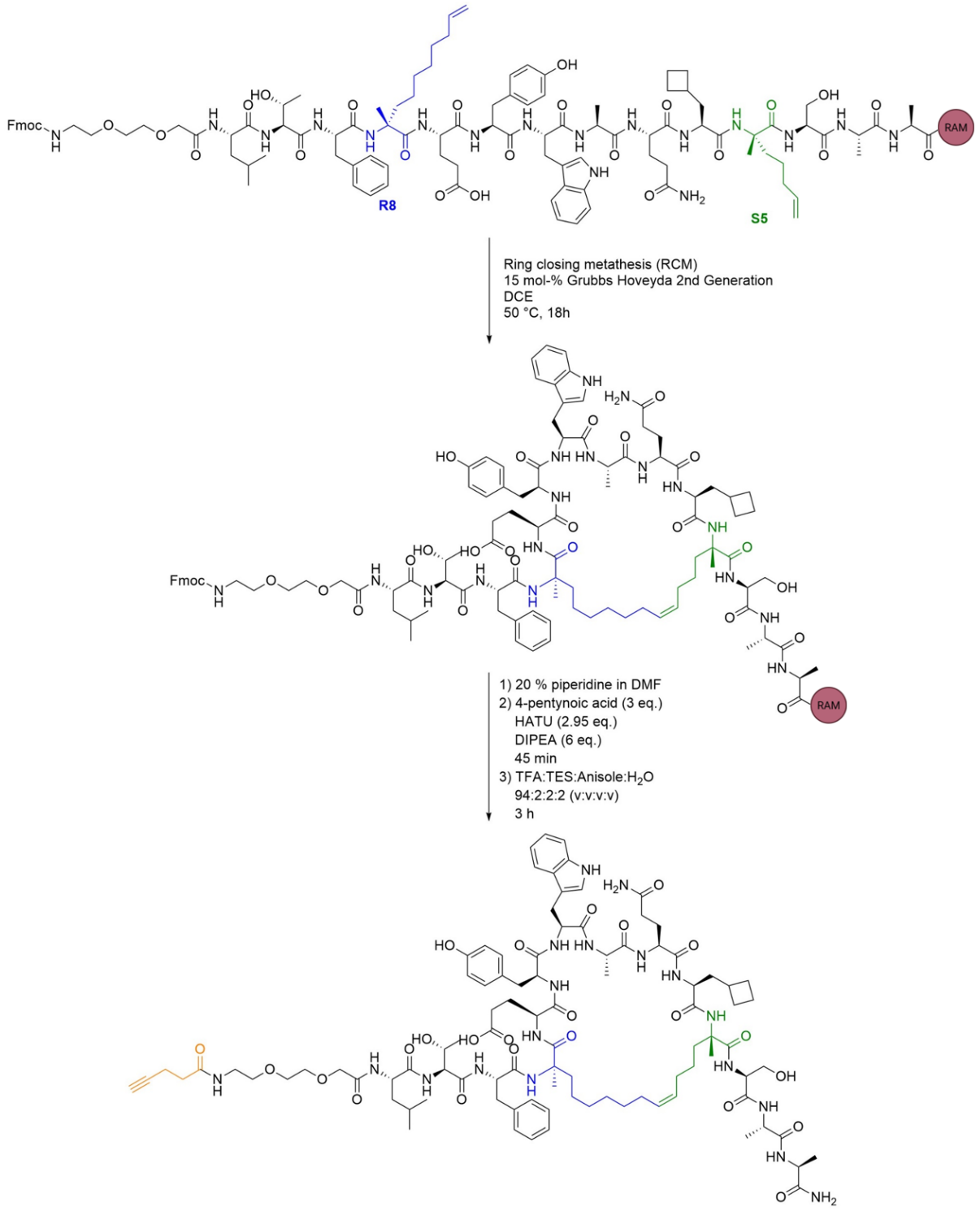

Figure 47| Reaction scheme for the synthesis of 4-pentynoic acid-PEG_2-ATSP-7041 **48**. Cyclisation occurred through ring closing metathesis (RCM) using the Grubbs Hoveyda 2nd Generation catalyst. An alkyne was introduced through manual coupling of 4-pentynoic acid with HATU and DIPEA.

The alkyne-apCC-Di-B peptide **49** was synthesized on an automated basis using a microwave-assisted peptide synthesizer. 4-pentynoic acid was coupled manually and supplied the alkyne moiety for the peptide.

The L17E-Pra **7**, alkyne-ATSP-7041 **48** and alkyne-apCC-Di-B **49** peptides were conjugated in a CuAAC reaction to the biotinylated dextran with 3.7 N_3-groups per dextran **46**, while the L17E/Q21E-Pra peptide **42** was conjugated to dextran with 6.3 N_3-groups per dextran **47**, for reasons of cytotoxicity and performance as mentioned previously. The IR spectra of the products biotin-dextran-L17E(3.7) **50**, biotin-dextran-ATSP-7041(3.7) **51**, biotin-dextran-apCC-Di-B(3.7) **52** and biotin-dextran-L17E/Q21E(6.3) **53** are shown in Figure 48, whereby here again, the bracketed numbers are an approximation of the number of peptides conjugated per dextran molecule, based on the number of carboxyethyl groups that were initially present.

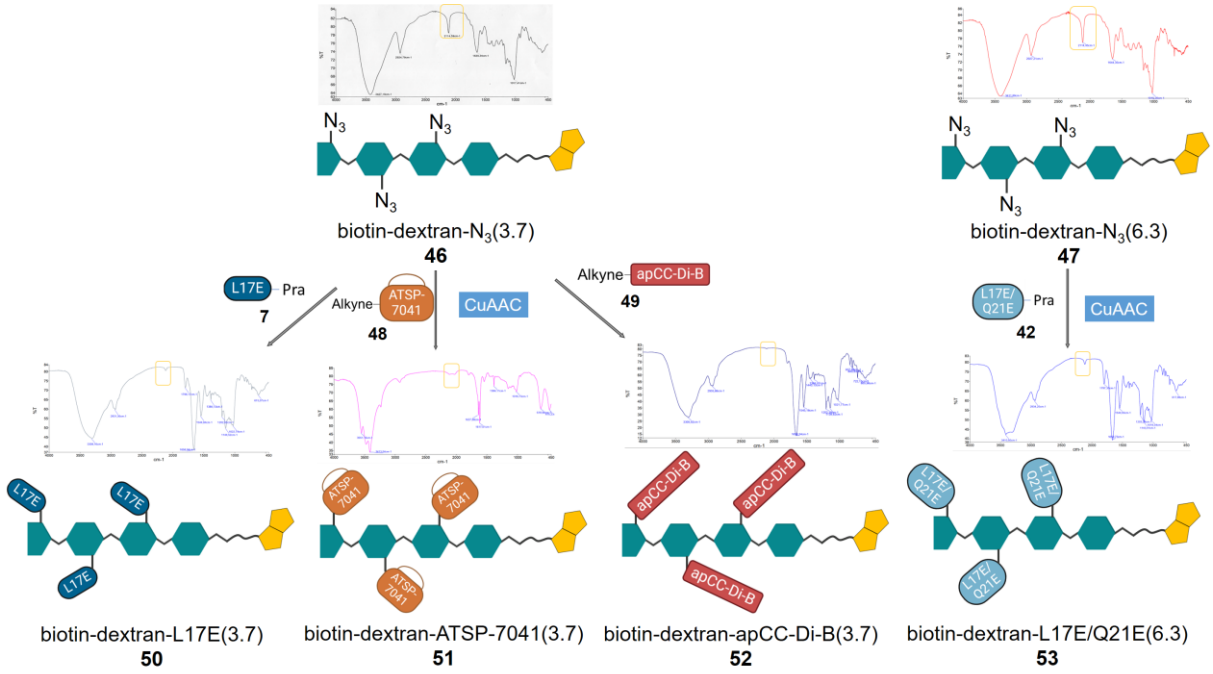

Figure 48| Schematic illustration of the click reactions of biotin-dextran with 3.7 or 6.3 N_3-groups per molecule (**46** and **47** respectively) to yield the products biotin-dextran-L17E(3.7) **50**, biotin-dextran-ATSP-7041(3.7) **51**, biotin-dextran-apCC-Di-B(3.7) **52** and biotin-dextran-L17E/Q21E(6.3) **53**. N_3-band is boxed in yellow.

The fluorogenic protein eGFP was chosen as cargo to be delivered, which would allow internalization to be evaluated by confocal microscopy imaging. Biotinylation of the protein was achieved through an *N*-terminal genetically added AviTag (GLNDIFEAQKIEWHE), which is a substrate of the *E. coli* enzyme biotin ligase (BirA).[207] Upon its production in *E. coli*, the lysine residue of the tag becomes biotinylated using the cell's natural machinery (Figure 49A).[207] Occurring site specifically, each protein is precisely labelled with one biotin molecule. The production of eGFP-biotin **54** was verified in a western blot (Figure 49B). Various streptavidin

delivery modules can then be generated by incubation of the dextran-CPP conjugates **50-53** and the payload **54** with streptavidin through stoichiometric control.

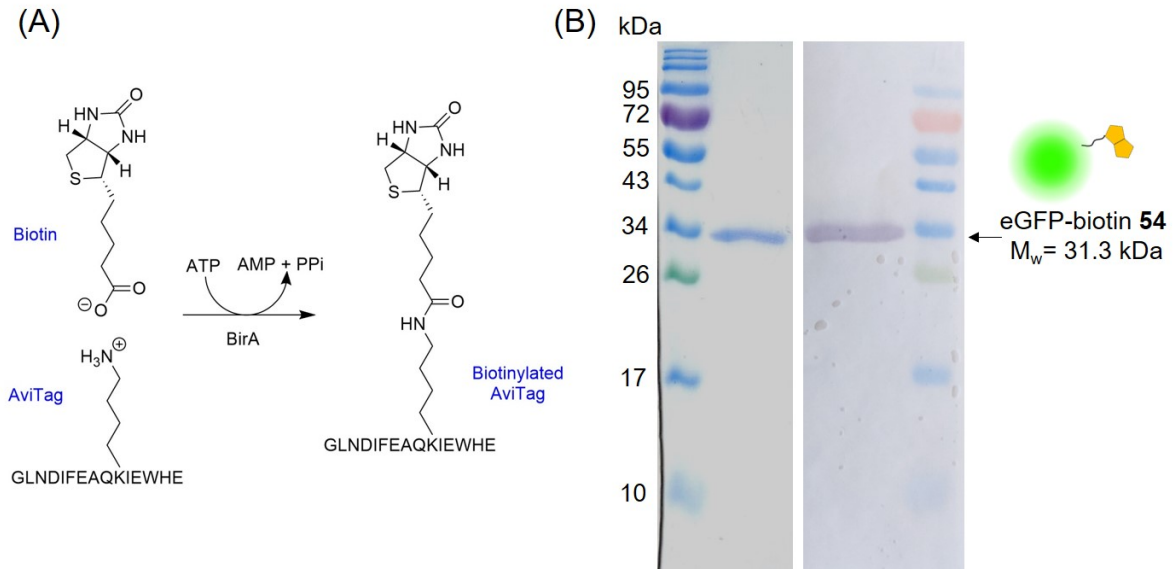

Figure 49| (A) Schematic illustration of the biotinylation of the AviTag by BirA under ATP hydrolysis.[207] (B) Reducing SDS Gel (left) and western blot (right) of eGFP-biotin **54**.

In addition, cellular uptake of the streptavidin-dextran-CPP architectures was to be evaluated in functional assays to verify cytoplasmic delivery. Herein, the split-GFP complementation, p53 accumulation (by mouse double minute 2/4 (MDM2/MDMX) inhibition) and NanoBiT® (Promega) assays were to be applied (Figure 50). The split-GFP complementation assay relies on the non-covalent reassembly of the GFP1-10 subunit and the fragment peptide GFP11 into a functional, fluorescent GFP. For the verification of cytosolic delivery, a GFP11-tagged intracellular delivery module can be exogenously incubated on cells that stably express GFP1-10 in the cytosol. Successful cytosolic localization of the GFP11-tagged delivery module should lead to reconstitution of the GFP fragments and result in detectable GFP fluorescence. The assay has been successfully applied for GFP11 fused directly to CPPs,[208] as well as dextran conjugates with covalently attached L17E and GFP11 peptides on the glucose repeating units.[140] For application to the streptavidin-dextran architectures, a biotin-dextran-GFP11 conjugate would need to be synthesized that could incubated with the biotin-dextran-CPP conjugates **50-53** to facilitate its intracellular delivery. Therefore, an alkyne-GFP11 **55** was synthesized and attached to dextran with 6.3 N_3-groups per dextran **47** via CuAAC, yielding biotin-dextran-GFP11(6.3) **56**. Dextran with higher number of N_3-groups (6.3) was chosen to increase the likelihood of GFP11 recombination to GFP1-10 upon its successful cytosolic localization. Figure 50A summarizes the split-GFP assay.

The second assay for cytoplasmic delivery verification was to be evaluated by measuring p53 accumulation in cells induced by the inhibition of the cytosolic proteins MDM2 and MDMX. The p53 protein is encoded by the tumor suppressor gene TP53, which is known as the “guardian of the genome”, as it prohibits the transfer of damaged DNA to daughter cells to maintain genomic integrity. The p53 protein responds to DNA damage and halts the cell cycle to enable the cell to repair the damage, or induces apoptosis when the damage is irreparable through the regulation of downstream target proteins. To halt p53 function, intracellular p53 levels are negatively regulated by MDM2 and MDMX. MDM2 inhibits the p53 protein by directly binding to it, which prevents p53 from binding to its target DNA. Additionally, MDM2 promotes p53 export from the nucleus, rendering p53 to an ineffective transcription factor, or uses its E3 ligase activity to ubiquitinate p53, leading to its proteasomal degradation. The MDM2 homologue MDMX coordinates its p53 inhibitory activity with MDM2, also by directly binding to p53 and promoting its degradation through the ubiquitination pathway.[209] Amplified expression of MDM genes is a common feature of may tumors, wherefore numerous inhibitors have been developed and tested in clinical trials.[210] The MDM2 and MDMX inhibitor to be used in the assay is the non-cell permeable KD3 peptide, which demonstrated p53 reactivation upon conjugation to cyclic R10 and TAT CPPs and incubation on cells at 1-12 μM concentration after 3-6 hours.[62] In the inhibition assay, an A549 reporter cell line modified to express a fusion of p53 and the yellow fluorescent protein mVenus was used to monitor p53 accumulation. The A549 cell line overexpresses MDM2 and MDMX that keeps p53 levels low, while inhibition of the MDM proteins leads an increase in p53-mVenus levels. This method has been used in the Löwer working group on multiple occasions for the detection of p53 levels.[62,63,211] It should be mentioned that p53 levels drop over time due to the accumulation of p53 that promotes the expression of MDM genes in a negative feedback loop. Therefore, the cells were to be observed regularly over at least 12 h. For cytosolic verification of the streptavidin delivery architecture, an alkyne functionalized KD3 peptide **57** was synthesized and a biotin-dextran-KD3 conjugate **58** was generated. Again, dextran with more i.e. 6.3 N_3-groups per dextran **47** was chosen to elicit a greater inhibitory effect. Figure 50B summarizes the assay.

The third assay for verification of cytoplasmic delivery is a NanoBiT® luciferase assay (Promega) that is based on the complementation of a HiBiT peptide with high affinity (K_D = 700 pM) to a large subunit LgBiT, forming a functional NanoBiT® enzyme.[212] This NanoBiT® technology is a reporter system based on the NanoLuc® luciferase, an engineered enzyme with enhanced stability and activity,[213] which oxidizes a furimazine substrate under the release of light. The bioluminescent assay has been used in literature for studying protein-protein

interactions without the need for cell lysis and, important for this work, to quantify the cytosolic delivery.[104] Thereby, the cytosolically expressed LgBiT subunit should spontaneously reconstitute to the HiBiT-tagged CPP-delivery module upon its successful internalization, forming a functional luciferase that with a cell permeable furimazine-derived substrate gives a detectable luminescent signal. Similar to the previous two described assays, a HiBiT peptide with alkyne functionality **59** was synthesized to generate a biotin-dextran-HiBiT conjugate **60** for verification of cytosolic delivery of the streptavidin delivery architecture. Figure 50C summarizes the assay.

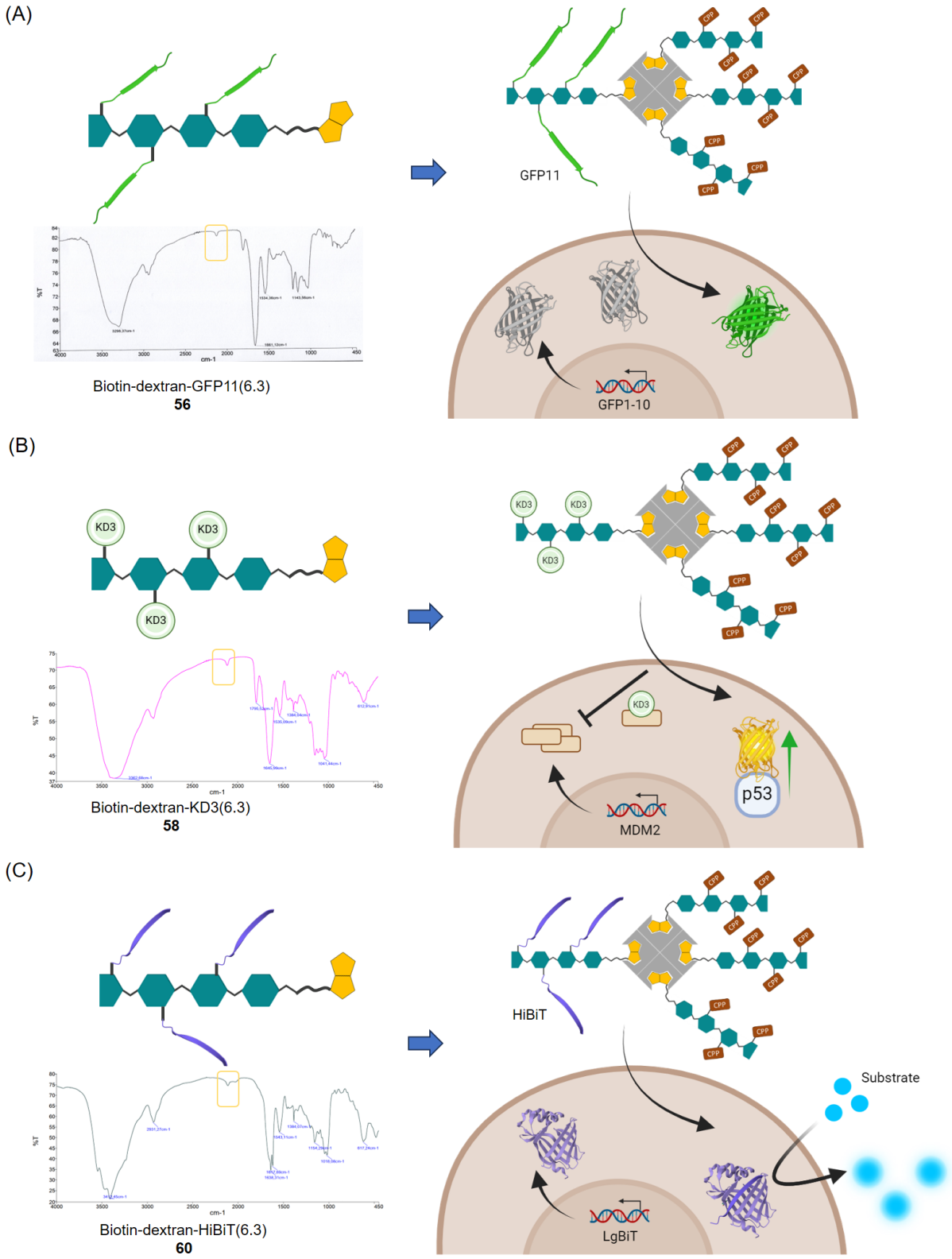

Figure 50| (A) Schematic representation of biotin-dextran-GFP11 **56** with IR spectrum and illustration of the split-GFP complementation assay. (B) Schematic representation of biotin-dextran-KD3 **58** with IR spectrum and illustration of the p53 accumulation assay. (C) Schematic representation of biotin-dextran-HiBiT **60** with IR spectrum and illustration of the NanoBiT® assay (NanoLuc® luciferase pdb: 5IBO). Images created with Biorender.com.

4.4.2 Cellular uptake assay of streptavidin-dextran-CPP architectures with eGFP as payload

The streptavidin (Sav) delivery modules for confocal imaging were generated by mixing streptavidin with dextran-CPP conjugate and biotinylated eGFP in the desired stoichiometric ratios with respect to streptavidin. With eGFP-biotin occupying one binding site on streptavidin, up to three dextran-CPP conjugates can be attached additionally. In case of cytotoxic behavior of the CPP, streptavidin conjugates with only two dextran-CPP conjugates were also investigated, whereby one equivalent free biotin was added additionally in the mixture to occupy the fourth site. The mixtures were incubated overnight and used directly the next day. The streptavidin delivery modules generated were: Sav(3xDex-L17E **50**, 1x eGFP **54**) **61**, Sav(2xDex-L17E **50**,1xbiotin, 1x eGFP **54**) **62**, Sav(3xDex-L17E/Q21E **53**, 1x eGFP **54**) **63**, Sav(2xDex-L17E/Q21E **53**,1xbiotin, 1x eGFP **54**) **64**, Sav(3xDex-ATSP-7041 **51**, 1x eGFP **54**) **65**, Sav(2xDex-ATSP-7041 **51**,1xbiotin, 1x eGFP **54**) **66**, Sav(3xDex-apccDi-B **52**, 1x eGFP **54**) **67** or Sav(2xDex-apccDi-B **52**,1xbiotin, 1x eGFP **54**) **68**. 2 μM (corresponding to streptavidin) was incubated on HeLa cells for 2 h and subsequently for 3 h in medium only in the cellular uptake assay. Figure 51A shows an illustration of the streptavidin delivery modules according to their stoichiometric employment and confocal microscopy images from two independent experiments. In experiment 1, intracellular fluorescence could be seen for the streptavidin delivery architectures **61-63** comprising of the L17E and L17E/Q21E peptides. Some accumulation around the cell periphery and punctuate signals can be observed, which are however, less prominent in experiment 2. It seems internalization of the delivery modules in the two experiments occurred through multiple mechanisms, which may concern the viability state of the cells in the two experiments. For instance, three dextran-L17E chains on streptavidin **63** largely compromised cell viability in experiment 2 as indicated by the unusual morphology of the cells, probably with significant disturbance of membrane integrity, and the observation of cell debris surrounding them. Two dextran-L17E chains on streptavidin **62** did not display cell debris and intact cell membranes. This was also observed for the streptavidin delivery architectures **63** and **64** with three and two dextran-L17E/Q21E chains. It should be noted that the number of L17E/Q21E peptides per dextran molecule was 1.7 times greater than the L17E peptide, but **62** with a calculated L17E peptide concentration of 14.8 μM still demonstrated similar intracellular fluorescence intensities compared to **63** with 37.8 μM L17E/Q21E peptide. This suggests the L17E peptide is the more efficient CPP, which also reflects the results obtained by Futaki and coworkers, where dimerization of the L17E/Q21E peptide was necessary to achieve at least a comparable intracellular delivery efficiency to the monomeric L17E

peptide.[95] **64** with two dextran-L17E/Q21E chains, which corresponds to 25.2 μM L17E/Q21E peptide, did not show signs of internalization in experiment 1, but did in experiment 2. This may be the lowest detectable concentration of the peptide for internalization. Again, cellular uptake seems to be dependent on the state of the cells. The streptavidin delivery architectures **65** and **66** with the ATSP-7041 peptide (peptide concentrations 14.8 μM and 22.2 μM) did not internalize into the cells. It is likely that more copies of the peptide per dextran are required for successful internalization considering that Chang *et al.* performed cellular uptake assays of the solitary peptide with fluorescent label at 20 μM concentration and 4.5 h incubation.[97] The streptavidin architectures with apCC-Di-B peptide **67** and **68** displayed a fine fluorescence outline on the cell membrane and punctuate signals in the cytosol in experiment 1 (including bright fluorescent spots of either cell debris or precipitated conjugate or both), while in experiment 2, a strong fluorescence outlining the cell membrane that partly extends to the interior of the cell was observed. While the first experiment suggested endosomal entrapment of the streptavidin delivery module, the second signified strong adsorption to the cell membrane, perhaps entrapped in the cell membrane, with some cytosolic delivery. These contradictory results necessitates further investigation through functional assays (attempted in the next sections). Streptavidin delivery modules without CPPs: Sav(3x-Dex-N_3(6.3) **47**, 1xeGFP **54**) **69** or Sav(2x-Dex-N_3(6.3) **47**, 1xbiotin, 1xeGFP **54**) **70** were used as control in the experiments. They did not exhibit intracellular fluorescence, indicating that the CPPs were necessary for cellular uptake (Figure S 11).

The overnight streptavidin-dextran mixtures **61-68** were subjected to size exclusion chromatography to verify the formation of the streptavidin delivery module. Due to an increase in size of the overall construct, a shift to lower retention times was expected. The size exclusion chromatograms are shown in Figure 51B. It can be seen that streptavidin and eGFP-biotin **54** with their molecular weights of 55 kDa and 33 kDa respectively show similar retention times. In contrast, the streptavidin delivery modules exhibit molecular weights of 131-178 kDa depending on the size of the CPP, the number of CPPs per dextran molecule, and the number of dextran chains per streptavidin. By examination of the size exclusion chromatograms of **61-66**, shifts to lower retention times can be seen, however it does not shift completely, showing that the samples used in the cellular uptake assay were not fully assembled on the streptavidin centerpiece. This is most likely attributed to the dextran framework, especially the reducing end of dextran, which was not fully functionalized with cadaverine and each cadaverine moiety may not have been fully biotinylated. Interestingly, a shift to lower retention times was not observed for streptavidin incubated with biotin-dextran-apCC-Di-B conjugate **67-68**. If not an artefact, it

suggests conjugation to the streptavidin centerpiece did not occur. Of the four CPPs, the apCC-Di-B peptide is the longest peptide with 30 amino acids and a 4-pentynoic acid chain for conjugation to the dextran, whilst the second longest are the L17E and L17E/Q21E peptides with 25 amino acids and a propargylglycine. The ATSP-7041 peptide is a stapled cyclic peptide, with a more compact structure. There is a possibility that the apCC-Di-B peptide may have masked the biotin so that the dextran conjugate **52** could not access streptavidin binding sites. Nevertheless, knowing that CPPs do not need to be directly conjugated to their payload to mediate cellular uptake, although it is beneficial,[140] the confocal images in Figure 51A remain a representation of their delivery efficiency.

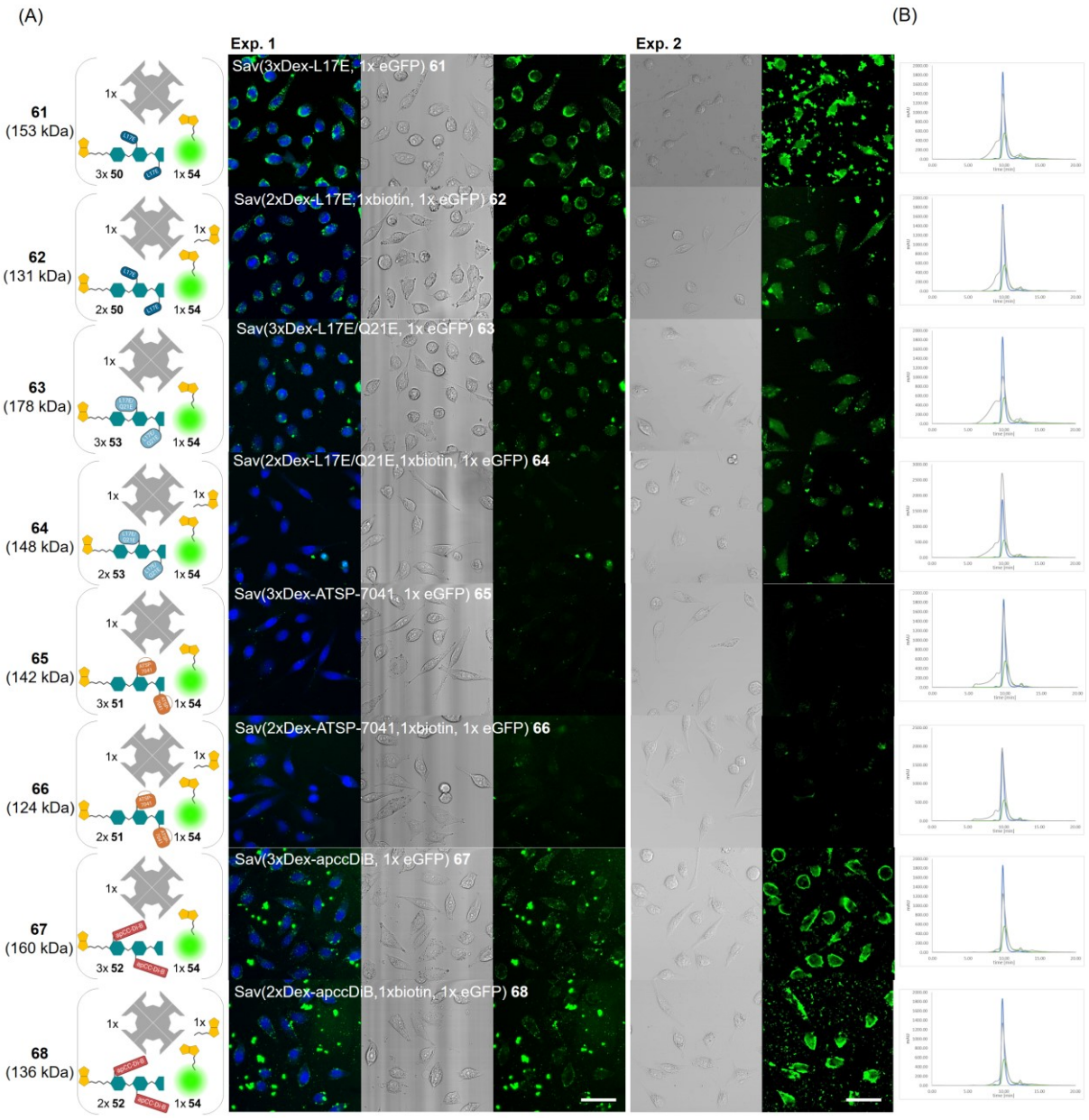

Figure 51| (A) Streptavidin delivery modules **61-68** with eGFP as payload and average molecular weight. CLSM images of HeLa cells treated with 2 µM **61-68** for 2 h and subsequent 3 h incubation. For experiment 1:

Left: overlay brightfield and fluorescence channel, center: brightfield channel, right: fluorescence channel. For experiment 2: left: brightfield channel, right: fluorescence channel. The scale bar denotes 50 µm. Images of the same experiment were taken under the same microscopy tuning parameters and processed with ImageJ. (B) SEC analysis of streptavidin delivery modules **61-68**, 220 nm. Gray curve: streptavidin delivery module, green curve: eGFP: blue curve: streptavidin.

The same cellular uptake assay using the streptavidin delivery architectures was repeated at 4 °C to observe if internalization occurred under conditions with limited energy. Additionally, cellular uptake was investigated using a second cell line, SKBR3 cells.

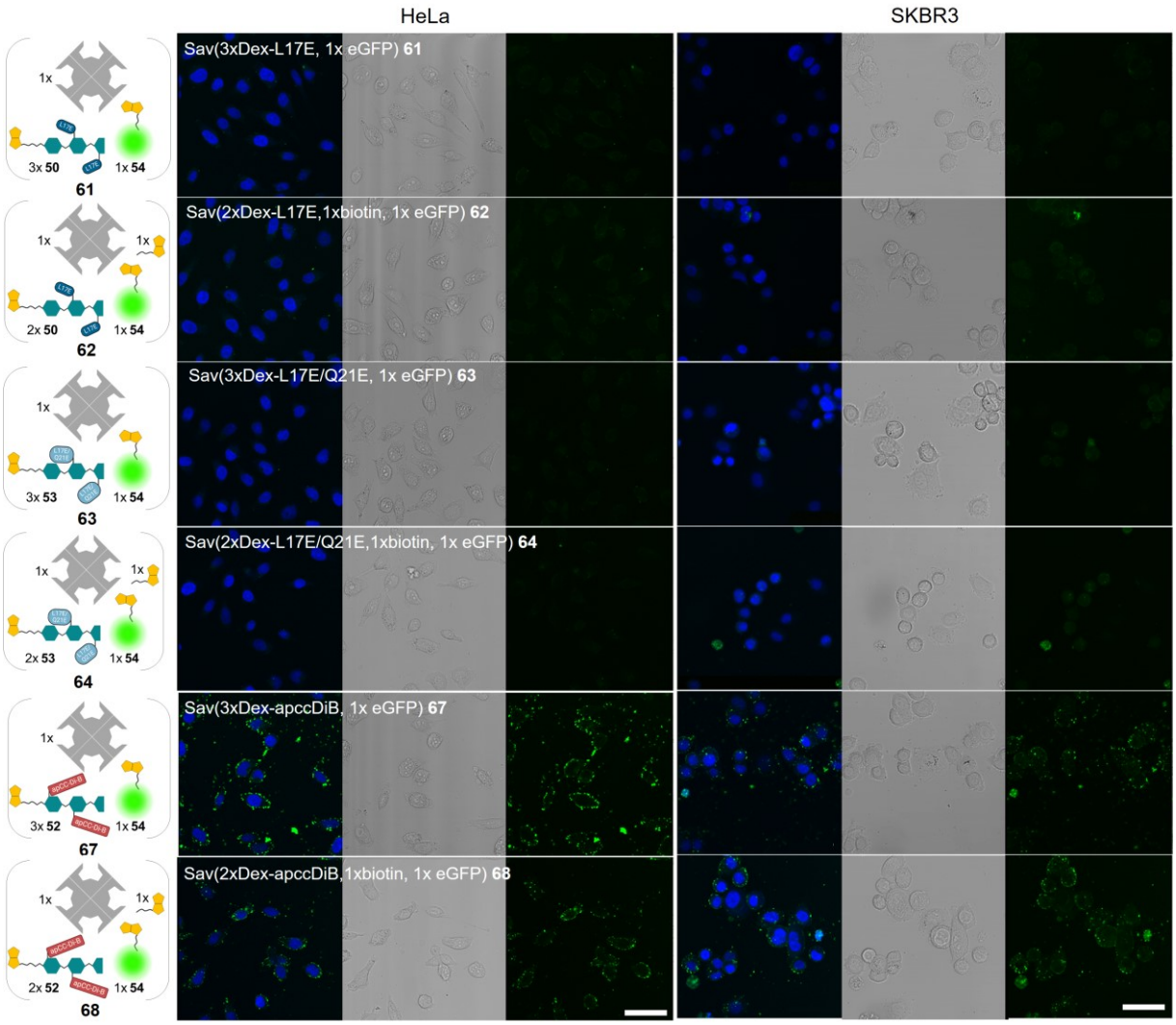

Figure 52| CLSM images of HeLa and SKBR3 cells treated with 2 µM **61-64, 67 and 68** for 2 h and subsequent 3 h incubation. Left: overlay brightfield and fluorescence channel, center: brightfield channel, right: fluorescence channel. The scale bar denotes 50 µm. Images were taken under the same microscopy tuning parameters and processed with ImageJ.

Under energy-depleted conditions, intracellular delivery of the streptavidin architectures **61-64**, **67** and **68** did not occur in both cell lines (Figure 52). Contrary to the assay at 37 °C, **61-64** with the L17E and L17E/Q21E peptides did not show any intracellular fluorescence, which means cellular uptake did not occur. The streptavidin delivery modules **67** and **68** with the

apCC-Di-B peptide showed punctuate fluorescent signals only on the cell membrane, which was more prominent on the HeLa cell line than on the SKBR3 cells line. This can be attributed to different phospholipid compositions between the two cell lines. For these large delivery modules, it was expected that they would internalize through energy-dependent mechanisms.

In summary, streptavidin decorated with dextran-L17E or dextran-L17E/Q21E conjugates **61-64** can be considered promising intracellular delivery modules, especially considering their large size. However, the L17E/Q21E peptide is less effective than the L17E peptide, and requires at least two dextran conjugates with 6.3 peptides on average for successful intracellular delivery, while two dextran-L17E conjugates with 3.7 L17E peptides per dextran are sufficient. Using the ATSP-7041 peptide for cargo delivery in form of a streptavidin delivery module **65** and **66** needs further optimization, likely by increasing the number of peptides per dextran conjugate. The effectiveness of streptavidin decorated with dextran-apCC-Di-B **67** and **68** in cytosolic delivery remains to be determined, as it is not clearly evident in the confocal images. Therefore, especially for this sample, the cytosolic verification assays are necessary.

The heterogeneity of these streptavidin architectures currently limits the applicability of these constructs as reliable delivery modules. Size exclusion chromatography of the streptavidin delivery modules revealed that thorough optimization in the synthesis of the dextran-CPP conjugates with highly efficient biotin-labelling are required for the efficient generation of streptavidin delivery modules. This also applies for biotinylation of the payload that should ideally occur site-specifically, as performed here using the AviTag for example, to yield a homogenous product. Furthermore, there is close interplay between cytotoxicity and cellular uptake, wherefore the cytotoxicities of these streptavidin architectures were investigated next.

4.4.3 Cellular proliferation assay of streptavidin delivery modules 61-68

In a cellular proliferation assay, the cytotoxicities of the streptavidin delivery modules were evaluated. HeLa cells were incubated for 72 h with a dilution series of **61-68** at 37 °C in a humidified incubator. The number of viable cells was determined using the CellTiter96®Aqueous One solution cell proliferation assay. The results for the streptavidin delivery modules with three dextran-CPP chains **61**,**63**, **65** and **67** are displayed in Figure 53.

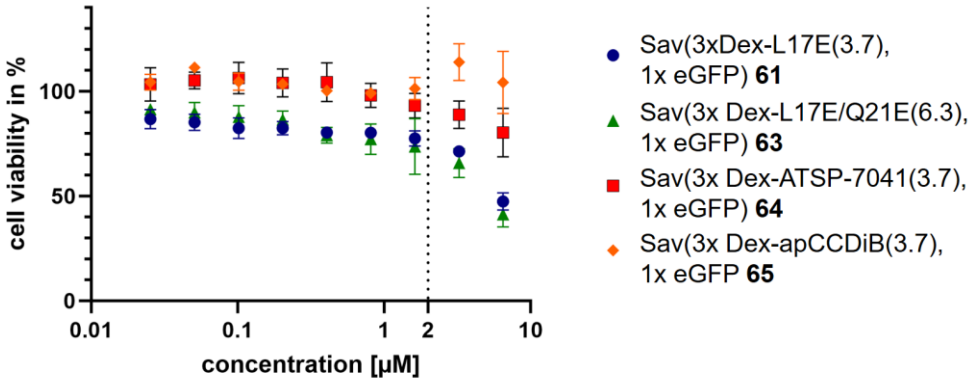

Figure 53| Cellular proliferation assay of streptavidin delivery modules with three dextran-CPP chains **61**,**63**, **65** and **67**. The error bars denote the standard deviation from triplicate measurements. The 2 µM concentration used in the cellular uptake assay is indicated by a dotted line.

The streptavidin delivery modules decorated with three dextran-L17E **61** or dextran-L17E/Q21E **63** chains that clearly demonstrated cellular uptake at 37 °C incubation (Figure 51) showed lower cell viability compared to the streptavidin delivery modules decorated with dextran-ATSP-7041 **63** and dextran-apCC-Di-B **65** with no or minimal cellular uptake. This was also observed for streptavidin delivery modules with two dextran-CPP chains (Figure S 12). This implies that for successful cellular uptake of the streptavidin delivery module a certain degree of cytotoxicity is to be expected. Considering that the cell membrane integrity is temporarily disrupted through internalization of these architectures, it is not surprising that cytotoxicity is seen, especially for large delivery modules that cause larger disturbances in the cell membrane. Cell membrane injury is accompanied by several sealing mechanisms to repair the damage, but the cells need to restore their intracellular homeostasis as well and if the damage is too great, cell cycle arrest or cell death are triggered.[214] For this reason, cellular uptake needs to be simultaneously evaluated with cell viability. Particularly for applications in cell-based therapies, where the cells should retain their full functional capacity for a successful treatment outcome, it is essential to find a balance between efficacy and cytotoxicity.

4.4.4 Split-GFP complementation assay

The next sections attempt to validate the cytosolic delivery of the streptavidin architectures, to support the results drawn from confocal imaging and especially evaluate the apCC-Di-B peptide in cell penetration which previously did not show clear cellular uptake. The split GFP-complementation assay as described previously is based on the recombination of cytosolically expressed GFP1-10 to a cytosolically internalized GFP11 peptide on a streptavidin delivery module. Each streptavidin molecule was decorated with two dextran-GFP11(6.3) chains **56** and two dextran-CPP chains **50-53** that should mediate cellular uptake, resulting in the streptavidin

delivery modules Sav(2xDex-L17E, 2xDex-GFP11) **71**, Sav(2xDex-L17E/Q21E, 2xDex-GFP11) **72**, Sav(2xDex-ATSP-7041, 2xDex-GFP11) **73** and Sav(2xDex-apCC-Di-B, 2xDex-GFP11) **74**. As control, Sav(2xDex-N_3, 2xDex-GFP11) **75** was used. The HeLa GFP1-10 cells were incubated for 20 h with 1 μM of the constructs and subsequently trypsinized for fluorescence measurement by flow cytometry. An illustration of the streptavidin delivery architectures **71-75** according to their stoichiometric employment and results of the split-GFP complementation assay are shown in Figure 54.

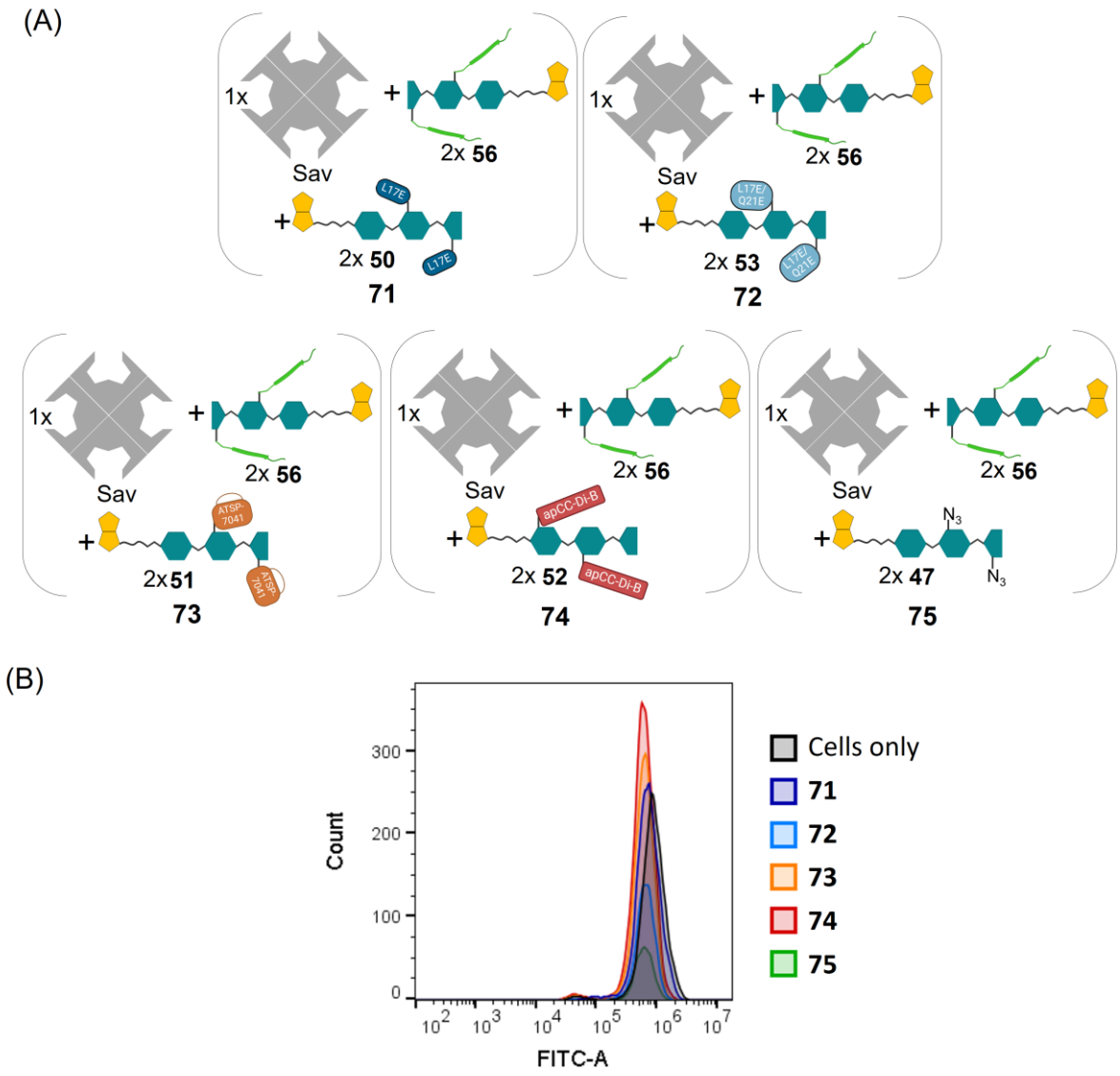

Figure 54| (A) Illustration of streptavidin delivery architectures **71-75** for the split-GFP assay with GFP11 peptide. (B) Flow cytometry analysis of the split-GFP assay. 1 µM **71-75** was incubated on HeLa GFP1-10 cells for 20 h at 37 °C. FACS plot of the count against fluorescence intensity (FITC-channel).

Contrary to expectations, an increase in fluorescence was not observed for all samples. Either two dextran-CPP chains were not sufficient to promote internalization, or the assay was not sensitive enough. A split-GFP complementation assay performed previously in our working

group used a dextran-L17E-GFP11 conjugate with an effective concentration of 40 μM for the GFP11 peptide.[140] The split-GFP11 assay attempted here used a lower effective GFP11 concentration of 12.6 μM. Cytotoxicity and requirement of at least two dextran-CPP chains for internalization limited the use of higher concentrations of the delivery architectures. Therefore, verification of cytosolic delivery by split-GFP complementation was terminated and the p53 accumulation assay was attempted next.

4.4.5 P53 accumulation assay

As previously mentioned, the p53 accumulation assay is based on the delivery of the KD3 peptide that is an inhibitor of the p53 negative regulators MDM2 and MDMX. The streptavidin delivery architectures were assembled using two equivalents dextran-CPP conjugate **50-53** and two equivalents biotin-dextran-KD3 **58**, generating Sav(2xDex-L17E, 2xDex-KD3) **76**, Sav(2xDex-L17E/Q21E, 2xDex- KD3) **77**, Sav(2xDex-ATSP-7041, 2xDex- KD3) **78** and Sav(2xDex-apCC-Di-B, 2xDex- KD3) **79**. Sav(2xDex-N_3, 2xDex-KD3) **80** served as negative control and Nutlin-3a, a cell-permeable small molecule inhibitor of MDM2 provided by the Löwer working group, as positive control. 1 μM **76-80** were incubated on the HeLa p53-mVenus cell line, whereby p53 levels were monitored by live-cell confocal imaging through mVenus fluorescence. For a set of samples, the cells were additionally treated with 1 μM saponin (provided by Jan Dürig, FU Berlin, Figure S 13), a plant derived glycoside that is known to permeabilize cell membranes through interaction with cholesterol in the cell membrane. It forms pores in the cell membrane, varying from a few nanometers to micrometers in diameter depending on literature.[215] With streptavidin alone demonstrating a hydrodynamic radius of about 4-7 nm,[216] saponin could serve as an additive to facilitate the internalization of the streptavidin-dextran delivery architectures. An illustration of the streptavidin delivery architectures **76-80** according to their stoichiometric employment and results of the p53 accumulation assay are shown in Figure 55.

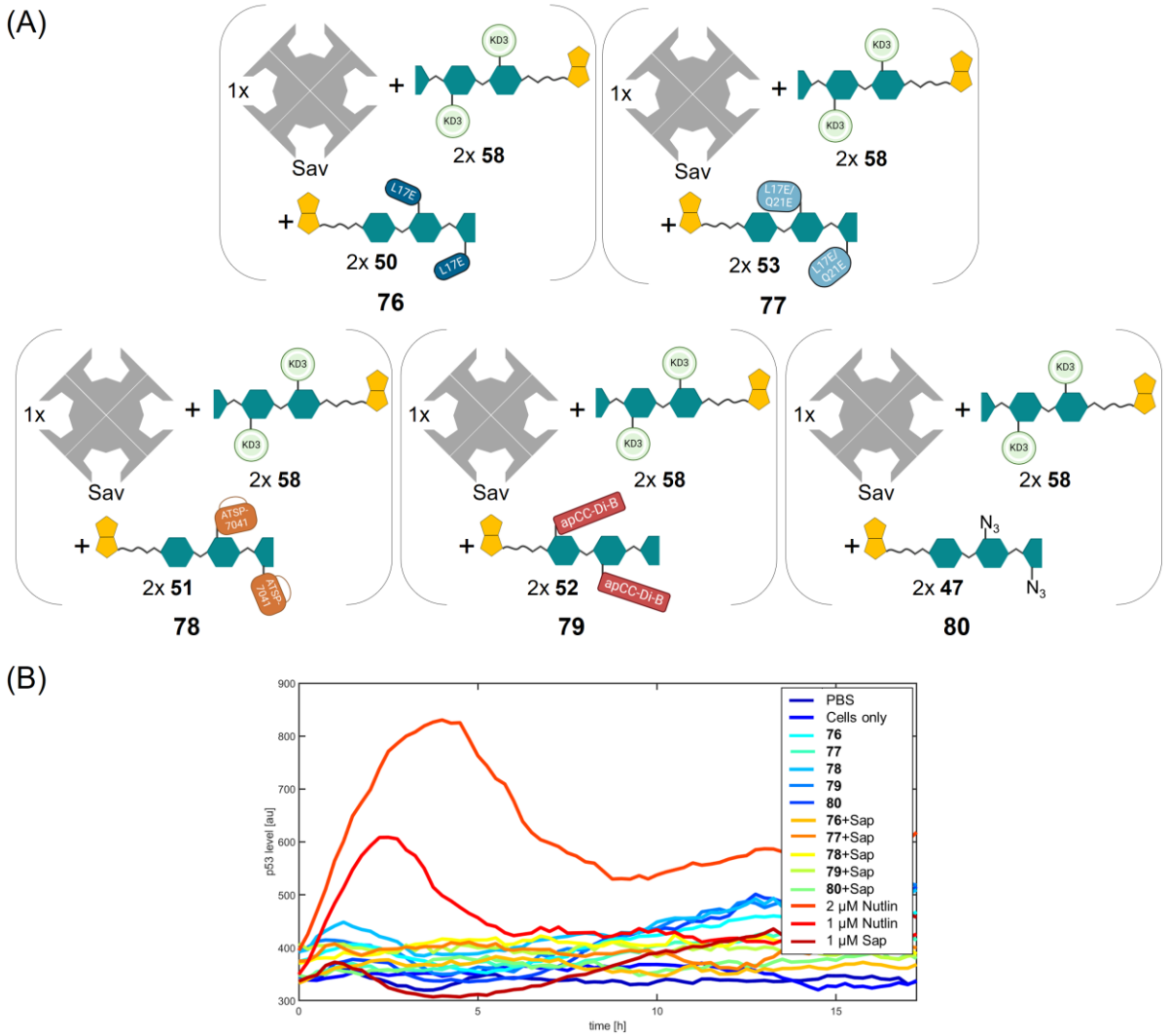

Figure 55| (A) Illustration of streptavidin delivery architectures **76-80** for the p53 accumulation assay with KD3 peptide. (B) Graphic showing the p53 accumulation assay in a plot of p53 level in arbitrary units against the time in hours. HeLa P53-mVenus cells were incubated with 1 µM **76-80** with or without saponin (Sap) and p53-mVenus fluorescence was monitored over 16 h. The data was analyzed using a custom-written MatLab script of the Löwer working group.

Contrary to the Nutlin-3a positive control, an increase in p53 levels could not be observed for all samples **76-79** over a time course of 16 h compared to the negative control **80** without a CPP. Additional treatment with saponin did not show a p53 level increase. On the one hand, it is possible that only two dextran-CPP chains are not sufficient for cytosolic uptake. On the other hand, using mVenus as a reporter may not have been suitable, as the streptavidin delivery architectures exhibited a yellow color due to the dextran-KD3 conjugate **58**. This may have caused high background fluorescence, interfering with mVenus, which is a yellow fluorescent protein. Therefore, a reporter cell line that expresses p53 fused to a fluorescent protein of other spectral properties may be more suitable. Furthermore, evaluation of the cytotoxicity of the streptavidin delivery architectures with the KD3 peptide is necessary, for p53 expression can be

generally induced through any stresses observed by the cell. This limits the concentration of the streptavidin delivery architectures that can be used, while low concentrations compromise cellular uptake.

4.4.6 NanoBiT® assay

The NanoBiT® assay is a well-established method for studying PPIs and cellular processes, known for its high sensitivity and ease of use. In an investigation comparing the split luciferase to the split GFP assay, the split luciferase assay was shown to be 10^4 times more sensitive than the split GFP assay.[104]

Complementation of LgBiT to HiBiT in the cytosol forms a functional luciferase that converts a furimazine substrate under the emission of light. Herein, HeLa cells that stably expressed LgBiT, generated by Carolin Dombrowsky, were used to verify cytosolic delivery of streptavidin-dextran architectures using the dextran-HiBiT conjugate **60**. The streptavidin delivery modules Sav(2xDex-L17E, 2xDex-HiBiT) **81**, Sav(2xDex-L17E/Q21E, 2xDex- HiBiT) **82**, Sav(2xDex-ATSP-7041, 2xDex- HiBiT) **83** and Sav(2xDex-apCC-Di-B, 2xDex- HiBiT) **84** were added at 2 μM concentrations on the cells. After 18 h incubation, the Endurazine™ substrate was added and luminescence was measured 1-2 h later. Sav(2xDex-N_3, 2xDex- HiBiT) **85** (without CPP) served as negative control. An illustration of the streptavidin delivery architectures **81-85** according to their stoichiometric employment and results of the NanoBiT® assay are displayed in Figure 56.

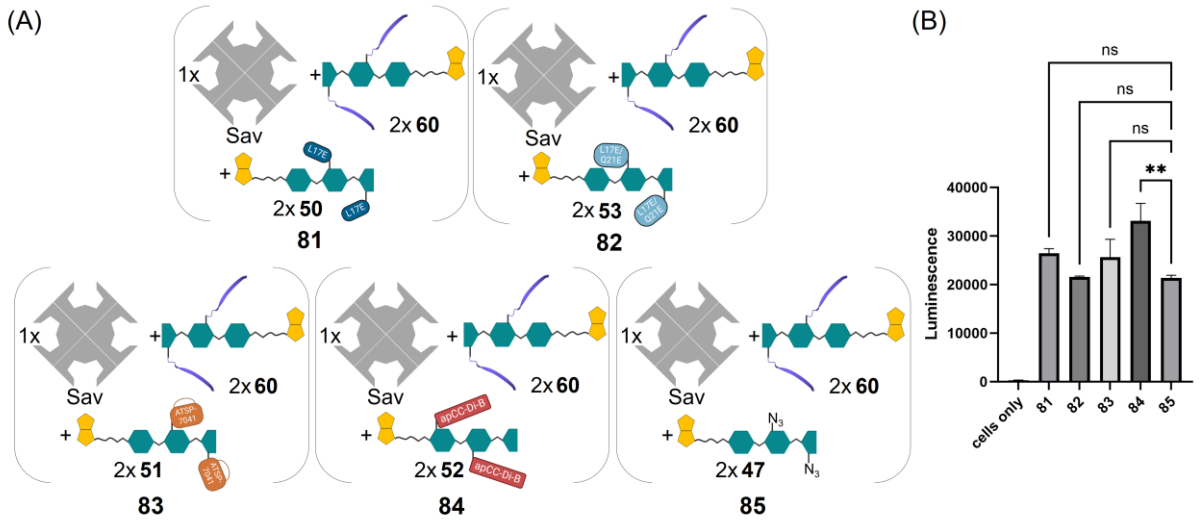

Figure 56| (A) Illustration of streptavidin delivery architectures **81-85** for the NanoBiT® assay with HiBiT peptide. (B) Bar chart plot of luminescence signal of **81-85** in the NanoBiT® assay. 2 µM **81-85** were incubated for 18 h on HeLa LgBiT cells. Endurazine™ substrate was added and luminescence was measured 1-2 h later. Data represents mean ± SEM. One-way ANOVA followed by Tukey's test was used to analyze the data (0.1234 (ns), *p<0.0332, **p<0.0021, ***p<0.0002, ****p<0.0001). The data was plotted and analyzed using GraphPad Prism.

At first glance, it can be seen in Figure 56B that the negative control **85** without CPP had produced a high luminescence signal, deeming the luminescence signals of three of four streptavidin delivery architectures not significant by statistical analysis. The question arose, whether the HiBiT peptide itself has cell permeabilizing properties. Containing eight hydrophobic (V, W, L, F, I) and basic (R, K, K) amino acids out of eleven amino acids total, it exhibits the characteristics of many membrane permeable peptides. For this reason, Okano et al. added a hydrophilic RD-motif to the peptide and fluorescent label, which showed endosomal localization upon confocal analysis,[217] but it is unknown whether it is cell permeable without this motif or more importantly for this project, whether it enters the cytosol as a dextran conjugate or streptavidin delivery module. For verification, a streptavidin module with four dextran conjugates without peptide **47** would need to be included in this assay. Alternatively, confocal imaging could be performed using eGFP as payload as described in section 4.4.2. Synthesis of a dextran-HiBiT conjugate with a fluorogenic cargo on the reducing end would be another possibility. Cytotoxicity could also have caused the high luminescence signal of **85**. If the cell membrane were compromised to such an extent that LgBiT in the cytosol escaped to the surrounding medium, it would complement with the HiBiT peptide in the extracellular fluid and result in false luminescent results. Therefore, cytosolic delivery assays using streptavidin delivery architectures needs to be assessed along with their toxicity profile, and the concentration for the assay adjusted accordingly.

5 Summary and Outlook

The multitude of intracellular protein-protein interaction sites presents a promising opportunity for therapeutic intervention, yet the intracellular delivery of therapeutic compounds is hampered by their inability to cross the cellular membrane and access the cytosol. One of the strategies for enhancing the delivery of cargos into the cytosol is by use of CPPs. While they have demonstrated the cellular delivery of therapeutic drugs, imaging agents, RNA, enzymes and antibodies, their use is limited due to the lack of cell type specificity. Therefore, the first part of this work dealt with the generation of an enzyme-activatable CPP with minimal side chain modification using the L17E peptide as model CPP, an attenuated lytic peptide derived from the venom *M. lycotoxin*. The L17E peptide is a cationic CPP that facilitates cargo delivery by destabilizing the cell membrane through interaction with negatively charged lipids on the cell surface. Assuming that the cell penetrating properties of the L17E peptide is associated to its positive charge derived from the five residing lysine residues, the lysine side chains were masked with protecting groups to conceal the positive charge, with the notion that only upon removal of these protecting groups would cell penetration be reactivated. Considering that the protecting groups would eventually need to be removed, the number of protecting groups introduced on the L17E peptide was first kept to a minimum, beginning with the masking of two of the five lysine residues simultaneously with the hydrophobic and uncharged alloc protecting group. Thereby, four peptide variants with the alloc protecting group on different lysine positions of the L17E peptide were tested for impairment of cellular uptake. Using TAMRA as delivery cargo, the alloc-L17E peptides however displayed high intracellular fluorescence intensities inside HeLa cells, similar to the original L17E peptide without masking groups. Since the masking of only two of the five lysine residues of the L17E peptide did not impair the intracellular delivery of the fluorophore TAMRA, all five lysine residues were masked next. Due to solubility issues of the alloc-peptides at higher concentrations and to allow for a biocompatible demasking method, the protecting group was exchanged for the enzymatically-removable acetyl group. Indeed, this time round with TAMRA as delivery cargo, the five-time acetylated L17E peptide impaired cellular uptake. Furthermore, the cell penetrating activity of the peptide could be reactivated by deacetylation of the masking groups by the SirT2 enzyme in a biological assay. With reactivation of the acetylated L17E peptide achieved, antibody-enzyme conjugates were generated for cell-targeted delivery by an ADEPT-like method, adapted for a proof of concept in *in vitro* assays. In this approach, the antigen-targeting antibody of the antibody-enzyme conjugate binds the target cells, thereby bringing the enzyme to the target site. After clearance of unbound conjugate by a washing step, the ACPP is administered, which

enables ACPP activation only in the presence of the enzyme on the target cells. Herein, the inhouse developed αB7H3 antibody was used to target HeLa cells, while trastuzumab was used as negative control, that does not bind HeLa cells. Increased delivery of TAMRA was observed for αB7H3-treated HeLa cells compared to trastuzumab-treated cells. Subsequently, the payload was exchanged for a cryptophycin cytotoxin and cell proliferation was measured as an indication for internalization. Therefore, a HER2-targeting trastuzumab-SirT2 conjugate was used to target high HER2-expressing SKBR3 cells, while HER2 negative MDA-MB468 cells served as control. Deacetylation of the masked acetylated L17E peptide by trastuzumab-deacetylase on SKBR3 cells resulted in cell killing comparable to deacetylation with free deacetylase; however, cell killing in both cases was not completely recovered to the level of the L17E peptide without protecting groups. As expected, the trastuzumab-SirT2 treated HER2-negative MDA-MB468 cells did not show increased cell killing, demonstrating the feasibility of the ADEPT-like approach for the conditional and selective intracellular delivery of cargos *via* CPPs. However, the instability of SirT2 had prompted the use of a modified cell proliferation assay at reduced temperature and shorter incubation time (2 h sample incubation and subsequently 72 h in medium only), such that EC_{50} values in the double-digit nanomolar range were obtained. A standard cell proliferation assay, whereby samples were incubated on cells continuously for 72 h displayed EC_{50} values in the picomolar range, as was expected for the cryptophycin toxin. Unexpectedly, the acetylated L17E peptide which should block cellular uptake, still displayed significant cytotoxicity. Therefore, with room for improvement in terms of stronger impairment of cellular uptake through the protecting group and instability of the SirT2 enzyme, the uncharged acetyl protecting group was exchanged for a succinyl protecting group, that is negatively charged at physiological pH. Succinyl deprotection could be performed by the enzyme SirT5, which coincidentally displayed enhanced stability compared to the SirT2 enzyme. Two succinyl groups on the L17E peptide were suitable to prevent the intracellular delivery of the TAMRA-labelled peptide, that was previously not achievable with two alloc protecting groups. Encouraged that the negative charges on the protecting group had a greater effect on the inhibition of cellular uptake, the cellular proliferation assay with cryptophycin was repeated. Contrary to expectations, the L17E peptide with five succinylated lysine residues still displayed significant cytotoxicity, concluding that internalization may have been mediated by the hydrophobic cryptophycin molecule itself. While not new, the differences observed between the intracellular TAMRA and cryptophycin using the same ACPP underline that cargo identity influences cellular uptake efficiency. Therefore, cytosolic delivery of diverse range of cargos remains to be analyzed and assessed individually.

The ADEPT approach for the activation of cargo delivery at the tumor site is a selective cytosolic transporter tool, that at the same time helps overcome the polycation dilemma, a factor which hinders the *in vivo* application of CPPs. Conditionally activatable CPPs, masked in transit and exposed at target sites, minimize off-target effects and improve therapeutic outcomes. Using a targeting antibody-enzyme conjugate expands the number of possible activation options beyond the tumor microenvironment, allowing customization of activation conditions and cell targeting.

The intracellular delivery of larger cargos may necessitate multiple attached CPPs. Dr. Bastian Becker and Dr. Simon Englert had showed the direct conjugation of CPPs to the cargo was more effective than coincubation of the CPP with the cargo, and first examined the multimerization of CPPs on a cargo-bearing dextran scaffold. Encouraged by the successes of the intracellular delivery of dextran-CPP conjugates, the project was directed towards to the generation of dextran-ACPP conjugates for conditional intracellular delivery. To accomplish this, dextran bearing TAMRA as delivery cargo was decorated with alloc- or acetyl-masked L17E peptide variants, whereby the number of protecting groups was kept to one or two. They were placed at different positions of the L17E peptide, to simplify deprotection in subsequent conditional activation experiments. While cellular internalization of the dextran conjugate could not be blocked by one alloc protecting group on the L17E peptide, cellular uptake was strongly weakened with the simultaneous masking of two lysine residues. However, the masking of lysine positions K1+K2 and K2+K4 showed strong adsorption to the outer cell membrane, which was not observed with the masking group at the positions K1+K3. This suggested that the lysine in K2 position of the L17E peptide played a significant role in cellular uptake. For initial conditional activation experiments of dextran-ACPP conjugates, a TAMRA-bearing dextran scaffold was decorated with an acetylated-L17E peptide with the acetyl protecting group on the K1 or K2 positions. Without deacetylase SirT2, accumulation of the dextran-ACPP conjugates on the surface of the cell membrane was observed. Coincubation with SirT2 resulted in strongly reduced adsorption to the cell membrane for the L17E peptide with acetylated K2 position, with very weak intracellular fluorescence. The weak intracellular fluorescence however, was accompanied with the appearance of bright extracellular fluorescent spots, which may have been precipitate due to instability of the SirT2 enzyme. With these observations, the conditional delivery of dextran-ACPP conjugates could not be verified. Furthermore, the removal of the acetyl groups on the dextran-ACPP conjugate by SirT2 could not be validated by MALDI or TNBS assay, leading to the termination of the project on dextran-ACPP conjugates. As the dextran molecule itself exhibits a molecular weight range between 9 and 11 kDa, and

the attachment of peptides on it also occurs statistically, a highly polydisperse product is obtained. It would require a dextran-ACPP conjugate with a cleavable linker between the dextran molecule and the peptide, so that the peptide can be isolated for further analysis after incubation with SirT2.

Experiments performed by Dr. Simon Englert indicated that dextran-L17E conjugates had toxicity issues at higher concentrations. This was also relevant for some dextran-ACPP conjugates, which showed signs of cytotoxicity through unusual cell morphology. Therefore, the CPPs L17E/Q21E and HAad, derivatives of the L17E peptide, were investigated for their cell penetrating properties and cytotoxicity. While the TAMRA-dextran-HAad conjugate precipitated in cellular uptake assays, the TAMRA-dextran-L17E/Q21E conjugate demonstrated similar intracellular fluorescence intensities compared to the TAMRA-dextran-L17E conjugate at the same concentration, with reduced cytotoxicity. With these favorable properties, the peptide was investigated in form of a streptavidin delivery architecture.

Dr. Simon Englert first investigated streptavidin delivery architectures as a modular approach for the intracellular delivery of cargos, aiming to simplify synthesis efforts, given that synthesizing dextran delivery modules with different cargos is a lengthy process. Streptavidin allows up to four biotinylated components to be attached non-covalently. The composition of the streptavidin delivery modules can be controlled by adjusting the stoichiometric ratios of the biotinylated components during incubation with streptavidin. These biotinylated components may be biotinylated dextran-CPP conjugates and biotinylated payloads. Cell-targeting moieties such as antibodies or peptides can be biotinylated and used for targeted intracellular delivery. Dr. Simon Englert demonstrated the potential of these architectures for intracellular delivery; however, streptavidin-dextran-L17E architectures consistently exhibited significant cytotoxicity, necessitating optimization. Given the finding that the L17E/Q21E dextran conjugate is less cytotoxic, the L17E/Q21E peptide was identified for further investigation alongside the L17E peptide as a streptavidin delivery module. Furthermore, using streptavidin for tetramerization reduced synthesis efforts, allowing for investigation of two additional CPPs: the stapled peptide ATSP-7041 and the α-helical rationally designed apCC-Di-B peptide.

Intracellular delivery of the streptavidin-dextran-CPP architectures was first evaluated on HeLa cells using eGFP as payload, that was “loaded” on streptavidin, such that each streptavidin molecule contained one eGFP molecule. The remaining sites were occupied by either three biotin-dextran-CPP conjugates or two biotin-dextran-CPP conjugates and free biotin by incubation overnight with streptavidin in the desired stoichiometric ratios. The streptavidin

delivery modules generated exhibited sizes between 130 and 160 kDa, depending on the molecular weight of the CPP, the number of CPPs conjugated per dextran conjugate and the number of dextran-CPP conjugates per streptavidin. For the streptavidin-dextran-L17E delivery module, that had demonstrated significant cytotoxicity in the experiments of Dr. Simon Englert, the number of L17E peptides per dextran molecule was reduced to 3.7 (compared to around 5 before[202]). The streptavidin delivery module with two dextran-L17E conjugates, each having an average of 3.7 L17E peptides per dextran molecule, was more effective in the cytosolic delivery of eGFP at 2 μM concentration with respect to streptavidin, than the streptavidin delivery module with two dextran-L17E/Q21E conjugates, carrying an average of 6.3 L17E/Q21E peptides per dextran molecule. This corresponded to 15 μM L17E peptide and 25 μM L17E/Q21E peptide in the sample. Notably, the streptavidin delivery module with the dextran-ATSP-7041(3.7) conjugate did not show cytosolic delivery, perhaps requiring optimization by increasing the number of peptides per dextran conjugate. Streptavidin decorated with dextran-apCC-Di-B(3.7) displayed punctuate signals in the cytosol of one experiment, but in a second experiment displayed strong fluorescence outlining the cell membrane that extended partly into the cell interior. While the first experiment suggested endosomal entrapment of the streptavidin delivery module, the second signified strong adsorption to the cell membrane, perhaps entrapped in the cell membrane, with some cytosolic delivery. These contradictory results using cell cultures that were grown in different days may differ with respect to intrinsic cell “fitness” made it difficult to evaluate the performance of the apCC-Di-B peptide as delivery moiety. The use of markers such as a lysosomal tracker[218] or a plasma membrane protein marker[219] could be used to clarify whether entrapment in endosomes or within the lipid bilayer had occurred. Under energy-depleted conditions at 4 °C, cytosolic delivery was not observed for the streptavidin delivery modules with L17E or L17E/Q21E peptides and the streptavidin delivery module with the apCC-Di-B peptide only showed punctuate signals on the cell membrane. With these large delivery modules over 130 kDa, it is likely that they internalize via energy-dependent mechanisms, i.e. being internalized into the cytoplasm by an endosomal route rather than direct cytosolic uptake. The same was observed for the R9 peptide, which can change its internalization pathway.[73] Whether endosomal uptake, which requires an endosomal escape step into the cell cytoplasm is an efficient route for cargo protein delivery remains to be carefully elucidated. It is important to mention, that size exclusion chromatography of the streptavidin delivery modules showed that the dextran-CPP conjugates and eGFP were not fully assembled on the streptavidin centerpiece, so that the concentration of the delivery-prone stoichiometric complex of GFP

cargo and dextran-loaded streptavidin may be lower than anticipated, thereby hampering effective delivery.

Interestingly, the streptavidin delivery modules decorated with either the L17E or L17E/Q21E peptides, that had shown successful cytosolic delivery of eGFP at 37 °C incubation, exhibited reduced cell viability (80 %) compared to the ATSP-7041 and apCC-Di-B peptides that did not show clear cytosolic localization. This suggests that for cytosolic internalization of large conjugates, some cytotoxicity should be expected. In all, it is not surprising since the internalization of large architectures cause large disturbances in the integrity of the cell membrane. The temporary injury of the cell membrane is accompanied by several sealing mechanism to repair the damage, but the cells must also restore their intracellular homeostasis.[214] If the damage is too extensive, it may trigger cell cycle arrest or cell death.[214] Especially for cell-based therapies that involve the modulation of PPIs, balancing efficacy and cytotoxicity of the delivery architecture is essential.

The preceding experiments involved the verification of cytosolic delivery of the streptavidin delivery modules through functional assays, with the expectation it would reflect the results observed in the delivery of eGFP. The first cellular uptake assay was a split-GFP complementation assay, that was based on the cytosolic location of an exogenously incubated GFP11-tagged streptavidin delivery module in cells that stably expressed GFP1-10 in the cytosol. Successful reconstitution of the GFP fragments should result in detectable GFP fluorescence. In a second assay, the successful intracellular delivery of a MDM2 and MDMX inhibitor, the KD3 peptide, as a dextran conjugate on a streptavidin delivery module, should result in the reactivation of p53, observable in an engineered cell line that expresses a p53-mVenus fusion protein by live cell confocal imaging. The third assay was based on the NanoBiT® luciferase assay from Promega. Thereby, the small subunit HiBiT, that is tagged on the streptavidin delivery module as dextran conjugate, should spontaneously reconstitute to the large subunit LgBiT, upon its cytosolic localization, forming a functional luciferase. The luciferase then oxidizes a cell-permeable furimazine substrate under the release of light, that is detected as a luminescent signal.

Taken together, the cytosolic delivery of streptavidin delivery modules with the L17E and L17E/Q21E peptides observed by confocal imaging with eGFP as payload could not be verified through the split-GFP complementation, p53 accumulation or NanoBiT® assays. While the split-GFP assay was most likely not sensitive enough for detection at the 1 μM concentration used with respect to streptavidin, the p53 accumulation assay with the yellow fluorescent

protein mVenus as reporter signal may have been compromised through the yellow colored dextran-KD3 conjugate or cytotoxicity of the delivery modules, which led to a high background signal. The streptavidin delivery module with the HiBiT peptide and without CPP in the NanoBiT® assay also showed a high luminescent signal, undermining the results. Lysis of the cell membrane could release the cellular located LgBiT into the surrounding medium, which can complement with the delivery module outside of the cell, thus leading to a high luminescent signal. The assays for verification of cytosolic delivery remain to be optimized and balanced against the cytotoxicity of the delivery architectures. Furthermore, the functionalization of dextran with biotin remains to be optimized to generate these streptavidin architectures more efficiently with higher purity.

For the streptavidin delivery architectures, it remains to be seen how the positioning of CPPs around the streptavidin centerpiece influences intracellular delivery. If the total CPP concentration is the key factor, a single dextran chain with a high loading of CPPs could facilitate the delivery of up to three biotinylated cargo molecules. This approach can eventually be combined with tumor targeting moieties for targeted intracellular delivery of the cargo, which is the ultimate goal.

6 Experimental Part

6.1 General

6.1.1 Solvents

Solvents were purchased from *Carl Roth GmbH + Co. KG*, *Acros Organics*, *Fischer Scientific* and *Sigma Aldrich* and used without further purification. Anhydrous dimethyl sulfoxide (DMSO), acetonitrile (MeCN), dimethylformamide (DMF), dichloromethane (DCM) and dichloroethane (DCE) were purchased from *Acros Organics* or dried by storage over molecular sieves. Millipore quality water was used for HPLC analysis.

6.1.2 Reagents

Reagents were purchased from *Sigma Aldrich* (subsidiary of *Merck KGaA*, Darmstadt, Germany), *Carl Roth GmbH + Co. KG* (Karlsruhe, Germany), *Acros Organics* and *Fischer Scientific* (subsidiaries of *Thermo Fischer Scientific*), *TCI* (Eschborn, Germany) or *BLD Pharmatech Ltd.* (Shanghai, China). Reagents for peptide synthesis and Fmoc-protected building blocks were purchased from *Sigma Aldrich*, *Iris Biotech GmbH* (Marktredwitz, Germany) and *Carbolution Chemicals GmbH* (St. Ingbert, Germany). Substrates for cell viability measurements and internalization assays were purchased from *Promega GmbH* (Walldorf, Germany). Streptavidin was purchased from *IBA Lifesciences* (Göttingen, Germany).

6.1.3 Buffers and Solutions

Table 3| Buffer composition and solutions.

Buffer/solution	**Content**
0.05 M borate buffer pH 8.5	0.05 M boric acid
Eluent A for HPLC	0.1 % (v/v) TFA in H_2O
Eluent B for HPLC	0.1 % (v/v) TFA in 90 % MeCN (aq.)
Eluent A for LC-MS	0.1 % (v/v) formic acid in H_2O
Eluent B for LC-MS	0.1 % (v/v) formic acid in MeCN
PBS (pH 7.4)	137 mM NaCl 2.7 mM KCl 10 mM Na_2PO_4 1.8 mM KH_2PO_4
dYT-medium	10 g/L yeast extract 16 g/L tryptone 5 g/L NaCl

IMAC A buffer	20 mM TRIS/HCl pH 7.5 150 mM NaCl 20 mM imidazole
IMAC B buffer	20 mM TRIS-HCl pH 7.5 150 mM NaCl 500 mM imidazole
SDS-PAGE 5x sample buffer	0.25 M TRIS-HCl 7.5 % (w/v) SDS 25 % (v/v) glycerol 12.5 % β-mercaptoethanol 0.25 g/L bromophenol blue
SDS-PAGE 1x SDS-running buffer	50 mM TRIS-HCl pH 8.8 0.19 M glycine 1 g/L SDS
SDS-PAGE 4x stacking-TRIS	0.5 M TRIS-HCl pH 6.8 4 g/L SDS
SDS-PAGE 4x separating-TRIS	3 M TRIS-HCl pH 8.85 4 g/L SDS
Coomassie staining solution	0.2 % (w/v) Coomassie brilliant blue R-250 0.2 % (w/v) Coomassie brilliant blue G-250 30 % (v/v) isopropanol (aq.) 7.5 % (v/v) acetic acid (aq.)
Western blot transfer buffer	25 mM TRIS-HCl pH 8 192 mM Glycin 20 % (v/v) MeOH (aq.)
PBS-Tween (PBST)	0.1 % (v/v) Tween®20 in PBS
Alkaline phosphatase (AP)-buffer	100 mM TRIS-HCl pH 9.1 100 mM NaCl 50 mM $MgCl_2 \cdot 6H_2O$

6.1.4 Lyophilization

Freeze-drying of samples was attained with the *Alpha 2-4 LSC* from *Martin Christ Gefriertrocknungsnlagen GmbH* (Osterode am Harz, Germany) using an *Ilmvac Typ 109012* high vacuum pump (*Ilmvac GmbH*, now *Welch an Ingersoll Ranch Business*, Ilmenau, Germany).

6.1.5 Centrifugation

Benchtop centrifuges *Fischer AccuSpin Micro 17* from *ThermoFischer Scientific* or *Biofuge fresco* from *Heraeus* (Hanau, Germany) were used for centrifugation of samples up to 2 mL in microcentrifuge tubes. For 15 mL or 50 mL falcons, a *Multifuge 3 L-R* from *Heraeus* was used. Centrifugation of cell debris from sonication in the protein production process was performed with a *Sigma 3K30* laboratory centrifuge from *Sigma Laborzentrifugen GmbH* (Osterode am Harz, Germany).

6.1.6 Determination of protein concentration

A BioSpec Nano™ photometer from *Shimadzu* (Kyoto, Japan), that measured the absorption of tryptophan and tyrosine amino acid residues at 280 nm, was used to determine protein concentrations.

6.1.7 Cell lines

Table 4| Description of cell lines used and their cultivation conditions.

Cell line	Description	Culture medium
HeLa wild-type (WT)	Human cervix adenocarcinoma cells (Henrietta Lacks).	Dulbecco‘s Modified Eagle‘s Medium (DMEM) (*Sigma Aldrich*) supplemented with 10 % fetal bovine serum (FBS) (*Merck KGaA*, Darmstadt, Germany) and 1 % penicillin/streptomycin (P/S) (*Life technologies*, Carlsbad, CA, USA).
HeLa EM2-11ht	A stably transfected human cervical adenocarcinoma cell line, originated from Weidenfeld et al.[220] and provided by Julien Béthune.	Same culture medium as for HeLa WT with additional supplementation of 0.2 mg/mL G418 and 0.2 mg/mL hygromycin for maintaining continuous selection of the stable cell line.
HeLa 11ht-LgBiT	A stably transfected HeLa cell line with inducible LgBiT expression generated by Carolin Dombrowsky from HeLa EM2-11ht.[221]	Same culture medium as for HeLa WT with additional supplementation of 0.2 mg/mL G418 and 40 μM ganciclovir.

HeLa GFP1-10	HeLa cells stably transfected with GFP1-10 plasmid generated by Carolin Dombrowsky.[140]	Same culture medium as for HeLa EM2-11ht.
A549 p53-mVenus	A stably transfected human lung epithelial cell line that expresses a p53-mVenus fusion, generated in the working group of Alexander Löwer. The cells additionally expressed the cyan fluorescent protein mCerulean as fusion to histone H2B that served as nuclear marker.	Gibco™ FluoroBrite™ DMEM (*Thermo Fischer Scientific*) supplemented with 10 % FBS and 1 % P/S. To maintain continuous selection of the stable cell line, 0.2 mg/mL G418, 0.25 μg/mL puromycin and 25 μg/mL hygromycin were added.
SKBR3	Human breast cancer cell line with overexpressed epidermal growth receptor 2 (HER2+).	Same culture medium as for HeLa WT.
MDA-MB468	Human breast cancer cell line with no detectable levels of epidermal growth receptor 2 (HER2-).	Same culture medium as for HeLa WT.

Mammalian cells lines were cultured in a humidified incubator at 37 °C and 5 % CO_2 and sub-cultured every 3-4 days.

6.2 Analysis

6.2.1 Analytical reversed-phase high performance liquid chromatography (RP-HPLC)

RP-HPLC analysis was performed on an *Agilent 1100* device or an *Agilent 1260* device (*Agilent Technologies*) using the columns *Agilent ZORBAX Eclipse Plus* (C18, 100x4.6mm, 3.5 μm, 95 Å) or *Uptisphere strategy* (C18, 100x4.6mm, 3 μm, 100 Å) from *Interchim* (Montluçon, France). Eluent A (0.1 % (v/v) TFA in H_2O) and eluent B (0.1 % (v/v) TFA in 90 % MeCN (aq.)) comprised the eluent system, which was run at a flow rate of 0.6 mL/min starting with 3 min

isocratic flow followed by a 20 min linear gradient flow and ending with a washing step of 100 % eluent B for 4 min and then initial eluent composition for 5 min. For cryptophycin samples, eluent A and eluent B did not contain TFA.

6.2.2 Semi-preparative RP-HPLC

Peptides were purified on an *Uptisphere Strategy* RP column (C18-HQ, 5 μm, 250 × 21.2 mm) with a semi-preparative RP-HPLC *Puriflash 4250* device, both from *Interchim*. The same eluents as for analytical RP-HPLC were used, with a flow rate of 18 mL/min. 3 min isocratic flow were followed by 20 min linear gradient flow and final washing phase which included 100 % eluent B flow for 2 min and then 2 min flow at the initial eluent composition.

6.2.3 Size exclusion chromatography (SEC)

SEC analysis and purification of small samples of peptides and dextrans was performed on an *Agilent 1100* device or an *Agilent 1260* device using a *Phenomenex* (Aschaffenburg, Germany) *BioSep SEC-s2000* (300x7.8 mm, 5 μm, 145 Å) column using the eluents A and B with or without TFA at a flow rate of 0.6 mL/ min and 30 % or 40 % eluent B isocratic flow. For purification of peptides, a *Superdex Peptide 10/300 GL* column was used with the same eluent composition and flow rate.

SEC analysis of protein samples was performed on an *Agilent 1260* device and *TOSOH Bioscience* (Griesheim, Hessen, Germany) *TSKgel® Super-SW3000* (300x4.6mm, 4 μm, 250 Å) column using phosphate buffered saline (PBS) at pH 7.4 (137 mM NaCl, 2.7 mM KCl, 10 mM Na_2PO_4, 1.8 mM KH_2PO_4) at a flow rate of 0.35 mL/min.

6.2.4 Electrospray Ionization Mass Spectrometry (ESI-MS)

ESI-MS analysis was performed on using a *Shimadzu* (Griesheim, Hessen, Germany) *LCMS-2020* device and *Phenomenex Synergy 4u Fusion-RP 80* (C-18, 250x4.6 mm, 2 μm, 80 Å) column. Eluent A (0.1 % (v/v) formic acid in H_2O) and eluent B (0.1 % (v/v) formic acid in MeCN) (LC-MS grade, *Fischer Scientific*) comprised the eluent system, which was run at a flow rate of 0.7 mL/min and 37 °C oven temperature. Samples were analyzed in the positive ion mode at 50-450 *m/z*, 100-700 *m/z*, 200-1000 *m/z* or 350-2000 *m/z*. LCMS-2020 parameters: nebulizing gas-nitrogen, nebulizing gas flow—1.5 L/min, drying gas flow—15 L/min, desolvation line (DL) temperature—200 °C, Heat block temperature—200 °C, detector voltage—1.45 kV.

Alternatively, ESI-MS was performed using a *Bruker Daltonics* (Bremen, Germany) *Impact II* device.

6.2.5 Matrix-assisted laser desorption/ionization-time of flight (MADLI-TOF)

A *Bruker Daltonics Autoflex speed TOF/TOF* was used for MALDI analysis. For dextrans, the matrix 2,5-dihydroxyacetophenon (2,5-DHAP) was used.

6.2.6 Nuclear Magnetic Resonance (NMR)

A *Bruker BioSpin GmbH* (Rheinstetten, Germany) *Avance III* or *Avance II* was used for ^{1}H-NMR (300 MHz) analysis. The δ-values denote the downfield chemical shifts in part per million (ppm). Dextran samples were dissolved in deuterium oxide obtained from *Sigma Aldrich*.

6.2.7 Infrared (IR) Spectroscopy

A *FTIR-Spectrometer Spectrum Two* from *Perkin Elmer* (Rodgau, Germany) was used for IR spectroscopy. Samples were measured in form of potassium bromide (KBr) pellets. Wave number area: 8300-350 cm^{-1}; spectral solution 0.5 cm^{-1}; wave number accuracy better than 0.01 cm^{-1} at 3000 cm^{-1}; wave number correctness: 0.1 cm^{-1} at 3000 cm^{-1}; signal-to-noise-ratio: 9300: 1 Peak to Peak, 5 s and 32000: 1 Peak to Peak, 1 min.

6.2.8 Determination of protein concentration and UV/Vis Spectroscopy

For protein concentration determination and UV/Vis spectroscopy, the *BioSpec-nano* photometer from *Shimadzu* (Kyoto, Japan) was used. Protein concentrations were determined by absorption of tryptophan and tyrosine residues at 280 nm.

6.2.9 Multifunctional microplate reader

Recording of absorbance for cell proliferation assays at 490 nm, absorbance at 335 nm for TNBS assays or luminescence measurements were performed using the CLARIO*star*® *Plus* (*BMG Labtech*, Ortenberg, Germany).

6.2.10 Microscopy

Confocal laser scanning microscopy (CLSM) was performed using a *LEICA TSC SP8* confocal microscope from *LEICA Microsystems CMS GmbH* (Wetzlar, Germany). Hoechst 33342 from *Fischer Scientific* (Hampton, NA, USA) and TAMRA dye were detected by laser excitation at 405 nm and 552 nm respectively. Images were taken under the same microscopy tuning parameters.

6.2.11 Flow Cytometry

Flow cytometry analysis was performed using a *CytoFLEX S* cytometer (*Beckman Coulter*, Krefeld, Germany).

6.2.12 SDS-Polyacrylamide Gel Electrophoresis (SDS-PAGE)

Samples were reduced and denatured by heating 12 μL of 3-5 μg protein or 30-50 μg dextran-protein conjugate with 3 μL SDS-PAGE 5x sample buffer at 98° C for 10 min. The sample was loaded into the pockets of the polyacrylamide gel containing 4 % acrylamide in the stacking gel and 15 % acrylamide in the separation gel. Gels were run at 300 V and 45 mA with the *blue prestained protein standard, broad range (11 – 250 kDa)* from *New England Biolabs* (Ipswich, MA, USA). The gels were stained with Coomassie staining solution and destained with 10 % (v/v) acetic acid using a microwave.

6.2.13 Western Blot

Western blots were performed using the trans-blot turbo transfer system from *BIO-RAD Laboratories* (Hercules, California, USA). 12x Whatman paper, the SDS-gel for western blotting and nitrocellulose membrane were soaked in western blot transfer buffer. From bottom to top: 6x Whatman paper, membrane, SDS-gel, 6x Whatman paper were stacked on the trans-blot turbo cassette and the lid closed. Blotting was running with the following settings: 0.3 A, 25 V, 35 min. The membrane was removed and washed 3x with PBST for 5 min. The membrane was blocked with 50 mL 2 % milk powder in PBST for 1 h and subsequently washed 3x with PBST for 5 min. Next, the membrane was incubated in 15 mL streptavidin-alkaline-phosphatase (strep-AP) in PBST (1:3000 dilution) for 1 h. The membrane was washed 3x with AP-buffer for 5 min. Colorimetric detection of alkaline phosphatase was achieved with 75 μL 5-bromo-4-chloro-3-indolyl-phosphate (BCIP) (50 mg/mL stock solution in DMF) and 25 μL nitro blue tetrazolium (NBT) (75 mg/mL stocks solution in 70 % DMF) in AP-buffer. The reaction was stopped with 10 % acetic acid.

6.3 Solid phase peptide synthesis (SPPS)

Peptides were synthesized on solid support from the *C*- to the *N*-terminus utilizing the Fmoc/tBu strategy on *AmphiSpheres 40* RAM resin with a loading of 0.345 mmol/g from *Agilent Technologies* Germany *GmbH & Co. KG* (Waldbronn, Germany).

6.3.1 Loading of first amino acid

Using *AmphiSpheres 40* RAM resin, the resin was swollen in a reaction vessel with a frit for 20 min in DCM and then washed 3x with DMF. After removal of the Fmoc protecting group on the resin, the first amino acid was pre-activated for 1 min by mixing 5 eq. amino with 4.95 eq. 3-[bis(dimethylamino)methyliumyl]-3H-benzotriazol-1-oxide hexafluorophosphate (HBTU) and 10 eq. diisopropylethylamine (DIPEA). The mixture was shaken with the resin for 30 min. The supernatant was removed and the resin was washed 6x with DMF.

Coupling of non-natural amino acids proceeded as with for natural amino acids with 2.5 eq. amino acid, 2.46 eq. 1-[bis(dimethylamino)methylene]-1H-1,2,3-triazolo[4,5-b] pyridinium 3-oxide hexafluorophosphate (HATU) and 5 eq. DIPEA in DMF or 2 eq. amino acid, 1.95 eq. HATU and 4 eq. DIPEA or 1.5 eq. amino acid, 1.46 eq. HATU and 3 eq. DIPEA were used. Coupling was performed for 45 min. For double coupling, the same mixture was replaced with a fresh one and proceeded as described.

6.3.2 Fmoc deprotection

Fmoc was removed by shaking the resin with 20 % (v/v) piperdine in DMF for 5 min at room temperature followed by 3x washing with DMF. Fresh piperidine solution was added again and shaken with the resin for 10 min. Afterwards the resin was washed thoroughly with DMF and was ready for the next coupling.

6.3.3 Peptide chain elongation

The peptide chain was assembled in cycles of amino acid coupling steps. For standard amino acids, a pre-activated mixture of 5 eq. amino acid, 4.95 eq. HBTU and 10 eq. DIPEA was shaken with the resin for 30 min at room temperature. For non-natural amino acids a pre-activated mixture of 2.5 eq. amino acid, 2.46 eq. HBTU and 5 eq DIPEA was used and shaken with the resin for 45 min. At the end of each coupling, the resin was washed 6x with DMF before proceeding with Fmoc deprotection and coupling of the next amino acid.

6.3.4 Automated peptide synthesis

Automated peptide synthesis was performed on a 0.1 mmol or 0.25 mmol scale using the *Liberty Blue*® from *CEM GmbH* (Kamp-Lintfort, Germany) with microwave-assistance (30 W). The dry resin (pre-loaded or unloaded) was transferred to the reaction vessel and swollen in the synthesizer. Amino acids were activated using *N,N*-diisopropylcarbodiimide (DIC)/ ethyl cyano(hydroxyamino)acetate (oxyma) in DMF. The concentrations prepared were 0.2 M amino

acid, 1 M Oxyma and 0.5 M DIC. Fmoc was deprotected using 20 % (v/v) piperdine and 0.1 M oxyma in DMF at 90 °C for 1 min. For 0.1 mmol scales 2.5 mL amino acid, 0.5 mL oxyma and 1 mL DIC were used for coupling and 4 mL deprotection solution for Fmoc deprotection. For 0.25 mmol scales 5 mL amino acid, 1 mL oxyma and 2 mL DIC for coupling and 10 mL deprotection solution for Fmoc deprotection. Coupling was performed at 90°C for 2 min, except histidine and cysteine which were coupled at 50 °C for 10 min and arginine at 75 °C for 5 min. Double coupling was performed for standard natural amino acids and single coupling for non-natural amino acids.

6.3.5 Dde deprotection

Dde protecting group was removed by treating the resin with 2 % hydrazine four times for 3 min with a DMF washing step in between. After the fourth cycle, the resin was washed 6x with DMF.

6.3.6 Resin storage

For storage overnight under the fume hood, the resin was thoroughly with DMF and then washed 6x with DCM and dried under air flow. For longer storage in a desiccator, the resin was additionally washed 6x with diethyl ether after washing with DCM and then dried under air flow.

6.3.7 Peptide cleavage from resin and workup

Cleavage of peptides from the resin was performed with a trifluoracetic acid (TFA) mixture consisting of TFA: triethylsilane (TES): Anisole: H_2O (97:1:1:1) (v:v:v:v). If the peptide contained a cysteine, dithiothreitol (DTT) was added additionally to obtain a cleavage mixture with composition TFA:TES:Anisole:H2O:DTT (96:1:1:1:1) (v:v:v:v:w). The resin was shaken with the cleavage mixture for 3 h at room temperature. The peptide was precipitated and washed 3x with cold diethyl ether. After drying under air flow, the residue was dissolved in a H_2O/MeCN mixture and lyophilized.

6.4 Conditional and selective intracellular CPP-cargo delivery

6.4.1 Synthesis of L17E-TAMRA 1

H-IWLTALKFLGKHAAKHEAKQQLSKL-K(*TAMRA*)-*NH*$_2$

$C_{165}H_{252}N_{42}O_{36}$

M_w: 3400.0 g/mol

0.72 g (0.25 mmol, 1 eq.) Amphispheres 40 RAM resin of loading 0.345 mmol/g was transferred into a syringe with frit. An orthogonal lysine with a 1-(4,4-dimethyl-2,6-dioxocyclohex-1-ylidene)ethy (Dde) protecting group was first introduced to generate a selective conjugation site for TAMRA at the *C*-terminus. An isomeric 5,6-TAMRA mixture was used. The procedure of loading the first amino acids as described in section 6.3.1 was followed using 333 mg Fmoc-Lys(Dde)-OH (0.625 mmol, 2.5 eq.), 233 mg HATU (0.613 mmol, 2.45 eq.) and 217 μL DIPEA (1.25 mmol, 5 eq.) in 8 mL DMF. Fmoc-Lys(Dde)-OH was double coupled. Coupling of the L17E peptide sequence was performed using the *Liberty Blue*® as described in section 6.3.4 with final Fmoc deprotection. The *N*-terminus was Boc-protected by agitating the resin with 459 μL Boc anhydride (2 mmol, 8 eq.) and 697 μL DIPEA (4 mmol, 16 eq.) in DMF for 1 h. The Dde protecting group was removed by treating the resin 4x in 3 min cycles with 2 % hydrazine in DMF with a 1x DMF wash in between cycles. After the last cycle, the resin was washed 6x with DMF and 6x with DCM and dried under air flow. 1/8th of the resin (0.031 mmol, 1 eq.) was taken for TAMRA labelling. 164 mg TAMRA-NHS (0.31 mmol, 10 eq.) and 108 μL DIPEA (0.62 mmol, 20 eq.) were agitated with the resin overnight in dry DMF at ambient temperature. The resin was washed 6x with DMF and 6x with DCM and cleaved from the resin as described in section 6.3.7. The peptide was purified by semi-preparative RP-HPLC with yield 19 mg (5.58 μmol, 19 %).

RP-HPLC 0to100% Eluent B: t_R = 14.108 min, 14.269 min.
ESI-MS calculated for $C_{165}H_{252}N_{42}O_{36}$: $[M+H]^+$ = 3401.0; $[M+2H]^{2+}$ = 1701.0; $[M+3H]^{3+}$ = 1134.3; $[M+4H]^{4+}$ = 851.0; $[M+5H]^{5+}$ = 681.0; $[M+6H]^{6+}$ = 567.7; $[M+7H]^{7+}$ = 486.7; observed: $[M+4H]^{4+}$ = 851.1; $[M+5H]^{5+}$ = 681.0; $[M+6H]^{6+}$ = 567.7; $[M+7H]^{7+}$ = 486.8.

6.4.2 Synthesis of L17E$_{K1+K2}^{Alloc}$-TAMRA 2

H-IWLTALK(Alloc)FLGK(Alloc)HAAKHEAKQQLSKL-K(*TAMRA*)-*NH*$_2$

$C_{173}H_{260}N_{42}O_{40}$

M_w: 3568.2 g/mol

L17E$_{K1+K2}^{Alloc}$-TAMRA **2** was synthesized analogously to L17E-TAMRA **1**, but on a smaller scale. 0.29 g (0.1 mmol, 1 eq.) Amphispheres 40 RAM resin of loading 0.345 mmol/g was transferred into a syringe with frit. An orthogonal lysine with a Dde protecting group was first introduced to generate a selective conjugation site for TAMRA at the *C*-terminus. The procedure of loading the first amino acids as described in section 6.3.1 was followed using 133 mg Fmoc-Lys(Dde)-OH (0.25 mmol, 2.5 eq.), 93 mg HATU (0.245 mmol, 2.45 eq.) and 87.1 μL DIPEA (0.5 mmol, 5 eq.) in 8 mL DMF. Fmoc-Lys(Dde)-OH was double coupled. Coupling of the L17E peptide

sequence was performed using the *Liberty Blue*® as described in section 6.3.4 with final Fmoc deprotection. Thereby, the Fmoc-Lys(Alloc)-OH building block was used for lysine residues with alloc units. The *N*-terminus was Boc-protected by agitating the resin with 188 μL Boc anhydride (0.8 mmol, 8 eq.) and 279 μL DIPEA (1.6 mmol, 16 eq.) in DMF for 1 h. The Dde protecting group was removed by treating the resin 4x in 3 min cycles with 2 % hydrazine in DMF with a 1x DMF wash in between cycles. After the last cycle, the resin was washed 6x with DMF and 6x with DCM and dried under air flow. 1/4th of the resin (0.025 mmol, 1 eq.) was taken for TAMRA labelling. 39.6 mg TAMRA-NHS (0.025 mmol, 3 eq.) and 26.1 μL DIPEA (0.15 mmol, 6 eq.) were agitated with the resin overnight in dry DMF at ambient temperature. The resin was washed 6x with DMF and 6x with DCM and cleaved from the resin as described in section 6.3.7. The peptide was purified by semi-preparative RP-HPLC with yield 1.1 mg (0.308 μmol, 1 %).

RP-HPLC 0to80% Eluent B: t_R = 18.243 min.
ESI-MS calculated for $C_{173}H_{260}N_{42}O_{40}$: $[M+H]^+$ = 3569.2; $[M+2H]^{2+}$ = 1785.1; $[M+3H]^{3+}$ = 1190.4; $[M+4H]^{4+}$ = 893.0; $[M+5H]^{5+}$ = 714.6; $[M+6H]^{6+}$ = 595.7; $[M+7H]^{7+}$ = 510.7; observed: $[M+4H]^{4+}$ = 893.2; $[M+5H]^{5+}$ = 714.7; $[M+6H]^{6+}$ = 595.7; $[M+7H]^{7+}$ = 510.8.

6.4.3 Synthesis of L17E$_{K1+K3}^{Alloc}$-TAMRA 3

H-IWLTALK(Alloc)FLGKHAAK(Alloc)HEAKQQLSKL-K(*TAMRA*)-*NH*$_2$

$C_{173}H_{260}N_{42}O_{40}$

M_w: 3568.2 g/mol

L17E$_{K1+K3}^{Alloc}$-TAMRA peptide **3** was synthesized analogously to L17E$_{K1+K2}^{Alloc}$-TAMRA **2** with yield 0.9 mg (0.252 μmol, 1 %).

RP-HPLC 0to80% Eluent B: t_R = 16.994 min.
ESI-MS calculated for $C_{173}H_{260}N_{42}O_{40}$: $[M+H]^+$ = 3569.2; $[M+2H]^{2+}$ = 1785.1; $[M+3H]^{3+}$ = 1190.4; $[M+4H]^{4+}$ = 893.0; $[M+5H]^{5+}$ = 714.6; $[M+6H]^{6+}$ = 595.7; $[M+7H]^{7+}$ = 510.7; observed: $[M+4H]^{4+}$ = 893.6; $[M+5H]^{5+}$ = 715.1; $[M+6H]^{6+}$ = 596.1; $[M+7H]^{7+}$ = 514.7.

6.4.4 Synthesis of L17E$_{K2+K4}^{Alloc}$-TAMRA 4

H-IWLTALKFLGK(Alloc)HAAKHEAK(Alloc)QQLSKL-K(*TAMRA*)-*NH*$_2$

$C_{173}H_{260}N_{42}O_{40}$

M_w: 3568.2 g/mol

L17E$_{K2+K4}^{Alloc}$-TAMRA peptide **4** was synthesized analogously to L17E$_{K1+K2}^{Alloc}$-TAMRA **2** with yield 1.1 mg (0.308 μmol, 1 %).

RP-HPLC 0to80% Eluent B: t_R = 17.740 min.
ESI-MS calculated for $C_{173}H_{260}N_{42}O_{40}$: $[M+H]^+$ = 3569.2; $[M+2H]^{2+}$ = 1785.1; $[M+3H]^{3+}$ = 1190.4; $[M+4H]^{4+}$ = 893.0; $[M+5H]^{5+}$ = 714.6; $[M+6H]^{6+}$ = 595.8; $[M+7H]^{7+}$ = 510.7; observed: $[M+3H]^{3+}$ = 1190.6; $[M+4H]^{4+}$ = 893.2; $[M+5H]^{5+}$ = 714.7; $[M+6H]^{6+}$ = 595.8; $[M+7H]^{7+}$ = 510.9.

6.4.5 Synthesis of L17E$_{K3+K5}^{Alloc}$-TAMRA 5

H-IWLTALKFLGKHAAK(Alloc)HEAKQQLSK(Alloc)L-K(*TAMRA*)-*NH$_2$*

$C_{173}H_{260}N_{42}O_{40}$

M_w: 3568.2 g/mol

L17E$_{K3+K5}^{Alloc}$-TAMRA peptide **5** was synthesized analogously to L17E$_{K1+K2}^{Alloc}$-TAMRA **2** with yield 1.3 mg (0.364 μmol, 2 %).

RP-HPLC 0to80% Eluent B: t_R = 17.327 min.
ESI-MS calculated for $C_{173}H_{260}N_{42}O_{40}$: $[M+H]^+$ = 3569.2; $[M+2H]^{2+}$ = 1785.1; $[M+3H]^{3+}$ = 1190.4; $[M+4H]^{4+}$ = 893.0; $[M+5H]^{5+}$ = 714.6; $[M+6H]^{6+}$ = 595.8; $[M+7H]^{7+}$ = 510.7; observed: $[M+3H]^{3+}$ = 1190.5; $[M+4H]^{4+}$ = 893.1; $[M+5H]^{5+}$ = 714.7; $[M+6H]^{6+}$ = 595.7; $[M+7H]^{7+}$ = 510.9.

6.4.6 Synthesis of L17E5K(Ac)-TAMRA 6

H-IWLTALK(Ac)FLGK(Ac)HAAK(Ac)HEAK(Ac)QQLSK(Ac)L-K(*TAMRA*)-*NH$_2$*

$C_{175}H_{262}N_{42}O_{41}$

M_w: 3610.2 g/mol

L17E5K(Ac)-TAMRA peptide **6** was synthesized analogously to L17E$_{K1+K2}^{Alloc}$-TAMRA **2** using the Fmoc-Lys(Ac)-OH building block on the *Liberty Blue*® with yield 15 mg (4.15 μmol, 17 %).

RP-HPLC 20to80% Eluent B: t_R = 15.977 min, 16.196 min.
ESI-MS calculated for $C_{175}H_{262}N_{42}O_{41}$: $[M+H]^+$ = 3611.2; $[M+2H]^{2+}$ = 1806.1; $[M+3H]^{3+}$ = 1204.4; $[M+4H]^{4+}$ = 903.5; $[M+5H]^{5+}$ = 723.0; $[M+6H]^{6+}$ = 602.7; $[M+7H]^{7+}$ = 517.6; observed: $[M+3H]^{3+}$ = 1024.5; $[M+4H]^{4+}$ = 903.6; $[M+5H]^{5+}$ = 723.1.

6.4.7 Synthesis of L17E-Pra 7

H-IWLTALKFLGKHAAKHEAKQQLSKL-Pra-*NH$_2$*

$C_{139}H_{225}N_{39}O_{32}$

M_w: 2954.5 g/mol

0.72 g (0.25 mmol, 1 eq.) Amphispheres 40 RAM resin of loading 0.345 mmol/g was transferred into a syringe fitted with a frit. A propargyl glycine (Pra) residue with alkyne functionality was introduced at the *C*-terminus to allow for further site selective modification. The procedure of loading the first amino acids as described in section 6.3.1 was followed using 209 mg Fmoc-Pra-OH (0.625 mmol, 2.5 eq.) were activated with 233 mg HATU (0.613 mmol, 2.45 eq.) and 217 μL DIPEA (1.25 mmol, 5 eq) in 8 mL DMF and added to the resin. After shaking for 45 min, the resin was washed 3x with DMF and a second freshly activated solution of Fmoc-Pra-OH, HATU and DIPEA was added and the mixture shaken for 45 min again for double coupling of the building block. Afterwards, the resin was washed with DMF and DCM and dried under air flow. Coupling of the L17E peptide sequence IWLTALKFLGKHAAKHEAKQQLSKL was performed using the *Liberty Blue*® as described in section 6.3.4 with final Fmoc deprotection. Cleavage from the resin was performed as described in section 6.3.7. The peptide was purified by semi-preparative RP-HPLC with yield 123 mg (17 %).

RP-HPLC 0to80% Eluent B: t_R = 15.740 min.
ESI-MS calculated for $C_{139}H_{225}N_{39}O_{32}$: $[M+H]^+$ = 2955.5; $[M+2H]^{2+}$ = 1478.3; $[M+3H]^{3+}$ = 985.9; $[M+4H]^{4+}$ = 739.6; $[M+5H]^{5+}$ = 591.9; $[M+6H]^{6+}$ = 493.4; observed: $[M+3H]^{3+}$ = 985.8; $[M+4H]^{4+}$ = 739.6; $[M+5H]^{5+}$ = 591.9; $[M+6H]^{6+}$ = 493.5.

6.4.8 Synthesis of L17E5K(Ac)-Pra 8

H-IWLTALK(Ac)FLGK(Ac)HAAK(Ac)HEAK(Ac)QQLSK(Ac)L-Pra-*NH₂*

$C_{149}H_{235}N_{39}O_{37}$

M_w: 3164.7 g/mol

0.29 g (0.1 mmol, 1 eq.) Amphispheres 40 RAM resin of loading 0.345 mmol/g was transferred into a syringe with frit. A propargyl glycine (Pra) residue with alkyne functionality was introduced at the *C*-terminus to allow for further site selective modification. The procedure of loading the first amino acids as described in section 6.3.1 was followed using 83.8 mg Fmoc-Pra-OH (0.25 mmol, 2.5 eq.), 93.1 mg HATU (0.245 mmol, 2.45 eq.) and 87.1 μL DIPEA (0.5 mmol, 5 eq.) in 3 mL DMF. Fmoc-Pra-OH was double coupled. Afterwards, the resin was washed with DMF and DCM and dried under air flow. Coupling of the L17E peptide sequence was performed using the *Liberty Blue*® as described in section 6.3.4 with final Fmoc

deprotection. Thereby, the Fmoc-Lys(Ac)-OH building block was used for lysine residues with acetyl units. Cleavage from the resin was performed as described in section 6.3.7. The peptide was purified by semi-preparative RP-HPLC with yield 45 mg (14 %).

RP-HPLC 0to80% Eluent B: t_R = 18.502 min.
ESI-MS calculated for $C_{149}H_{235}N_{39}O_{37}$: $[M+H]^+$ = 3165.5; $[M+2H]^{2+}$ = 1583.3; $[M+3H]^{3+}$ = 1055.9; $[M+4H]^{4+}$ = 792.1; $[M+5H]^{5+}$ = 633.9; $[M+6H]^{6+}$ = 528.4; observed: $[M+3H]^{3+}$ = 1055.9; $[M+4H]^{4+}$ = 792.2.

6.4.9 Synthesis of L17E-Cys 9

H-IWLTALKFLGKHAAKHEAKQQLSKL-C-*NH*$_2$

$C_{137}H_{225}N_{39}O_{32}S$

M_w: 2962.6 g/mol

L17E peptide was modified with a cysteine residue on the *C*-terminus to introduce a site-specific conjugation site. 0.72 g (0.25 mmol, 1 eq.) Amphispheres 40 RAM resin of loading 0.345 mmol/g was transferred into the reaction vessel of the *Liberty Blue*® as described in section 6.3.4 and completely synthesized with microwave assistance with final Fmoc deprotection. The peptide was cleaved from the resin as described in section 6.3.7 and purified by semi-preparative RP-HPLC with yield 155.6 mg (0.053 mmol, 21 %).

RP-HPLC 0to80% Eluent B: t_R = 15.335 min.
ESI-MS calculated for $C_{137}H_{225}N_{39}O_{32}S$: $[M+H]^+$= 2963.6; $[M+2H]^{2+}$ = 1482.3; $[M+3H]^{3+}$ = 988.5; $[M+4H]^{4+}$= 741.6; $[M+5H]^{5+}$ = 593.5; $[M+6H]^{6+}$ = 494.8; $[M+7H]^{7+}$ = 424.2; observed: $[M+3H]^{3+}$ = 988.5; $[M+4H]^{4+}$= 741.7; $[M+5H]^{5+}$ = 593.5; $[M+6H]^{6+}$ = 494.9; $[M+7H]^{7+}$ = 424.4.

6.4.10 Synthesis of L17E5K(Ac)-Cys 10

H-IWLTALK(Ac)FLGK(Ac)HAAK(Ac)HEAK(Ac)QQLSK(Ac)L-C-*NH*$_2$

$C_{147}H_{235}N_{39}O_{37}S$

M_w: 3172.7 g/mol

L17E5K(Ac) peptide was modified with a cysteine residue on the *C*-terminus to introduce a site-specific conjugation site. 0.29 g (0.1 mmol, 1 eq.) Amphispheres 40 RAM resin of loading 0.345 mmol/g was transferred into the reaction vessel of the *Liberty Blue*® as described in section 6.3.4 and completely synthesized with microwave assistance. Fmoc-Lys(Ac)-OH was used for the acetylated lysine residues. The peptide was cleaved from the resin as described in

section 6.3.7 and purified by semi-preparative RP-HPLC with yield 56.1 mg (0.018 mmol, 18 %).

RP-HPLC 0to80% Eluent B: t_R = 18.637 min.
ESI-MS calculated for $C_{147}H_{235}N_{39}O_{37}S$: $[M+H]^{+}$= 3173.7; $[M+2H]^{2+}$ = 1587.4; $[M+3H]^{3+}$ = 1058.6; $[M+4H]^{4+}$= 794.2; observed: $[M+3H]^{3+}$ = 1058.6; $[M+4H]^{4+}$= 794.1.

6.4.11 Synthesis of L17E-cry 11

L17E-cry **11** was synthesized from L17E-Cys **9** (see section 6.4.9).

H-IWLTALKFLGKHAAKHEAKQQLSKL-C(*Cryptophycin*)-NH_2

$C_{200}H_{306}ClN_{49}O_{47}S$

M_w: 4126.4 g/mol

5 mg L17E-Cys peptide **9** (1.68 μmol, 1 eq.) and 152 μL Mal-ValCit-PAB-cryptophycin of a 10 mM stock solution in DMSO (1.52 μmol, 0.9 eq.) were gently agitated overnight in 30 % DMSO and 70 % NH_4HCO_3 buffer (pH 7.2) at ambient temperature. The product was purified by manual collection of the respective fraction over multiple analytical RP-HPLC runs and lyophilized.

RP-HPLC 20to100% Eluent B: t_R = 12.267 min.
ESI-MS calculated for $C_{200}H_{306}ClN_{49}O_{47}S$: $[M+H]+$ = 4217.4; $[M+2H]^{2+}$ = 2109.2; $[M+3H]^{3+}$ = 1406.5; $[M+4H]^{4+}$ = 1055.1; $[M+5H]^{5+}$ = 844.3; $[M+6H]^{6+}$ = 703.7; observed: $[M+3H]^{3+}$ = 1406.5; $[M+4H]^{4+}$ = 1055.1; $[M+5H]^{5+}$ 844.3; $[M+6H]^{6+}$ = 703.7.

6.4.12 Synthesis of L17E5K(Ac)-cry 12

L17E5K(Ac)-cry **12** was synthesized from L17E5K(Ac)-Cys **10** (see section 6.4.10).

H-IWLTALK(Ac)FLGK(Ac)HAAK(Ac)HEAK(Ac)QQLSK(Ac)L-C(*Cryptophycin*)-NH_2

$C_{210}H_{316}ClN_{49}O_{52}S$

M_w: 4426.6 g/mol

5 mg L17E5K(Ac)-Cys peptide **10** (1.57 μmol, 1 eq.) and 142 μL Mal-Val-Cit-PAB-cryptophycin of a 10 mM stock solution in DMSO (1.42 μmol, 0.9 eq.) were gently agitated overnight in 80 % DMSO and 20 % NH_4HCO_3 buffer (pH 7.2) at ambient temperature. The product was purified by manual collection of the respective fraction over multiple analytical RP-HPLC runs and lyophilized.

RP-HPLC 20to100% Eluent B: t_R = 15.053 min.

ESI-MS calculated for $C_{210}H_{316}ClN_{49}O_{52}S$: $[M+H]^+$ = 4427.6; $[M+2H]^{2+}$ = 2214.3; $[M+3H]^{3+}$ = 1476.5; $[M+4H]^{4+}$ = 1107.6; $[M+5H]^{5+}$ = 886.3; $[M+6H]^{6+}$ = 738.8; observed: $[M+3H]^{3+}$ = 1476.6; $[M+4H]^{4+}$ = 1107.7; $[M+5H]^{5+}$ = 886.3.

6.4.13 Synthesis of L17E$_{K1+K2}^{Succ}$-Cys 13

H-IWLTALK(Succ)FLGK(Succ)HAAKHEAKQQLSKL-C-*NH*$_2$

$C_{145}H_{233}N_{39}O_{38}S$

M_w: 3162.7 g/mol

L17E$_{K1+2}^{Succ}$-Cys peptide **13** was modified with a cysteine residue on the *C*-terminus to introduce a site-specific conjugation site. 0.29 g (0.1 mmol, 1 eq.) Amphispheres 40 RAM resin of loading 0.345 mmol/g was transferred into the reaction vessel of the *Liberty Blue*® as described in section 6.3.4 and completely synthesized with microwave assistance. Fmoc-Lys(Dde)-OH was used for the lysines to be modified with a succinyl protecting group. Afterwards the *N*-terminus was Boc-protected by treatment of the resin with 184 μL Boc anhydride (0.8 mmol, 8 eq.) and 279 μL DIPEA (1.6 mmol, 16 eq.) in DMF for 1 h. The Dde protecting group was removed by treating the resin 4x in 3 min cycles with 2 % hydrazine in DMF with a 1x DMF wash in between cycles. After the last cycle, the resin was washed 6x with DMF. The succinyl protecting group was introduced by treating the resin with 174 mg mono-tert-butyl succinate (1 mmol, 5 eq. per Lys), 376 mg HATU (0.99 mmol, 4.95 eq. per Lys) and 348 μL DIPEA (2 mmol, 10 eq. per Lys) in DMF for 30 min. The peptide was cleaved from the resin as described in section 6.3.7 and purified by semi-preparative RP-HPLC with yield 46.2 mg (14.6 μmol, 15 %).

RP-HPLC 0to100% Eluent B: t_R = 15.315 min.

ESI-MS calculated for $C_{145}H_{233}N_{39}O_{38}S$: $[M+H]^+$ = 3163.7; $[M+2H]^{2+}$ = 1582.4; $[M+3H]^{3+}$ = 1055.3; $[M+4H]^{4+}$ = 791.7; $[M+5H]^{5+}$ = 633.6; $[M+6H]^{6+}$ = 528.1; observed: $[M+3H]^{3+}$ = 1055.3; $[M+4H]^{4+}$ = 791.7; $[M+5H]^{5+}$ = 633.6; $[M+6H]^{6+}$ = 528.2.

6.4.14 Synthesis of L17E5K(Ac)-Cys 14

H-IWLTALK(Succ)FLGK(Succ)HAAK(Succ)HEAK(Succ)QQLSK(Succ)L-C-*NH*$_2$

$C_{157}H_{245}N_{39}O_{47}S$

M_w: 3462.9 g/mol

L17E5K(Succ)-Cys peptide **14** was synthesized analogously to the L17E$_{K1+2}^{Succ}$-Cys peptide **13** on a 0.1 mmol scale. For the five succinyl protecting groups, the resin was treated with 435 mg

mono-tert-butyl succinate (2.5 mmol, 5 eq. per Lys), 941 mg HATU (2.48 mmol, 4.95 eq. per Lys) and 871 μL DIPEA (5 mmol, 10 eq. per Lys) in DMF for 30 min. The peptide was cleaved from the resin as described in section 6.3.7 and purified by semi-preparative RP-HPLC with yield 20.2 mg (5.83 μmol, 6 %).

RP-HPLC 0to100% Eluent B: t_R = 16.876 min.
ESI-MS calculated for $C_{157}H_{245}N_{39}O_{47}S$: $[M+H]^+$ = 3463.9; $[M+2H]^{2+}$ = 1732.5; $[M+3H]^{3+}$ = 1155.3; $[M+4H]^{4+}$ = 866.7; $[M+5H]^{5+}$ = 693.6; observed: $[M+3H]^{3+}$ = 1155.4; $[M+4H]^{4+}$ = 866.8.

6.4.15 Synthesis of L17E$_{K1+K2}^{Succ}$-TAMRA 15

H-IWLTALK(Succ)FLGK(Succ)HAAKHEAKQQLSKL-C(TAMRA)-*NH$_2$*

$C_{176}H_{261}N_{43}O_{44}S$

M_w: 3715.3 g/mol

3.2 mg L17E$_{K1+2}^{Succ}$-Cys peptide **13** (1.01 μmol, 1 eq.) and 2.24 mg maleimide-TAMRA (4.05 μmol, 4 eq.) were gently agitated overnight in 40 % DMSO and 60 % NH_4HCO_3 buffer (pH 7.2) at ambient temperature. The product was purified by manual collection of the respective fraction over a *Superdex Peptide 10/300 GL* column and lyophilized with yield 2.2 mg (0.59 μmol, 59 %).

RP-HPLC 30to100% Eluent B: t_R = 9-14 min.
ESI-MS calculated for $C_{176}H_{261}N_{43}O_{44}S$: $[M+H]^+$ = 3716.3; $[M+2H]^{2+}$ = 1858.6; $[M+3H]^{3+}$ = 1239.4; $[M+4H]^{4+}$ = 929.8; $[M+5H]^{5+}$ = 744.1; observed: $[M+5H]^{5+}$ = 744.9 (broad HPLC peak, inconclusive MS).

6.4.16 Synthesis of L17E5K(Succ)-TAMRA 16

H-IWLTALK(Succ)FLGK(Succ)HAAK(Succ)HEAK(Succ)QQLSK(Succ)L-C(TAMRA)-*NH$_2$*

$C_{190}H_{279}N_{43}O_{53}S$

M_w: 4045.6 g/mol

L17E5K(Succ)-TAMRA **16** was synthesized analogously to L17E$_{K1+K2}^{Succ}$-TAMRA **15**. 5 mg L17E5K(Succ)-Cys **14** (1.44 μmol, 1 eq.) and 3.19 mg maleimide TAMRA (5.78 μmol, 4 eq.) were gently agitated overnight in 60 % DMSO and 40 % NH_4HCO_3 buffer (pH 7.2) at ambient temperature. The product was purified by manual collection of the respective fraction over a *Superdex Peptide 10/300 GL* column and lyophilized with yield 3.8 mg (0.94 μmol, 65 %).

RP-HPLC 30to100% Eluent B: t_R = 11-19 min.

ESI-MS calculated for $C_{190}H_{279}N_{43}O_{53}S$: $[M+H]^+ = 4046.6$; $[M+2H]^{2+} = 2023.8$; $[M+3H]^{3+} = 1349.5$; $[M+4H]^{4+} = 1012.4$; observed: $[M+2H]^{2+} = 1759.9$; $[M+3H]^{3+} = 1173.9$ (broad HPLC peak, inconclusive MS).

6.4.17 Synthesis of L17E$_{K1+K2}^{Succ}$-cry 17

H-IWLTALK(Succ)FLGK(Succ)HAAKHEAKQQLSKL-C(cryptophycin)-*NH*$_2$

$C_{208}H_{314}ClN_{49}O_{53}S$

M_w: 4416.5 g/mol

2.2 mg L17E$_{K1+2}^{Succ}$-Cys peptide **13** (0.63 μmol, 1 eq.) and 56.9 μL Mal-Val-Cit-PAB-cryptophycin of stock concentration 10 mM (0.57 μmol, 0.9 eq.) were gently agitated overnight in 50 % DMSO and 50 % NH_4HCO_3 buffer (pH 7.2) at ambient temperature. The product was not purified. The sample still contained free cryptophycin.

RP-HPLC 30to100% Eluent B: $t_R = 14.868$ min.
ESI-MS calculated for $C_{208}H_{314}ClN_{49}O_{53}S$: $[M+H]^+ = 4417.5$; $[M+2H]^{2+} = 2209.3$; $[M+3H]^{3+} = 1473.2$; $[M+4H]^{4+} = 1105.2$; $[M+5H]^{5+} = 884.3$; $[M+6H]^{6+} = 737.1$; observed: $[M+3H]^{3+} = 1473.3$; $[M+4H]^{4+} = 1105.2$; $[M+5H]^{5+} = 884.4$; $[M+6H]^{6+} = 737.1$.

6.4.18 Synthesis of L17EK(Succ)-cry 18

H-IWLTALK(Succ)FLGK(Succ)HAAK(Succ)HEAK(Succ)QQLSK(Succ)L-C(cryptophycin)-*NH*$_2$

$C_{220}H_{326}ClN_{49}O_{62}S$

M_w: 4716.8 g/mol

2 mg L17E5K(Succ)-Cys peptide **14** (0.64 μmol, 1 eq.) and 57.2 μL Mal-Val-Cit-PAB-cryptophycin of stock concentration 10 mM (0.57 μmol, 0.9 eq.) were gently agitated overnight in 50 % DMSO and 50 % NH_4HCO_3 buffer (pH 7.2) at ambient temperature. The product was not purified.

RP-HPLC 30to100% Eluent B: $t_R = 14.306$ min.
ESI-MS calculated for $C_{220}H_{326}ClN_{49}O_{62}S$: $[M+H]^+ = 4717.8$; $[M+2H]^{2+} = 2359.4$; $[M+3H]^{3+} = 1573.3$; $[M+4H]^{4+} = 1180.2$; $[M+5H]^{5+} = 944.4$; $[M+6H]^{6+} = 787.1$; observed: $[M+3H]^{3+} = 1573.3$; $[M+4H]^{4+} = 1180.3$.

6.4.19 Cellular uptake assay of L17E-TAMRA 1 and Alloc-L17E peptides 2 - 5

3 x 10^3 HeLa EM2-11ht cells/ well were seeded in DMEM (w/ 10 % FBS and 1 % PS) in 18-well microscopy slides at 37 °C and 5 % CO_2 overnight in a humidified incubator. 10x peptide stock solutions were prepared and incubated with the cells such that the final peptide concentration was 4 μM. After incubation for 1 h at 37 °C and 5 % CO_2 the cells were washed

by exchanging the medium three times by adding and removing 60 μL DMEM (w/ 10 % FBS and 1 % PS), so that the cells remained covered with solution at all times. The cells were incubated for another 3 h at 37 °C, washed once with PBS by aspiration of the medium and fixed with 4 % paraformaldehyde (PFA) at room temperature. The same procedure was performed at 4 °C on ice.

6.4.20 Conditional cellular uptake assay of acetylated L17E peptide 6

In the assay with the SirT2 enzyme, 3 x 10^3 HeLa EM2-11ht cells/ well were seeded in DMEM (w/ 10 % FBS and 1 % PS) in 18-well microscopy slides at 37 °C and 5 % CO_2 overnight in a humidified incubator. The next day, the microscopy slides were acclimatized to 30 °C by placing it in a 30 °C incubator for 1 h. 10x peptide stock solutions were prepared such that the final peptide concentration was 5 μM. For deacetylation, the cells were additionally incubated with 1 μM deacetylase (0.2 eq.) and 400 μM NAD (40 eq.). Samples were incubated on the cells for 1 h at 30 °C, washed once and then directly fixed with 4 % PFA. The cells were observed by CLSM.

In the assay with antibody-SirT2 conjugates, 8 x 10^3 HeLa EM2-11ht cells/ well were seeded in DMEM (w/ 10 % FBS and 1 % PS) in 18-well microscopy slides at 37 °C and 5 % CO_2 overnight in a humidified incubator. The next day, the microscopy slides were acclimatized to 30 °C by placing it in a 30 °C incubator for 1 h. The cells were incubated with 50 nM antibody-SirT2 or PBS (as control) for 15 min. Afterwards the cells were washed by exchanging the medium three times, keeping the cells covered in medium at all times. The cells were treated with 5 μM peptide samples, or where relevant with 50 nM SirT2 and 400 nM NAD for 2 h at 30 °C. The cells were washed again by medium exchange and incubated another 3 h at 37 °C. Finally, the cells were washed with PBS, stained with Hoechst 33342 and fixed with 4 % PFA. The cells were observed by CLSM.

6.4.21 Quantification of cellular uptake of TAMRA

4 x 10^4 HeLa EM2-11ht cells/ well were seeded in 100 μL DMEM (w/ 10 % FBS and 1 % PS) in a 96-well flat-bottom plate at 37 °C and 5 % CO_2 overnight in a humidified incubator. The next day, the plate was placed in a 30 °C incubator to acclimatize the cells to the reduced temperature. After washing the cells once, the cells were incubated with 5x sample stock solutions to final concentrations of 5 μM peptide (**1** or **6**), 400 μM NAD (80 eq.) and 4 μM SirT2 (0.08 eq.) where applicable, for 1 h at 30 °C. Afterwards the supernatant was removed and the cells washed once with DMEM (w/ 10 % FBS and 1 % PS). The plate was incubated for 1 h at

37 °C and then washed once with PBS. The cells were trypsinized, diluted in 200 μL PBS and measured in the *CytoFLEX S* using the PE channel that registered TAMRA fluorescence. Samples were measured in duplicates.

6.4.22 Analytics of the deacetylation of acetylated L17E peptide 8

50 μM L17E5K(Ac)-Pra **8** (1 eq.), 4 μM SirT2 (0.08 eq.) and 400 μM NAD (8 eq.) in PBS were incubated for 1 h at 30 °C. The enzyme was precipitated by denaturation at 96 °C for 10 min and the supernatant was taken for RP-HPLC and LC-ESI-MS analysis.

6.4.23 Anti-B7H3 binding assay on HeLa cells

The on-cell binding affinity of anti-B7H3 to HeLa cells was performed by Carolin Dombrowsky. 2.5 x 10^5 viable HeLa cells/ well were seeded in a 96-well round-bottom plate. The cells were washed by centrifugation of the plate at 800 x g for 4 min at 4 °C and subsequently 50 μL 0.1 % BSA-PBS were added. Antibody dilutions ranging from 0.98-1000 nM were incubated with the cells for 45 min. Afterwards, the cells were washed three times with 50 μL 0.1 % BSA-PBS. For detection of the antibody, the secondary antibody Goat anti-Human IgG Fc, eBioscience™ PE antibody (*Invitrogen*, Waltham, MA, USA) in 1:75 dilution in 0.1 % BSA-PBS (25 μL/ well) was incubated for 30 min on the cells at 4 °C in the dark. The cells were washed three times and resuspended in 200 μL 0.1 % BSA-PBS before measurement by a *CytoFLEX S* System.

6.4.24 Generation of antibody-enzyme conjugates by sortase A coupling

Conjugation of anti-B7H3 and Trastuzumab to SirT2 or SirT5 was performed by Carolin Dombrowsky. 2 μM antibody, 4 μM (G4S)-SirT2 or (G4S)-SirT5 and 0.4 μM SrTA Mut5-E in 1x SrtA buffer (0.05 M Tris, 0.15 M NaCl, 0.005 M $CaCl_2$, pH 7.5), supplemented with 2.5 mM β-cyclodextrin to prevent protein aggregation, were incubated 16-24 h at room temperature. The reaction mixture was used without further purification.

6.4.25 Cell proliferation assays of L17E-cry 11 and L17E5K(Ac)-cry 12

In a 96-well flat bottom plate, 6 x 10^3 SKBR3, triple negative MDA-MB468 or HeLa cells/ well were seeded in 100 μL DMEM (w/ 10 % FBS and 1 % PS) and incubated overnight at 37 °C and 5 % CO_2 in a humidified incubator. The plate was placed in an incubator for 1 h at 30 °C to acclimatize the cells to the reduced temperature. The cells were incubated with 50 nM Trastuzumab-SirT2 (10x stock concentration used) or PBS (for all other samples without antibody-enzyme conjugate) for 15 min at 30 °C in DMEM. The medium was aspirated and washed once with PBS. Fresh DMEM was added and the cells were incubated for 2 h at 30 °C with a serial dilution of the peptide samples and 80 eq. NAD for SirT2-containing samples in

triplicates. After washing the cells once with PBS, fresh DMEM was added and the cells were incubated for 72 h at 37 °C at 5 % CO_2 in a humidified incubator. The number of viable cells was measured using CellTiter96®Aqueous One Solution Cell Proliferation Assay (*Promega*) by absorbance at 490 nm, which was recorded using the CLARIOstar® Plus (BMG Labtech). For standard cell proliferation assays, all steps were performed at 37 °C and the peptide samples were incubated continuously on the cells for 72 h.

6.4.26 RP-HPLC and LC-MS evaluation of deacetylation of succinylated L17E peptide 14

50 μM L17E5K(Succ)-Cys **14** (1 eq.), 4 μM SirT5 (0.08 eq.) and 400 μM NAD (8 eq.) in PBS were incubated for 1 h at 37 °C. The enzyme was precipitated by denaturation at 96 °C for 10 min and the supernatant was taken for RP-HPLC and LC-ESI-MS analysis.

6.4.27 Conditional cellular uptake assay of succinylated L17E peptides 15 and 16

8 x 10^3 HeLa EM2-11ht cells/ well were seeded in DMEM (w/ 10 % FBS and 1 % PS) in 18-well microscopy slides and incubated overnight at 37 °C and 5 % CO_2 in a humidified incubator. The next day, the cells were incubated with 50 nM αB7H3-SirT5, trastuzumab-SirT5 or PBS (as control) for 15 min. Afterwards the cells were washed by exchanging the medium three times, keeping the cells covered in the medium at all times. The cells were treated with 5 μM peptide samples, or where relevant with 50 nM SirT2 and 400 nM NAD for 2 h at 37 °C. The cells were washed again by medium exchange and incubated another 3 h at 37 °C. Finally, the cells were washed with PBS, stained with Hoechst 33342 and fixed with 4 % PFA. The cells were observed by CLSM.

6.4.28 Cell proliferation assays of L17E-cry 11 succinylated L17E-cry peptides 17 and 18

In a 96-well flat bottom plate, 6 x 10^3 SKBR3 or HeLa cells/ well were seeded in 100 μL DMEM (w/ 10 % FBS and 1 % PS) and incubated overnight at 37 °C and 5 % CO_2 in a humidified incubator. The cells were incubated with 50 nM trastuzumab-SirT5, αB7H3-SirT5 (10x stock concentration used) or PBS (for all other samples without antibody-enzyme conjugate) for 15 min at 37 °C in medium. The medium was aspirated and washed once with PBS. Fresh DMEM was added and the cells were incubated for 72 h at 37 °C and 5 % CO_2 in a humidified incubator with a serial dilution of the peptide samples and 80 eq. NAD for SirT2-containing samples in duplicates. The number of viable cells was measured using CellTiter96®Aqueous One Solution Cell Proliferation Assay (*Promega*) by absorbance at 490 nm, which was recorded using the CLARIOstar® Plus (BMG Labtech).

6.5 Dextran modification

6.5.1 Synthesis of *N*-Boc-cadaverine-dextran 19

Multiple batches of *N*-Boc-cadaverine-dextran were synthesized as described in literature.[133] For batch 1, 2 g Dextran (0.2 mmol, 1 eq.), 0.20 g $NaBH_3CN$ (3.18 mmol, 15.9 eq.) and 1.05 mL *N*-Boc-cadaverine were dissolved in 5 mL 0.05 M borate buffer pH 8.2 and stirred for 72 h in darkness at 30 °C. The product was precipitated in cold MeOH, washed three times with MeOH and dried under air flow. Afterwards, the white product was dissolved in 10 mL water and purified using PD10 desalting columns according to the instructions of the supplier. After lyophilization a white powder was obtained. Yield **19** (batch 1): 1.094 g (107 μmol, 54 %)

Batch 2 was synthesized as described in batch 1 using 1 g Dextran (0.1 mmol, 1 eq.), 0.1 g $NaBH_3CN$ (1.59 mmol, 15.9 eq.) and 521 μL *N*-Boc-cadaverine (2.5 mmol, 25 eq.) in 2.5 mL 0.05 M borate buffer. Yield **19** (batch 2): 689 mg (67.6 μmol, 68 %)

Batch 1: ^{1}**H-NMR** (300 MHz, D_2O) δ = 5.70 – 4.89 (m, 62H, C(1)**H**), 4.35 – 3.38 (m, C(2-6)**H** glucose units)), 3.22 – 2.91 (m, 4H, -C**H**$_2$(CH_2)$_3$-C**H**$_2$-NHBoc), 1.96 –1.29 (overlapped m, 24H, -NH-CH_2(C**H**$_2$)$_3$$CH_2$-NH-CO-O-C-C(C**H**$_3$)$_3$) ppm.

Batch 2: ^{1}**H-NMR** (300 MHz, D_2O) δ = 6.04 – 4.87 (m, 62H, C(1)**H**), 4.21 – 3.21 (m, C(2-6)**H** glucose units)), 3.03 – 2.94 (m, 4H, -C**H**$_2$(CH_2)$_3$-C**H**$_2$-NHBoc), 1.81 –1.15 (overlapped m, 19H, -NH-CH_2(C**H**$_2$)$_3$$CH_2$-NH-CO-O-C-C(C**H**$_3$)$_3$) ppm.

6.5.2 Synthesis of *N*-Boc-cadaverine-dextran-CE 20

Multiple batches of *N*-Boc-cadaverine-dextran-CE with different numbers of carboxyethyl groups per dextran molecule were synthesized as described in literature.[133]

For batch 1, 197 mg *N*-Boc-cadaverine-dextran **19** (batch 1) (19.3 μmol, 1 eq.) and 16.5 mg acrylamide (229 μmol, 11.8 eq.) were dissolved in 5.5 mL 1 M NaOH (aq.) and stirred for 24 h at 30°C. Afterwards the temperature was raised to 50 °C and stirred at this temperature for another 24 h. The reaction mixture was neutralized with 0.1 M or 1 M HCl under vigorous stirring and then purified using PD10 desalting columns according to the instructions of the manufacturer. The product was lyophilized and a white powder was obtained when dry. The number of carboxyethyl groups per dextran were determined by ^{1}H-NMR. Yield **20** (batch 1): 139 mg (13.2 μmol, 68 %); CE-groups/dextran: 5.6.

Batch 2 was synthesized as described in batch 1 using 550 mg *N*-Boc-cadaverine-dextran **19** (batch 1) (0.054 mmol, 1 eq.) and 52.6 mg acrylamide (0.74 mmol, 13.7 eq.) in 5.5 mL 1 M NaOH (aq.). Yield **20** (batch 2): 139 mg (13.2 μmol, 68 %); CE-groups/dextran: 5.

Batch 3 was synthesized as described in batch 1 using 689 mg *N*-Boc-cadaverine-dextran **19** (batch 2) (0.067 mmol, 1 eq.) and 61.3 mg acrylamide (0.86 mmol, 12.8 eq.) Yield **20** (batch 3): 501 mg (47.5 μmol, 72 %); CE-groups/dextran: 3.7.

Batch 4 was synthesized as described batch 1 using 188 mg *N*-Boc-cadaverine-dextran **19** (batch 1) (0.018 mmol, 1 eq.), 20.4 mg acrylamide (0.29 mmol, 15.6 eq.) in 2 mL 1 M NaOH. Yield **20** (batch 4): 149 mg (14.1 μmol, 77 %); CE-groups/dextran: 6.3.

Batch 1: **^{1}H-NMR** (300 MHz, D_2O) δ = 5.68 – 4.97 (m, 62H, C(1)**H**), 4.33 – 3.26 (m, C(2-6)**H** (glucose units)), 3.22 – 3.09 (m, 2H, -C**H**$_2$(CH$_2$)$_3$-C**H**$_2$-NHBoc), 2.64 – 2.47 (m, 10H, CH$_2$C**H**$_2$COOH), 1.98 – 1.35 (overlapped m, 10H, -NH-CH$_2$(C**H**$_2$)$_3$CH$_2$-NH-CO-O-C-C(C**H**$_3$)$_3$) ppm.

Batch 2: **^{1}H-NMR** (300 MHz, D_2O) δ = 5.41 – 4.92 (m, 62H, C(1)**H**), 4.35 – 3.30 (m, C(2-6)**H** (glucose units)), 3.13 – 3.04 (m, 3H, -C**H**$_2$(CH$_2$)$_3$-C**H**$_2$-NHBoc), 2.58 – 2.41 (m, 11H, CH$_2$C**H**$_2$COOH), 1.85 – 1.25 (overlapped m, 10H, -NH-CH$_2$(C**H**$_2$)$_3$CH$_2$-NH-CO-O-C-C(C**H**$_3$)$_3$) ppm.

Batch 3: **^{1}H-NMR** (300 MHz, D_2O) δ = 6.67 – 4.85 (m, 62H, C(1)**H**), 4.35 – 3.30 (m, C(2-6)**H** (glucose units)), 3.04 – 2.59 (m, 2H, -C**H**$_2$(CH$_2$)$_3$-C**H**$_2$-NHBoc), 2.50 – 2.21 (m, 7H, CH$_2$C**H**$_2$COOH), 1.84 – 1.11 (overlapped m, 10H, -NH-CH$_2$(C**H**$_2$)$_3$CH$_2$-NH-CO-O-C-C(C**H**$_3$)$_3$) ppm.

Batch 4: **^{1}H-NMR** (300 MHz, D_2O) δ = 7.42 – 4.82 (m, 62H, C(1)**H**), 4.23 – 3.31 (m, C(2-6)**H** (glucose units)), 3.06 – 2.93 (m, 1H, -C**H**$_2$(CH$_2$)$_3$-C**H**$_2$-NHBoc), 2.50 – 2.32 (m, 13H, CH$_2$C**H**$_2$COOH), 1.94 – 1.09 (overlapped m, 10H, -NH-CH$_2$(C**H**$_2$)$_3$CH$_2$-NH-CO-O-C-C(C**H**$_3$)$_3$) ppm.

6.5.3 Synthesis of azide linker N-(5-aminopentyl)-2-azidoacetamide 21 for dextran

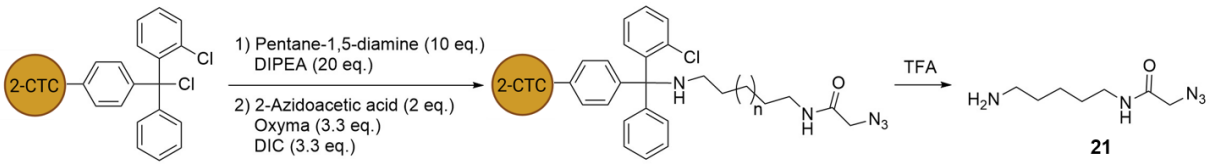

Figure 57| Reaction scheme for the synthesis of the azide linker N-(5-Aminopentyl)-2-azidoacetamide **21**.

N-(5-Aminopentyl)-2-azidoacetamide was synthesized as shown in Figure 57 on a 2 mmol scale using 2-chlorotrityl chloride (2-CTC) resin with a loading of 1.60 mmol/g from *Iris Biotech*. The 1.25 g resin (2 mmol, 1 eq.) was swollen in a reaction vessel with a frit for 20 min in DCM and then washed 3x with DMF. 2.34 mL pentane-1,5-diamine (20 mmol, 10 eq.) were dissolved in 5 mL DMF and afterwards 6.97 mL DIPEA (40 mmol, 20 eq.) was added. The mixture was shaken with the resin for 2 h at room temperature and then washed 6x with DMF. 299 μL 2-azidoacetic acid (4 mmol, 2 eq.), 938 mg Oxyma (6.6 mmol, 3.3 eq.) and 1.021 mL DIC (6.6 mmol, 3.3 eq.) were dissolved in 10 mL DMF and agitated with the resin for 16 h. The resin was washed 6x with DMF and DCM and dried under air flow. The linker was cleaved by treating the resin with TFA for 3 h and isolated by precipitation in cold diethyl ether and subsequent evaporation of the ether. The residue was dissolved in water and purified by semi-preparative RP-HPLC. Multiple batches were performed with yield: 219 mg (1.18 mmol, 59 %), 284 mg (1.54 mmol, 77 %), 268 mg (1.45 mmol, 72 %), 150 mg (40 %).

ESI-MS calculated for $C_7H_{15}N_5O$: $[M+H]^+ = 185.2$; observed $[M+H]^+ = 186.5$.
RP-HPLC 0to40% Eluent B: $t_R = 7.175$ min.

6.5.4 Synthesis of *N*-Boc-cadaverine-dextran-N_3 22

139 mg *N*-Boc-cadaverine-dextran-CE **20** (batch 1) (13.1 μmol, 1 .) and 133 mg *N*-ethoxycarbonyl-2-ethoxy-1,2-dihydroquinoline (EEDQ) (0.54 mmol, 7.3 eq. per CE group) were dissolved in 5 mL 40 % MeCN (aq.) and stirred for 30 min at 30 °C. 94 mg *N*-(5-Aminopentyl)-2-azidoacetamide (0.47 mmol, 6.4 eq. per CE) were added and the mixture was stirred for 4 h at 30 °C. The product was diluted in water, lyophilized, then re-dissolved in water and purified over PD10 desalting columns according to the instructions of the manufacturer. Yield *N*-Boc-cadaverine-dextran-N_3(5.6) **22**: 125 mg (10.8 μmol, 82 %); by ^{1}H-NMR analysis N_3-groups/dextran: 4.1 (CE-groups: 5.6)

Batch 2 was synthesized as described in batch 1 with 265 mg *N*-Boc-cadaverine-dextran-CE **20** (batch 2) (25.1 μmol, 1 eq.) and 263 mg EEDQ (0.71 mmol, 8.5 eq. per CE group) and 185.9 mg *N*-(5-Aminopentyl)-2-azidoacetamide (1.00 mmol, 8 eq. per CE). Yield *N*-Boc-cadaverine-dextran-N_3(5) **22**: 277 mg (24.3 μmol, 97 %); by ^{1}H-NMR analysis N_3-groups/dextran: 5.2 (CE-groups: 5).

Batch 3 was synthesized as described in batch 1 with 501 mg *N*-Boc-cadaverine-dextran-CE **20** (batch 3) (48.0 μmol, 1 eq.) and 483 mg EEDQ (1.95 mmol, 8.5 eq. per CE group) and 340 mg *N*-(5-Aminopentyl)-2-azidoacetamide (1.84 mmol, 8 eq. per CE) in 5 mL 40 % MeCN (aq.).

Yield *N*-Boc-cadaverine-dextran-N_3(3.7) **22**: 454 mg (39.9 μmol, 83 %); by ^{1}H-NMR analysis N_3-groups/dextran: 2.8 (CE-groups 3.7).

Batch 4 was synthesized as described in batch 1 with 149 mg *N*-Boc-cadaverine-dextran-CE **20** (batch 4) (14.0 μmol, 1 eq.) and 185 mg EEDQ (0.75 mmol, 8.5 eq. per CE group) and 130 mg *N*-(5-Aminopentyl)-2-azidoacetamide (0.71 mmol, 8 eq. per CE) in 3 mL 40 % MeCN (aq.). Yield *N*-Boc-cadaverine-dextran-N_3(6.3) **22**: 150 mg (12.8 μmol, 92 %); by ^{1}H-NMR analysis N_3-groups/dextran: 4.9 (CE-groups 6.3).

Batch 1: **^{1}H-NMR** (300 MHz, D_2O) δ = 5.91 – 4.94 (m, 62H, C(1)**H**), 4.41 – 3.39 (m, C(2-6)**H** (glucose units)), 3.37 – 3.19 (m, 25H, -C**H**$_2$(CH_2)$_3$-C**H**$_2$-NH), 2.53 – 2.38 (m, 10H, CH_2C**H**$_2$COOH), 1.54 – 1.40 (overlapped m, 26H, -NH-CH_2-C**H**$_2$-CH_2-C**H**$_2$-CH_2NHCO, 1.35 (s, 8H, O-C(C**H**$_3$)$_3$, 1.32 – 1.16 (overlapped m, 14H, -NH-(CH_2)$_2$-C**H**$_2$-(CH_2)$_2$-NH-) ppm.

Batch 2: **^{1}H-NMR** (300 MHz, D_2O) δ = 5.65 – 4.94 (m, 62H, C(1)**H**), 4.36 – 3.36 (m, C(2-6)**H** (glucose units)), 3.31 – 3.16 (m, 17H, -C**H**$_2$(CH_2)$_3$-C**H**$_2$-NH), 2.62 – 2.46 (m, 9H, CH_2C**H**$_2$COOH), 1.92 – 1.48 (overlapped m, 20H, -NH-CH_2-C**H**$_2$-CH_2-C**H**$_2$-CH_2NHCO, 1.35 (s, 8H, O-C(C**H**$_3$)$_3$, 1.32 – 1.16 (overlapped m, 14H, -NH-(CH_2)$_2$-C**H**$_2$-(CH_2)$_2$-NH-) ppm.

Batch 3: **^{1}H-NMR** (300 MHz, D_2O) δ = 6.21 – 4.82 (m, 62H, C(1)**H**), 4.11 – 3.24 (m, C(2-6)**H** (glucose units)), 3.20 – 3.06 (m, 16H, -C**H**$_2$(CH_2)$_3$-C**H**$_2$-NH), 2.53 – 2.38 (m, 8H, CH_2C**H**$_2$COOH), 1.54 – 1.40 (overlapped m, 14H, -NH-CH_2-C**H**$_2$-CH_2-C**H**$_2$-CH_2NHCO, 1.45 (s, 6H, O-C(C**H**$_3$)$_3$, 1.40 – 1.23 (overlapped m, 13H, -NH-(CH_2)$_2$-C**H**$_2$-(CH_2)$_2$-NH-) ppm.

Batch 4: **^{1}H-NMR** (300 MHz, D_2O) δ = 6.03 – 4.95 (m, 62H, C(1)**H**), 4.11 – 3.24 (m, C(2-6)**H** (glucose units)), 3.34 – 2.98 (m, 24H, -C**H**$_2$(CH_2)$_3$-C**H**$_2$-NH), 2.79 – 2.48 (m, 10H, CH_2C**H**$_2$COOH), 1.92 – 1.48 (overlapped m, 24H, -NH-CH_2-C**H**$_2$-CH_2-C**H**$_2$-CH_2NHCO, 1.44 (s, 6H, O-C(C**H**$_3$)$_3$, 1.39 – 1.15 (overlapped m, 13H, -NH-(CH_2)$_2$-C**H**$_2$-(CH_2)$_2$-NH-) ppm.

6.5.5 Synthesis of cadaverine-dextran-N_3 23

Cleavage of the Boc-groups on dextran was undertaken with 1-3 mL neat TFA by stirring for 30 min at ambient temperature. The TFA was evaporated under air flow, and the residue was dissolved in water, neutralized with NaOH and purified over PD10 desalting columns. A white powder was obtained after lyophilization.

Yield cadaverine-dextran-N_3(5.6) **23** (batch 1): 108 mg (9.38 μmol, 87 %)
Yield cadaverine-dextran-N_3(5) **23** (batch 2): 255 mg (22.6 μmol, 86 %)

Yield cadaverine-dextran-N_3(3.7) **23** (batch 3): 407 mg (37.1 μmol, 87 %)

Yield cadaverine-dextran-N_3(6.3) **23** (batch 4): 134 mg (11.5 μmol, 82 %)

23 (batch 1) **^{1}H-NMR** (300 MHz, D_2O) δ = 5.85 – 4.92 (m, 62H, C(1)**H**), 4.15 – 3.35 (m, C(2-6)**H** (glucose units)), 3.30 – 3.15 (m, 15H, -C**H**$_2$(CH_2)$_3$-C**H**$_2$-NH), 2.66 – 2.45 (m, 8H, CH_2C**H**$_2$CO-), 1.96 – 1.53 (overlapped m, 24H, -NH-CH_2-C**H**$_2$-CH_2-C**H**$_2$-CH_2NHCO, 1.47 – 1.21 (overlapped m, 12H, -NH-(CH_2)$_2$-C**H**$_2$-(CH_2)$_2$-NH-) ppm.

23 (batch 2) **^{1}H-NMR** (300 MHz, D_2O) δ = 5.70 – 4.93 (m, 62H, C(1)**H**), 4.37 – 3.39 (m, C(2-6)**H** (glucose units)), 3.35 – 3.20 (m, 21H, -C**H**$_2$(CH_2)$_3$-C**H**$_2$-NH), 3.15 – 3.00 (m, 2H, -C**H**$_2$(CH_2)$_3$-C**H**$_2$-NH_2), 2.71 – 2.53 (m, 10H, CH_2C**H**$_2$CO-), 1.90 – 1.46 (overlapped m, 24H, -NH-CH_2-C**H**$_2$-CH_2-C**H**$_2$-CH_2NHCO, 1.44 – 1.20 (overlapped m, 12H, -NH-(CH_2)$_2$-C**H**$_2$-(CH_2)$_2$-NH-) ppm.

23 (batch 3) **^{1}H-NMR** (300 MHz, D_2O) δ = 6.23 – 4.91 (m, 62H, C(1)**H**), 4.37 – 3.37 (m, C(2-6)**H** (glucose units)), 3.29 – 3.14 (m, 21H, -C**H**$_2$(CH_2)$_3$-C**H**$_2$-NH), 3.05 – 2.96 (m, 2H, -C**H**$_2$(CH_2)$_3$-C**H**$_2$-NH_2), 2.60 – 2.48 (m, 7H, CH_2C**H**$_2$CO-), 1.97 – 1.43 (overlapped m, 20H, -NH-CH_2-C**H**$_2$-CH_2-C**H**$_2$-CH_2NHCO, 1.40 – 1.16 (overlapped m, 10H, -NH-(CH_2)$_2$-C**H**$_2$-(CH_2)$_2$-NH-) ppm.

23 (batch 4) **^{1}H-NMR** (300 MHz, D_2O) δ = 6.06 – 4.91 (m, 62H, C(1)**H**), 4.36 – 3.38 (m, C(2-6)**H** (glucose units)), 3.32 – 3.13 (m, 21H, -C**H**$_2$(CH_2)$_3$-C**H**$_2$-NH), 3.07 – 2.98 (m, 2H, -C**H**$_2$(CH_2)$_3$-C**H**$_2$-NH_2), 2.72 – 2.45 (m, 12H, CH_2C**H**$_2$COOH-), 1.90 – 1.43 (overlapped m, 25H, -NH-CH_2-C**H**$_2$-CH_2-C**H**$_2$-CH_2NHCO, 1.38 – 1.16 (overlapped m, 14H, -NH-(CH_2)$_2$-C**H**$_2$-(CH_2)$_2$-NH-) ppm.

6.6 Conditional intracellular delivery of dextran-ACPP conjugates

6.6.1 Synthesis of TAMRA-dextran-N_3 24

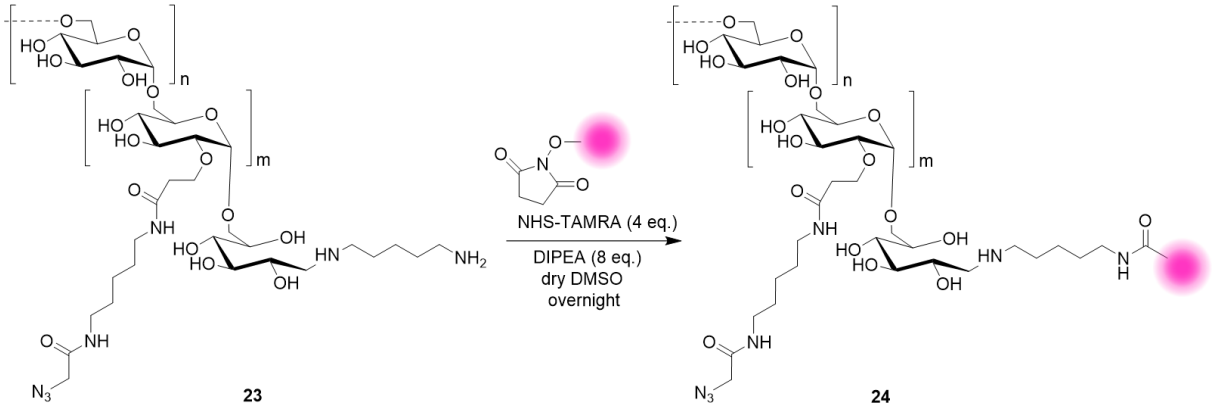

Figure 58| Reaction scheme NHS-TAMRA coupling to cadaverine-dextran-N_3 **23** to yield TAMRA-dextran-N_3 **24**.

108 mg cadaverine-dextran-N_3(5.6) **23** (batch 1) (9.38 μmol, 1 eq.) was dissolved in 3 mL DMSO. 19.8 mg TAMRA-NHS (37.5 μmol, 4 eq.) and 16.3 μL DIPEA (93.7 μmol, 10 eq.) were added and stirred overnight. The product was precipitated in MeOH and washed 3x. After air drying the product was dissolved in water, purified over a PD10 desalting column and lyophilized. A pink powder was obtained of yield TAMRA-dextran-N_3(5.6) **24** (batch 1): 97 mg (8.13 μmol, 87 %).

TAMRA-dextran-N_3(5) **24** (batch 2) was synthesized analogously using 50 mg cadaverine-dextran-N_3(5) **23** (batch 2) (4.34 μmol, 1 eq.), 9.28 mg TAMRA-NHS (17.6 μmol, 4 eq.) and 6.12 μL DIPEA (35.2 μmol, 8 eq.) in 2 mL DMSO. Yield TAMRA-dextran-N_3(5) **24** (batch 2): 41.0 mg (3.48 μmol, 79.1 %).

24 (batch 2) **^{1}H-NMR** (300 MHz, D_2O) δ = 8.17 – 8.03 (s, 1H, from TAMRA -C=C(COOH)-C**H**=C(CONH)-), 7.91 – 7.75 (d, 2H, (from TAMRA -C-CH=C**H**-C(CONH)-), 7.36 – 7.22 (d, 1H, from TAMRA -C-C**H**=CH-C(CONH)-), 7.10 – 6.91 (overlapped m, 2H, from TAMRA $(CH_3)_2$N-C-C**H**=CH-C-; C-CH=C**H**-C-N$(CH_3)_2$), 6.81 – 6.63 (overlapped m, 2H, $(CH_3)_2$N-C-CH=C**H**-C-; C-C**H**=CH-C-N$(CH_3)_2$), 6.57 – 6.38 (s, 2H, from TAMRA $(CH_3)_2$N-C-C**H**=C-O-C=C**H**-C=N$(CH_3)_2$) 6.15 – 4.71 (m, 62H, C(1)**H**), 4.11 – 3.13 (m, C(2-6)**H** (glucose units)), 3.09 – 2.88 (m, 20H, -C**H**$_2$$(CH_2)_3$-C**H**$_2$-NH), 2.44 – 2.19 (m, 10H, CH_2C**H**$_2$CO-), 1.69 – 1.25 (overlapped m, 24H, -NH-CH_2-C**H**$_2$-CH_2-C**H**$_2$-CH_2NHCO, 1.21 – 0.93 (overlapped m, 12H, -NH-$(CH_2)_2$-C**H**$_2$-$(CH_2)_2$-NH-) ppm.

6.6.2 Synthesis of L17E$_{K1}^{Alloc}$-Pra 25

H-IWLTALK(Alloc)FLGKHAAKHEAKQQLSKL-Pra-*NH_2*

$C_{143}H_{229}N_{39}O_{34}$

M_w: 3038.6 g/mol

L17E$_{K1}^{Alloc}$-Pra peptide **25** was synthesized on a 0.25 mmol scale using 0.72 g (0.25 mmol, 1 eq.) Amphispheres 40 RAM resin of loading 0.345 mmol/g. An alkyne was first introduced to generate a selective conjugation site at the *C*-terminus. The procedure of loading the first amino acid as described in section 6.3.1 was followed using 209 mg Fmoc-Pra-OH (0.625 mmol, 2.5 eq.) which was activated with 233 mg HATU (0.613 mmol, 2.45 eq.) and 217 μL DIPEA (1.25 mmol, 5 eq) in 8 mL DMF. The mixture was agitated with the resin for 45 min, then removed and was washed 3x with DMF. A second freshly activated solution of Fmoc-Pra-OH, HATU and DIPEA was added and the mixture shaken for 45 min again for double coupling of the building block. After the resin was washed with DMF, it was transferred to the reaction

vessel of the Liberty Blue® and the sequence up to the alloc-protected lysine synthesized automatically with microwave assistance as described in section 6.3.4. 113 mg Fmoc-Lys(Alloc)-OH (0.25 mmol, 2.5 eq.), 93.1 mg HATU (0.245 mmol, 2.45 eq.) and 87.1 μL DIPEA (0.5 mmol, 5 eq.) were agitated with the resin for 45 min. Manual amino acid coupling was continued using HBTU and DIPEA as described in section 6.3.3. Upon completion of the peptide, the resin was washed 6x with DMF and 6x with DCM, dried under air flow and cleaved from the resin as described in section 6.3.7. The peptide was purified by semi-preparative RP-HPLC with yield 224 mg (0.073 mmol, 29 %).

RP-HPLC 0to80% Eluent B: t_R = 15.973 min.
ESI-MS calculated for $C_{143}H_{229}N_{39}O_{34}$: $[M+H]^+$ = 3039.6; $[M+2H]^{2+}$ = 1520.3; $[M+3H]^{3+}$ = 1013.9; $[M+4H]^{4+}$ = 760.7; $[M+5H]^{5+}$ = 608.7; $[M+6H]^{6+}$ = 507.4; observed: $[M+3H]^{3+}$ = 1014.0; $[M+4H]^{4+}$ = 760.7; $[M+5H]^{5+}$ = 608.8; $[M+6H]^{6+}$ = 507.6.

6.6.3 Synthesis of L17E$_{K2}^{Alloc}$-Pra 26

H-IWLTALKFLGK(Alloc)HAAKHEAKQQLSKL-Pra-*NH*$_2$

$C_{143}H_{229}N_{39}O_{34}$

M_w: 3038.6 g/mol

L17E$_{K2}^{Alloc}$-Pra peptide **25** was synthesized analogously to the L17E$_{K1}^{Alloc}$-Pra peptide **24** with yield 311 mg (0.102 mmol, 41 %).

RP-HPLC 0to80% Eluent B: t_R = 15.899 min.
ESI-MS calculated for $C_{143}H_{229}N_{39}O_{34}$: $[M+H]^+$ = 3039.6; $[M+2H]^{2+}$ = 1520.3; $[M+3H]^{3+}$ = 1013.9; $[M+4H]^{4+}$ = 760.7; $[M+5H]^{5+}$ = 608.7; $[M+6H]^{6+}$ = 507.4; observed: $[M+5H]^{5+}$ = 608.8; $[M+6H]^{6+}$ = 507.6.

6.6.4 Synthesis of TAMRA-dextran-L17E(1xAlloc) conjugates 27/28

7 mg TAMRA-dextran-N_3(5.6) **24** (batch 1, 0.59 μmol, 1 eq.) and 16.1 mg L17E(1xAlloc) peptides **25/26** (5.30 μmol, 1.6 eq. per N_3) were dissolved in 1 mL 30 % MeCN. 21.2 μL of a 500 mM ascorbic acid (aq.) stock solution (10.6 μmol, 3.2 eq. per N_3) and 10.6 μL of a 500 mM $CuSO_4 \cdot 5H_2O$ (aq.) stock solution (5.30 μmol, 1.6 eq. per N_3) were added and stirred for 3 h at 30 °C and subsequently overnight at room temperature. The products were purified by multiple analytical SEC runs (isocratic gradient 30 % Eluent B, 0.6 mL/min) and fractions were collected manually.

Yield TAMRA-dextran-L17E$_{K1}^{Alloc}$(5.6) **25**: 3.6 mg (86.3 nmol, 21 %); **SEC** 30% B isocrat.: t_R = 9.499 min.

Yield TAMRA-dextran-L17E$_{K2}^{Alloc}$(5.6) **26**: 2.5 mg (86.3 nmol, 15 %); **SEC** 30% B isocrat.: t_R = 9.506 min.

6.6.5 Synthesis of TAMRA-Dextran-L17E 29

7 mg TAMRA-dextran-N_3(5) **24** (batch 2) (0.60 μmol, 1 eq.) and 14.1 mg L17E-Pra peptide **7** (4.79 μmol, 1.6 eq. per N_3) were dissolved in 1 mL H_2O. 19.2 μL of a 500 mM ascorbic acid (aq.) stock solution (9.58 μmol, 3.2 eq. per N_3) and 9.58 μL of a 500 mM $CuSO_4 \cdot 5H_2O$ (aq.) stock solution (4.79 μmol, 1.6 eq. per N_3) were added and stirred for 3 h at 30 °C. MeCN was added to the reaction mix to a total content of 30 %. The product was purified by multiple analytical SEC runs (isocratic gradient 30 % Eluent B, 0.6 mL/min) and fractions were collected manually.

Yield TAMRA-dextran-L17E(5) **29**: 5.3 mg (0.20 μmol, 33 %); **SEC** 30% B isocrat.: t_R = 9.650 min.

6.6.6 Synthesis of L17E$_{K1+K2}^{Alloc}$-Pra 30

H-IWLTALK(Alloc)FLGK(Alloc)HAAKHEAKQQLSKL-Pra-*NH*$_2$

$C_{147}H_{233}N_{39}O_{36}$

M_w: 3122.7 g/mol

1.44 g (0.5 mmol, 1 eq.) Amphispheres 40 RAM resin of loading 0.345 mmol/g was transferred into a syringe with frit. An alkyne was first introduced to generate a selective conjugation site at the *C*-terminus. The procedure of loading the first amino acids as described in section 6.3.1 was followed using 419 mg Fmoc-Pra-OH (1.25 mmol, 2.5 eq.), 465 mg HATU (1.23 mmol, 2.45 eq.) and 435 μL DIPEA (2.5 mmol, 5 eq.) in 8 mL DMF. Fmoc-Pra-OH was double coupled. The resin was split equally in five parts and synthesis was continued on a 0.1 mmol scale. Coupling of the L17E peptide sequence was performed using the *Liberty Blue*® as described in section 6.3.4 using the building block Fmoc-Lys(Alloc)-OH for the Alloc protected lysines, with final Fmoc deprotection. The resin was washed 6x with DMF and 6x with DCM, dried under air flow and cleaved from the resin as described in section 6.3.7. The peptide **30** was purified by semi-preparative RP-HPLC.

RP-HPLC 30to80% Eluent B: t_R = 12.182 min.

ESI-MS calculated for $C_{147}H_{233}N_{39}O_{36}$: $[M+H]^{+}$ = 3123.7; $[M+2H]^{2+}$ = 1562.3; $[M+3H]^{3+}$ = 1041.9; $[M+4H]^{4+}$ = 781.7; $[M+5H]^{5+}$ = 625.5; observed: $[M+3H]^{3+}$ = 1042.1; $[M+4H]^{4+}$ = 781.7; $[M+5H]^{5+}$ = 625.6.

6.6.7 Synthesis of L17E$_{K1+K3}^{Alloc}$-Pra 31

H-IWLTALK(Alloc)FLGKHAAK(Alloc)HEAKQQLSKL-Pra-*NH$_2$*

$C_{147}H_{233}N_{39}O_{36}$

M_w: 3122.7 g/mol

L17E$_{K1+K3}^{Alloc}$-Pra peptide **31** was synthesized from on part of the split resin with coupled propargylglycine described in the synthesis of L17E$_{K1+K2}^{Alloc}$-Pra peptide **30** and synthesized analogously using the *Liberty Blue*®.

RP-HPLC 30to80% Eluent B: t_R = 10.383 min.

ESI-MS calculated for $C_{147}H_{233}N_{39}O_{36}$: $[M+H]^{+}$ = 3123.7; $[M+2H]^{2+}$ = 1562.3; $[M+3H]^{3+}$ = 1041.9; $[M+4H]^{4+}$ = 781.7; $[M+5H]^{5+}$ = 625.5; $[M+6H]^{6+}$ = 521.1; observed: $[M+3H]^{3+}$ = 1042.0; $[M+4H]^{4+}$ = 781.7; $[M+5H]^{5+}$ = 625.6.

6.6.8 Synthesis of L17E$_{K2+K4}^{Alloc}$-Pra 32

H-IWLTALKFLGK(Alloc)HAAKHEAK(Alloc)QQLSKL-Pra-*NH$_2$*

$C_{147}H_{233}N_{39}O_{36}$

M_w: 3122.7 g/mol

L17E$_{K2+K4}^{Alloc}$-Pra peptide **32** was synthesized from the split resin with coupled propargylglycine described in the synthesis of L17E$_{K1+K2}^{Alloc}$-Pra peptide **30** and synthesized analogously using the *Liberty Blue*®.

RP-HPLC 30to80% Eluent B: t_R = 10.904 min.

ESI-MS calculated for $C_{147}H_{233}N_{39}O_{36}$: $[M+H]^{+}$ = 3123.7; $[M+2H]^{2+}$ = 1562.3; $[M+3H]^{3+}$ = 1041.9; $[M+4H]^{4+}$ = 781.7; $[M+5H]^{5+}$ = 625.5; $[M+6H]^{6+}$ = 521.1; observed: $[M+3H]^{3+}$ = 1042.0; $[M+4H]^{4+}$ = 781.8; $[M+5H]^{5+}$ = 625.6; $[M+6H]^{6+}$ = 521.6.

6.6.9 Synthesis of L17E$_{K3+K5}^{Alloc}$-Pra 33

H-IWLTALKFLGKHAAK(Alloc)HEAKQQLSK(Alloc)L-Pra-*NH$_2$*

$C_{147}H_{233}N_{39}O_{36}$

M_w: 3122.7 g/mol

L17E$_{K3+K5}^{Alloc}$-Pra peptide **33** was synthesized from the split resin with coupled propargylglycine described in the synthesis of L17E$_{K1+K2}^{Alloc}$-Pra peptide **30** and synthesized analogously using the *Liberty Blue*®.

RP-HPLC 30to80% Eluent B: t_R = 10.366 min.

ESI-MS calculated for $C_{147}H_{233}N_{39}O_{36}$: $[M+H]^+$ = 3123.7; $[M+2H]^{2+}$ = 1562.3; $[M+3H]^{3+}$ = 1041.9; $[M+4H]^{4+}$ = 781.7; $[M+5H]^{5+}$ = 625.5; $[M+6H]^{6+}$ = 521.1; observed: $[M+2H]^{2+}$ = 1562.5; $[M+3H]^{3+}$ = 1041.9; $[M+4H]^{4+}$ = 781.8; $[M+5H]^{5+}$ = 625.6.

6.6.10 Synthesis of TAMRA-Dextran-L17E(2xAlloc) conjugates 34-37

7 mg TAMRA-dextran-N_3(5) **24** (batch 2) (0.60 μmol, 1 eq.) and 15.0 mg L17E(2xAlloc) peptides **30-33** (4.79 μmol, 1.6 eq. per N_3) were dissolved in 1 mL 30 % MeCN. 19.2 μL of a 500 mM ascorbic acid (aq.) stock solution (9.58 μmol, 3.2 eq. per N_3) and 9.58 μL of a 500 mM $CuSO_4 \cdot 5H_2O$ (aq.) stock solution (4.79 μmol, 1.6 eq. per N_3) were added and stirred for 3 h at 30 °C. For **37**, 40 % DMSO was added to aid in solubilization. The products were purified by multiple analytical SEC runs (isocratic gradient 30 % Eluent B, 0.6 mL/min) and fractions were collected manually.

Yield TAMRA-dextran-L17E$_{K1+K2}^{Alloc}$(5) **34**: 2.6 mg (0.10 μmol, 16 %); **SEC** 30% B isocrat.: t_R = 9.521 min.
Yield TAMRA-dextran-L17E$_{K1+K3}^{Alloc}$(5)**35**: 3.0 mg (0.11 μmol, 18 %); **SEC** 30% B isocrat.: t_R = 9.548 min.
Yield TAMRA-dextran-L17E$_{K2+K4}^{Alloc}$(5) **36**: 3.9 mg (0.14 μmol, 24 %); **SEC** 30% B isocrat.: t_R = 9.465 min.
Yield TAMRA-dextran-L17E$_{K3+K5}^{Alloc}$(5) **37**: 3.6 mg (0.13 μmol, 22 %); **SEC** 30% B isocrat.: t_R = 9.423 min.

6.6.11 Cellular uptake assay: intracellular delivery of TAMRA-dextran-L17E(Alloc) conjugates 27-29 and 34-37

1 x 10^4 HeLa WT cells/ well were seeded in DMEM (w/ 10 % FBS and 1 % PS) in 8-well microscopy slides and incubated overnight at 37 °C and 5 % CO_2 in a humidified incubator. The next day, the cells were treated with 10x stock solutions of the dextran conjugates to a final concentration of 5 μM for the TAMRA-dextran-L17E(1xAlloc) conjugates **27** and **28** and incubated on the cells for 90 min. For TAMRA-dextran-L17E (5) **29**, the cells were incubated with the sample for 1 h. The cells were washed three times with PBS and fixed immediately with 4 % PFA at room temperature. The cells were observed by CLSM.

The cellular uptake assay for the TAMRA-dextran-L17E(2xAlloc) conjugates **34-37** was performed using the same procedure at 4 μM concentration and 1 h incubation at 37 °C or 4 °C. At 4 °C, the cells were pre-incubated on ice for 30 min before the sample was added and all steps were performed on ice up to the fixation step with 4 % PFA that was performed at room temperature.

6.6.12 Synthesis of L17E$_{K1}^{Ac}$-Pra 38

H-IWLTALK(Ac)FLGKHAAKHEAKQQLSKL-Pra-*NH$_2$*

$C_{141}H_{227}N_{39}O_{33}$

M_w: 2996.6 g/mol

L17E$_{K1}^{Ac}$-Pra peptide **38** was synthesized analagously to the L17E$_{K1}^{Alloc}$-Pra peptide **25** using the building block Fmoc-Lys(Ac)-OH instead of Fmoc-Lys(Alloc)-OH with yield 206 mg (0.068 mmol, 27 %).

RP-HPLC 0to80% Eluent B: t_R = 15.738 min.

ESI-MS calculated for $C_{141}H_{227}N_{39}O_{33}$: $[M+H]^+$ = 2997.6; $[M+2H]^{2+}$ = 1499.8; $[M+3H]^{3+}$ = 1000.2; $[M+4H]^{4+}$ = 750.4; $[M+5H]^{5+}$ = 600.5; $[M+6H]^{6+}$ = 500.6; observed: $[M+2H]^{2+}$ = 1499.3; $[M+3H]^{3+}$ = 999.9; $[M+4H]^{4+}$ = 750.2; $[M+5H]^{5+}$ = 600.3; $[M+6H]^{6+}$ = 500.5.

6.6.13 Synthesis of L17E$_{K2}^{Ac}$-Pra 39

H-IWLTALKFLGK(Ac)HAAKHEAKQQLSKL-Pra-*NH$_2$*

$C_{141}H_{227}N_{39}O_{33}$

M_w: 2996.6 g/mol

L17E$_{K2}^{Ac}$-Pra peptide **39** was synthesized analogously to the L17E$_{K1}^{Ac}$-Pra peptide **38** with yield 200 mg (0.067 mmol, 27 %).

RP-HPLC 0to80% Eluent B: t_R = 15.489 min.

ESI-MS calculated for $C_{141}H_{227}N_{39}O_{33}$: $[M+H]^+$ = 2997.6; $[M+2H]^{2+}$ = 1499.8; $[M+3H]^{3+}$ = 1000.2; $[M+4H]^{4+}$ = 750.4; $[M+5H]^{5+}$ = 600.5; $[M+6H]^{6+}$ = 500.6; observed: $[M+2H]^{2+}$ = 1499.4; $[M+3H]^{3+}$ = 1000.0; $[M+4H]^{4+}$ = 750.2; $[M+5H]^{5+}$ = 600.4; $[M+6H]^{6+}$ = 500.6.

6.6.14 Synthesis of TAMRA-Dextran-L17E^{Ac} conjugates 40 and 41

15 mg TAMRA-dextran-N_3(5) (batch synthesized prior to this work) (1.28 μmol, 1 eq.) and 30.7 mg L17E$_{K1}^{Ac}$-Pra **38** or L17E$_{K2}^{Ac}$-Pra **39** (10.3 μmol, 1.6 eq. per N_3) were dissolved in 30 % MeCN. 41.0 μL of a 500 mM ascorbic acid (aq.) stock solution (20.5 μmol, 3.2 eq. per N_3) and

20.5 μL of a 500 mM $CuSO_4 \cdot 5H_2O$ (aq.) stock solution (10.3 μmol, 1.6 eq. per N_3) were added and the mixture was stirred for 3 h at 30 °C. The products were isolated by precipitation in MeOH and purified by washing with MeOH 3-5 times.

Yield TAMRA-dextran-L17E_{K1}^{Ac}(5) **40**: 6.0 mg (0.22 μmol, 17 %); **SEC** 30% B isocrat.: t_R = 11.784 min.
Yield TAMRA-dextran-L17E_{K2}^{Ac}(5) **41**: 6.5 mg (0.24 nmol, 19 %); **SEC** 30% B isocrat.: t_R = 11.971 min.

6.6.15 Conditional cellular uptake assay: intracellular delivery of TAMRA-dextran-L17E^{Ac} conjugates 40 and 41

6 x 10^3 HeLa 11ht cells/ well were seeded in DMEM (w/ 10 % FBS and 1 % PS) in 18-well microscopy slides and incubated overnight at 37 °C and 5 % CO_2 in a humidified incubator. The next day, the cells were acclimatized to 30 °C by incubation for 1 h at the respective temperature. The cells were then treated with 10x stock solutions of the dextran conjugates **40** and **41** to a final concentration of 5 μM or also additionally with 50 nM SirT2 and 400 μM NAD for conditional activation and incubated on the cells for 30 min. The cells were washed three times with PBS and incubated another 3 h at 37 °C. The cells were finally washed with PBS and fixed with 4 % PFA. The cells were observed by CLSM.

6.6.16 Verfication of SirT2 deacetylation of TAMRA-dextran-L17E$_{K2}^{Ac}$ conjugate 41

For MALDI analysis, 50 μM TAMRA-dextran-L17E_{K2}^{Ac} **41**, 5 μM SirT2 and 2 mM NAD were incubated in PBS for 1 h at 30 °C. The sample was heated to 96 °C for 10 min on a heat block and centrifuged. The supernatant was taken for MALDI analysis.

For the TNBS assay, 60 μM TAMRA-dextran-L17E_{K2}^{Ac} **41**, 5 μM SirT2 and 2 mM NAD and in parallel the same sample preparation without NAD were incubated in PBS for 1 h at 30 °C. The samples were heated to 96 °C for 10 min on a heat block and centrifuged. In a 384-well plate, 5 μL of the supernatant and 15 μL sodium bicarbonate buffer (pH 8.5) were mixed. 10 μL 0.01 % (v/v) TNBS in sodium bicarbonate buffer (pH 8.5) was added and incubated for 1 h at 30 °C. Samples were prepared in triplicates and measured using the CLARIO*star*® *Plus* microplate reader.

6.6.17 Synthesis of L17E/Q21E-Pra 42

H-IWLTALKFLGKHAAKHEAKQELSKL-Pra-*NH_2*

$C_{139}H_{224}N_{38}O_{33}$

M_w: 2955.5 g/mol

L17E/Q21E-Pra peptide **42** was synthesized analogously to the L17E-Pra peptide **7** with yield 96.9 mg (13 %).

RP-HPLC 0to80% Eluent B: t_R = 15.792 min.

ESI-MS calculated for $C_{139}H_{224}N_{38}O_{33}$: $[M+H]^{+}$ = 2956.5; $[M+2H]^{2+}$ = 1478.8; $[M+3H]^{3+}$ = 986.2; $[M+4H]^{4+}$ = 739.9; $[M+5H]^{5+}$ = 592.1; $[M+6H]^{6+}$ = 493.5; observed: $[M+3H]^{3+}$ = 986.4; $[M+4H]^{4+}$ = 740.1; $[M+5H]^{5+}$ = 592.3; $[M+6H]^{6+}$ = 493.8.

6.6.18 Synthesis of HAad-Pra 43

H-IWLTALKFLGKAAAKAXAKQXLSKL-Pra-*NH₂*

X = L-2-aminoadipic acid (Aad)

$C_{135}H_{224}N_{34}O_{33}$

M_w: 2851.4 g/mol

HAad-Pra peptide **43** was completely synthesized by manual coupling steps as described in section 6.3.3 using 0.72 g (0.25 mmol, 1 eq.) Amphispheres 40 RAM resin of loading 0.345 mmol/g. Double coupling was performed for 209 mg Fmoc-Pra-OH (0.625 mmol, 2.5 eq.) and 275 mg Fmoc-L-Aad(tBu)-OH (0.625 mmol, 2.5 eq.) which were activated with 233 mg HATU (0.613 mmol, 2.45 eq.) and 217 μL DIPEA (1.25 mmol, 5 eq) in 8 mL DMF. The resin was agitated with the mixture for 1 h. Coupling of standard amino acids was performed for 30 min with 5 eq. amino acid, 4.95 eq. HBTU and 10 eq. DIPEA in DMF. After completion of the peptide and final Fmoc deprotection, the resin was washed 6x with DMF and 6x with DCM, dried under air flow and cleaved from the resin as described in section 6.3.7. The peptide was purified by semi-preparative RP-HPLC with yield 75.4 mg (0.026 mmol, 11 %).

RP-HPLC 0to80% Eluent B: t_R = 17.329 min.

ESI-MS calculated for $C_{135}H_{224}N_{34}O_{33}$: $[M+H]^{+}$ = 2851.4; $[M+2H]^{2+}$ = 1426.7; $[M+3H]^{3+}$ = 951.5; $[M+4H]^{4+}$ = 713.9; $[M+5H]^{5+}$ = 571.3; $[M+6H]^{6+}$ = 476.2; observed: $[M+3H]^{3+}$ = 951.9; $[M+4H]^{4+}$ = 714.2; $[M+5H]^{5+}$ = 571.6; $[M+6H]^{6+}$ = 476.6.

6.6.19 Synthesis of TAMRA-dextran-L17E/Q21E(5) 44

8 mg TAMRA-dextran-N_3(5) (batch synthesized prior to this work) (0.68 μmol, 1 eq.) and 16.1 mg L17E/Q21E-Pra **42** (10.3 μmol, 1.6 eq. per N_3) were dissolved in H_2O. 21.9 μL of a 500 mM ascorbic acid (aq.) stock solution (10.9 μmol, 3.2 eq. per N_3) and 10.9 μL of a 500 mM $CuSO_4 \cdot 5H_2O$ (aq.) stock solution (5.47 μmol, 1.6 eq. per N_3) were added and the mixture was stirred for 3 h at 30 °C. Since the CuAAC reaction was not complete, fresh $CuSO_4 \cdot 5H_2O$ and

ascorbic acid were added additionally and stirred overnight at room temperature. The product mixture was diluted with MeCN to make up 30 % of the reaction volume and purified by multiple analytical SEC runs (isocratic gradient 30 % Eluent B, 0.6 mL/min) and fractions were collected manually. Yield TAMRA-dextran-L17E/Q21E(5) **44**: 10.1 mg (0.38 μmol, 56 %).

SEC 30% B isocrat.: t_R = 9.808 min.

6.6.20 Synthesis of TAMRA-dextran-HAad(5) 45

TAMRA-dextran-HAad(5) **45** was synthesized analogously to TAMRA-Dextran-L17E/Q21E(5) **44** using 15.6 mg HAad-Pra **43** (5.47 μmol, 1.6 eq. per N_3). Yield **45**: 8.4 mg (0.32 μmol, 48 %).

SEC 30% B isocrat.: t_R = 10.141 min.

6.6.21 Cellular proliferation assay of TAMRA-dextran-L17E(5) 29 and TAMRA-dextran-L17E/Q21E(5) 44

In a 96-well flat bottom plate, 6 x 10^3 HeLa cells/ well were seeded in DMEM (w/ 10 % FBS and 1 % PS) and incubated overnight at 37 °C and 5 % CO_2 in a humidified incubator. 10x stock solutions of a serial dilution of TAMRA-dextran-L17E/Q21E(5) **44** and TAMRA-dextran-L17E(5) **29** were prepared and added to the cells in a 1:10 dilution. The cells were incubated for 72 h at 37 °C at 5 % CO_2 in a humidified incubator. The number of viable cells was measured using CellTiter96®Aqueous One Solution Cell Proliferation Assay (*Promega*) by absorbance at 490 nm, recorded using the CLARIOstar® Plus.

6.7 Streptavidin modular delivery architectures

6.7.1 Synthesis of biotin-dextran-N_3(3.7) 46

104.5 mg cadaverine-dextran-N_3(3.7) **23** (batch 3) (9.53 μmol, 1 eq.), 3.9 mg biotin-NHS (11.4 μmol, 1.2 eq.) and 1.62 μL DIPEA (11.4 μmol, 1.2 eq.) were dissolved in dry DMSO and stirred overnight at room temperature. The product was precipitated and washed 3x in cold MeOH. The white precipitate was dried under air flow, dissolved in water and purified by PD10 disposable columns. A white powder was obtained after lyophilization. Yield biotin-dextran-N_3(3.7) **45**: 87 mg (7.75 μmol, 81 %).

SEC 30% B isocrat.: t_R = 15.471 min.

^{1}H-NMR (300 MHz, D_2O) δ = 6.49 – 4.91 (m, 62H, C(1)**H**), 4.49 – 4.39 (m, 1H, -$(CH_2)_4$-CH-S-CH_2-C**H**-NH-), 4.25 – 4.19 (m, 1H, -$(CH_2)_4$-CH-C**H**-NH-), 4.15 – 3.30 (m, C(2-6)**H** (glucose units)), 3.29 – 3.14 (m, 21H, -C**H**$_2$$(CH_2)_3$-C**H**$_2$-NH), 3.05 – 2.96 (m, 2H, -C**H**$_2$$(CH_2)_3$-C**H**$_2$-$NH_2$), 2.59 – 2.48 (m, 8H, CH_2C**H**$_2$CO-), 2.30 – 2.21 (m, 2H, -C**H**$_2$$(CH_2)_3$CH-S-), 1.87 – 1.12

(overlapped m, 36H, -NH-CH_2-C**H**$_2$-CH_2-C**H**$_2$-CH_2NHCO, -NH-$(CH_2)_2$-C**H**$_2$-$(CH_2)_2$-NH-, -CH_2(C**H**$_2$)$_3$CH-S-) ppm.

6.7.2 Synthesis of biotin-dextran-N_3(6.3) 47

80.0 mg cadaverine-dextran-N_3(6.3) (6.94 μmol, 1 eq.), 2.8 mg biotin-NHS (8.33 μmol, 1.2 eq.) and 1.18 μL DIPEA (3.33 μmol, 1.2 eq.) were dissolved in dry DMSO and stirred overnight at room temperature. The product was precipitated and washed 3x in cold MeOH. The white precipitate was dried under air flow, dissolved in water and purified by PD10 disposable columns. A white powder was obtained after lyophilization. Yield biotin-dextran-N_3(6.3) **47**: 70.0 mg (7.75 μmol, 86 %).

SEC 30% B isocrat.: t_R = 15.193 min.

^{1}H-NMR (300 MHz, D_2O) δ = 6.49 – 4.92 (m, 62H, C(1)**H**), 4.49 – 4.39 (m, 1H, -$(CH_2)_4$-CH-S-CH_2-C**H**-NH-), 4.25 – 4.18 (m, 1H, -$(CH_2)_4$-CH-C**H**-NH-), 4.15 – 3.32 (m, C(2-6)**H** (glucose units)), 3.30 – 3.14 (m, 21H, -C**H**$_2$$(CH_2)_3$-C**H**$_2$-NH), 3.05 – 2.96 (m, 2H, -C**H**$_2$$(CH_2)_3$-C**H**$_2$-$NH_2$), 2.63 – 2.46 (m, 11H, CH_2C**H**$_2$CO-), 2.33 – 2.22 (m, 2H, -C**H**$_2$$(CH_2)_3$CH-S-), 1.94 – 1.09 (overlapped m, 42H, -NH-CH_2-C**H**$_2$-CH_2-C**H**$_2$-CH_2NHCO, -NH-$(CH_2)_2$-C**H**$_2$-$(CH_2)_2$-NH-, -CH_2(C**H**$_2$)$_3$CH-S-) ppm.

6.7.3 Synthesis of alkyne-ATSP-7041 48

4-pentynoic acid-AEEAc-LTF-R8-EYWAQ-Cba-S5-SAA-*NH_2*

$C_{96}H_{138}N_{18}O_{24}$

M_w: 1928.2 g/mol

4-pentynoic acid-AEEAc-ATSP-7041 was completely synthesized in a syringe with frit by manual coupling as described in section 6.3.3 starting with 0.72 g (0.25 mmol, 1 eq.) Amphispheres 40 RAM resin of loading 0.345 mmol/g. Coupling of standard amino acids was performed for 30 min with 5 eq. amino acid, 4.95 eq. HBTU and 10 eq. DIPEA in DMF. Double coupling was performed for 142 mg Fmoc-(S)-2-(4-pentenyl)Ala-OH (Fmoc-S5-OH) (0.375 mmol, 1.5 eq.), 158 mg Fmoc-(R)-2-(7-octenyl)Ala-OH (Fmoc-R8-OH) (0.375 mmol, 1.5 eq.) and 137 mg Fmoc-Ala(β-cyclobutyl)-OH (Fmoc-Cba-OH) (0.375 mmol, 1.5 eq.), which were activated with 142 mg HATU (0.373 mmol, 1.5 eq.) and 130.6 μL DIPEA (0.75 mmol, 3 eq.) in DMF. The mixture was agitated with the resin for 1 h at ambient temperature. After completion of the amino acid sequence of ATSP-7041, The resin was split in two parts and one part (0.125 mmol) was taken for further coupling. 145 mg (2-[2-(Fmoc-amino)ethoxy]ethoxy)acetic acid (Fmoc-AEEAc-OH) (0.375 mmol, 3 eq.) was coupled using 140 mg HATU (0.369 mmol, 2.95 eq.) and

130 μL DIPEA (0.75 mmol, 6 eq.) in DMF by agitation for 45 min. The resin was washed 6x with DMF and 6x with DCM. Ring closing metathesis (RCM) was performed with a 15 mol-% solution of (1,3-bis-(2,4,6-trimethylphenyl)-2-imidazolidinylidene)dichloro(o-isopropoxyphenylmethylene)ruthenium (Grubbs Hoveyda 2nd Generation) catalyst in argon-flushed dichloroethane (DCE). The mixture was gently agitated with the resin for 18 h at 50 °C. Afterwards, the resin was washed 6x with DCE and after Fmoc deprotection, 36.8 mg 4-pentynoic acid (0.375 mmol, 3 eq.), 140 mg HATU (0.369 mmol, 2.95 eq.) and 130 μL DIPEA (0.75 mmol, 6 eq.) were added to the resin and agitated for 45 min at ambient temperature. The resin was washed 6x with DMF and 6x with DCM, dried under air flow and cleaved from the resin as described in section 6.3.7. The peptide was purified by semi-preparative RP-HPLC with yield 37 mg (0.019 mmol, 15 %).

RP-HPLC 40to100% Eluent B: t_R = 18.393 min.

ESI-MS calculated for $C_{96}H_{138}N_{18}O_{24}$: $[M+H]^+$ = 1929.2; $[M+2H]^{2+}$ = 965.1; $[M+3H]^{3+}$ = 643.7; observed: $[M+H]^+$ = 1929.4; $[M+2H]^{2+}$ = 965.1.

6.7.4 Synthesis of alkyne-apCC-Di-B 49

4-pentynoic acid- GQLKQRRAALKQRIAALKQRAAALKWQIQG -*NH*$_2$

$C_{158}H_{275}N_{57}O_{37}$

M_w: 3565.2 g/mol

To enable further modification, apCC-Di-B peptide was additionally modified with an alkyne on the *C*-terminus. 0.72 g (0.25 mmol, 1 eq.) Amphispheres 40 RAM resin of loading 0.345 mmol/g was transferred into the reaction vessel of the *Liberty Blue*® and completely synthesized with microwave assistance as described in section 6.3.4 with final Fmoc deprotection. The resin was split in two, and synthesis was continued with one part (0.125 mmol scale). Next, 49.1 mg 4-pentynoic acid (0.5 mmol, 4 eq.), 188 mg HATU (0.494 mmol, 3.95 eq.) and 174 μL DIPEA (1 mmol, 8 eq.) were added to the resin and agitated for 45 min at ambient temperature. The resin was washed 6x with DMF and 6x with DCM, dried under air flow and cleaved from the resin as described in section 6.3.7. The peptide was purified by semi-preparative RP-HPLC with yield 128 mg (0.036 mmol, 29 %).

RP-HPLC 10to60% Eluent B: t_R = 14.610 min.

ESI-MS calculated for $C_{158}H_{275}N_{57}O_{37}$: $[M+H]^+$ = 3566.2; $[M+2H]^{2+}$ = 1783.6; $[M+3H]^{3+}$ = 1189.4; $[M+4H]^{4+}$ = 892.3; $[M+5H]^{5+}$ = 714.0; $[M+6H]^{6+}$ = 595.2; $[M+7H]^{7+}$ = 510.5;

observed: $[M+3H]^{3+}$ = 1189.6; $[M+4H]^{4+}$ = 892.5; $[M+5H]^{5+}$ = 714.2; $[M+6H]^{6+}$ = 595.3; $[M+7H]^{7+}$ = 510.5.

6.7.5 Synthesis of biotin-dextran-L17E(3.7) 50

7 mg biotin-dextran-N_3(3.7) **46** (0.624 μmol, 1 eq.) and 10.9 mg L17E-Pra **7** (3.70 μmol, 1.6 eq. per N_3) were dissolved in 2 mL H_2O. 14.8 μL of a 500 mM ascorbic acid (aq.) stock solution (7.39 μmol, 3.2 eq. per N_3) and 7.39 μL of a 500 mM $CuSO_4 \cdot 5H_2O$ (aq.) stock solution (3.70 μmol, 1.6 eq. per N_3) were added and stirred for 3 h at 30 °C. The product was purified by multiple analytical SEC runs (isocratic gradient 30 % B, 0.6 mL/min) and fractions were collected manually. Yield biotin-dextran-L17E(3.7) **50**: 1.8 mg (81.3 nmol, 13 %).

SEC 30% B isocrat.: t_R = 11.800 min.

6.7.6 Synthesis of biotin-dextran-ATSP-7041(3.7) 51

7 mg biotin-dextran-N_3(3.7) **46** (0.624 μmol, 1 eq.) and 7.12 mg Alkyne -ATSP-7041 **48** (3.70 μmol, 1.6 eq. per N_3) were dissolved in 2 mL 50 % MeCN (aq.). 14.8 μL of a 500 mM ascorbic acid (aq.) stock solution (7.39 μmol, 3.2 eq. per N_3) and 7.39 μL of a 500 mM $CuSO_4 \cdot 5H_2O$ (aq.) stock solution (3.70 μmol, 1.6 eq. per N_3) were added and stirred for 14 h at 30 °C. The product was purified by multiple analytical SEC runs (isocratic gradient 40 % B, 0.6 mL/min) and fractions were collected manually. Yield biotin-dextran-ATSP-7041(3.7) **51**: 1.3 mg (70.9 nmol, 11.4 %).

SEC 40% B isocrat.: t_R = 15.803 min.

6.7.7 Synthesis of biotin-dextran-apCC-Di-B(3.7) 52

6 mg biotin-dextran-N_3(3.7) **46** (0.535 μmol, 1 eq.) and 11.3 mg alkyne-apCC-Di-B (3.17 μmol, 1.6 eq. per N_3) were dissolved in 2 mL 50 % MeCN (aq.). 12.7 μL of a 500 mM ascorbic acid (aq.) stock solution (6.33 μmol, 3.2 eq. per N_3) and 6.33 μL of a 500 mM $CuSO_4 \cdot 5H_2O$(aq.) stock solution (3.17 μmol, 1.6 eq. per N_3) were added and stirred for 14 h at 30 °C. The product was purified by multiple analytical SEC runs (isocratic gradient 30 % B, 0.6 mL/min) and fractions were collected manually. Yield biotin-dextran-apCC-Di-B(3.7) **52**: 4.6 mg (188 nmol, 35 %).

SEC 30% B isocrat.: t_R = 15.803 min.

6.7.8 Synthesis of biotin-dextran-L17E/Q21E(6.3) 53

14 mg biotin-dextran-N_3(6.3) **47** (1.18 μmol, 1 eq.) and 35.2 mg L17E/Q21E-Pra (11.9 μmol, 1.6 eq. per N_3) were dissolved in 4 mL H_2O. 47.7 μL of a 500 mM ascorbic acid (aq.) stock solution (23.8 μmol, 3.2 eq. per N_3) and 23.8 μL of a 500 mM $CuSO_4 \cdot 5H_2O$ (aq.) stock solution

(11.9 μmol, 1.6 eq. per N_3) were added and stirred for 14 h at 30 °C. The product was purified by multiple analytical SEC runs (isocratic gradient 30 % B, 0.6 mL/min) and fractions were collected manually. Yield biotin-dextran-L17E/Q21E(6.3) **53**: 7.4 mg (243 nmol, 21 %).

SEC 30% B isocrat.: t_R = 11.580 min.

6.7.9 Production of biotinylated eGFP in *E. coli*

The eGFP plasmid contained a 15 amino acid AviTag peptide (GLNDIFEAQKIEWHE) in which the lysine residue is biotinylated by *E. coli* biotin ligase (BirA) upon production in *E. coli*.[207] The plasmid was transformed into *E. coli* BL1 (DE3), cultivated and selected for kanamycin resistance on dYT-agar plates overnight at 37 °C. A single colony was picked and transferred to 50 mL dYT medium containing 50 μL kanamycin (0.1 % v/v) and incubated overnight at 37 °C. The next day, 1 L dYT-medium containing 1 mL kanamycin (0.1 % v/v) was inoculated to an OD_{600}=0.1 using the overnight culture and grown to an OD_{600} of 0.6-0.8 at 37 °C. Protein production was induced with 1 mL isopropyl ß-D-1-thiogalactopyranoside IPTG (1 M) overnight at 30 °C and 180 rpm. Cells were harvested by centrifugation and resuspended in 25 mL IMAC A buffer. Lysis of the cells was achieved by sonication in 3 min cycles at 30-40 % power with 3 min rest in between on ice. The cell debris was removed by centrifugation for 30 min at 14.000 rpm. The supernatant was filtered through a 0.45 μm syringe filter and loaded on a HisTrap™ HP column (1 mL, GE Healthcare) for purification with an ÄKTA start™ chromatography system (GE Healthcare). The main fractions were pooled and dialyzed overnight against PBS.

6.7.10 Synthesis of Pra-GSSG-GFP11 55

H-Pra-GSSG-RDHMVLHEYVNAAGIT-*NH*$_2$

$C_{94}H_{146}N_{30}O_{30}S$

M_w: 2208.4 g/mol

To enable further modification, GFP11 peptide was additionally modified with an alkyne on the *N*-terminus with a GSSG spacer to the GFP11 peptide. 0.72 g (0.25 mmol, 1 eq.) Amphispheres 40 RAM resin of loading 0.345 mmol/g was transferred to the reaction vessel of the *Liberty Blue*® and synthesized as described in section 6.3.4. The alkyne Fmoc-Pra-OH was introduced by manual coupling. 209 mg Fmoc-Pra-OH (0.625 mmol, 2.5 eq.) were activated with 233 mg HATU (0.613 mmol, 2.45 eq.) and 217 μL DIPEA (1.25 mmol, 5 eq) in 8 mL DMF were double coupled. After final Fmoc-deprotection, the resin was washed 6x with DMF and 6x with DCM, dried under air flow and cleaved from the resin as described in section 6.3.7. The peptide **55** was purified by semi-preparative RP-HPLC with yield 238 mg (0.108 mmol, 43 %).

RP-HPLC 0to100% Eluent B: t_R = 12.053 min.

ESI-MS calculated for $C_{94}H_{146}N_{30}O_{30}S$: $[M+H]^+$ = 2209.4; $[M+2H]^{2+}$ = 1105.2; $[M+3H]^{3+}$ = 737.1; $[M+4H]^{4+}$ = 553.1; observed: $[M+2H]^{2+}$ = 1105.2; $[M+3H]^{3+}$ = 737.1; $[M+4H]^{4+}$ = 553.1.

6.7.11 Synthesis of biotin-dextran-GFP11(6.3) 56

7 mg biotin-dextran-N_3(6.3) **47** (0.591 μmol, 1 eq.) and 13.2 mg Pra-GSSG-GFP11 **55** (5.96 μmol, 1.6 eq. per N_3) were dissolved in 2 mL 30 % MeCN (aq.). 23.8 μL of a 500 mM ascorbic acid (aq.) stock solution (11.9 μmol, 3.2 eq. per N_3) and 11.9 μL of a 500 mM $CuSO_4 \cdot 5H_2O$ (aq.) stock solution (5.96 μmol, 1.6 eq. per N_3) were added and stirred for 14 h at 30 °C. The product was purified by multiple analytical SEC runs (isocratic gradient 30 % B, 0.6 mL/min) and fractions were collected manually. Yield biotin-dextran-GFP11(6.3) **56**: 3.2 mg (124 nmol, 21 %).

SEC 30% B isocrat.: t_R = 11.163 min.

6.7.12 Synthesis of 4-pentynoic acid-PEG_2-KD3 57

4-pentynoic acid-PEG_2-LTFKEYWDQLTSAA-*NH_2*

$C_{89}H_{126}N_{18}O_{27}$

M_w: 1880.1 g/mol

4-pentynoic acid-PEG_2-KD3 peptide **57** was completely synthesized in a syringe with frit by manual coupling as described in section 6.3.4 starting with 0.72 g (0.25 mmol, 1 eq.) Amphispheres 40 RAM resin of loading 0.345 mmol/g. Coupling of standard amino acids was performed for 30 min with 5 eq. amino acid, 4.95 eq. HBTU and 10 eq. DIPEA in DMF. Except for asparagine and lysine the following was used: 355 mg Fmoc-Asp(2-phenylisopropyl)-OH (Fmoc-Asp(OPp) OH) (0.75 mmol, 3 eq.) and 469 mg Fmoc-Lys(methyltrityl)-OH (Fmoc-Lys(Mtt)-OH) (0.75 mmol, 3 eq.) which were activated with 280 mg HATU (0.738 mmol, 2.95 eq.) and 261 μL DIPEA (1.5 mmol, 6 eq.). The resin was split in two and synthesis was continued on 0.125 mmol scale. 36.8 mg 4-pentynoic acid (0.375 mmol, 3 eq.), 140 mg HATU (0.369 mmol, 2.95 eq.) and 130 μL DIPEA (0.75 mmol, 6 eq.) were added to the resin and agitated for 45 min at ambient temperature. After washing the resin 6x with DMF and 6x with DCM, the Mtt and OPp protecting groups were cleaved by treatment with 1 % TFA, 2 % MeOH in DCM overnight at ambient temperature. The peptide was cyclicised using 92.7 mg HATU (0.244 mmol, 2 eq.) and 87.1 μL DIPEA (0.5 mmol, 4 eq.) in DMF for 1 h. Afterwards, the resin was washed 6x with DMF and 6x with DCM, dried under air flow and cleaved from the resin as

described in section 6.3.7. *4-pentynoic acid-PEG$_2$*-KD3 **57** was purified by semi-preparative RP-HPLC with yield 13.8 mg (0.019 mmol, 15 %).

RP-HPLC 40to100% Eluent B: t_R = 18.518 min.

ESI-MS calculated for $C_{89}H_{126}N_{18}O_{27}$: $[M+H]^+$ = 1881.1; $[M+2H]^{2+}$ = 941.0; $[M+3H]^{3+}$ = 627.7; $[M+4H]^{4+}$ = 471.0; observed: $[M+H]^+$ = 1881.0; $[M+2H]^{2+}$ = 940.6.

6.7.13 Synthesis of biotin-dextran-KD3(6.3) 58

7 mg biotin-dextran-N_3(6.3) **47** (0.591 μmol, 1 eq.) and 11.3 mg *4-pentynoic acid-PEG$_2$*-KD3 **57** (5.96 μmol, 1.6 eq. per N_3) were dissolved in 2 mL 30 % MeCN (aq.). 23.8 μL of a 500 mM ascorbic acid (aq.) stock solution (11.9 μmol, 3.2 eq. per N_3) and 11.9 μL of a 500 mM $CuSO_4 \cdot 5H_2O$ (aq.) stock solution (5.96 μmol, 1.6 eq. per N_3) were added and stirred for 14 h at 30 °C. The product was purified by multiple analytical SEC runs (isocratic gradient 30 % B, 0.6 mL/min) and fractions were collected manually. Yield biotin-dextran-KD3(6.3) **58**: 2.0 mg (84.1 nmol, 14 %).

SEC 30% B isocrat.: t_R = 14.102 min.

6.7.14 Synthesis of 4-pentynoic acid-GSSG-HiBiT 59

4-pentynoic acid-GSSG-VSGWRLFKKIS-*NH$_2$*

$C_{78}H_{122}N_{22}O_{20}$

M_w: 1687.9 g/mol

To enable further modification, HiBiT peptide was additionally modified with an alkyne on the *C*-terminus with a GSSG spacer to the HiBiT peptide. Synthesis was performed analogously to the *4-pentynoic acid*-apCC-Di-B peptide using the *Liberty Blue*® and manual 4-pentynoic acid coupling. The peptide was purified by semi-preparative RP-HPLC with yield 161 mg (0.095 mmol, 38 %).

RP-HPLC 0to80% Eluent B: t_R = 15.273 min.

ESI-MS calculated for $C_{78}H_{122}N_{22}O_{20}$: $[M+H]^+$ = 1688.9; $[M+2H]^{2+}$ = 845.0; $[M+3H]^{3+}$ = 563.7; $[M+4H]^{4+}$ = 423.0; observed: $[M+H]^+$ = 1688.8; $[M+2H]^{2+}$ = 844.9; $[M+3H]^{3+}$ = 563.7.

6.7.15 Synthesis of biotin-dextran-HiBiT(6.3) 60

7 mg biotin-dextran-N_3(6.3) **47** (0.591 μmol, 1 eq.) and 10.1 mg Alkyne-GSSG-HiBiT (5.96 μmol, 1.6 eq. per N_3) were dissolved in 2 mL 30 % MeCN (aq.). 23.8 μL of a 500 mM

ascorbic acid (aq.) stock solution (11.9 μmol, 3.2 eq. per N_3) and 11.9 μL of a 500 mM $CuSO_4 \cdot 5H_2O$ (aq.) stock solution (5.96 μmol, 1.6 eq. per N_3) were added and stirred for 14 h at 30 °C. The product was purified by multiple analytical SEC runs (isocratic gradient 30 % B, 0.6 mL/min) and fractions were collected manually. Yield biotin-dextran-HiBiT(6.3) **60**: 4.2 mg (84.1 nmol, 32 %).

SEC 30% B isocrat.: t_R = 9.826 min.

6.7.16 Streptavidin concentration determination

Streptavidin was weighed in and dissolved in PBS to give a concentration of around 300 μM. The exact concentration of streptavidin was determined with the BioSpec Nano™ by absorbance at 280 nm using the molecular weight 55 kDa and extinction coefficient 176 000 $M^{-1}cm^{-1}$.

6.7.17 Generation of streptavidin-dextran-CPP architectures with eGFP as payload

Streptavidin was mixed with biotinylated-eGFP **54** and biotin-dextran-CPP conjugates **50-53** in the desired molar ratio under assumption that all four binding sites of streptavidin are equally accessible to all constructs. Free biotin was used to occupy the fourth remaining site, if required. The mixture was incubated overnight at ambient temperature. The concentrations of streptavidin-biotin-dextran architectures are given with respect to streptavidin. Table 5 shows the stock concentrations of the individual compounds and volumes taken for a final concentration of 20 μM with respect to streptavidin. The mixtures were incubated overnight at room temperature and used the next day in the cellular uptake assay.

Table 5| Stock concentrations and volumes of individual compounds taken to generate streptavidin-dextran-CPP architectures with eGFP at 20 µM concentration with respect to streptavidin for the cellular uptake of eGFP-biotin).

	c(Stock)/ µM	Volume /µL
Sav(1xbiotin-eGFP, 3xbiotin-dextran-CPP)	**20**	**30**
Sav	323	1.86
biotin-eGFP **54**	134	4.48
biotin-dextran-CPP conjugate	600	3.00
PBS		19.66
Sav(1xbiotin-eGFP, 1xbiotin, 2xbiotin-dextran-CPP)	**20**	**30**
Sav	323	1.86
biotin-eGFP **54**	134	4.48
biotin-dextran-CPP conjugate	600	2.00
biotin	600	1.00
PBS		19.66

6.7.18 Cellular uptake assay of streptavidin-dextran-CPP architectures with eGFP as payload

8 x 10^3 HeLa EM2-11ht cells/ well were seeded in DMEM (w/ 10 % FBS and 1 % PS) in 18-well microscopy slides and incubated overnight at 37 °C and 5 % CO_2 in a humidified incubator. The next day, the cells were washed by exchanging the half the volume of the medium three times, ensuring the cells were covered with medium at all times. The cells were treated with 10x stock solutions of the streptavidin delivery architectures (final concentration 2 μM with respect to streptavidin) for 2 h at 37 °C. The cells were washed again by medium exchange and incubated another 3 h at 37 °C and 5 % CO_2. Finally, the cells were washed with PBS, and fixed with 4 % PFA. In experiment 1, the cells were additionally stained with Hoechst 33342 The cells were observed by CLSM.

The cellular uptake assay at 4 °C was performed using HeLa and SKBR3 cells under the same procedure, with an additional pre-incubation step for 1 h on ice prior to the experiment. The microscopy slide was kept on ice at all times and fixed with 4 % PFA at room temperature.

6.7.19 Cellular proliferation assay of streptavidin-dextran-CPP architectures with eGFP as payload

6 x 10^3 HeLa EM2-11ht cells/ well were seeded in DMEM (w/ 10 % FBS and 1 % PS) in 18-well microscopy slides and incubated overnight at 37 °C and 5 % CO_2 in a humidified incubator. The next day, the cells were treated with a dilution series of 10x stock solutions of the streptavidin delivery architectures (starting concentration 6.5 μM) for 72 h at 37 °C at 5 % CO_2 in a humidified incubator. The number of viable cells was measured using CellTiter96®Aqueous One Solution Cell Proliferation Assay by absorbance at 490 nm, which

was recorded using the CLARIOstar® Plus microplate reader. Samples were measured in triplicates.

6.7.20 Generation of streptavidin-dextran-CPP architectures for GFP11, KD3 or HiBiT delivery

Streptavidin-dextran-CPP architectures for GFP11/KD3/HiBiT delivery were generated similarly to section 6.7.20. Streptavidin was mixed with biotin-dextran-GFP11(6.3) **56**, biotin-dextran-KD3(6.3) **58**, biotin-dextran-HiBiT(6.3) **60** and biotin-dextran-CPP conjugates in stoichiometric ratios as shown in Table 6 and incubated overnight.

Table 6| Stock concentrations and volumes of individual compounds taken to generate streptavidin-dextran-CPP architectures at 20 µM concentration with respect to streptavidin for for GFP11, KD3 or HiBiT delivery and verification of cytosolic delivery.

	c(Stock)/ µM	**Volume /µL**
Sav(1xbiotin-dextran-GFP11/KD3/HiBiT(6.3) 56/58/60, 3xbiotin-dextran-CPP)	**20**	**30**
Sav	302	1.98
biotin-dextran-GFP11/KD3/HiBiT(6.3) **56/58/60**	600	1.00
biotin-dextran-CPP conjugate	600	3.00
PBS		24.01
Sav(2xbiotin-dextran-KD3(6.3) 58, 2xbiotin-dextran-CPP)	**20**	**30**
Sav	302	1.86
biotin-dextran- GFP11/KD3/HiBiT(6.3) **56/58/60**	600	2.00
biotin-dextran-CPP conjugate	600	2.00
PBS		24.01

6.7.21 Split-GFP complementation assay

2 x 10^4 HeLa GFP1-10 cells/ well were seeded in DMEM (w/ 10 % FBS and 1 % PS) in a 96-well flat bottom plate and incubated overnight at 37 °C and 5 % CO_2 in a humidified incubator. The cells were treated with 5x stock solutions of the streptavidin delivery architectures (final concentration 1 μM with respect to streptavidin) for 20 h at 37 °C. The cells were washed with PBS and trypsinized. The cells were resuspended in 250 μL PBS and transferred to a 96-well round bottom plate flow cytometry measurement (FITC channel) using the *Cytoflex S*.

6.7.22 Live-cell time-lapse microscopy of p53 accumulation

Two days prior to the cellular assay, 4 x 10^3 A549 p53-mVenus cells/ well were seeded in FluoroBrite™ medium in 96-well optical-bottom plates with polymer base and incubated at 37 °C and 5 % CO_2 in a humidified incubator. Live-cell time-lapse microscopy was performed in the Löwer Lab. The day of the experiment, the medium was aspirated and the streptavidin delivery architectures in fresh medium (Gibco™ FluoroBrite™ DMEM supplemented with 5 %

FBS, 1 % HEPES, 1 % P/S and 4 mM GlutaMax) were incubated on the cells with a final concentration of 2 μM with respect to streptavidin. 1 μM and 2 μM Nutlin-3 was used as positive control. The 96-well plate was placed in a humidified incubation chamber of a Nikon Ti inverted fluorescence microscope with constant temperature of 37 °C and 5 % CO_2. Cells were imaged at regular intervals for the duration of the experiment. mVenus and mCerulean fluorescence were measured using the appropriate filter sets. A custom-written Matlab (MathWorks, Natick, MA, USA) script of the Löwer Lab was used to quantify the average fluorescence intensity of p53-mVenus for individually tracked cells.[62,63,211]

6.7.23 NanoBiT® assay

2 x 10^4 HeLa LgBiT cells/ well were seeded in a 96-well flat bottom plate in DMEM (w/ 10 % FBS and 1 % PS), 0.2 mg/mL G418 and 1 μg/mL doxycycline to induce LgBiT expression and incubated overnight at 37 °C and 5 % CO_2 in a humidified incubator. The cells were treated with 5x stock solutions of the streptavidin delivery architectures (final concentration 2 μM with respect to streptavidin) for 18 h at 37 °C. The medium was removed and replaced with 100 μL fresh DMEM (w/ 10 % FBS and 1 % PS) containing Nano-Glo® Endurazine™ substrate (Promega) at 1:100 dilution according to the recommendation of the supplier. The luminescence signal was measured using the CLARIOstar® Plus microplate reader after 1-2 h incubation at 37 °C and 5 % CO_2 in a humidified incubator. Samples were measured in duplicates.

7 References

[1] L. Falzone, S. Salomone, M. Libra, *Frontiers in pharmacology* **2018**, *9*, 1300.
[2] P. Brookes, P. D. Lawley, *The Biochemical journal* **1960**, *77*, 478.
[3] A. Gilman, F. S. Philips, *Science (New York, N.Y.)* **1946**, *103*, 409.
[4] C. Heidelberger, N. K. Chaudhuri, P. Danneberg, D. Moooren, L. Griesbach, R. Duschinsky, R. J. Schnitzer, E. Pleven, J. Scheiner, *Nature* **1957**, *179*, 663.
[5] I. F. Tannock, *Radiotherapy and oncology : journal of the European Society for Therapeutic Radiology and Oncology* **1989**, *16*, 83.
[6] G. Bonadonna, R. Zucali, S. Monfardini, M. de Lena, C. Uslenghi, *Cancer* **1975**, *36*, 252.
[7] C. J. Schimmoeller, C. Bastian, J. Fleming, J. Morales, *Cureus* **2023**, *15*, e41660.
[8] K. Strebhardt, A. Ullrich, *Nature reviews. Cancer* **2008**, *8*, 473.
[9] C. A. Kettleborough, J. Saldanha, V. J. Heath, C. J. Morrison, M. M. Bendig, *Protein engineering* **1991**, *4*, 773.
[10] Y. Safdari, S. Farajnia, M. Asgharzadeh, M. Khalili, *Biotechnology & genetic engineering reviews* **2013**, *29*, 175.
[11] R. F. van Vollenhoven, R. M. Fleischmann, D. E. Furst, S. Lacey, P. B. Lehane, *The Journal of rheumatology* **2015**, *42*, 1761.
[12] S. B. Ebrahimi, D. Samanta, *Nature communications* **2023**, *14*, 2411.
[13] C. Chalouni, S. Doll, *Journal of experimental & clinical cancer research : CR* **2018**, *37*, 20.
[14] M. Barok, H. Joensuu, J. Isola, *Breast cancer research : BCR* **2014**, *16*, 209.
[15] R. Bedford, C. Tiede, R. Hughes, A. Curd, M. J. McPherson, M. Peckham, D. C. Tomlinson, *Biophysical reviews* **2017**, *9*, 299.
[16] A. Stahl, M. T. Stumpp, A. Schlegel, S. Ekawardhani, C. Lehrling, G. Martin, M. Gulotti-Georgieva, D. Villemagne, P. Forrer, H. T. Agostini et al., *Angiogenesis* **2013**, *16*, 101.
[17] F. Sha, G. Salzman, A. Gupta, S. Koide, *Protein science : a publication of the Protein Society* **2017**, *26*, 910.
[18] M. Rosestedt, K. G. Andersson, B. Mitran, V. Tolmachev, J. Löfblom, A. Orlova, S. Ståhl, *Scientific reports* **2015**, *5*, 15226.
[19] S. Miersch, S. S. Sidhu, *F1000Research* **2016**, *5*.
[20] D. C. Rubinsztein, P. Codogno, B. Levine, *Nature reviews. Drug discovery* **2012**, *11*, 709.
[21] S. Nishikawa, T. Iwakuma, *Cancers* **2023**, *15*.
[22] O. Hassin, M. Oren, *Nature reviews. Drug discovery* **2023**, *22*, 127.
[23] H. E. Marei, A. Althani, N. Afifi, A. Hasan, T. Caceci, G. Pozzoli, A. Morrione, A. Giordano, C. Cenciarelli, *Cancer cell international* **2021**, *21*, 703.
[24] K. Venkatesan, J.-F. Rual, A. Vazquez, U. Stelzl, I. Lemmens, T. Hirozane-Kishikawa, T. Hao, M. Zenkner, X. Xin, K.-I. Goh et al., *Nature methods* **2009**, *6*, 83.
[25] Y. Han, J. Pan, Y. Ma, D. Zhou, W. Xu, *Biosafety and Health* **2022**, *4*, 87.
[26] Q.-Q. Zhou, H.-T. Xiao, F. Yang, Y.-D. Wang, P. Li, Z.-G. Zheng, *Pharmacological research* **2023**, *188*, 106627.
[27] Y. Zhai, R. Moosavi, M. Chen, *Frontiers in immunology* **2021**, *12*, 645699.
[28] "New Drugs at FDA: CDER's New Molecular Entities and New Therapeutic Biological Products. Novel Drug Approvals for 2023", can be found under https://www.fda.gov/drugs/new-drugs-fda-cders-new-molecular-entities-and-new-therapeutic-biological-products/novel-drug-approvals-2023, **2024**.
[29] F. Bray, M. Laversanne, H. Sung, J. Ferlay, R. L. Siegel, I. Soerjomataram, A. Jemal, *CA: a cancer journal for clinicians* **2024**.
[30] "Protein Therapeutics Market. Global Protein Therapeutics Market Outlook 2031", can be found under https://www.transparencymarketresearch.com/protein-therapeutics-market.html, **2024**.
[31] A. Hoeben, E. A. J. Joosten, M. H. J. van den Beuken-van Everdingen, *Cancers* **2021**, *13*.
[32] M. M. Zhu, M. Mollet, R. S. Hubert, Y. S. Kyung, G. G. Zhang in *Handbook of Industrial Chemistry and Biotechnology* (Eds.: J. A. Kent, T. V. Bommaraju, S. D. Barnicki), Springer International Publishing, Cham, **2017**, pp. 1639–1669.
[33] "Peptide Therapeutics Market Size & Trends", can be found under https://www.grandviewresearch.com/industry-analysis/peptide-therapeutics-market#.

[34] S. Faivre, G. Demetri, W. Sargent, E. Raymond, *Nature reviews. Drug discovery* **2007**, *6*, 734.
[35] D. Al Shaer, O. Al Musaimi, F. Albericio, B. G. de La Torre, *Pharmaceuticals (Basel, Switzerland)* **2024**, *17*.
[36] L. Wang, N. Wang, W. Zhang, X. Cheng, Z. Yan, G. Shao, X. Wang, R. Wang, C. Fu, *Signal transduction and targeted therapy* **2022**, *7*, 48.
[37] S.-S. Cheng, G.-J. Yang, W. Wang, C.-H. Leung, D.-L. Ma, *Journal of hematology & oncology* **2020**, *13*, 26.
[38] M. C. Smith, J. E. Gestwicki, *Expert reviews in molecular medicine* **2012**, *14*, e16.
[39] L. Zhong, Y. Li, L. Xiong, W. Wang, M. Wu, T. Yuan, W. Yang, C. Tian, Z. Miao, T. Wang et al., *Signal transduction and targeted therapy* **2021**, *6*, 201.
[40] M. R. Arkin, Y. Tang, J. A. Wells, *Chemistry & biology* **2014**, *21*, 1102.
[41] X. Liu, F. Wu, Y. Ji, L. Yin, *Bioconjugate chemistry* **2019**, *30*, 305.
[42] T. A. Slastnikova, A. V. Ulasov, A. A. Rosenkranz, A. S. Sobolev, *Frontiers in pharmacology* **2018**, *9*, 1208.
[43] L. H. Estrada, S. Chu, J. A. Champion, *Journal of pharmaceutical sciences* **2014**, *103*, 1863.
[44] P. Ghosh, X. Yang, R. Arvizo, Z.-J. Zhu, S. S. Agasti, Z. Mo, V. M. Rotello, *Journal of the American Chemical Society* **2010**, *132*, 2642.
[45] H. Rilo-Alvarez, A. M. Ledo, A. Vidal, M. Garcia-Fuentes, *Drug delivery and translational research* **2021**, *11*, 426.
[46] S. J. Kaczmarczyk, K. Sitaraman, H. A. Young, S. H. Hughes, D. K. Chatterjee, *Proceedings of the National Academy of Sciences of the United States of America* **2011**, *108*, 16998.
[47] D. B. Thompson, J. J. Cronican, D. R. Liu, *Methods in enzymology* **2012**, *503*, 293.
[48] T. H. Rabbitts, *Antibodies (Basel, Switzerland)* **2023**, *12*.
[49] T. Asai, T. Tsuzuku, S. Takahashi, A. Okamoto, T. Dewa, M. Nango, K. Hyodo, H. Ishihara, H. Kikuchi, N. Oku, *Biochemical and biophysical research communications* **2014**, *444*, 599.
[50] E. de Souza Von Zuben, J. O. Eloy, V. H. S. Araujo, M. P. D. Gremião, M. Chorilli, *Colloids and Surfaces A: Physicochemical and Engineering Aspects* **2021**, *622*, 126624.
[51] N. Devi, C. Cokca, R. Sharma, M. Kumar, K. Peneva, R. K. Sharma, N. Wangoo, *Materials Today Communications* **2022**, *33*, 104233.
[52] N. J. Yang, M. J. Hinner, *Methods in molecular biology (Clifton, N.J.)* **2015**, *1266*, 29.
[53] H. Watson, *Essays in biochemistry* **2015**, *59*, 43.
[54] G. Lenoir, J. M. D'Ambrosio, T. Dieudonné, A. Čopič, *Frontiers in cell and developmental biology* **2021**, *9*, 737907.
[55] M. Son, E. London, *Journal of lipid research* **2013**, *54*, 3385.
[56] D. M. Engelman, *Nature* **2005**, *438*, 578.
[57] M. Green, M. Ishino, P. M. Loewenstein, *Cell* **1989**, *58*, 215.
[58] J. Xie, Y. Bi, H. Zhang, S. Dong, L. Teng, R. J. Lee, Z. Yang, *Frontiers in pharmacology* **2020**, *11*, 697.
[59] W. Hu, W. Cai, Y. Wu, C. Ren, D. Yu, T. Li, T. Shen, D. Xu, J. Yu, *International journal of nanomedicine* **2024**, *19*, 35.
[60] Y. Tian, M. Zhou, H. Shi, S. Gao, G. Xie, M. Zhu, M. Wu, J. Chen, Z. Niu, *Nano letters* **2018**, *18*, 5453.
[61] R. R. Lulla, S. Goldman, T. Yamada, C. W. Beattie, L. Bressler, M. Pacini, I. F. Pollack, P. G. Fisher, R. J. Packer, I. J. Dunkel et al., *Neuro-oncology* **2016**, *18*, 1319.
[62] G. J.-B. Philippe, A. Mittermeier, N. Lawrence, Y.-H. Huang, N. D. Condon, A. Loewer, D. J. Craik, S. T. Henriques, *ACS chemical biology* **2021**, *16*, 414.
[63] G. J.-B. Philippe, Y.-H. Huang, A. Mittermeier, C. J. Brown, Q. Kaas, S. R. Ramlan, C. K. Wang, D. Lane, A. Loewer, S. Troeira Henriques et al., *Journal of medicinal chemistry* **2024**, *67*, 1197.
[64] I. Sadeghian, B. Khalvati, Y. Ghasemi, S. Hemmati, *Toxicology and applied pharmacology* **2018**, *346*, 9.
[65] J. Gaston, N. Maestrali, G. Lalle, M. Gagnaire, A. Masiero, B. Dumas, T. Dabdoubi, K. Radošević, P.-F. Berne, *Scientific reports* **2019**, *9*, 18688.

[66] K. Singh, W. Ejaz, K. Dutta, S. Thayumanavan, *Bioconjugate chemistry* **2019**, *30*, 1028.
[67] J. Bae, Y. Song, *Synthetic and systems biotechnology* **2021**, *6*, 343.
[68] M. Di Pisa, G. Chassaing, J.-M. Swiecicki, *Biochemistry* **2015**, *54*, 194.
[69] G. Klocek, T. Schulthess, Y. Shai, J. Seelig, *Biochemistry* **2009**, *48*, 2586.
[70] N. Sitaram, R. Nagaraj, *Biochimica et biophysica acta* **1999**, *1462*, 29.
[71] H. Jenssen, P. Hamill, R. E. W. Hancock, *Clinical microbiology reviews* **2006**, *19*, 491.
[72] C.-C. Lee, Y. Sun, H. W. Huang, *Biophysical journal* **2010**, *98*, 2236.
[73] F. Duchardt, M. Fotin-Mleczek, H. Schwarz, R. Fischer, R. Brock, *Traffic (Copenhagen, Denmark)* **2007**, *8*, 848.
[74] M. Kaksonen, A. Roux, *Nature reviews. Molecular cell biology* **2018**, *19*, 313.
[75] A. Ferrari, V. Pellegrini, C. Arcangeli, A. Fittipaldi, M. Giacca, F. Beltram, *Molecular therapy : the journal of the American Society of Gene Therapy* **2003**, *8*, 284.
[76] I. M. Kaplan, J. S. Wadia, S. F. Dowdy, *Journal of controlled release : official journal of the Controlled Release Society* **2005**, *102*, 247.
[77] J. S. Wadia, R. V. Stan, S. F. Dowdy, *Nature medicine* **2004**, *10*, 310.
[78] A. Gori, G. Lodigiani, S. G. Colombarolli, G. Bergamaschi, A. Vitali, *ChemMedChem* **2023**, *18*, e202300236.
[79] S. Guha, J. Ghimire, E. Wu, W. C. Wimley, *Chemical reviews* **2019**, *119*, 6040.
[80] W. B. Kauffman, T. Fuselier, J. He, W. C. Wimley, *Trends in biochemical sciences* **2015**, *40*, 749.
[81] M. T. d. P. Favaro, N. Serna, L. Sánchez-García, R. Cubarsi, M. Roldán, A. Sánchez-Chardi, U. Unzueta, R. Mangues, N. Ferrer-Miralles, A. R. Azzoni et al., *Nanomedicine : nanotechnology, biology, and medicine* **2018**, *14*, 1777.
[82] A. Ziegler, J. Seelig, *Biochemistry* **2011**, *50*, 4650.
[83] M. Buyanova, A. Sahni, R. Yang, A. Sarkar, H. Salim, D. Pei, *Molecular pharmaceutics* **2022**, *19*, 1378.
[84] J. P. Richard, K. Melikov, H. Brooks, P. Prevot, B. Lebleu, L. V. Chernomordik, *Journal of Biological Chemistry* **2005**, *280*, 15300.
[85] K. Ho, C. Morfin, K. Slowinska, *Molecules (Basel, Switzerland)* **2019**, *24*.
[86] A. F. L. Schneider, M. Kithil, M. C. Cardoso, M. Lehmann, C. P. R. Hackenberger, *Nature chemistry* **2021**, *13*, 530.
[87] J. V. V. Arafiles, J. Franke, L. Franz, J. Gómez-González, K. Kemnitz-Hassanin, C. P. R. Hackenberger, *Journal of the American Chemical Society* **2023**, *145*, 24535.
[88] S. G. Patel, E. J. Sayers, L. He, R. Narayan, T. L. Williams, E. M. Mills, R. K. Allemann, L. Y. P. Luk, A. T. Jones, Y.-H. Tsai, *Scientific reports* **2019**, *9*, 6298.
[89] S. F. Dowdy, C. J. Gallagher, D. Vitarella, J. Brown, *Expert opinion on drug delivery* **2023**, *20*, 1157.
[90] J. D. Carruthers, S. Fagien, J. H. Joseph, S. D. Humphrey, B. S. Biesman, C. J. Gallagher, Y. Liu, R. G. Rubio, *Plastic and reconstructive surgery* **2020**, *145*, 45.
[91] N. Solish, J. Carruthers, J. Kaufman, R. G. Rubio, T. M. Gross, C. J. Gallagher, *Drugs* **2021**, *81*, 2091.
[92] M. Hallett, *Toxicon : official journal of the International Society on Toxinology* **2015**, *107*, 64.
[93] M. Akishiba, T. Takeuchi, Y. Kawaguchi, K. Sakamoto, H.-H. Yu, I. Nakase, T. Takatani-Nakase, F. Madani, A. Gräslund, S. Futaki, *Nature chemistry* **2017**, *9*, 751.
[94] M. Akishiba, S. Futaki, *Molecular pharmaceutics* **2019**, *16*, 2540.
[95] Y. Nomura, K. Sakamoto, M. Akishiba, T. Iwata, H. Hirose, S. Futaki, *Bioorganic & medicinal chemistry letters* **2020**, *30*, 127362.
[96] K. Sakamoto, M. Akishiba, T. Iwata, K. Murata, S. Mizuno, K. Kawano, M. Imanishi, F. Sugiyama, S. Futaki, *Angewandte Chemie (International ed. in English)* **2020**, *59*, 19990.
[97] Y. S. Chang, B. Graves, V. Guerlavais, C. Tovar, K. Packman, K.-H. To, K. A. Olson, K. Kesavan, P. Gangurde, A. Mukherjee et al., *Proceedings of the National Academy of Sciences of the United States of America* **2013**, *110*, E3445-54.
[98] C. J. Brown, S. Lain, C. S. Verma, A. R. Fersht, D. P. Lane, *Nature reviews. Cancer* **2009**, *9*, 862.
[99] E. H. Baugh, H. Ke, A. J. Levine, R. A. Bonneau, C. S. Chan, *Cell death and differentiation* **2018**, *25*, 154.

[100] A. Chandramohan, H. Josien, T. Y. Yuen, R. Duggal, D. Spiegelberg, L. Yan, Y.-C. A. Juang, L. Ge, P. G. Aronica, H. Y. K. Kaan et al., *Nature communications* **2024**, *15*, 489.
[101] G. G. Rhys, J. A. Cross, W. M. Dawson, H. F. Thompson, S. Shanmugaratnam, N. J. Savery, M. P. Dodding, B. Höcker, D. N. Woolfson, *Nature chemical biology* **2022**, *18*, 999.
[102] J. A. Cross, M. S. Chegkazi, R. A. Steiner, D. N. Woolfson, M. P. Dodding, *Cell chemical biology* **2021**, *28*, 1347-1355.e5.
[103] A. Klipp, M. Burger, J.-C. Leroux, *Advanced drug delivery reviews* **2023**, *200*, 115047.
[104] S. L. Y. Teo, J. J. Rennick, D. Yuen, H. Al-Wassiti, A. P. R. Johnston, C. W. Pouton, *Nature communications* **2021**, *12*, 3721.
[105] J. R. LaRochelle, G. B. Cobb, A. Steinauer, E. Rhoades, A. Schepartz, *Journal of the American Chemical Society* **2015**, *137*, 2536.
[106] R. Rezgui, K. Blumer, G. Yeoh-Tan, A. J. Trexler, M. Magzoub, *Biochimica et biophysica acta* **2016**, *1858*, 1499.
[107] Y. Behzadipour, S. Hemmati, *Molecules (Basel, Switzerland)* **2019**, *24*.
[108] A. K. Cardozo, V. Buchillier, M. Mathieu, J. Chen, F. Ortis, L. Ladrière, N. Allaman-Pillet, O. Poirot, S. Kellenberger, J. S. Beckmann et al., *Biochimica et biophysica acta* **2007**, *1768*, 2222.
[109] K. S. Kawamura, M. Sung, E. Bolewska-Pedyczak, J. Gariépy, *Biochemistry* **2006**, *45*, 1116.
[110] F. S. Hassane, G. D. Ivanova, E. Bolewska-Pedyczak, R. Abes, A. A. Arzumanov, M. J. Gait, B. Lebleu, J. Gariépy, *Bioconjugate chemistry* **2009**, *20*, 1523.
[111] M. Grillaud, A. Bianco, *Journal of peptide science : an official publication of the European Peptide Society* **2015**, *21*, 330.
[112] J. Kwak, A. de Capua, E. Locardi, M. Goodman, *Journal of the American Chemical Society* **2002**, *124*, 14085.
[113] A. M. Angeles-Boza, A. Erazo-Oliveras, Y.-J. Lee, J.-P. Pellois, *Bioconjugate chemistry* **2010**, *21*, 2164.
[114] D. Singh, S. K. Bisland, K. Kawamura, J. Gariépy, *Bioconjugate chemistry* **1999**, *10*, 745.
[115] T. A. Pringle, O. Coleman, A. Kawamura, J. C. Knight, *RSC advances* **2022**, *12*, 27716.
[116] E. Díaz-Montes, *Polysaccharides* **2021**, *2*, 554.
[117] D. Kim, J. F. Robyt, S.-Y. Lee, J.-H. Lee, Y.-M. Kim, *Carbohydrate research* **2003**, *338*, 1183.
[118] R. M. Prechtl, D. Janßen, J. Behr, C. Ludwig, B. Küster, R. F. Vogel, F. Jakob, *Frontiers in microbiology* **2018**, *9*, 2796.
[119] T. Heinze, T. Liebert, B. Heublein, S. Hornig in *Advances in Polymer Science* (Ed.: D. Klemm), Springer Berlin Heidelberg, **2006**, pp. 199–291.
[120] M. Naessens, an Cerdobbel, W. Soetaert, E. J. Vandamme, *J of Chemical Tech & Biotech* **2005**, *80*, 845.
[121] W. Gan, H. Zhang, Y. Zhang, X. Hu, *Carbohydrate polymers* **2014**, *112*, 387.
[122] Z. Su, J. Luo, M. Pinelo, Y. Wan, *Journal of Membrane Science* **2018**, *555*, 268.
[123] R. Shukla, I. Iliev, A. Goyal, *Biotechnology & Biotechnological Equipment* **2010**, *24*, 576.
[124] E. Tiryaki, Y. Başaran Elalmış, B. Karakuzu İkizler, S. Yücel, *Journal of Drug Delivery Science and Technology* **2020**, *56*, 101517.
[125] A. R. Petrovici, M. Pinteala, N. Simionescu, *Molecules (Basel, Switzerland)* **2023**, *28*.
[126] J. Han, F. Hang, B. Guo, Z. Liu, C. You, Z. Wu, *Carbohydrate polymers* **2014**, *112*, 556.
[127] J. Lundqvist, "Fundamentals of size exclusion chromatography. How size exclusion chromatography (SEC) works and how you use it to purify proteins", can be found under https://www.cytivalifesciences.com/en/us/solutions/protein-research/knowledge-center/protein-purification-methods/size-exclusion-chromatography, **2022**.
[128] "Sephadex Ion Exchange Resins. Ion Exchange Chromatography", can be found under https://cdn.cytivalifesciences.com/api/public/content/digi-11385-original, **2020**.
[129] F. d. S. Campos, D. L. Cassimiro, M. S. Crespi, A. E. Almeida, M. P. D. Gremião, *Braz. J. Pharm. Sci.* **2013**, *49*, 75.
[130] M. Zhang, Y. Huang, W. Pan, X. Tong, Q. Zeng, T. Su, X. Qi, J. Shen, *Carbohydrate polymers* **2021**, *253*, 117213.

[131] Y. Pérez, A. Valdivia, H. L. Ramírez, R. Villalonga, *Macromol. Rapid Commun.* **2005**, *26*, 1304.
[132] X. Zhang, T. Zhang, X. Ma, Y. Wang, Y. Lu, D. Jia, X. Huang, J. Chen, Z. Xu, F. Wen, *Asian journal of pharmaceutical sciences* **2020**, *15*, 605.
[133] H. Schneider, L. Deweid, T. Pirzer, D. Yanakieva, S. Englert, B. Becker, O. Avrutina, H. Kolmar, *ChemistryOpen* **2019**, *8*, 354.
[134] P. Bitsch, E. S. Baum, I. Beltrán Hernández, S. Bitsch, J. Harwood, S. Oliveira, H. Kolmar, *Pharmaceutics* **2023**, *15*.
[135] J. Xu, Y. Liu, S.-H. Hsu, *Molecules (Basel, Switzerland)* **2019**, *24*.
[136] R. Axén, J. Porath, S. Ernback, *Nature* **1967**, *214*, 1302.
[137] J. Maia, R. A. Carvalho, J. F. Coelho, P. N. Simões, M. H. Gil, *Polymer* **2011**, *52*, 258.
[138] M. Curcio, G. Cirillo, A. Paolì, G. D. Naimo, L. Mauro, D. Amantea, A. Leggio, F. P. Nicoletta, F. Iemma, *Colloids and surfaces. B, Biointerfaces* **2020**, *185*, 110537.
[139] M. Richter, A. Chakrabarti, I. R. Ruttekolk, B. Wiesner, M. Beyermann, R. Brock, J. Rademann, *Chemistry (Weinheim an der Bergstrasse, Germany)* **2012**, *18*, 16708.
[140] B. Becker, S. Englert, H. Schneider, D. Yanakieva, S. Hofmann, C. Dombrowsky, A. Macarrón Palacios, S. Bitsch, A. Elter, T. Meckel et al., *Journal of peptide science : an official publication of the European Peptide Society* **2021**, *27*, e3298.
[141] M. Howarth, D. J.-F. Chinnapen, K. Gerrow, P. C. Dorrestein, M. R. Grandy, N. L. Kelleher, A. El-Husseini, A. Y. Ting, *Nature methods* **2006**, *3*, 267.
[142] P. C. Weber, D. H. Ohlendorf, J. J. Wendoloski, F. R. Salemme, *Science (New York, N.Y.)* **1989**, *243*, 85.
[143] K. H. Lim, H. Huang, A. Pralle, S. Park, *Biotechnology and bioengineering* **2013**, *110*, 57.
[144] C. E. Chivers, A. L. Koner, E. D. Lowe, M. Howarth, *The Biochemical journal* **2011**, *435*, 55.
[145] C. de Las Heras Alarcon, S. Pennadam, C. Alexander, *Chemical Society reviews* **2005**, *34*, 276.
[146] T. Kawato, E. Mizohata, T. Meshizuka, H. Doi, T. Kawamura, H. Matsumura, K. Yumura, K. Tsumoto, T. Kodama, T. Inoue et al., *Journal of bioscience and bioengineering* **2015**, *119*, 642.
[147] C. F. Cahall, J. L. Lilly, E. A. Hirschowitz, B. J. Berron, *Breast cancer : basic and clinical research* **2015**, *9*, 1.
[148] E. Ruoslahti, *Nature reviews. Cancer* **2002**, *2*, 83.
[149] M. Essler, E. Ruoslahti, *Proceedings of the National Academy of Sciences of the United States of America* **2002**, *99*, 2252.
[150] M. Mäe, H. Myrberg, S. El-Andaloussi, Ü. Langel, *Int J Pept Res Ther* **2009**, *15*, 11.
[151] H. Myrberg, L. Zhang, M. Mäe, U. Langel, *Bioconjugate chemistry* **2008**, *19*, 70.
[152] M. Nieberler, U. Reuning, F. Reichart, J. Notni, H.-J. Wester, M. Schwaiger, M. Weinmüller, A. Räder, K. Steiger, H. Kessler, *Cancers* **2017**, *9*.
[153] M. Tucci, S. Stucci, F. Silvestris, *The Lancet. Oncology* **2014**, *15*, e584-e585.
[154] C. Mas-Moruno, F. Rechenmacher, H. Kessler, *Anti-cancer agents in medicinal chemistry* **2010**, *10*, 753.
[155] L. Feni, S. Parente, C. Robert, S. Gazzola, D. Arosio, U. Piarulli, I. Neundorf, *Bioconjugate chemistry* **2019**, *30*, 2011.
[156] M. Jain, S. C. Chauhan, A. P. Singh, G. Venkatraman, D. Colcher, S. K. Batra, *Cancer research* **2005**, *65*, 7840.
[157] Y. Liu, L. Mei, C. Xu, Q. Yu, K. Shi, L. Zhang, Y. Wang, Q. Zhang, H. Gao, Z. Zhang et al., *Theranostics* **2016**, *6*, 177.
[158] E. Kondo, K. Saito, Y. Tashiro, K. Kamide, S. Uno, T. Furuya, M. Mashita, K. Nakajima, T. Tsumuraya, N. Kobayashi et al., *Nature communications* **2012**, *3*, 951.
[159] S. K. Maity, P. Stahl, A. Hensel, S. Knauer, C. Hirschhäuser, C. Schmuck, *Chemistry (Weinheim an der Bergstrasse, Germany)* **2020**, *26*, 3010.
[160] N. M. Anderson, M. C. Simon, *Current biology : CB* **2020**, *30*, R921-R925.
[161] H. de Jong, K. M. Bonger, D. W. P. M. Löwik, *RSC chemical biology* **2020**, *1*, 192.
[162] A. Bernkop-Schnürch, *Advanced drug delivery reviews* **2018**, *136-137*, 62.
[163] S. Mustafa, S. Koran, L. AlOmair, *Frontiers in molecular biosciences* **2022**, *9*, 896099.

[164] T. Jiang, E. S. Olson, Q. T. Nguyen, M. Roy, P. A. Jennings, R. Y. Tsien, *Proceedings of the National Academy of Sciences of the United States of America* **2004**, *101*, 17867.
[165] T. A. Aguilera, E. S. Olson, M. M. Timmers, T. Jiang, R. Y. Tsien, *Integrative biology : quantitative biosciences from nano to macro* **2009**, *1*, 371.
[166] E. S. Olson, T. A. Aguilera, T. Jiang, L. G. Ellies, Q. T. Nguyen, E. H. Wong, L. A. Gross, R. Y. Tsien, *Integrative biology : quantitative biosciences from nano to macro* **2009**, *1*, 382.
[167] J. S. Ryu, F. Kratz, D. Raucher, *IJMS* **2021**, *22*.
[168] J. Yoo, N. Sanoj Rejinold, D. Lee, S. Jon, Y.-C. Kim, *Journal of controlled release : official journal of the Controlled Release Society* **2017**, *264*, 89.
[169] M. Whitney, J. L. Crisp, E. S. Olson, T. A. Aguilera, L. A. Gross, L. G. Ellies, R. Y. Tsien, *The Journal of biological chemistry* **2010**, *285*, 22532.
[170] M. Whitney, E. N. Savariar, B. Friedman, R. A. Levin, J. L. Crisp, H. L. Glasgow, R. Lefkowitz, S. R. Adams, P. Steinbach, N. Nashi et al., *Angewandte Chemie (International ed. in English)* **2013**, *52*, 325.
[171] T. Sato, S. Takahashi, T. Mizumoto, M. Harao, M. Akizuki, M. Takasugi, T. Fukutomi, J. Yamashita, *Surgical oncology* **2006**, *15*, 217.
[172] S. A. Bode, M. B. Hansen, R. A. J. F. Oerlemans, J. C. M. van Hest, D. W. P. M. Löwik, *Bioconjugate chemistry* **2015**, *26*, 850.
[173] H. Han, Y. Hou, X. Chen, P. Zhang, M. Kang, Q. Jin, J. Ji, M. Gao, *Journal of the American Chemical Society* **2020**, *142*, 4944.
[174] Y. Zhang, L. Li, L. Chang, H. Liu, J. Song, Y. Liu, H. Bao, B. Liu, R. Wang, J. Ni, *Chemical biology & drug design* **2019**, *94*, 1884.
[175] B. Xiang, X.-L. Jia, J.-L. Qi, L.-P. Yang, W.-H. Sun, X. Yan, S.-K. Yang, D.-Y. Cao, Q. Du, X.-R. Qi, *International journal of nanomedicine* **2017**, *12*, 2385.
[176] R. Weinstain, E. N. Savariar, C. N. Felsen, R. Y. Tsien, *Journal of the American Chemical Society* **2014**, *136*, 874.
[177] Y. Shamay, L. Adar, G. Ashkenasy, A. David, *Biomaterials* **2011**, *32*, 1377.
[178] G. C. Kim, J. H. Ahn, J. H. Oh, S. Nam, S. Hyun, J. Yu, Y. Lee, *Biomacromolecules* **2018**, *19*, 2863.
[179] P. D. Senter, C. J. Springer, *Advanced drug delivery reviews* **2001**, *53*, 247.
[180] S. K. Sharma, K. D. Bagshawe, *Advanced drug delivery reviews* **2017**, *118*, 2.
[181] Z. Sun, J. Huang, Z. Fishelson, C. Wang, S. Zhang, *Biomedicines* **2023**, *11*.
[182] S. Afshar, T. Asai, S. L. Morrison, *Molecular cancer therapeutics* **2009**, *8*, 185.
[183] Q.-J. Wu, T.-N. Zhang, H.-H. Chen, X.-F. Yu, J.-L. Lv, Y.-Y. Liu, Y.-S. Liu, G. Zheng, J.-Q. Zhao, Y.-F. Wei et al., *Signal transduction and targeted therapy* **2022**, *7*, 402.
[184] K. G. Hoff, J. L. Avalos, K. Sens, C. Wolberger, *Structure (London, England : 1993)* **2006**, *14*, 1231.
[185] E. Fabbrizi, F. Fiorentino, V. Carafa, L. Altucci, A. Mai, D. Rotili, *Cells* **2023**, *12*.
[186] G. A. Eggimann, S. Buschor, T. Darbre, J.-L. Reymond, *Organic & biomolecular chemistry* **2013**, *11*, 6717.
[187] S. Hofmann, C. Dombrowsky, D. Happel, C. Dessin, E. Cermjani, M. Cica, O. Avrutina, N. Sewald, H. Neumann, H. Kolmar, *ACS chemical biology* **2024**, *19*, 1320.
[188] C.-Y. Jiao, D. Delaroche, F. Burlina, I. D. Alves, G. Chassaing, S. Sagan, *The Journal of biological chemistry* **2009**, *284*, 33957.
[189] H. Young Kim, S. Young Yum, G. Jang, D.-R. Ahn, *Scientific reports* **2015**, *5*, 11719.
[190] I. Nakase, M. Niwa, T. Takeuchi, K. Sonomura, N. Kawabata, Y. Koike, M. Takehashi, S. Tanaka, K. Ueda, J. C. Simpson et al., *Molecular therapy : the journal of the American Society of Gene Therapy* **2004**, *10*, 1011.
[191] H. Yamashita, T. Kato, M. Oba, T. Misawa, T. Hattori, N. Ohoka, M. Tanaka, M. Naito, M. Kurihara, Y. Demizu, *Scientific reports* **2016**, *6*, 33003.
[192] H. C. Hymel, A. Rahnama, O. M. Sanchez, D. Liu, T. J. Gauthier, A. T. Melvin, *Cells* **2022**, *11*.
[193] K. Zhao, R. Harshaw, X. Chai, R. Marmorstein, *Proceedings of the National Academy of Sciences of the United States of America* **2004**, *101*, 8563.
[194] P. Barbier, C. Gregoire, F. Devred, M. Sarrazin, V. Peyrot, *Biochemistry* **2001**, *40*, 13510.

[195] M. J. Edelman, D. R. Gandara, P. Hausner, V. Israel, D. Thornton, J. DeSanto, L. A. Doyle, *Lung cancer (Amsterdam, Netherlands)* **2003**, *39*, 197.
[196] E. Figueras, A. Borbély, M. Ismail, M. Frese, N. Sewald, *Beilstein journal of organic chemistry* **2018**, *14*, 1281.
[197] V. A. Verma, T. H. Pillow, L. DePalatis, G. Li, G. L. Phillips, A. G. Polson, H. E. Raab, S. Spencer, B. Zheng, *Bioorganic & medicinal chemistry letters* **2015**, *25*, 864.
[198] N. G. Caculitan, J. Dela Cruz Chuh, Y. Ma, D. Zhang, K. R. Kozak, Y. Liu, T. H. Pillow, J. Sadowsky, T. K. Cheung, Q. Phung et al., *Cancer research* **2017**, *77*, 7027.
[199] C. Peng, Z. Lu, Z. Xie, Z. Cheng, Y. Chen, M. Tan, H. Luo, Y. Zhang, W. He, K. Yang et al., *Molecular & cellular proteomics : MCP* **2011**, *10*, M111.012658.
[200] D. Klemm (Ed.) *Advances in Polymer Science*, Springer Berlin Heidelberg, **2006**.
[201] B. Becker, *Dissertation*, TU Darmstadt, **2021**.
[202] S. P. Englert, *Dissertation*, TU Darmstadt, **2023**.
[203] S. Agudo-Álvarez, S. S. Díaz-Mínguez, R. Benito-Arenas, *Pure and Applied Chemistry* **2024**, *96*, 691.
[204] A. J. Schmitz, D. G. Hogle, X. S. Gai, E. E. Fenlon, S. H. Brewer, M. J. Tucker, *The journal of physical chemistry. B* **2016**, *120*, 9387.
[205] A. Samudram, B. M. Mangalassery, M. Kowshik, N. Patincharath, G. K. Varier, *Cell biology international* **2016**, *40*, 991.
[206] "Instructions. TNBSA (2,4,6-Trinitrobenzene Sulfonic Acid)", **2008**.
[207] M. Fairhead, M. Howarth, *Methods in molecular biology (Clifton, N.J.)* **2015**, *1266*, 171.
[208] N. Milech, B. A. C. Longville, P. T. Cunningham, M. N. Scobie, H. M. Bogdawa, S. Winslow, M. Anastasas, T. Connor, F. Ong, S. R. Stone et al., *Scientific reports* **2015**, *5*, 18329.
[209] Y. Huang, Z. Jiao, Y. Fu, Y. Hou, J. Sun, F. Hu, S. Yu, K. Gong, Y. Liu, G. Zhao, *European journal of medicinal chemistry* **2024**, *265*, 116121.
[210] K. I. Pellot Ortiz, J. S. Rechberger, L. F. Nonnenbroich, D. J. Daniels, J. N. Sarkaria, *Biomedicines* **2023**, *11*.
[211] A. Finzel, A. Grybowski, J. Strasen, E. Cristiano, A. Loewer, *Molecular biology of the cell* **2016**, *27*, 2360.
[212] A. S. Dixon, M. K. Schwinn, M. P. Hall, K. Zimmerman, P. Otto, T. H. Lubben, B. L. Butler, B. F. Binkowski, T. Machleidt, T. A. Kirkland et al., *ACS chemical biology* **2016**, *11*, 400.
[213] M. P. Hall, J. Unch, B. F. Binkowski, M. P. Valley, B. L. Butler, M. G. Wood, P. Otto, K. Zimmerman, G. Vidugiris, T. Machleidt et al., *ACS chemical biology* **2012**, *7*, 1848.
[214] G. Houthaeve, S. C. de Smedt, K. Braeckmans, W. H. de Vos, *Nano convergence* **2022**, *9*, 6.
[215] M. P. Stewart, A. Sharei, X. Ding, G. Sahay, R. Langer, K. F. Jensen, *Nature* **2016**, *538*, 183.
[216] J. P. Dhandhukia, D. A. Brill, A. Kouhi, M. K. Pastuszka, J. A. MacKay, *Protein science : a publication of the Protein Society* **2017**, *26*, 1785.
[217] S. Okano, Y. Kawaguchi, K. Kawano, H. Hirose, M. Imanishi, S. Futaki, *Bioorganic & medicinal chemistry letters* **2022**, *72*, 128875.
[218] B. Zhitomirsky, H. Farber, Y. G. Assaraf, *Journal of cellular and molecular medicine* **2018**, *22*, 2131.
[219] M. Terasaki, L. A. Jaffe, *Methods in cell biology* **2004**, *74*, 469.
[220] I. Weidenfeld, M. Gossen, R. Löw, D. Kentner, S. Berger, D. Görlich, D. Bartsch, H. Bujard, K. Schönig, *Nucleic acids research* **2009**, *37*, e50.
[221] C. S. Dombrowsky, D. Happel, J. Habermann, S. Hofmann, S. Otmi, B. Cohen, H. Kolmar, *Antibodies (Basel, Switzerland)* **2024**, *13*.

7 Appendix

7.1 Supporting Information

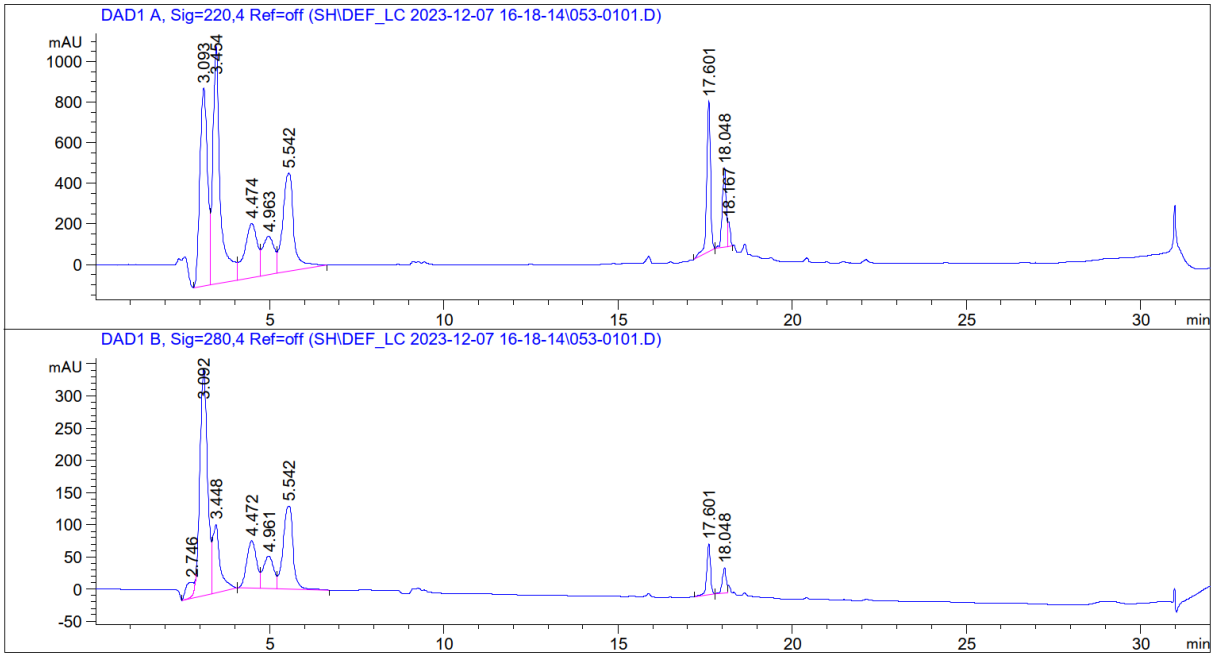

Figure S 1| Analytical RP-HPLC chromatogram (0 to 60 % Eluent B, 220 nm) of L17E5K(Ac)-Pra **8** deacetylated with SirT2. Fully deacetylated peptide: t_R = 17.601 min, peptide with 1 acetyl group remaining: t_R = 18.048 min.

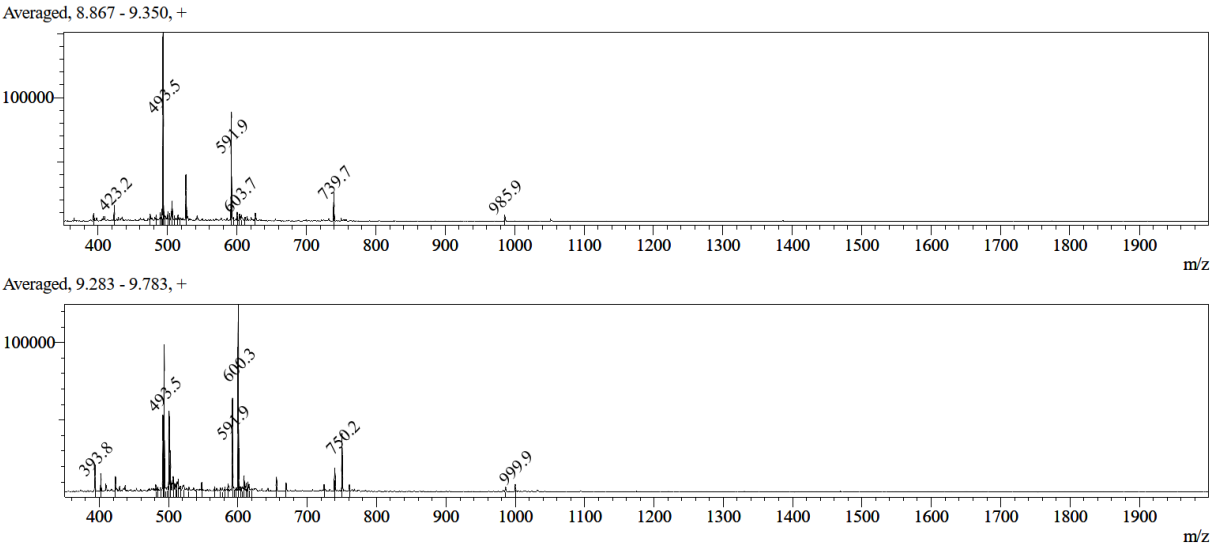

Figure S 2| MS (ESI) spectra of the deacetylation of L17E5K(Ac)-Pra **8** with SirT2 showing masses of the fully deacetylated peptide (top spectrum) and peptide with one acetyl group remaining (bottom spectrum). Fully deacetylated peptide MS (ESI) calculated: $[M+H]^+$ = 2955.5; $[M+2H]^{2+}$ = 1478.3; $[M+3H]^{3+}$ = 985.9; $[M+4H]^{4+}$ = 739.6; $[M+5H]^{5+}$ = 591.9; $[M+6H]^{6+}$ = 493.4; observed: $[M+3H]^{3+}$ = 985.9; $[M+4H]^{4+}$ = 739.7; $[M+5H]^{5+}$ = 591.9; $[M+6H]^{6+}$ = 493.5. Peptide with one acetyl group MS (ESI) calculated: $[M+H]^+$ = 2997.5; $[M+2H]^{2+}$ = 1499.7; $[M+3H]^{3+}$ = 1000.2; $[M+4H]^{4+}$ = 750.4; $[M+5H]^{5+}$ = 600.5; $[M+6H]^{6+}$ = 500.6; observed: $[M+3H]^{3+}$ = 999.9; $[M+4H]^{4+}$ = 750.2; $[M+5H]^{5+}$ = 600.3.

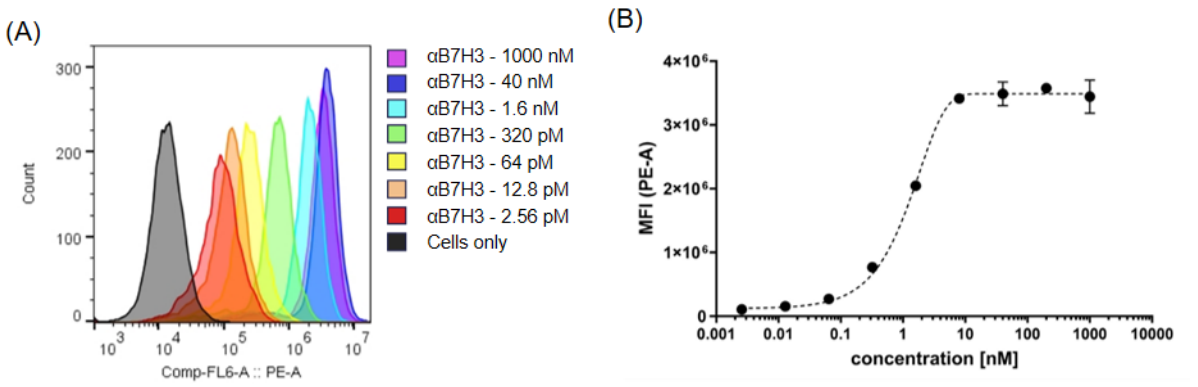

Figure S 3| Binding assay of the antibody anti-B7H3 to HeLa cells in various concentrations. A) Binding assay depicted as FACS plot. B) Plot of GeoMean (PE-A channel) against the concentration (plotted using GraphPad Prism).

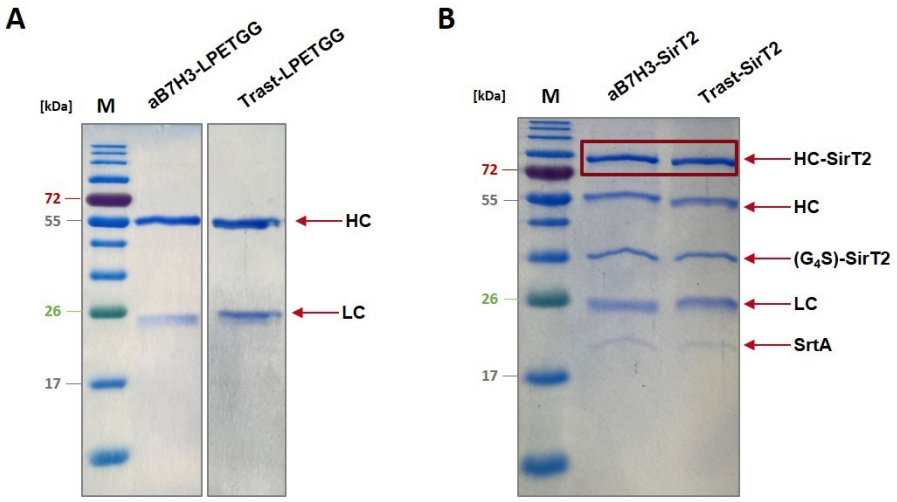

Figure S 4| A) Reducing SDS Gel of anti-B7H3-LPETGG and trastuzumab-LPETGG. B) Reducing SDS Gel of the antibodies after SirT2 conjugation by sortase A ligation.

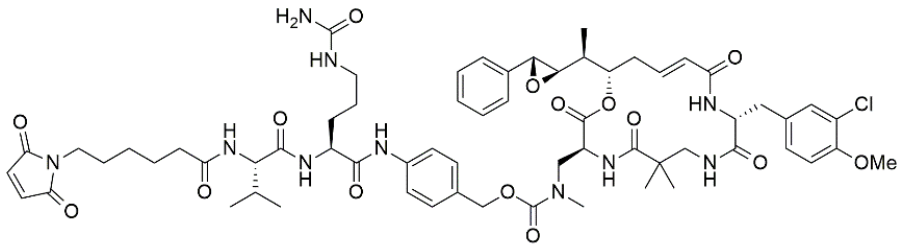

Figure S 5| Molecular structure of Maleimide-Val-Cit-PAB-cryptophycin. Chemical formula: $C_{63}H_{81}ClN_{10}O_{15}$; Molecular weight: 1253.8 g/mol. Synthesized by Cedric Dessin (Working group Norbert Seewald, Bielefeld University).

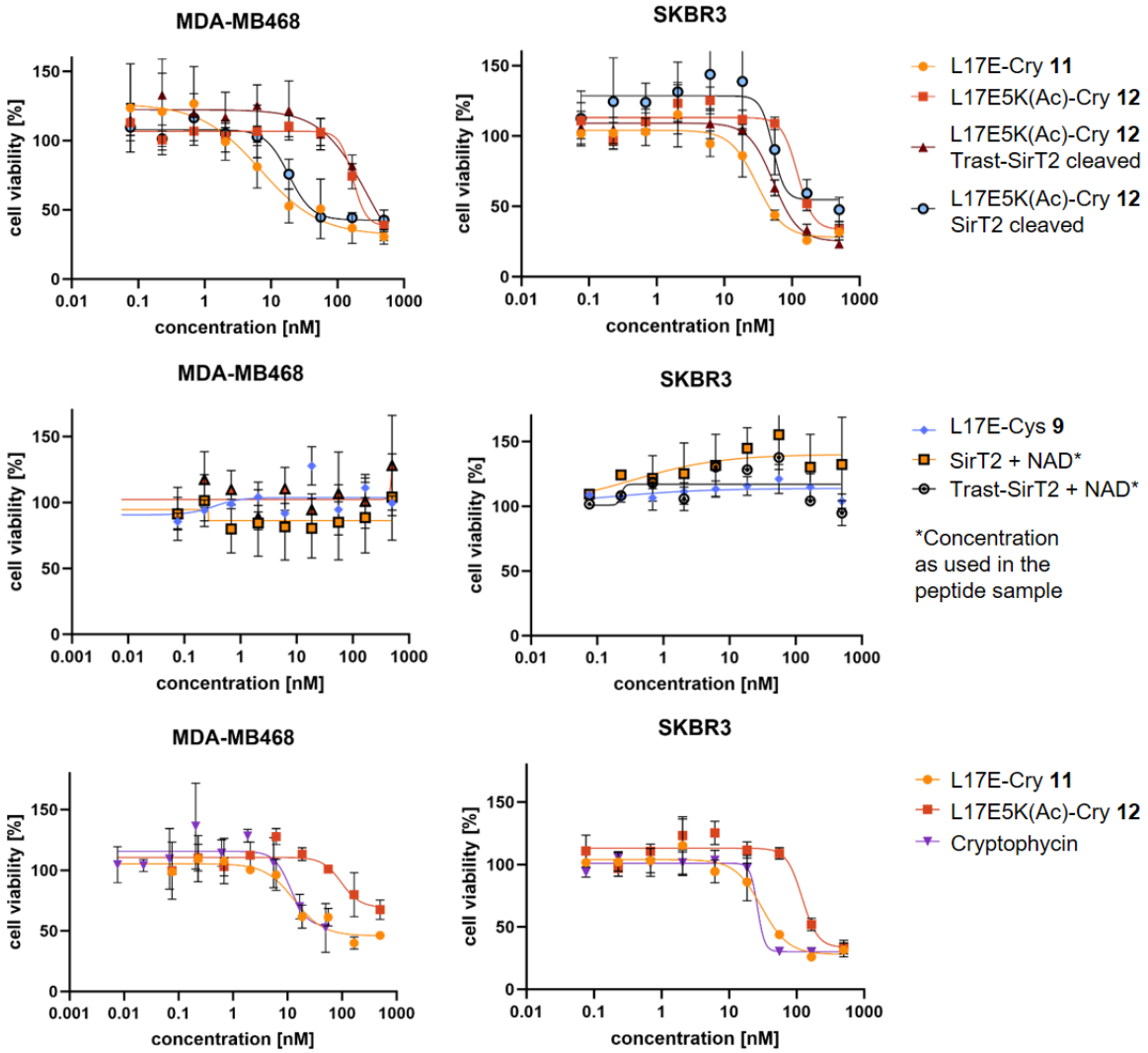

Figure S 6| Further modified cell proliferation assays of L17E-cry **11** and L17E5K(Ac)-cry **12** with controls on SKBR3 and MDA-MB468 cells.

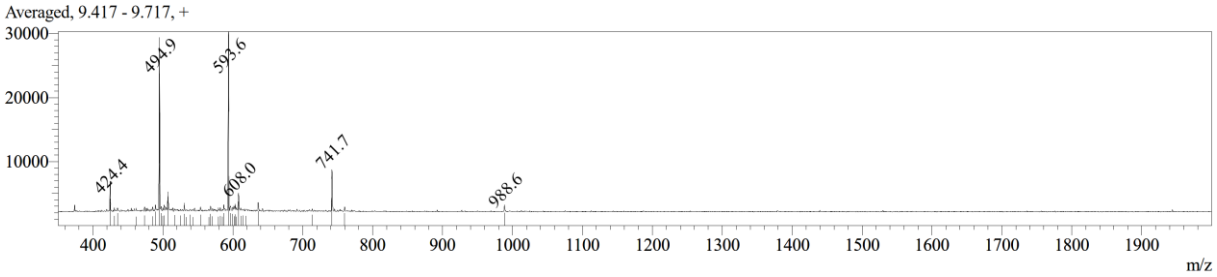

Figure S 7| MS (ESI) spectrum of the desuccinylation of L17E5K(Succ)-Cys **14** with SirT5 showing masses of the fully desuccinylated peptide. MS (ESI) calculated: $[M+H]^{+}$ = 2963.6; $[M+2H]^{2+}$ = 1482.3; $[M+3H]^{3+}$ = 988.5; $[M+4H]^{4+}$ = 741.7; $[M+5H]^{5+}$ = 593.5; $[M+6H]^{6+}$ = 494.8; observed: $[M+3H]^{3+}$ = 988.6; $[M+4H]^{4+}$ = 741.7; $[M+5H]^{5+}$ = 593.6; $[M+6H]^{6+}$ = 494.9.

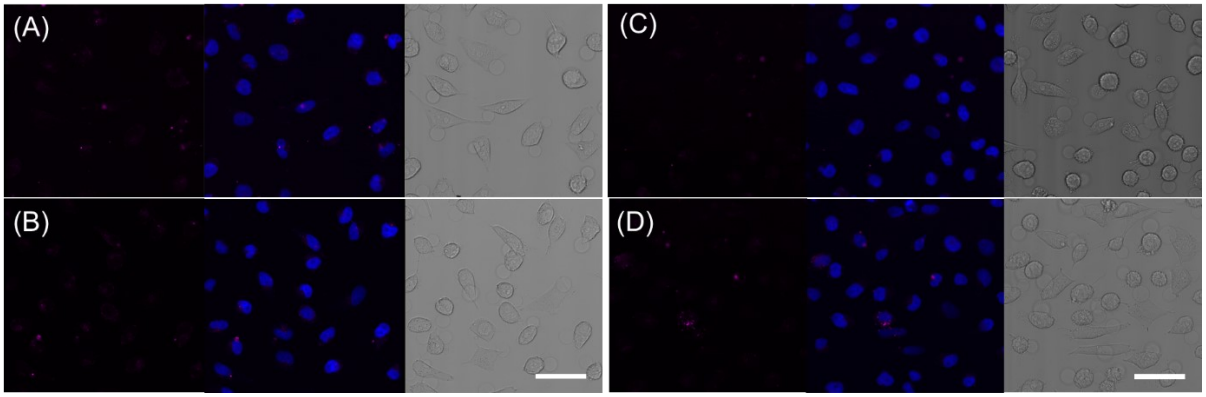

Figure S 8| CLSM images of repeated cellular uptake assay of succinylated L17E peptides on HeLa cells. (A) αB7H3-SirT5 treated and (B) trastuzumab-SirT5 treated cells with L17E5K(Succ)-TAMRA **18**. (C) αB7H3-SirT5 treated and (D) trastuzumab-SirT5 treated cells with $L17E_{K1+K2}^{Succ}$-TAMRA **17**. Scale bar denotes 50 µm.

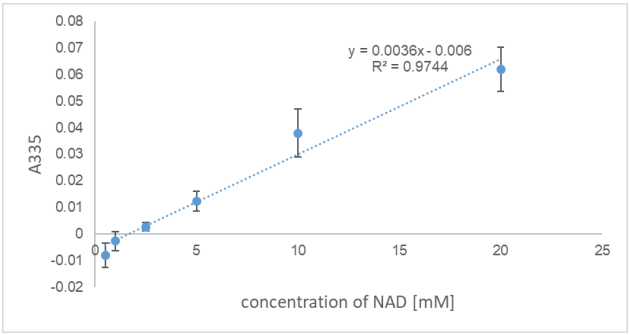

Figure S 9| Plot of the absorption at 335 nm against the NAD concentration in mM (TNBS assay). 2 mM NAD exhibits a negligible absorption value of 0.0012.

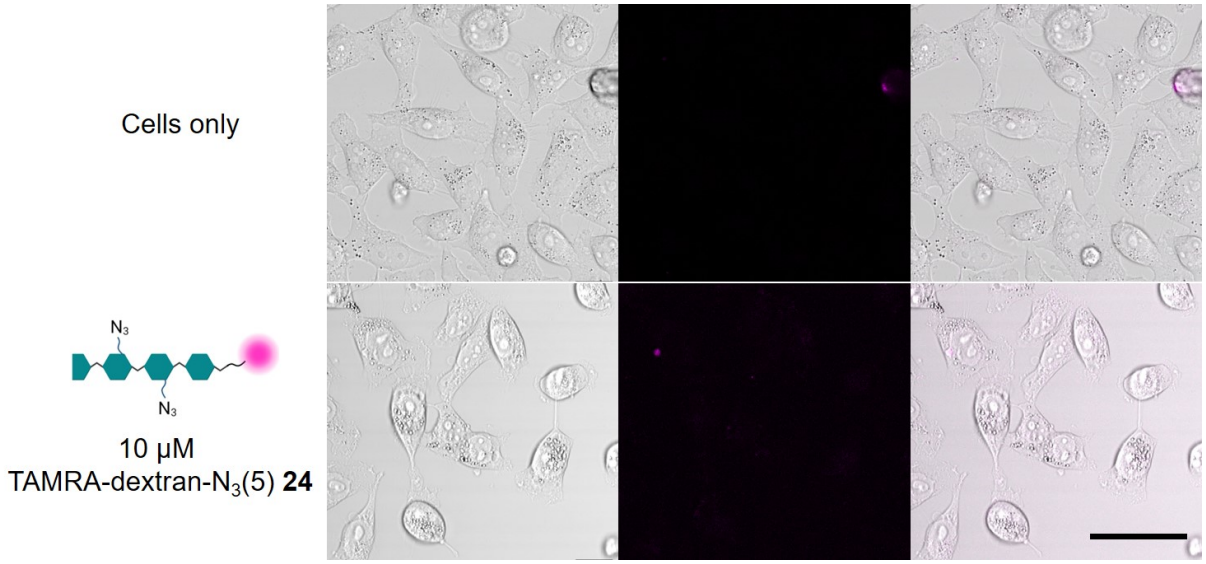

Figure S 10| CLSM images of HeLa cells: cells only and treated with 10 µM TAMRA-dextran-N_3(5) **24** for 1 h and subsequently for 3 h in medium only. Left: brightfield channel, center: fluorescence channel, right: overlay brightfield and fluorescence. The scale bar denotes 50 µm. Images were taken under the same microscopy tuning parameters and processed with ImageJ.

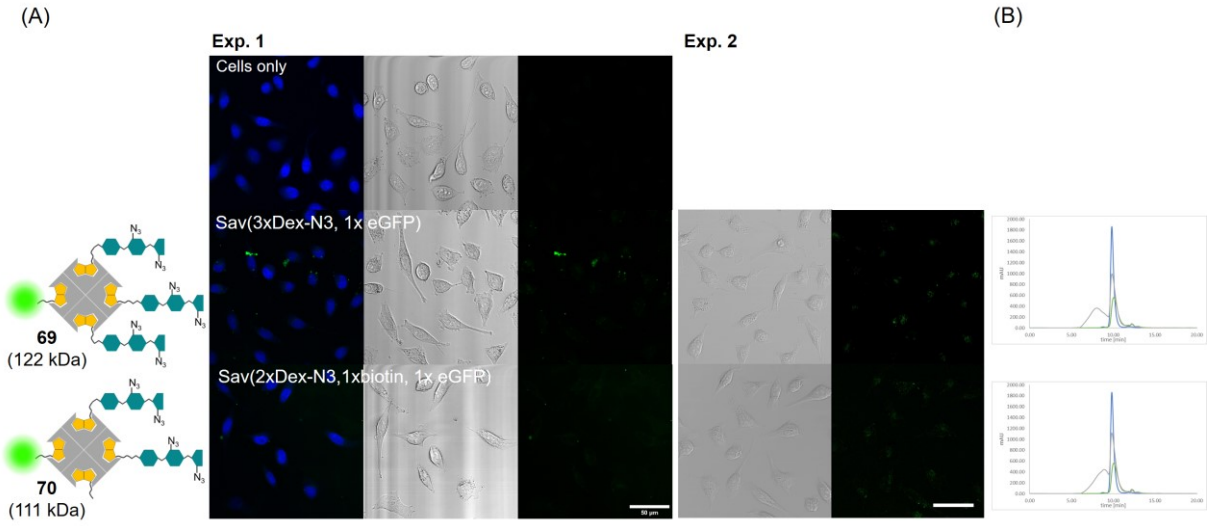

Figure S 11| (A) Control experiments for the intracellular delivery of streptavidin delivery modules with eGFP as payload. CLSM images of HeLa cells treated with medium only, 2 µM Sav(3x-Dex-N_3(6.3) **47**, 1xeGFP **54**) **69** or Sav(2x-Dex-N_3(6.3) **47**, 1xbiotin, 1xeGFP **54**) **70** for 2 h and subsequent 3 h incubation in medium only. For experiment 1: Left: overlay brightfield and fluorescence channel, center: brightfield channel, right: fluorescence channel. For experiment 2: left:brightfield channel, right: fluorescence channel. The scale bar denotes 50 µm. Images of the same experiment were taken under the same microscopy tuning parameters and processed with ImageJ. (B) SEC analysis of streptavidin delivery modules **69+70**, 220 nm. Gray curve: streptavidin delivery module, green curve: eGFP: blue curve: streptavidin.

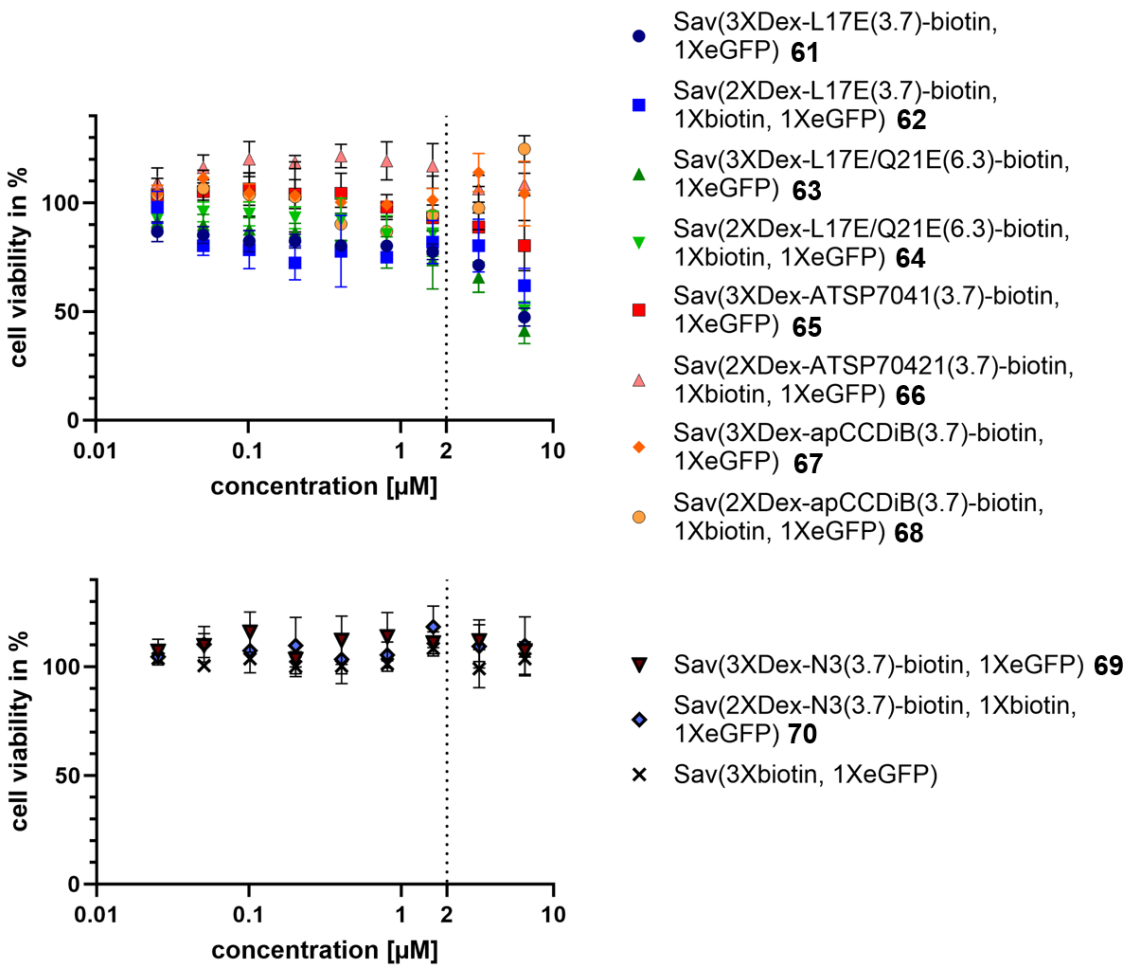

Figure S 12| Cellular proliferation assay of streptavidin delivery modules **61-70** including Sav(3xbiotin, 1xeGFP). The error bars denote the standard deviation from triplicate measurements.

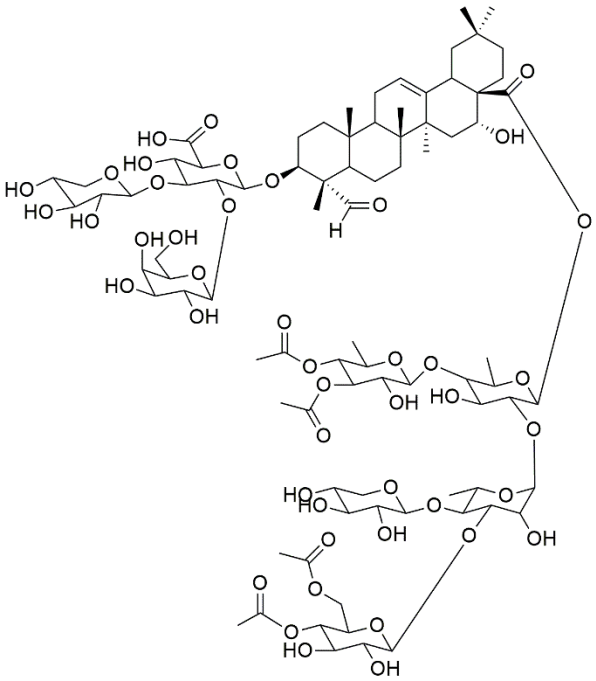

Figure 59| Chemical structure of saponin (provided by Jan Dürig, FU Berlin).

7.2 Analytical Data

7.2.1 Maleimide-Val-Cit-PAB-cryptophycin

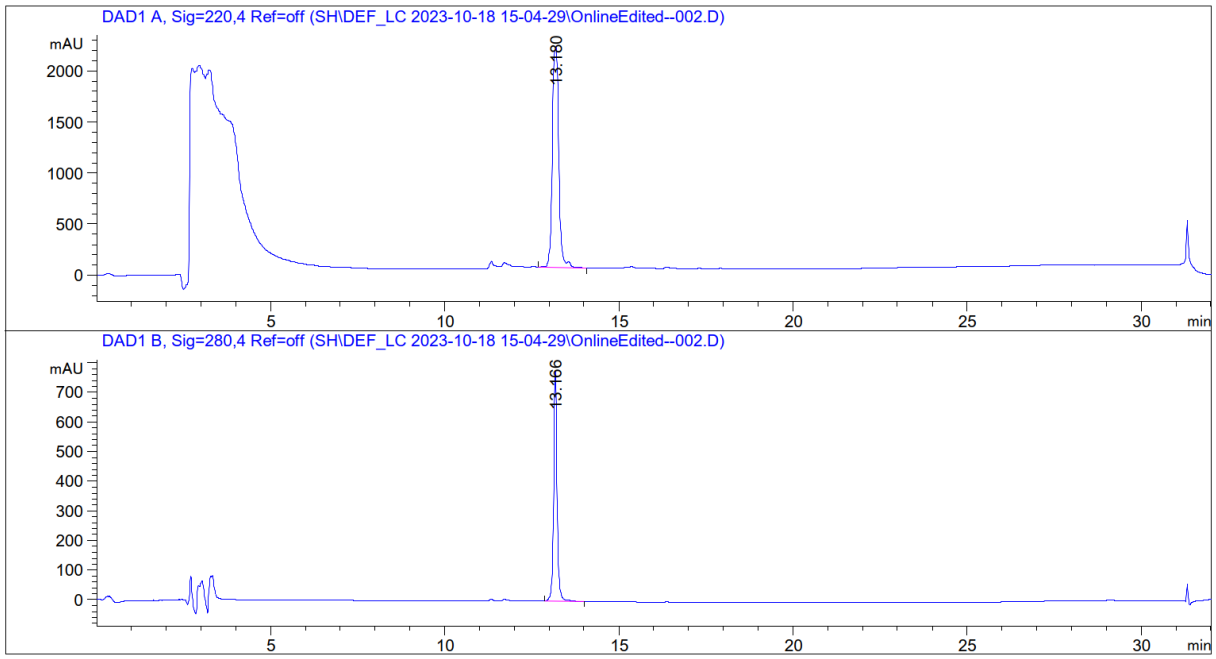

Figure S 13| Analytical RP-HPLC chromatogram of Mal-Val-Cit-PAB-cryptophycin, 30 to 100% B (no TFA) (0.6 mL/min, 20 min gradient), 220 nm (top) and 280 nm (bottom), t_R = 13.180 min.

7.2.2 L17E-TAMRA 1

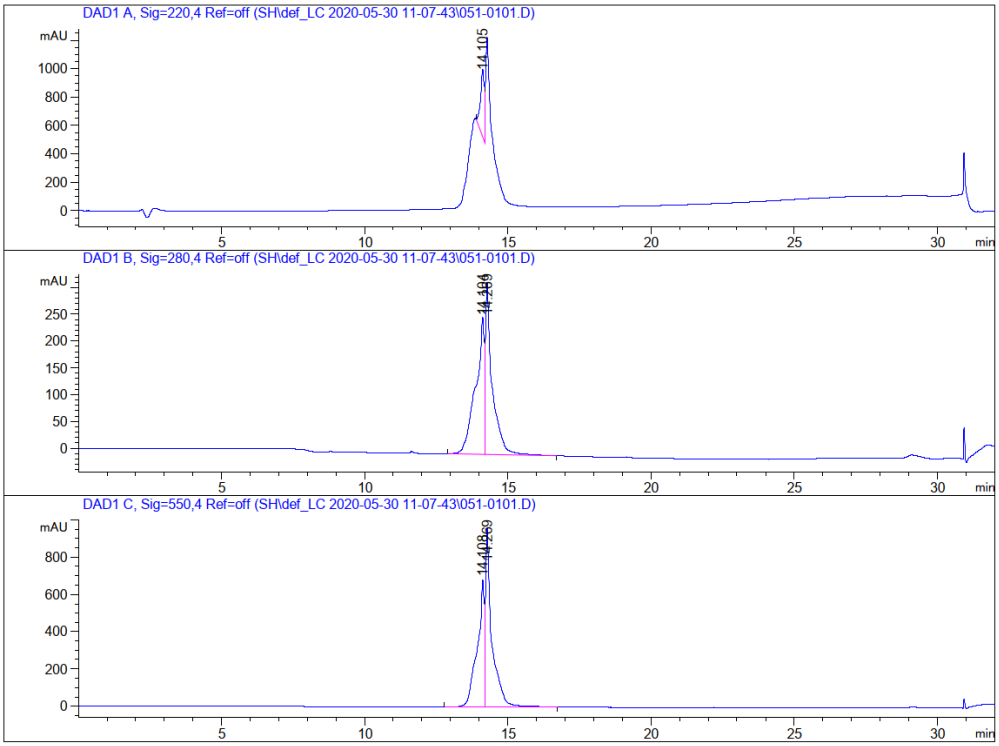

Figure S 14| Analytical RP-HPLC chromatogram of purified L17E-TAMRA peptide **1**, 0 to 100% B (0.6 mL/min, 20 min gradient), 220 nm, 280 nm and 550 nm, t_R = 14.108, 14.269 min. The two peaks denote the 5,6-TAMRA mixed isomer used for labelling of the peptide.

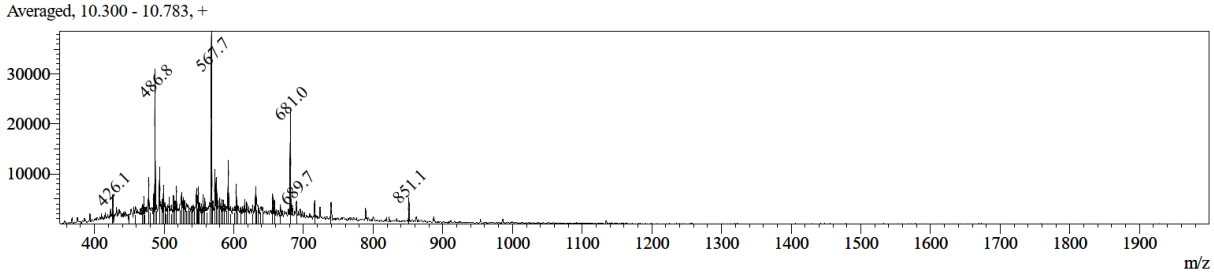

Figure S 15| MS (ESI) spectrum (positive mode) of L17E-TAMRA peptide **1**. Calculated: $[M+H]^{+}$ = 3401.0; $[M+2H]^{2+}$ = 1701.0; $[M+3H]^{3+}$ = 1134.3; $[M+4H]^{4+}$ = 851.0; $[M+5H]^{5+}$ = 681.0; $[M+6H]^{6+}$ = 567.7; $[M+7H]^{7+}$ = 486.7; observed: $[M+4H]^{4+}$ = 851.1; $[M+5H]^{5+}$ = 681.0; $[M+6H]^{6+}$ = 567.7; $[M+7H]^{7+}$ = 486.8.

7.2.3 L17E$_{K1+K2}^{Alloc}$-TAMRA 2

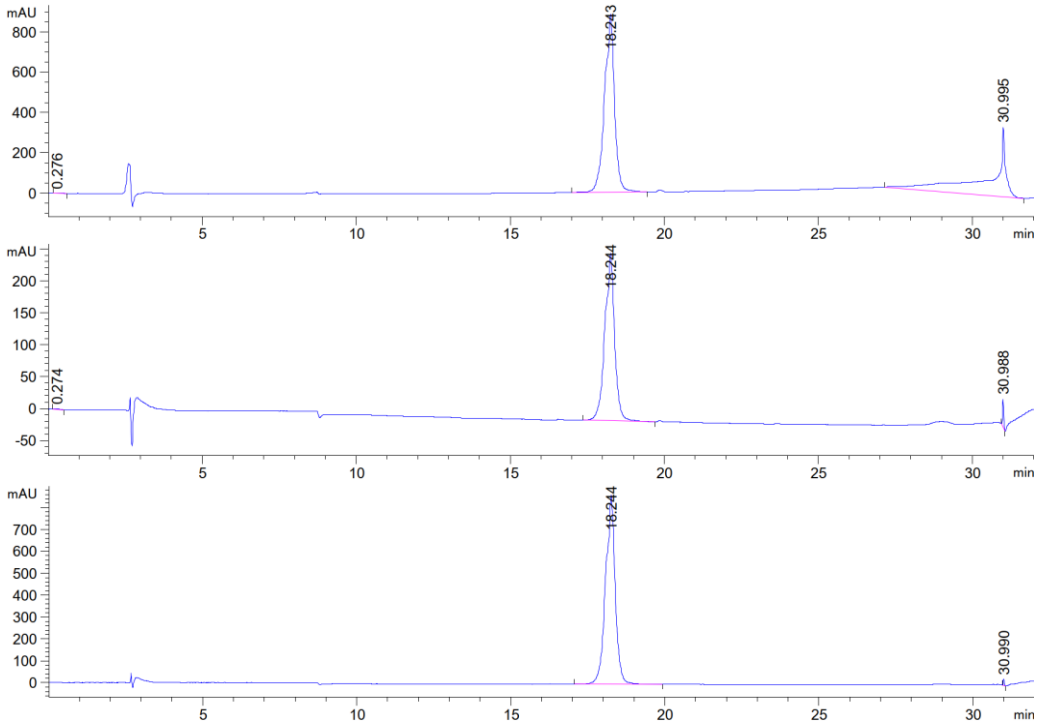

Figure S 16| Analytical RP-HPLC chromatogram of purified L17E$_{K1+K2}^{Alloc}$-TAMRA peptide **2**, 0 to 80% B (0.6 mL/min, 20 min gradient), 220 nm (top), 280 nm (middle) and 550 nm (bottom), t_R = 18.243 min.

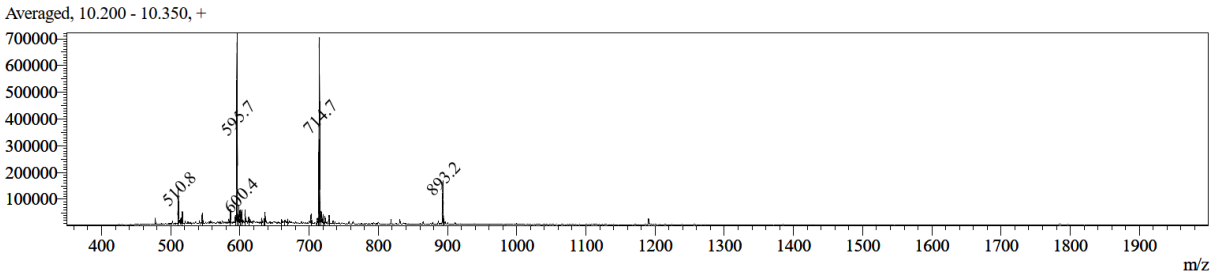

Figure S 17| MS (ESI) spectrum (positive mode) of L17E$_{K1+K2}^{Alloc}$-TAMRA peptide **2**. Calculated: $[M+H]^{+}$ = 3569.2; $[M+2H]^{2+}$ = 1785.1; $[M+3H]^{3+}$ = 1190.4; $[M+4H]^{4+}$ = 893.0; $[M+5H]^{5+}$ = 714.6; $[M+6H]^{6+}$ = 595.7; $[M+7H]^{7+}$ = 510.7; observed: $[M+4H]^{4+}$ = 893.2; $[M+5H]^{5+}$ = 714.7; $[M+6H]^{6+}$ = 595.7; $[M+7H]^{7+}$ = 510.8.

7.2.4 L17E$_{K1+K3}^{Alloc}$-TAMRA 3

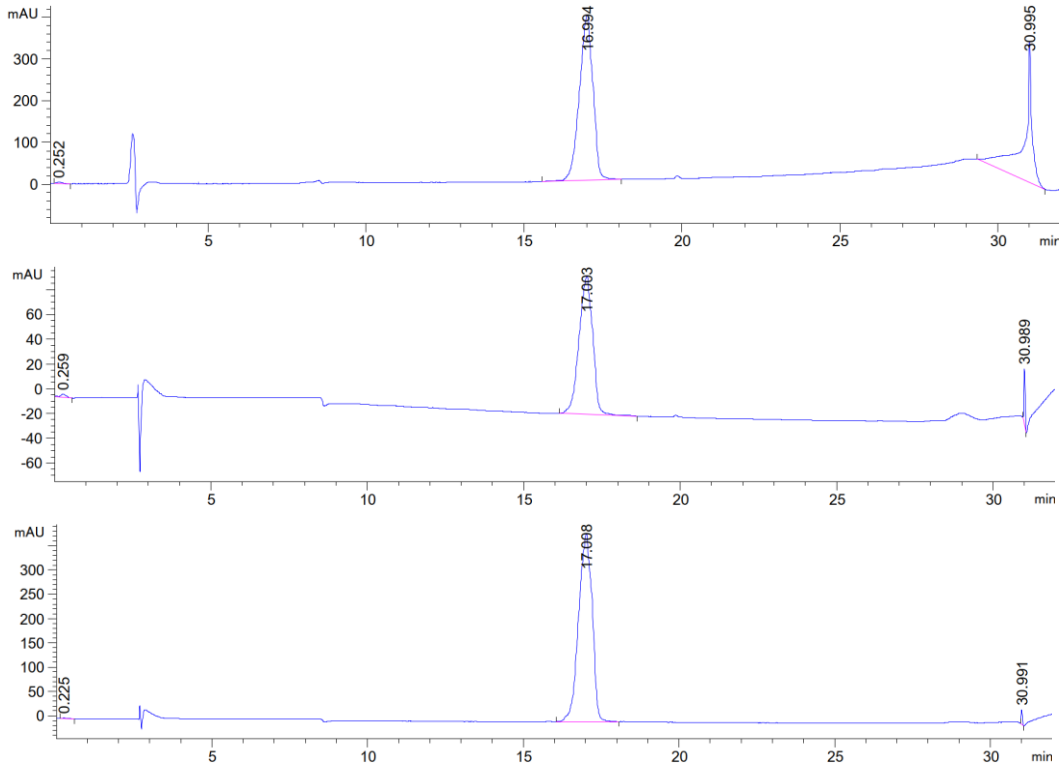

Figure S 18| Analytical RP-HPLC chromatogram of purified L17E$_{K1+K3}^{Alloc}$-TAMRA peptide **3**, 0 to 80% B (0.6 mL/min, 20 min gradient), 220 nm (top), 280 nm (middle) and 550 nm (bottom), t_R = 16.994 min.

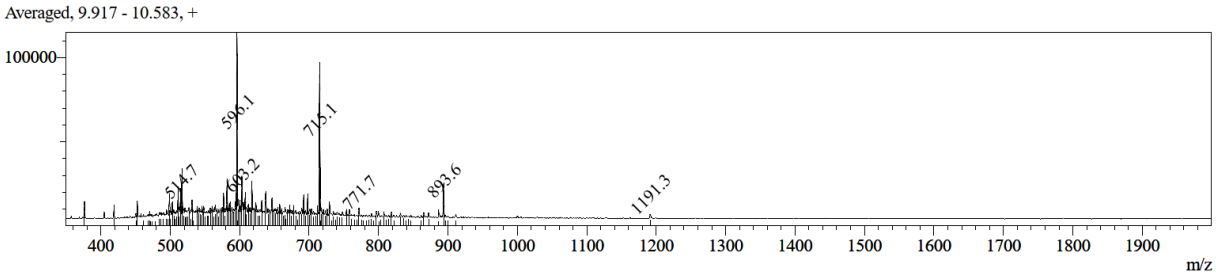

Figure S 19| MS (ESI) spectrum (positive mode) of L17E$_{K1+K3}^{Alloc}$-TAMRA peptide **3**. Calculated: $[M+H]^+$ = 3569.2; $[M+2H]^{2+}$ = 1785.1; $[M+3H]^{3+}$ = 1190.4; $[M+4H]^{4+}$ = 893.0; $[M+5H]^{5+}$ = 714.6; $[M+6H]^{6+}$ = 595.7; $[M+7H]^{7+}$ = 510.7; observed: $[M+4H]^{4+}$ = 893.6; $[M+5H]^{5+}$ = 715.1; $[M+6H]^{6+}$ = 596.1; $[M+7H]^{7+}$ = 514.7.

7.2.5 L17E$_{K2+K4}^{Alloc}$-TAMRA 4

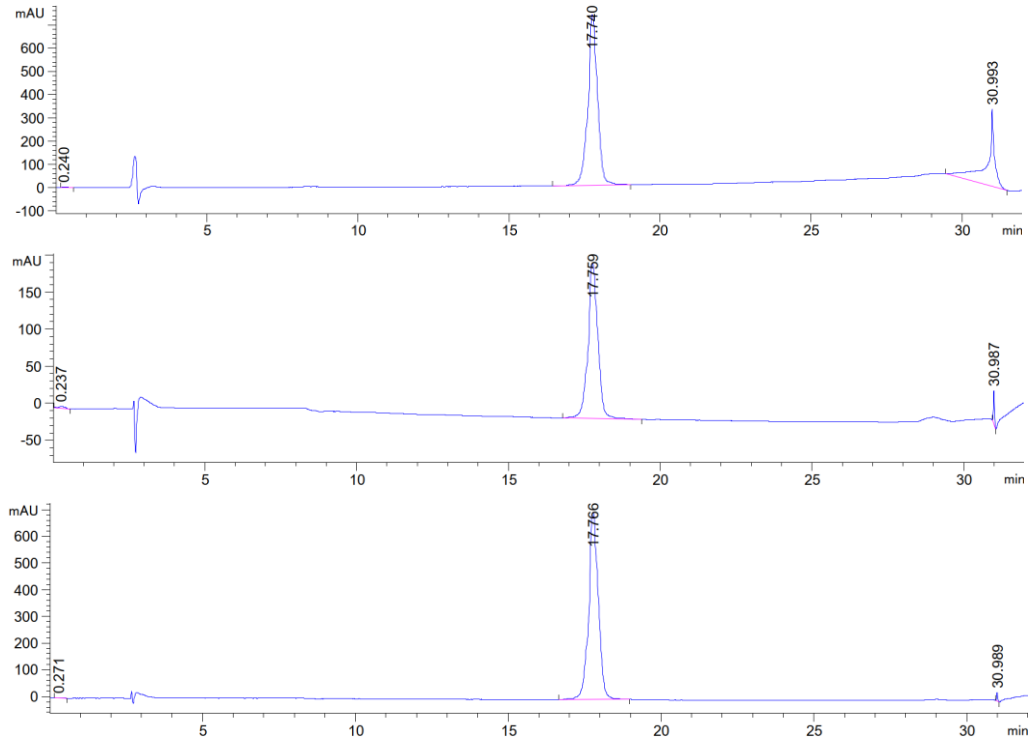

Figure S 20| Analytical RP-HPLC chromatogram of purified L17E$_{K2+K4}^{Alloc}$-TAMRA peptide **4**, 0 to 80% B (0.6 mL/min, 20 min gradient), 220 nm (top), 280 nm (middle) and 550 nm (bottom), t_R = 17.740 min.

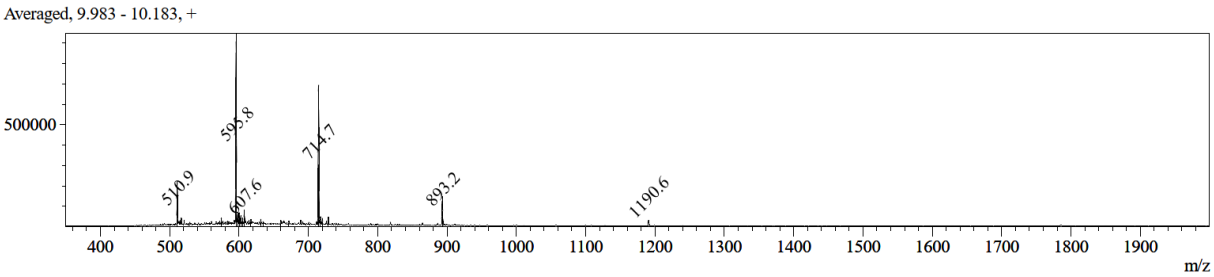

Figure S 21| MS (ESI) spectrum (positive mode) of L17E$_{K2+K4}^{Alloc}$-TAMRA peptide **4**. Calculated: $[M+H]^+$ = 3569.2; $[M+2H]^{2+}$ = 1785.1; $[M+3H]^{3+}$ = 1190.4; $[M+4H]^{4+}$ = 893.0; $[M+5H]^{5+}$ = 714.6; $[M+6H]^{6+}$ = 595.8; $[M+7H]^{7+}$ = 510.7; observed: $[M+3H]^{3+}$ = 1190.6; $[M+4H]^{4+}$ = 893.2; $[M+5H]^{5+}$ = 714.7; $[M+6H]^{6+}$ = 595.8; $[M+7H]^{7+}$ = 510.9.

7.2.6 L17E$_{K3+K5}^{Alloc}$-TAMRA 5

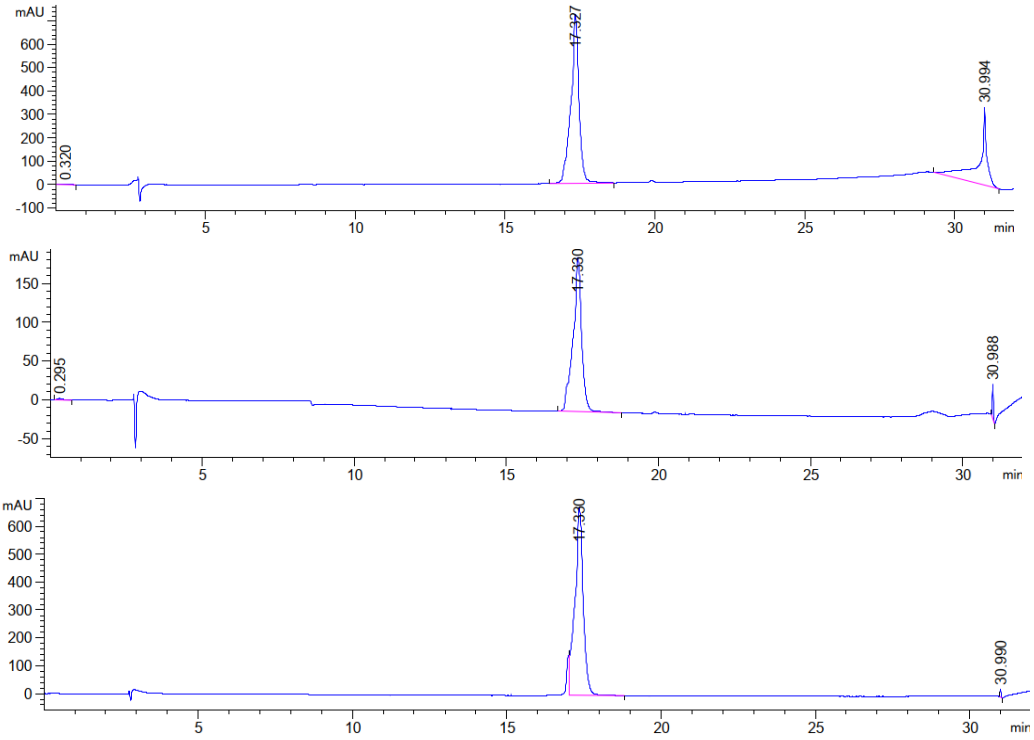

Figure S 22| Analytical RP-HPLC chromatogram of purified L17E$_{K3+K5}^{Alloc}$-TAMRA peptide **5**, 0 to 80% B (0.6 mL/min, 20 min gradient), 220 nm (top), 280 nm (middle) and 550 nm (bottom), t_R = 17.327 min.

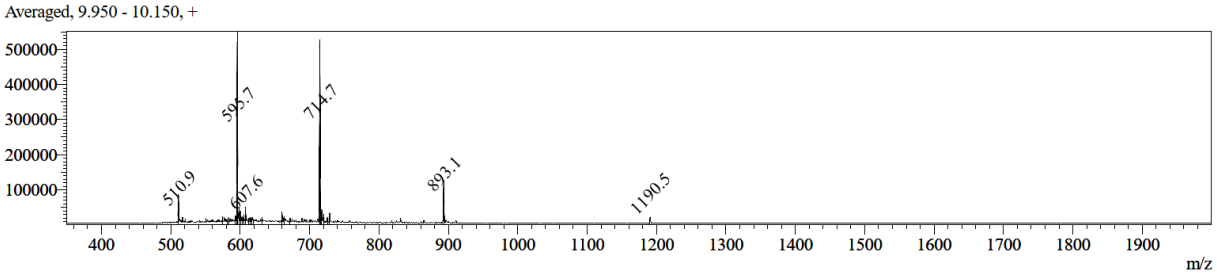

Figure S 23| MS (ESI) spectrum (positive mode) of L17E$_{K3+K5}^{Alloc}$-TAMRA peptide **5**. Calculated: $[M+H]^{+}$ = 3569.2; $[M+2H]^{2+}$ = 1785.1; $[M+3H]^{3+}$ = 1190.4; $[M+4H]^{4+}$ = 893.0; $[M+5H]^{5+}$ = 714.6; $[M+6H]^{6+}$ = 595.8; $[M+7H]^{7+}$ = 510.7; observed: $[M+3H]^{3+}$ = 1190.5; $[M+4H]^{4+}$ = 893.1; $[M+5H]^{5+}$ = 714.7; $[M+6H]^{6+}$ = 595.7; $[M+7H]^{7+}$ = 510.9.

7.2.7 L17E5K(Ac)-TAMRA 6

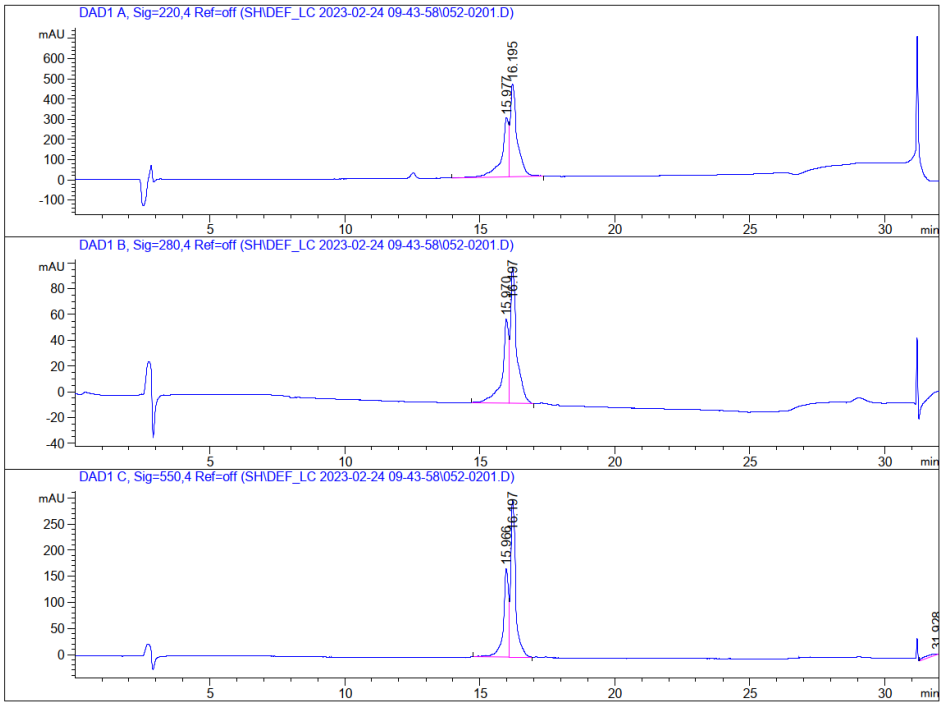

Figure S 24| Analytical RP-HPLC chromatogram of purified L17E5K(Ac)-TAMRA peptide **6**, 20 to 80% B (0.6 mL/min, 20 min gradient), 220 nm, 280 nm and 550 nm, t_R = 15.977, 16.195 min. The two peaks correspond to the 5,6-TAMRA mixed isomer used for labelling of the peptide.

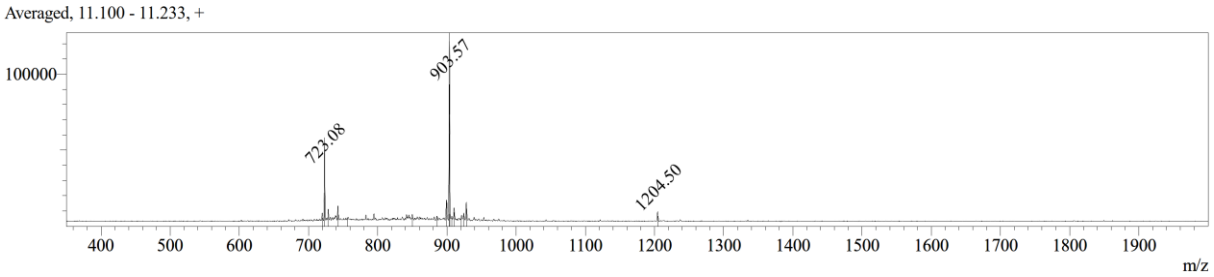

Figure S 25| MS (ESI) spectrum (positive mode) of L17E5K(Ac)-TAMRA peptide **6**. Calculated: $[M+H]^+$ = 3611.2; $[M+2H]^{2+}$ = 1806.1; $[M+3H]^{3+}$ = 1204.4; $[M+4H]^{4+}$ = 903.5; $[M+5H]^{5+}$ = 723.0; $[M+6H]^{6+}$ = 602.7; $[M+7H]^{7+}$ = 517.6; observed: $[M+3H]^{3+}$ = 1024.5.1; $[M+4H]^{4+}$ = 903.6; $[M+5H]^{5+}$ = 723.1.

7.2.8 L17E-Pra 7

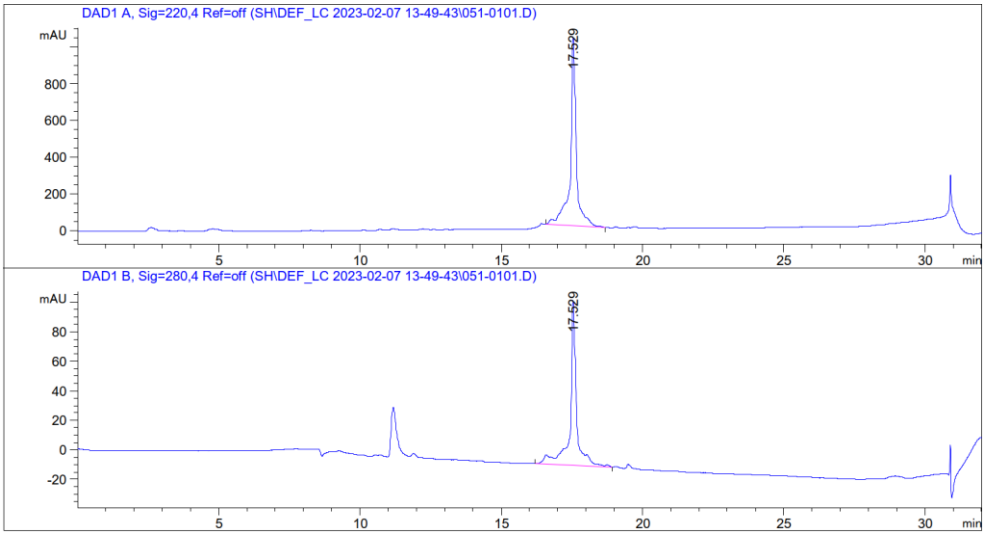

Figure S 26| Analytical RP-HPLC chromatogram of purified L17E-Pra peptide **7**, 0 to 60% B (0.6 mL/min, 20 min gradient), 220 nm, and 280 nm, t_R = 17.529 min.

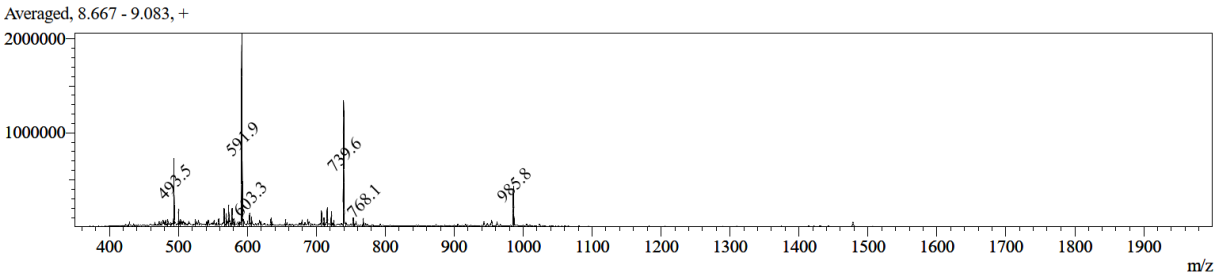

Figure S 27| MS (ESI) spectrum (positive mode) of L17E-Pra peptide **7**. Calculated: $[M+H]^{+}$ = 2955.5; $[M+2H]^{2+}$ = 1478.3; $[M+3H]^{3+}$ = 985.9; $[M+4H]^{4+}$ = 739.6; $[M+5H]^{5+}$ = 591.9; $[M+6H]^{6+}$ = 493.4; observed: $[M+3H]^{3+}$ = 985.8; $[M+4H]^{4+}$ = 739.6; $[M+5H]^{5+}$ = 591.9; $[M+6H]^{6+}$ = 493.5.

7.2.9 L17E5K(Ac)-Pra 8

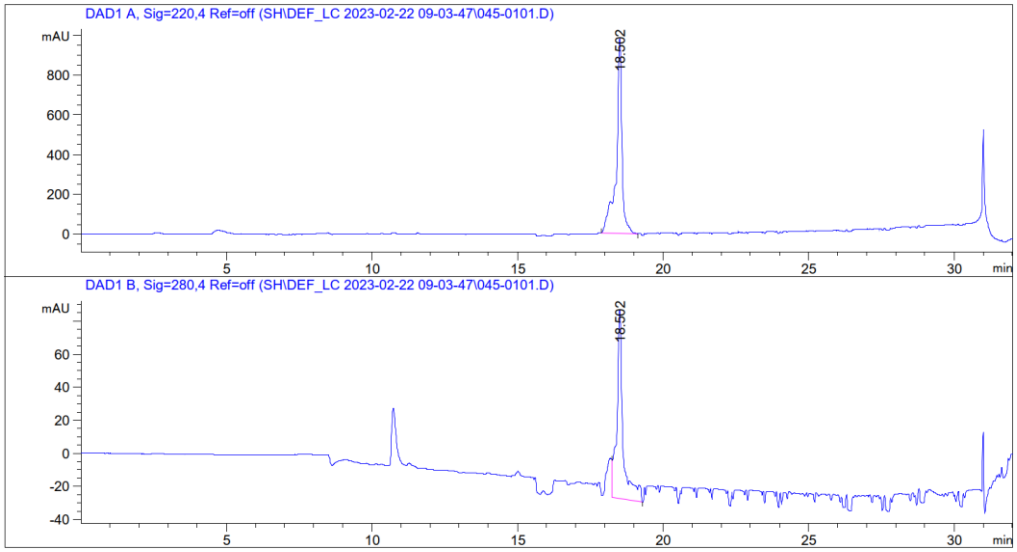

Figure S 28| Analytical RP-HPLC chromatogram of purified L17E5K(Ac)-Pra peptide **8**, 0 to 80% B (0.6 mL/min, 20 min gradient), 220 nm and 280 nm, t_R = 18.502 min.

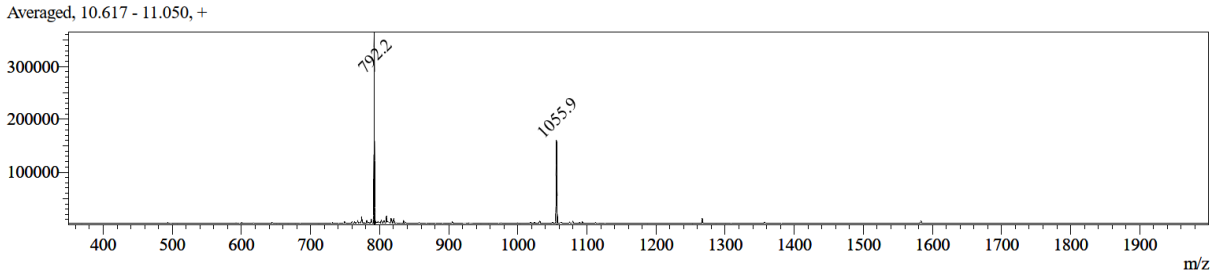

Figure S 29| MS (ESI) spectrum (positive mode) of L17E5K(Ac)-Pra peptide **8**. Calculated: $[M+H]^{+}$ = 3165.5; $[M+2H]^{2+}$ = 1583.3; $[M+3H]^{3+}$ = 1055.9; $[M+4H]^{4+}$ = 792.1; $[M+5H]^{5+}$ = 633.9; $[M+6H]^{6+}$ = 528.4; observed: $[M+3H]^{3+}$ = 1055.9; $[M+4H]^{4+}$ = 792.2.

7.2.10 L17E-Cys 9

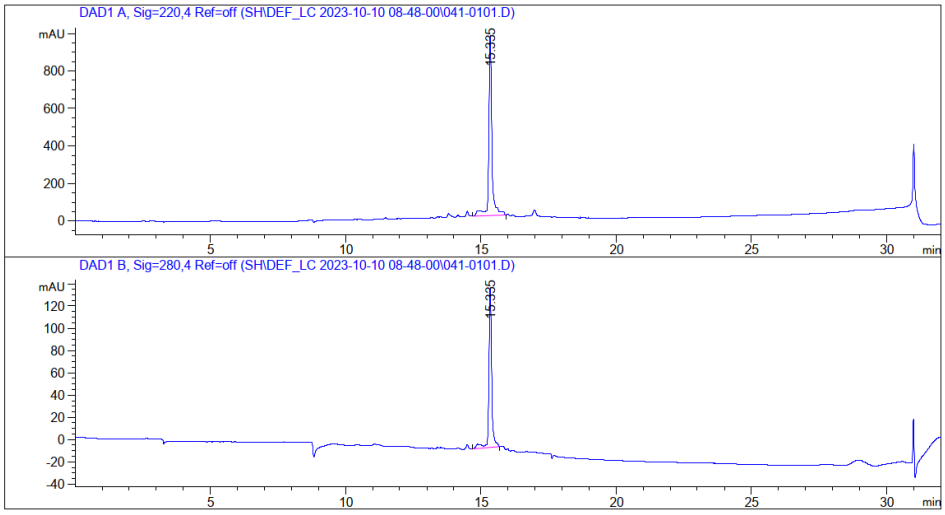

Figure S 30| Analytical RP-HPLC chromatogram of purified L17E-Cys peptide **9**, 0 to 80% B (0.6 mL/min, 20 min gradient), 220 nm (top) and 280 nm (bottom), t_R = 15.335 min.

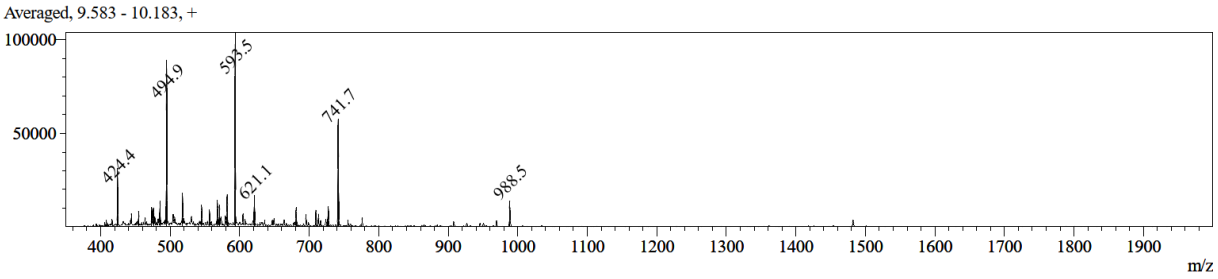

Figure S 31| MS (ESI) spectrum (positive mode) of L17E-Cys peptide **9**. Calculated: $[M+H]^{+}$= 2963.6; $[M+2H]^{2+}$ = 1482.3; $[M+3H]^{3+}$ = 988.5; $[M+4H]^{4+}$= 741.6; $[M+5H]^{5+}$ = 593.5; $[M+6H]^{6+}$ = 494.8; $[M+7H]^{7+}$ = 424.2; observed: $[M+3H]^{3+}$ = 988.5; $[M+4H]^{4+}$= 741.7; $[M+5H]^{5+}$ = 593.5; $[M+6H]^{6+}$ = 494.9; $[M+7H]^{7+}$ = 424.4.

7.2.11 L17E5K(Ac)-Cys 10

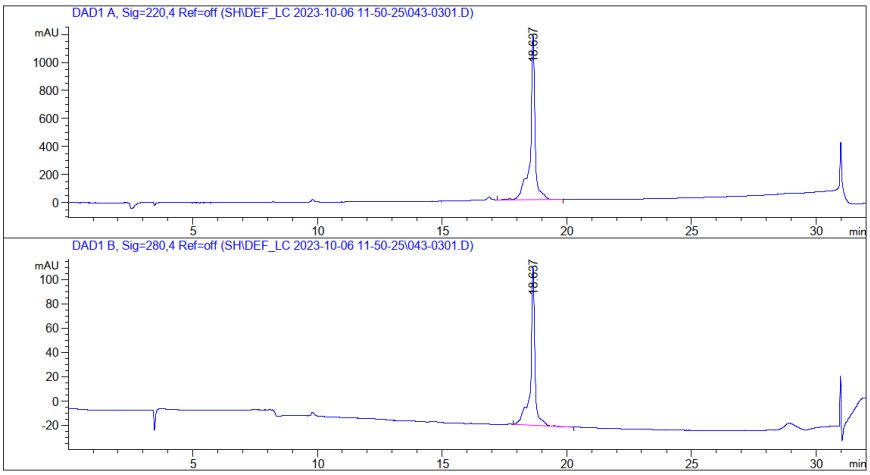

Figure S 32| Analytical RP-HPLC chromatogram of purified L17E5K(Ac)-Cys peptide **10**, 0 to 80% B (0.6 mL/min, 20 min gradient), 220 nm (top) and 280 nm (bottom), t_R = 18.637 min.

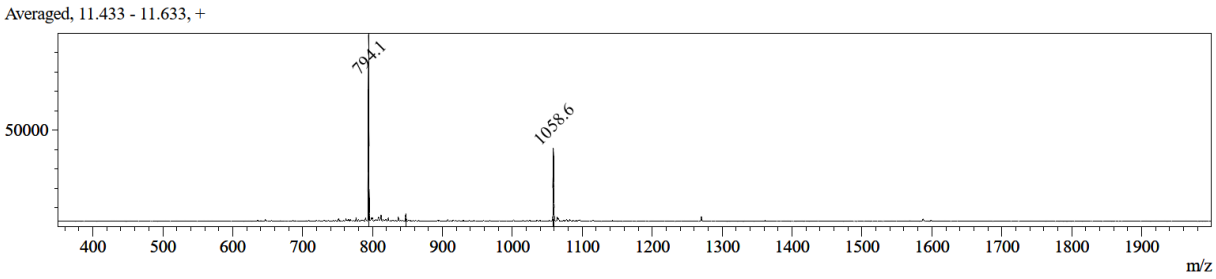

Figure S 33| MS (ESI) spectrum (positive mode) of L17E5K(Ac)-Cys peptide **10**. Calculated: $[M+H]^{+}$= 3173.7; $[M+2H]^{2+}$ = 1587.4; $[M+3H]^{3+}$ = 1058.6; $[M+4H]^{4+}$= 794.2; observed: $[M+3H]^{3+}$ = 1058.6; $[M+4H]^{4+}$= 794.1.

7.2.12 L17E-cry 11

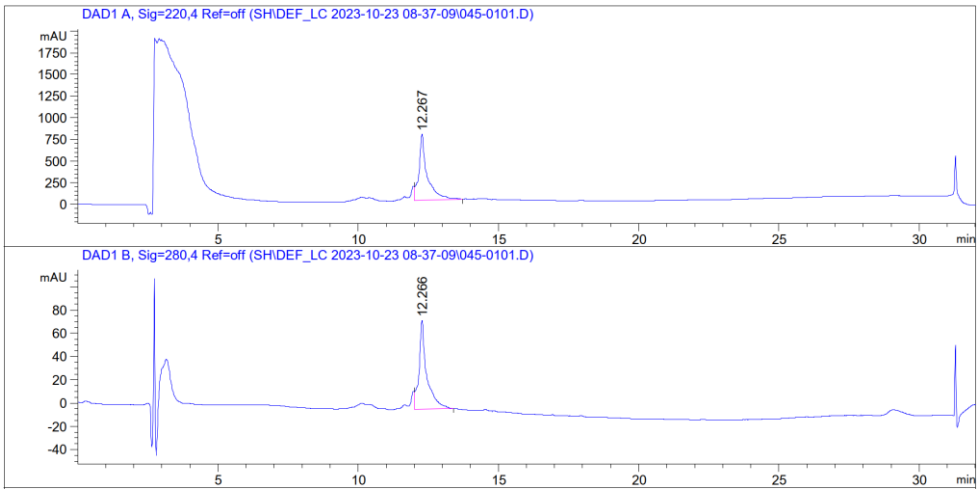

Figure S 34| Analytical RP-HPLC chromatogram of purified L17E-cry peptide **11**, 20 to 100% B (no TFA) (0.6 mL/min, 20 min gradient), 220 nm (top) and 280 nm (bottom), t_R = 12.267 min.

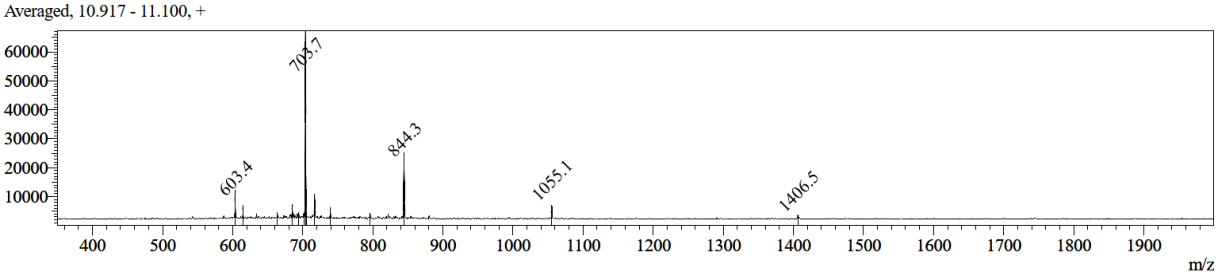

Figure S 35| MS (ESI) spectrum (positive mode) of L17E-cry peptide **11**. Calculated: $[M+H]^{+}$ = 4217.4; $[M+2H]^{2+}$ = 2109.2; $[M+3H]^{3+}$ = 1406.5; $[M+4H]^{4+}$ = 1055.1; $[M+5H]^{5+}$ = 844.3; $[M+6H]^{6+}$ = 703.7; observed: $[M+3H]^{3+}$ = 1406.5; $[M+4H]^{4+}$ = 1055.1; $[M+5H]^{5+}$ 844.3; $[M+6H]^{6+}$ = 703.7.

7.2.13 L17E5K(Ac)-cry 12

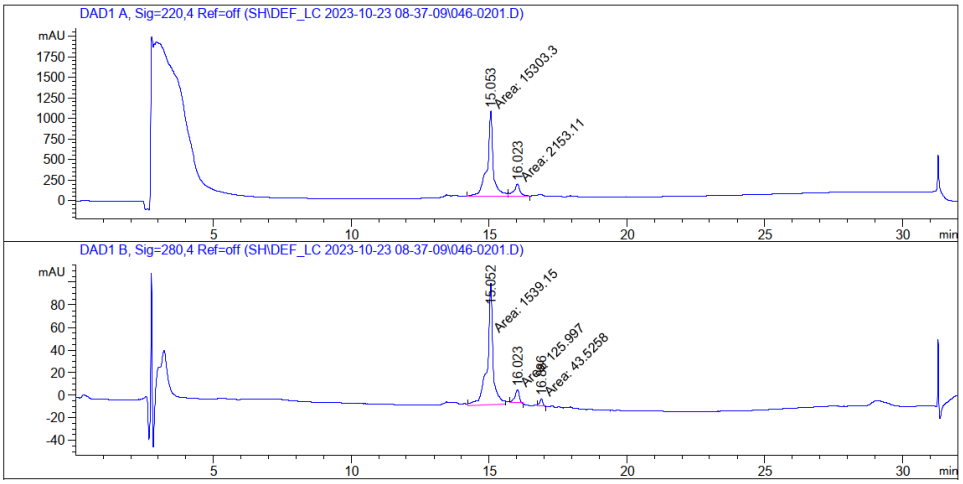

Figure S 36| Analytical RP-HPLC chromatogram of purified L17E5K(Ac)-cry peptide **12**, 20 to 100% B (no TFA) (0.6 mL/min, 20 min gradient), 220 nm and 280 nm, t_R = 15.053 min.

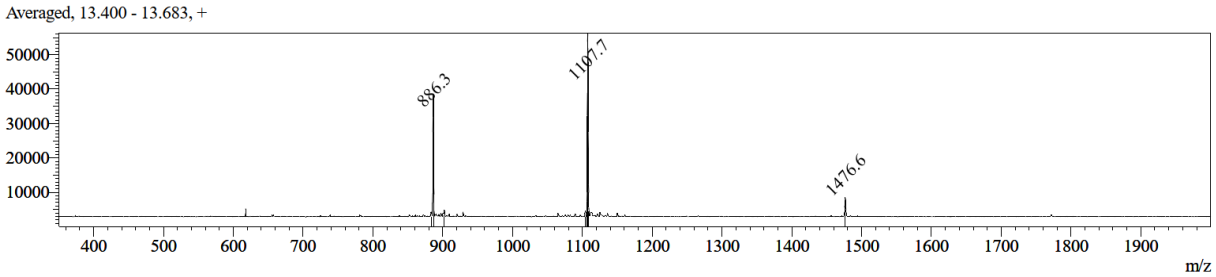

Figure S 37| MS (ESI) spectrum (positive mode) of L17E5K(Ac)-cry peptide **12**. Calculated: $[M+H]^{+}$ = 4427.6; $[M+2H]^{2+}$ = 2214.3; $[M+3H]^{3+}$ = 1476.5; $[M+4H]^{4+}$ = 1107.6; $[M+5H]^{5+}$ = 886.3; $[M+6H]^{6+}$ = 738.8; observed: $[M+3H]^{3+}$ = 1476.6; $[M+4H]^{4+}$ = 1107.7; $[M+5H]^{5+}$ = 886.3.

7.2.14 L17E$_{K1+K2}^{Succ}$-Cys 13

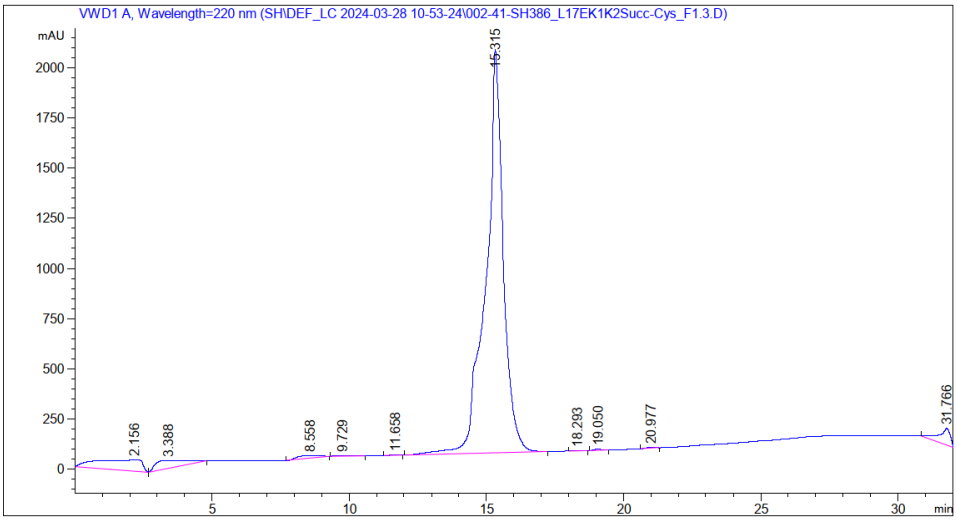

Figure S 38| Analytical RP-HPLC chromatogram of purified L17E$_{K1+K2}^{Succ}$-Cys peptide **13**, 0 to 100% B (220 nm, 0.6 mL/min, 20 min gradient), t_R = 15.315 min.

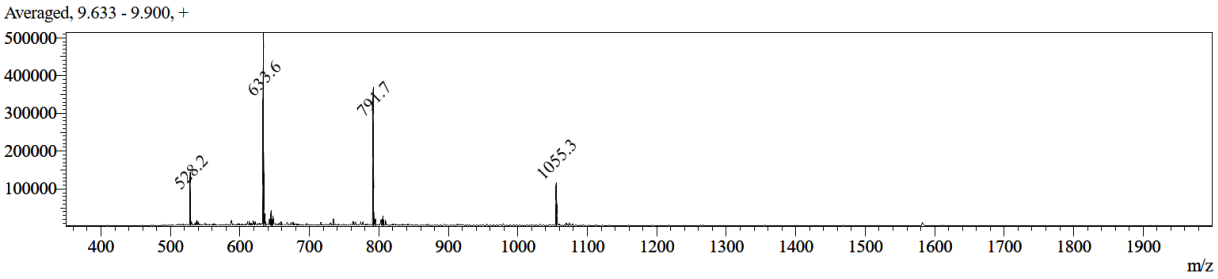

Figure S 39| MS (ESI) spectrum (positive mode) of L17E$_{K1+K2}^{Succ}$-Cys peptide **13**. Calculated: $[M+H]^{+}$ = 3163.7; $[M+2H]^{2+}$ = 1582.4; $[M+3H]^{3+}$ = 1055.3; $[M+4H]^{4+}$ = 791.7; $[M+5H]^{5+}$ = 633.6; $[M+6H]^{6+}$ = 528.1; observed: $[M+3H]^{3+}$ = 1055.3; $[M+4H]^{4+}$ = 791.7; $[M+5H]^{5+}$ = 633.6; $[M+6H]^{6+}$ = 528.2.

7.2.15 L17E5K(Succ)-Cys 14

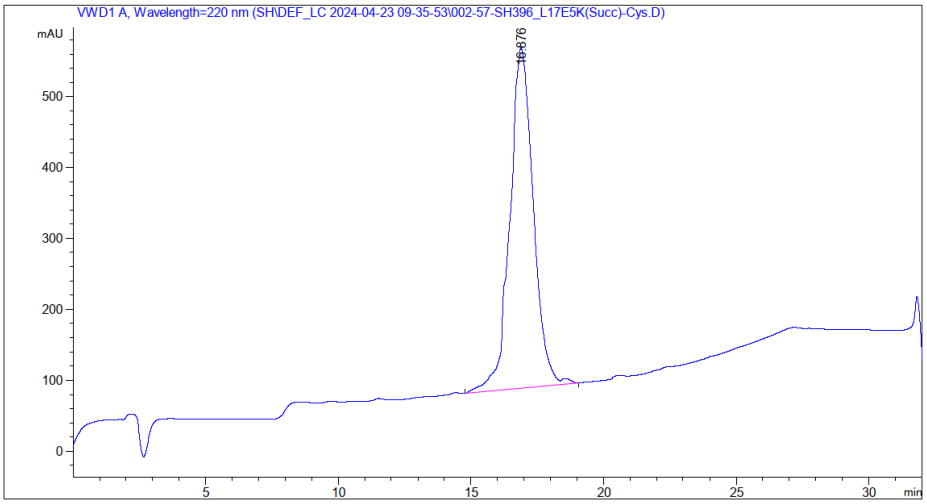

Figure S 40| Analytical RP-HPLC chromatogram of purified L17E5K(Ac)-Cys peptide **14**, 0 to 100% B (220 nm 0.6 mL/min, 20 min gradient), t_R = 16.876 min.

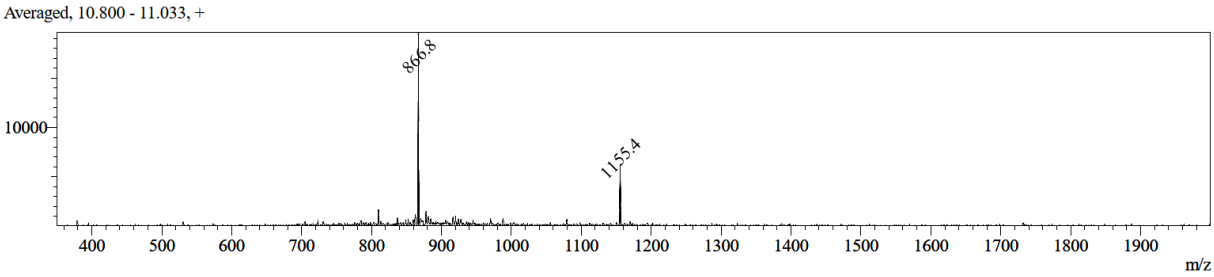

Figure S 41| MS (ESI) spectrum (positive mode) of L17E5K(Ac)-Cys peptide **14**. Calculated: $[M+H]^{+}$ = 3463.9; $[M+2H]^{2+}$ = 1732.5; $[M+3H]^{3+}$ = 1155.3; $[M+4H]^{4+}$ = 866.7; $[M+5H]^{5+}$ = 693.6; observed: $[M+3H]^{3+}$ = 1155.4; $[M+4H]^{4+}$ = 866.8.

7.2.16 L17E$_{K1+K2}^{Succ}$-TAMRA 15

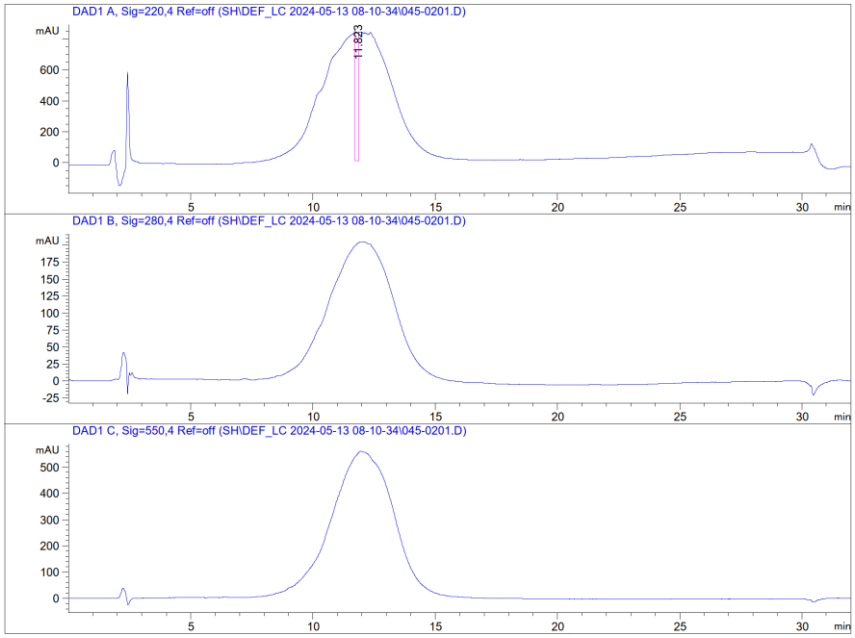

Figure S 42| Analytical RP-HPLC chromatogram of purified L17E$_{K1+K2}^{Succ}$-TAMRA peptide **15**, 30 to 100% B (0.6 mL/min, 20 min gradient), 220 nm (top), 280 nm (middle), 550 nm (bottom) t_R = 9-14 min.

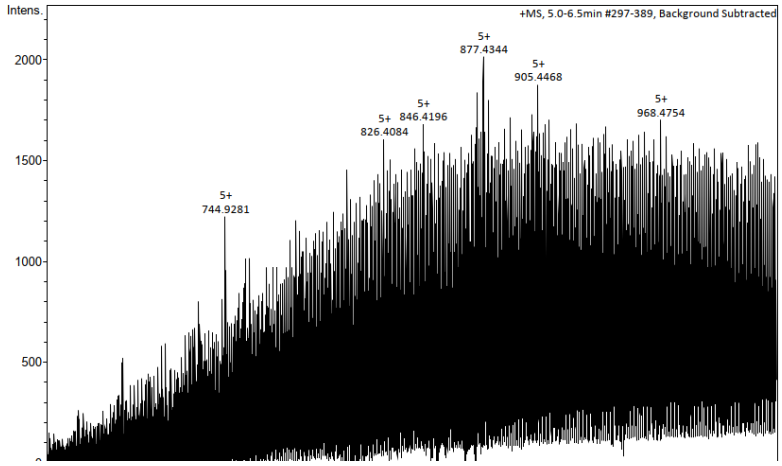

Figure S 43| MS (ESI) spectrum (positive mode) of L17E$_{K1+K2}^{Succ}$-TAMRA peptide **15**. Calculated: $[M+H]^+$ = 3716.3; $[M+2H]^{2+}$ = 1858.6; $[M+3H]^{3+}$ = 1239.4; $[M+4H]^{4+}$ = 929.8; $[M+5H]^{5+}$ = 744.1; observed: $[M+5H]^{5+}$ = 744.9 (broad HPLC peak, inconclusive MS).

7.2.17 L17E5K(Succ)-TAMRA 16

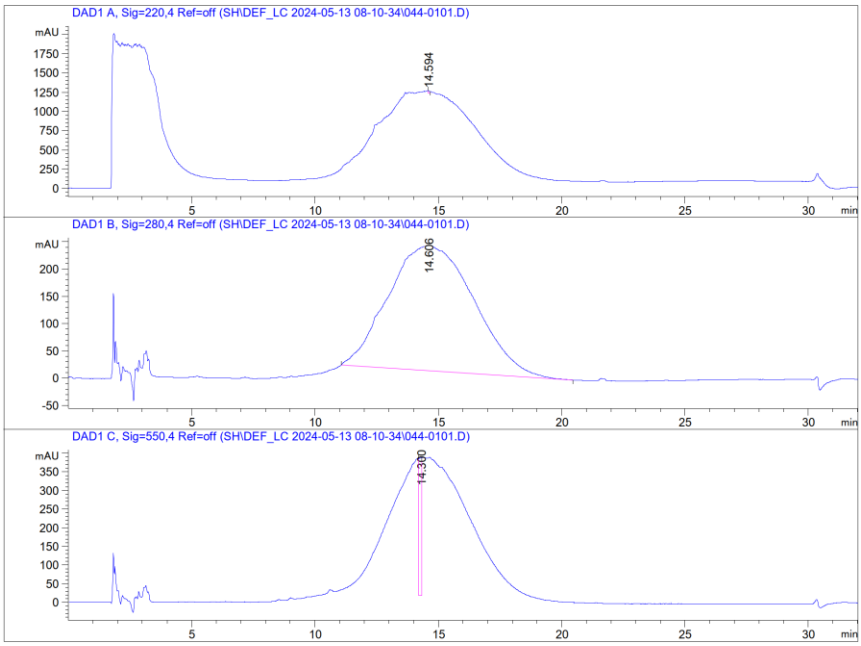

Figure S 44| Analytical RP-HPLC chromatogram of purified L17E5K(Ac)-TAMRA peptide **16**, 30 to 100% B (0.6 mL/min, 20 min gradient), 220 nm (top), 280 nm (middle), 550 nm (bottom) t_R = 11-19 min.

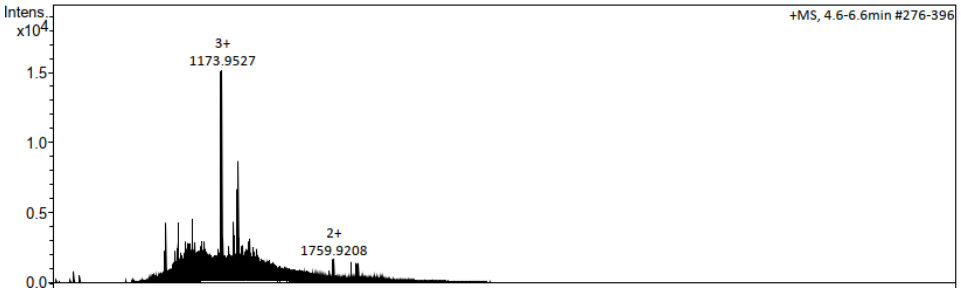

Figure S 45| MS (ESI) spectrum (positive mode) of L17E5K(Succ)-TAMRA peptide **16**. Calculated: $[M+H]^+$ = 4046.6; $[M+2H]^{2+}$ = 2023.8; $[M+3H]^{3+}$ = 1349.5; $[M+4H]^{4+}$ = 1012.4; observed: $[M+2H]^{2+}$ = 1759.9; $[M+3H]^{3+}$ = 1173.9 (broad HPLC peak, inconclusive MS).

7.2.18 L17E$_{K1+K2}^{Succ}$-Cry 17

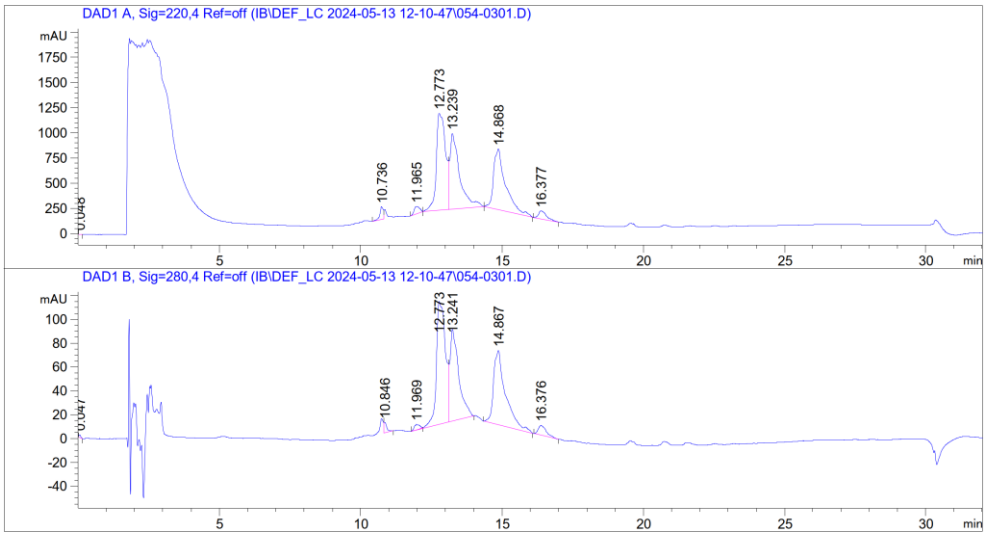

Figure S 46| Analytical RP-HPLC chromatogram of purified L17E$_{K1+K2}^{Succ}$-cry peptide **17**, 30 to 100% B (0.6 mL/min, 20 min gradient), 220 nm (top), 280 nm (bottom), t_R = 14.868 min. Free cryptophycin at t_R = 13.239 min.

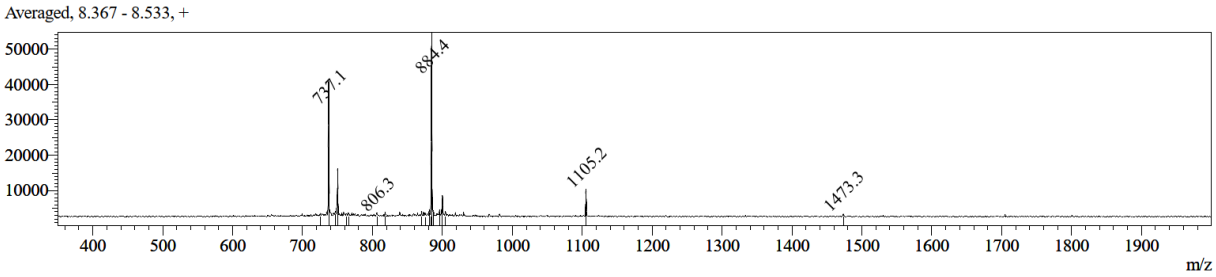

Figure S 47| MS (ESI) spectrum (positive mode) of L17E$_{K1+K2}^{Succ}$-cry peptide **17**. Calculated: $[M+H]^{+}$ = 4417.5; $[M+2H]^{2+}$ = 2209.3; $[M+3H]^{3+}$ = 1473.2; $[M+4H]^{4+}$ = 1105.2; $[M+5H]^{5+}$ = 884.3; $[M+6H]^{6+}$ = 737.1; observed: $[M+3H]^{3+}$ = 1473.3; $[M+4H]^{4+}$ = 1105.2; $[M+5H]^{5+}$ = 884.4; $[M+6H]^{6+}$ = 737.1.

7.2.19 L17E5K(Succ)-Cry 18

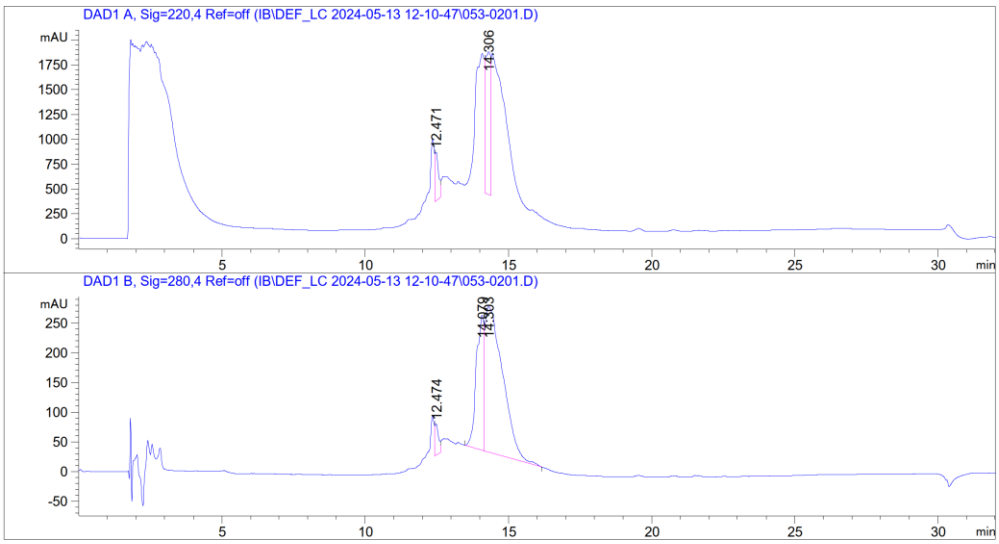

Figure S 48| Analytical RP-HPLC chromatogram of purified L17E5K(Succ)-cry peptide **18**, 30 to 100% B (0.6 mL/min, 20 min gradient), 220 nm (top), 280 nm (bottom), t_R = 14.306 min.

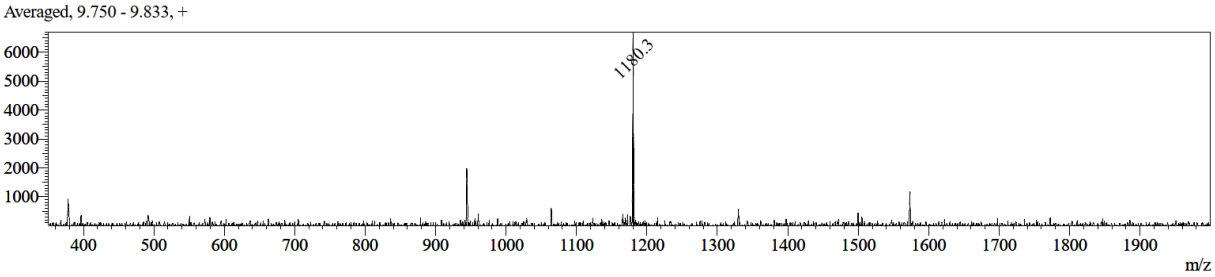

Figure S 49| MS (ESI) spectrum (positive mode) of L17E5K(Succ)-cry peptide **18**. Calculated: $[M+H]^{+}$ = 4717.8; $[M+2H]^{2+}$ = 2359.4; $[M+3H]^{3+}$ = 1573.3; $[M+4H]^{4+}$ = 1180.2; $[M+5H]^{5+}$ = 944.4; $[M+6H]^{6+}$ = 787.1; observed: $[M+3H]^{3+}$ = 1573.3; $[M+4H]^{4+}$ = 1180.3.

7.2.20 *N*-Boc-cadaverine-dextran 19 (batch 2)

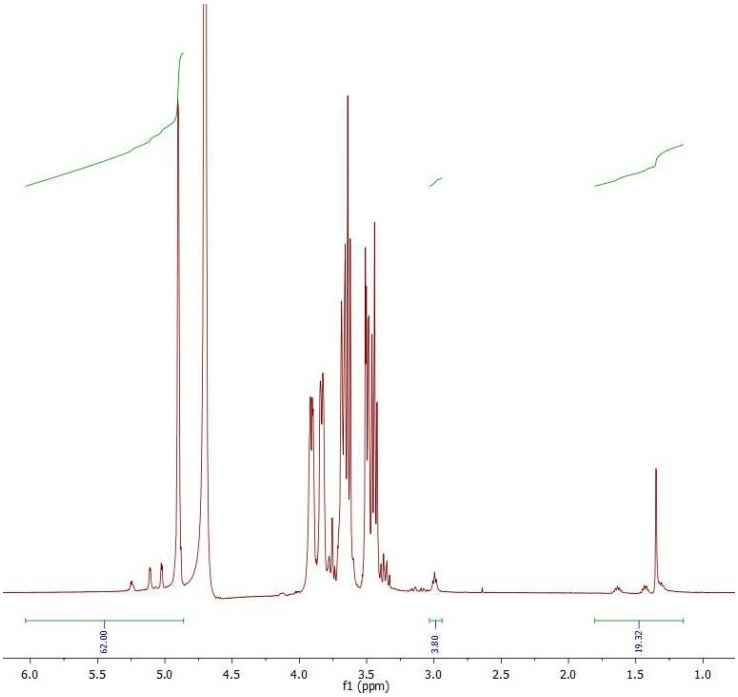

Figure S 50| ^{1}H-NMR spectrum (300 MHz, D_2O) of *N*-Boc-cadaverine-dextran **19** (batch 2).

7.2.21 *N*-Boc-cadaverine-dextran-CE 20 (batch 2)

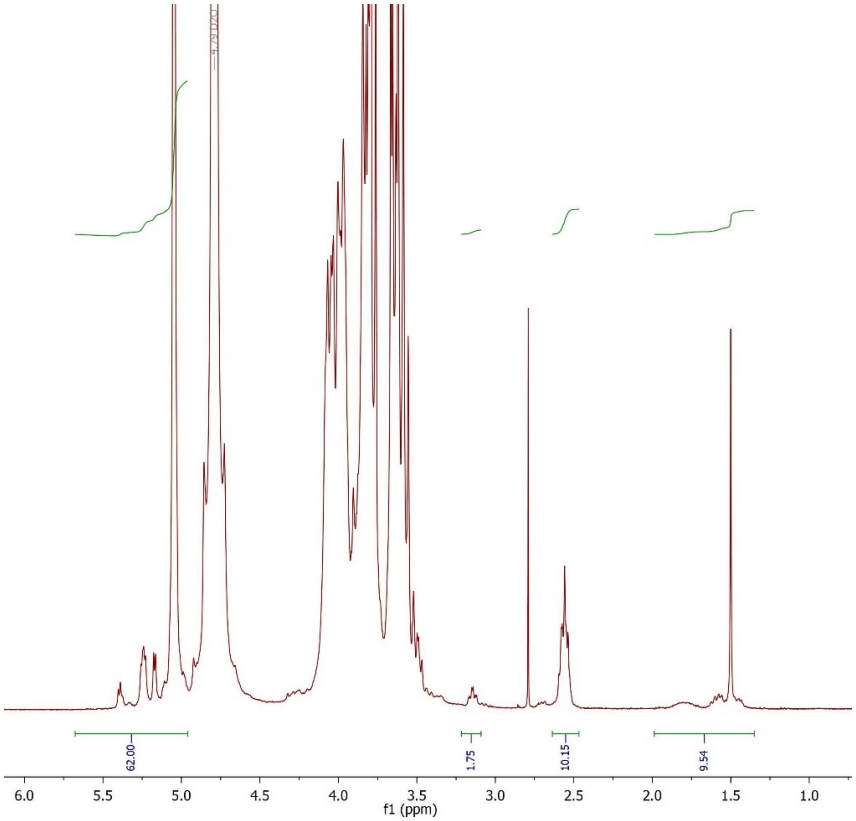

Figure S 51| ^{1}H-NMR spectrum (300 MHz, D_2O) of *N*-Boc-cadaverine-dextran-CE **20** (batch 2).

7.2.22 *N*-Boc-cadaverine-dextran-CE 20 (batch 3)

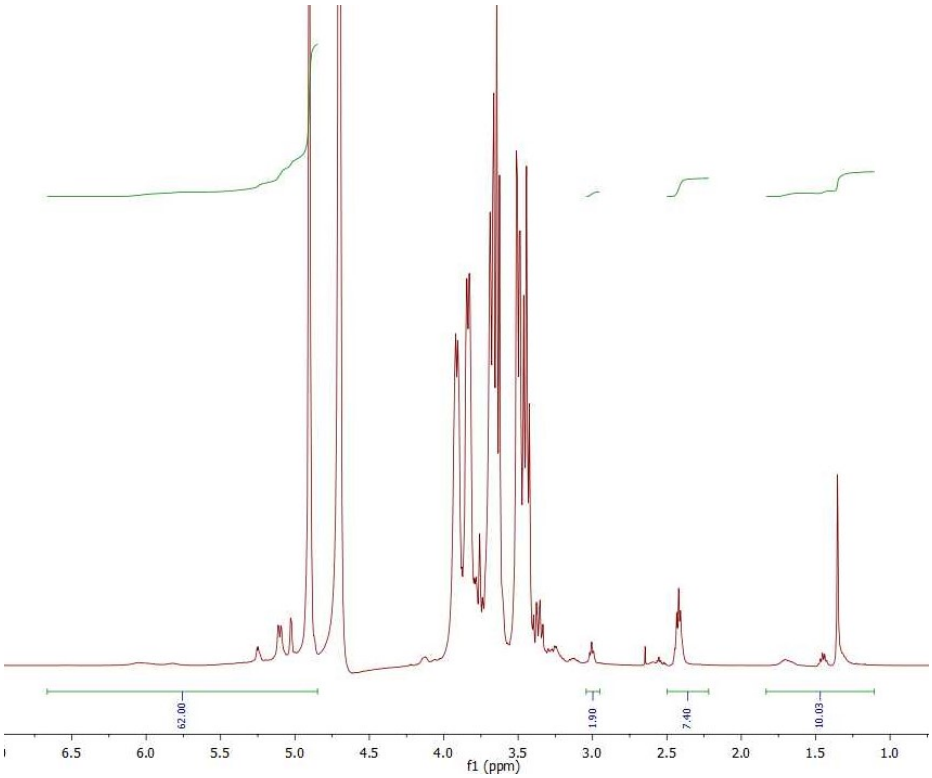

Figure S 52| ^{1}H-NMR spectrum (300 MHz, D_2O) of *N*-Boc-cadaverine-dextran-CE **20** (batch 3).

7.2.23 *N*-Boc-cadaverine-dextran-CE 20 (batch 4)

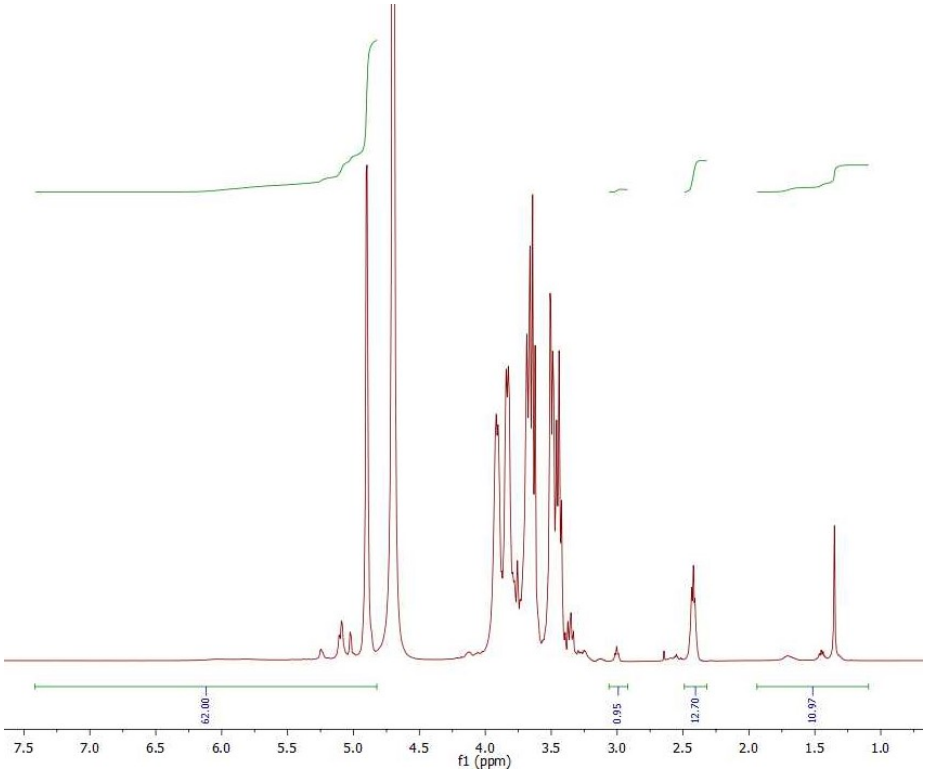

Figure S 53| ^{1}H-NMR spectrum (300 MHz, D_2O) of *N*-Boc-cadaverine-dextran-CE **20** (batch 4).

7.2.24 Azide linker N-(5-aminopentyl)-2-azidoacetamide 21

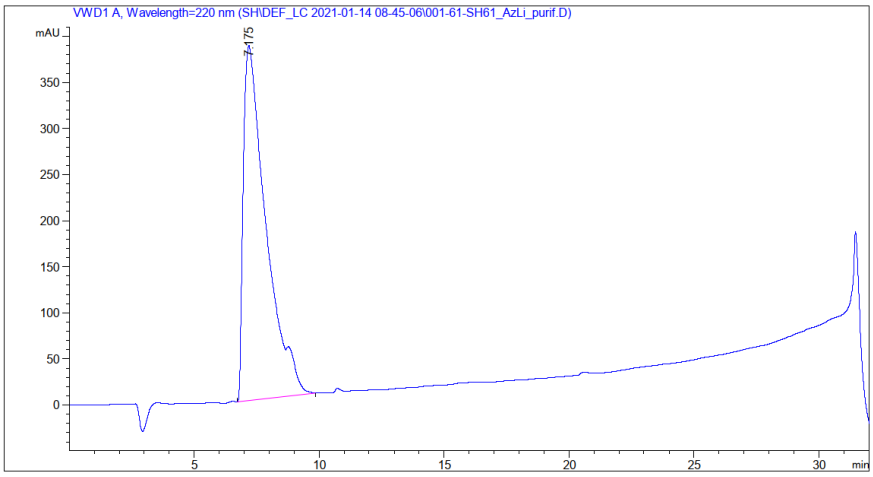

Figure S 54| Exemplary analytical RP-HPLC chromatogram of purified azide linker N-(5-aminopentyl)-2-azidoacetamide **21**, 0 to 40% B (0.6 mL/min, 20 min gradient), 220 nm, t_R = 7.175 min.

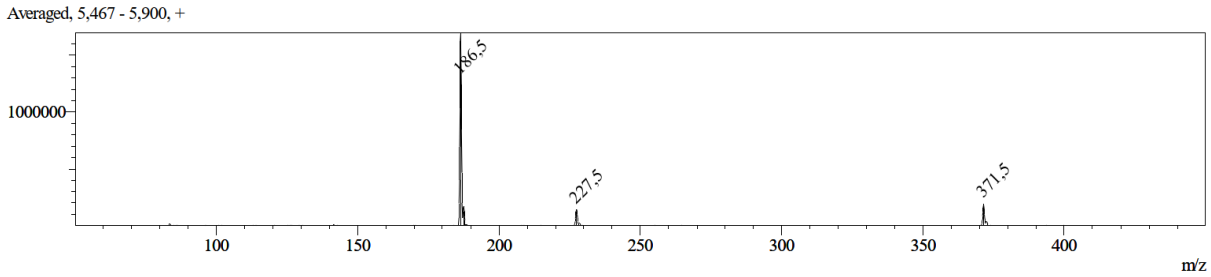

Figure S 55| MS (ESI) spectrum (positive mode) of N-(5-aminopentyl)-2-azidoacetamide **21**. Calculated: $[M+H]^+$ = 185.2; observed $[M+H]^+$ = 186.5.

7.2.25 *N*-Boc-cadaverine-dextran-N_3 22 (batch 2)

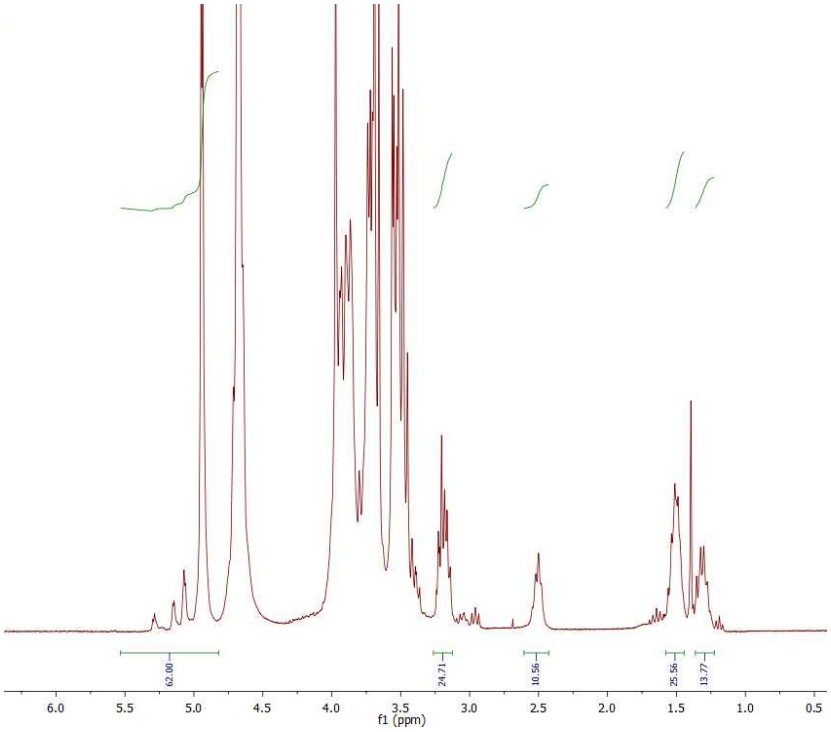

Figure S 56| ^{1}H-NMR spectrum (300 MHz, D_2O) of *N*-Boc-cadaverine-dextran-N_3 **22** (batch 2).

7.2.26 *N*-Boc-cadaverine-dextran-N_3 22 (batch 3)

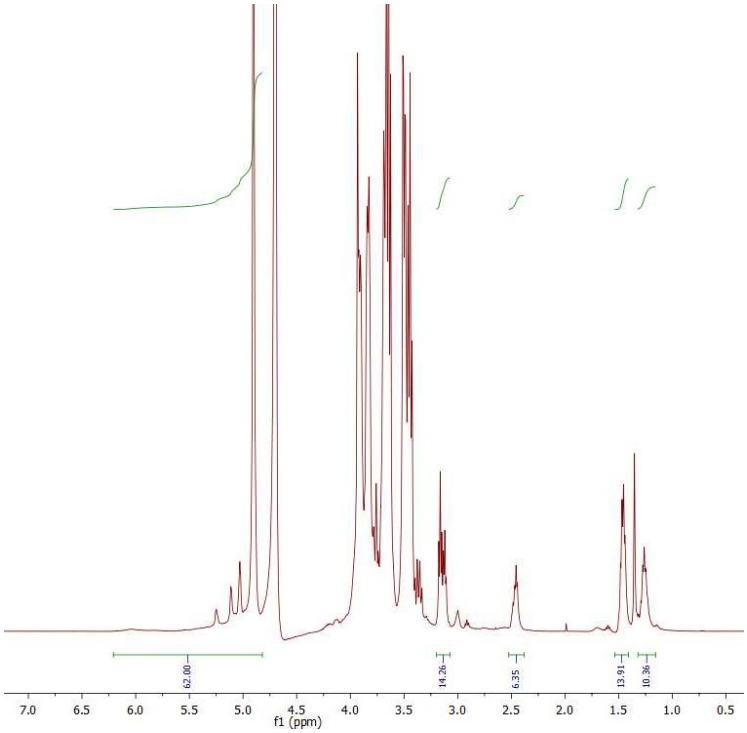

Figure S 57| ^{1}H-NMR spectrum (300 MHz, D_2O) of *N*-Boc-cadaverine-dextran-N_3 **22** (batch 3).

7.2.27 *N*-Boc-cadaverine-dextran-N_3 22 (batch 4)

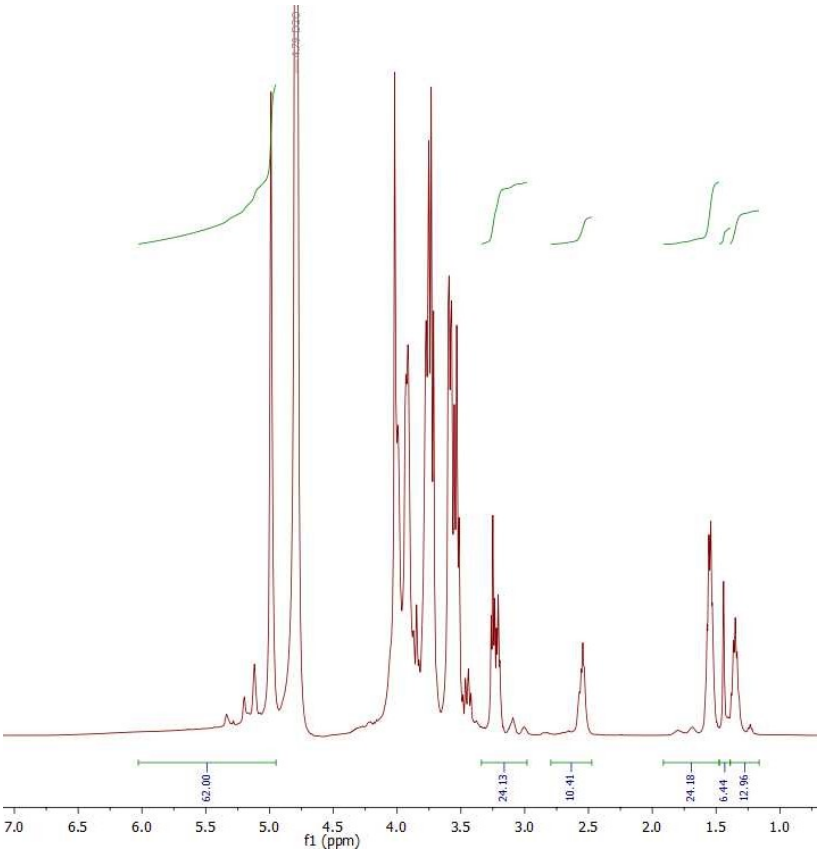

Figure S 58| ^{1}H-NMR spectrum (300 MHz, D_2O) of *N*-Boc-cadaverine-dextran-N_3 **22** (batch 4).

7.2.28 Cadaverine-dextran-N_3 23 (batch 2)

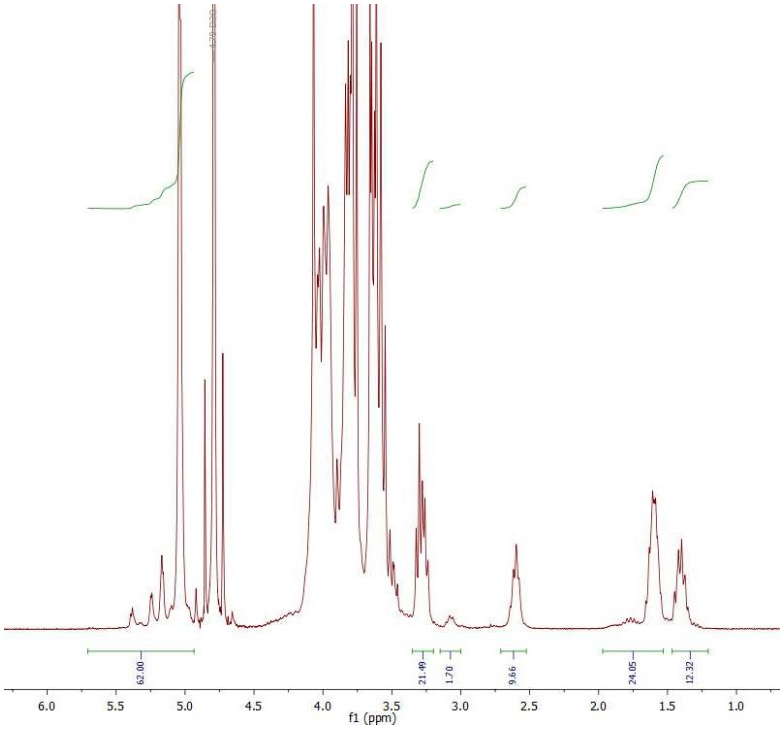

Figure S 59| ^{1}H-NMR spectrum (300 MHz, D_2O) of cadaverine-dextran-N_3 **23** (batch 2).

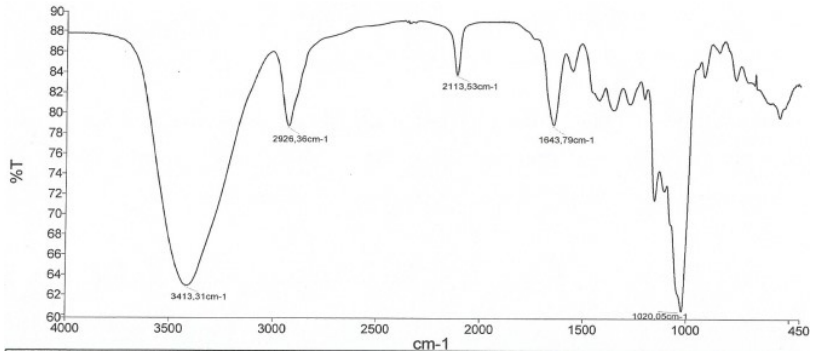

Figure S 60| IR spectrum of cadaverine-dextran-N_3 **23** (batch 2).

7.2.29 Cadaverine-dextran-N_3 23 (batch 3)

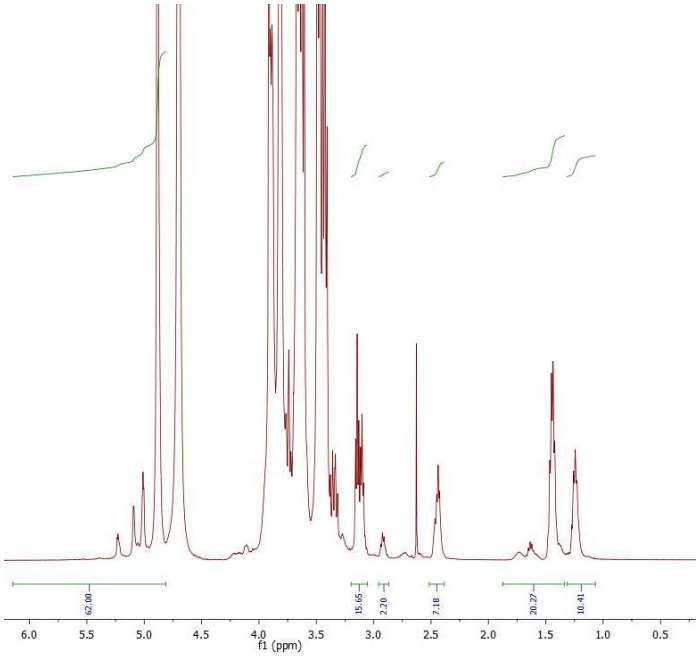

Figure S 61| ^{1}H-NMR spectrum (300 MHz, D_2O) of cadaverine-dextran-N_3 **23** (batch 3).

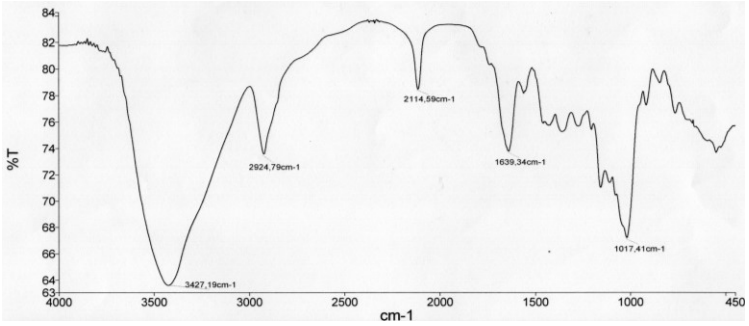

Figure S 62| IR spectrum of cadaverine-dextran-N_3 **23** (batch 3).

7.2.30 Cadaverine-dextran-N_3 23 (batch 4)

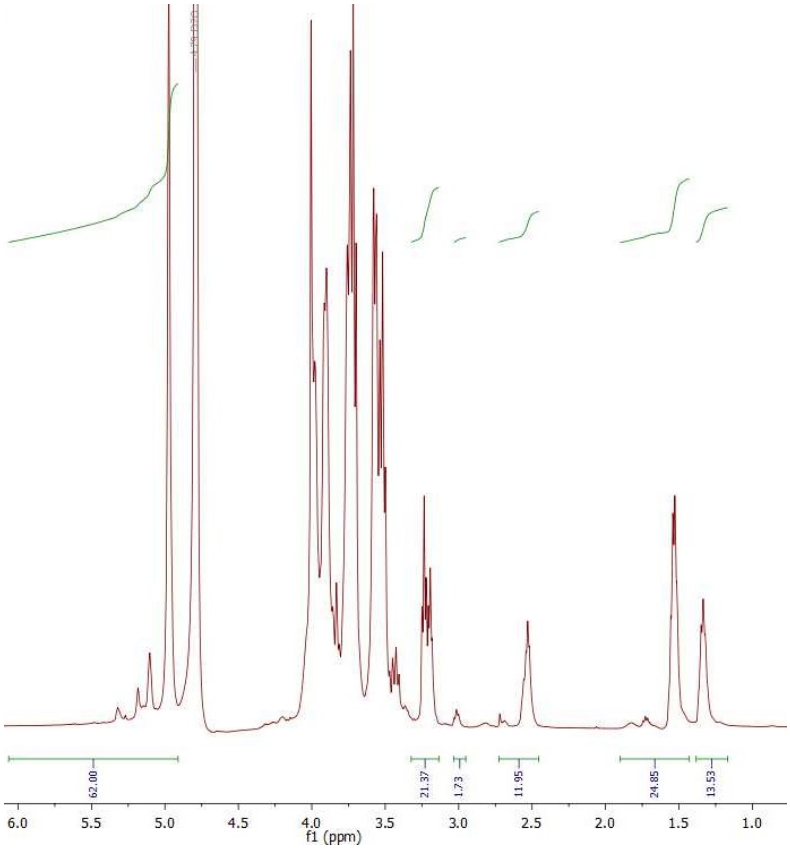

Figure S 63| ^{1}H-NMR spectrum (300 MHz, D_2O) of cadaverine-dextran-N_3 **23** (batch 4).

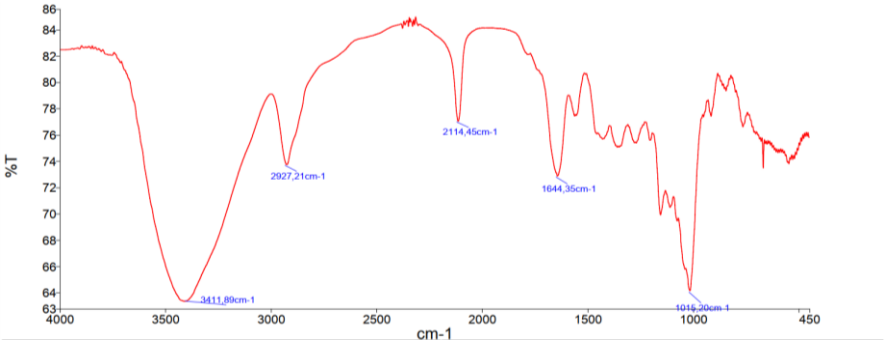

Figure S 64| IR spectrum of cadaverine-dextran-N_3 **23** (batch 4).

7.2.31 TAMRA-dextran-N_3 24 (batch 2)

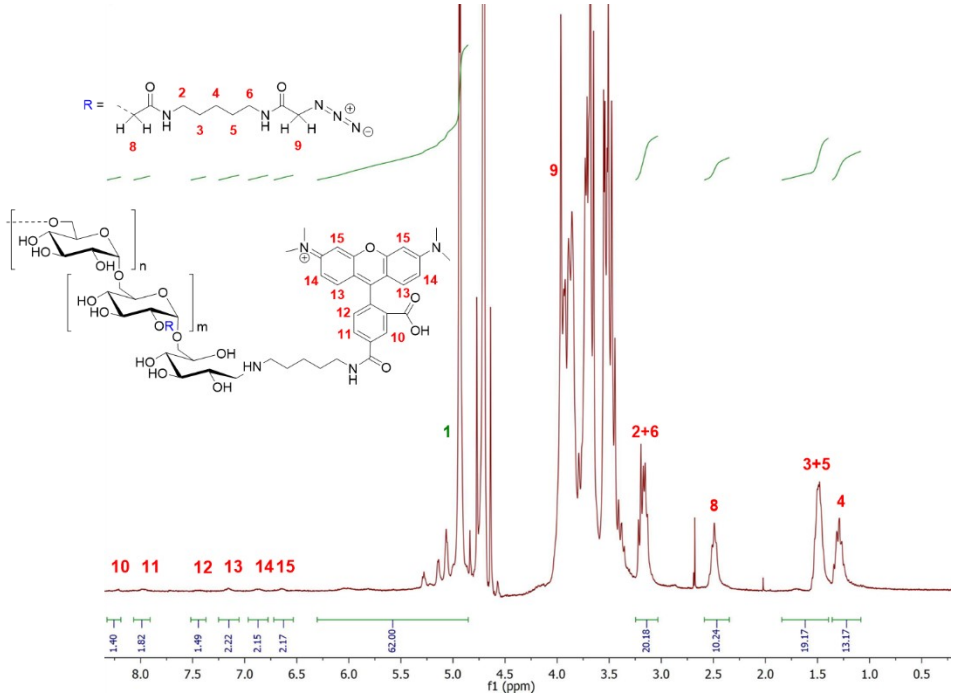

Figure S 65| ^{1}H-NMR spectrum (300 MHz, D_2O) of TAMRA-dextran-N_3 **24** (batch 2).

7.2.32 L17E$_{K1}^{Alloc}$-Pra 25

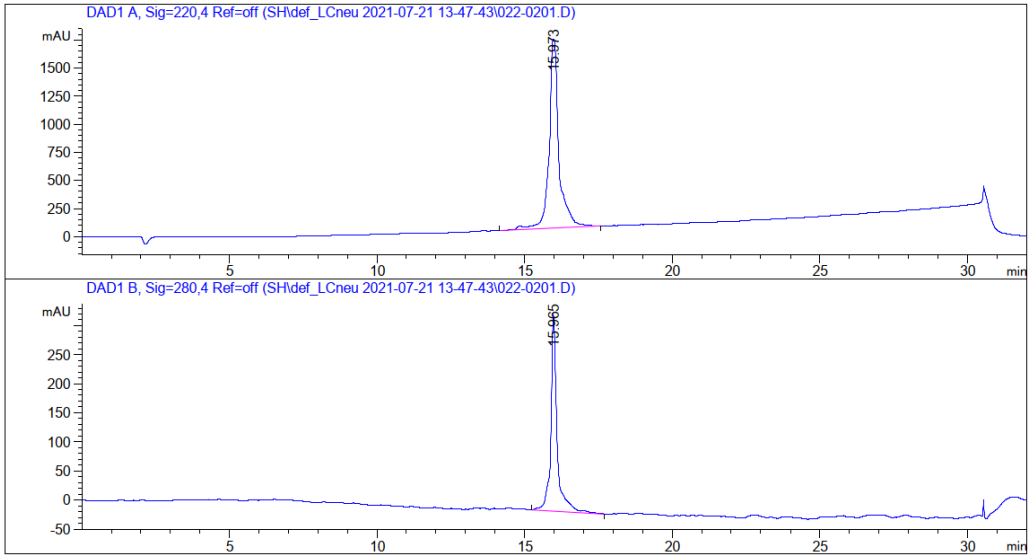

Figure S 66| Analytical RP-HPLC chromatogram of purified L17E$_{K1}^{Alloc}$-Pra peptide **25**, 0 to 80% B (0.6 mL/min, 20 min gradient), 220 nm (top), 280 nm (bottom), t_R = 15.973 min.

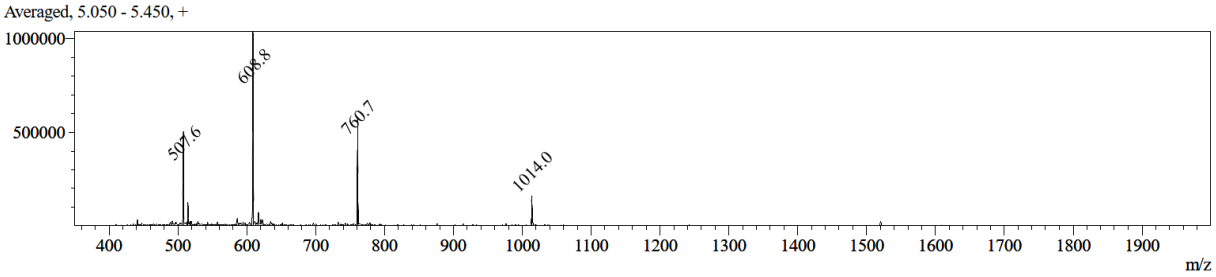

Figure S 67| MS (ESI) spectrum (positive mode) of L17E$_{K1}^{Alloc}$-Pra peptide **25**. Calculated: $[M+H]^{+}$ = 3039.6; $[M+2H]^{2+}$ = 1520.3; $[M+3H]^{3+}$ = 1013.9; $[M+4H]^{4+}$ = 760.7; $[M+5H]^{5+}$ = 608.7; $[M+6H]^{6+}$ = 507.4; observed: $[M+3H]^{3+}$ = 1014.0; $[M+4H]^{4+}$ = 760.7; $[M+5H]^{5+}$ = 608.8; $[M+6H]^{6+}$ = 507.6.

7.2.33 L17E$_{K2}^{Alloc}$-Pra 26

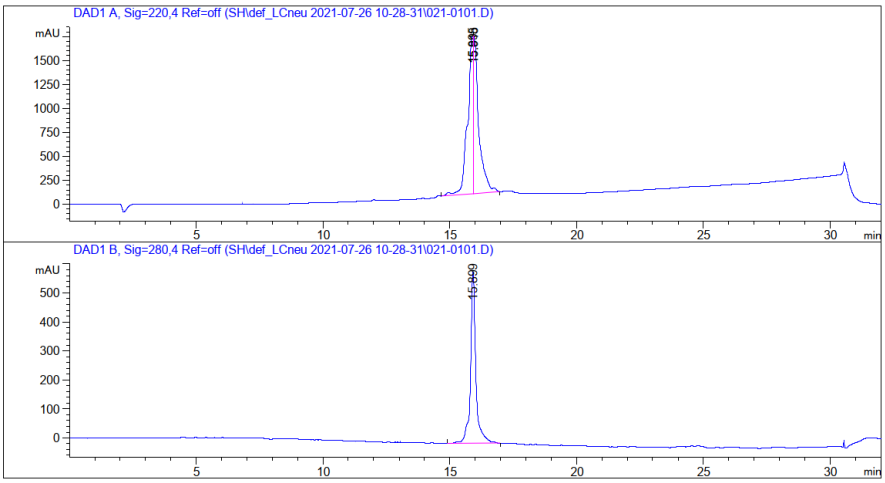

Figure S 68| Analytical RP-HPLC chromatogram of purified L17E$_{K2}^{Alloc}$-Pra peptide **26**, 0 to 80% B (0.6 mL/min, 20 min gradient), 220 nm (top), 280 nm (bottom), t_R = 15.899 min.

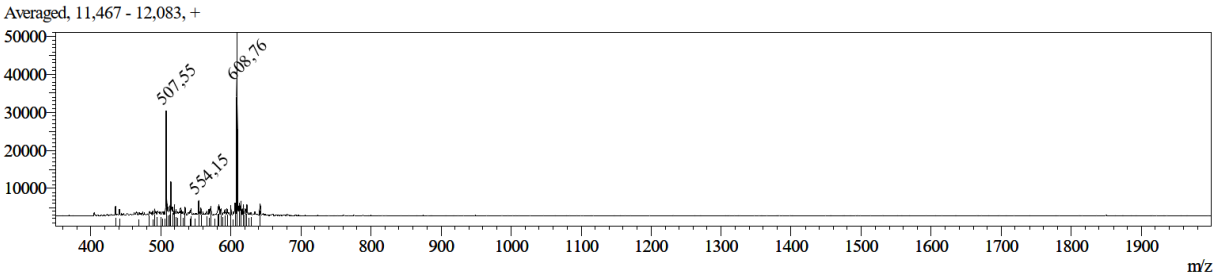

Figure S 69| MS (ESI) spectrum (positive mode) of L17E$_{2}^{Alloc}$-Pra peptide **26**. Calculated: $[M+H]^{+}$ = 3039.6; $[M+2H]^{2+}$ = 1520.3; $[M+3H]^{3+}$ = 1013.9; $[M+4H]^{4+}$ = 760.7; $[M+5H]^{5+}$ = 608.7; $[M+6H]^{6+}$ = 507.4; observed: $[M+5H]^{5+}$ = 608.8; $[M+6H]^{6+}$ = 507.6.

7.2.34 TAMRA-dextran-L17E$_{K1}^{Alloc}$(5.6) 27

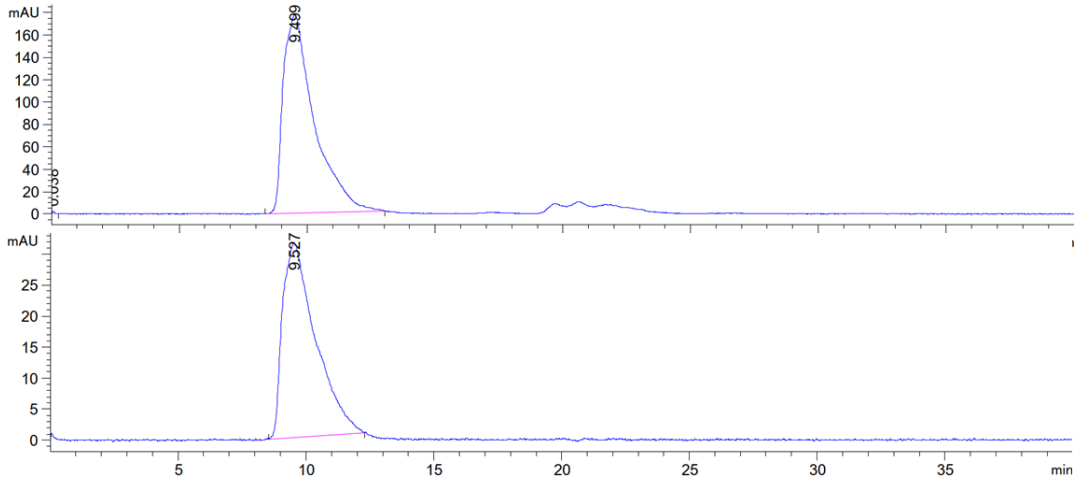

Figure S 70| Analytical SEC chromatogram of purified TAMRA-dextran-L17E$_{K1}^{Alloc}$ **27**, isocrat. 30% B, 0.6 mL/min, 220 nm (top), 550 nm (bottom), t_R = 9.499 min.

7.2.35 TAMRA-dextran-L17E$_{K2}^{Alloc}$(5.6) 28

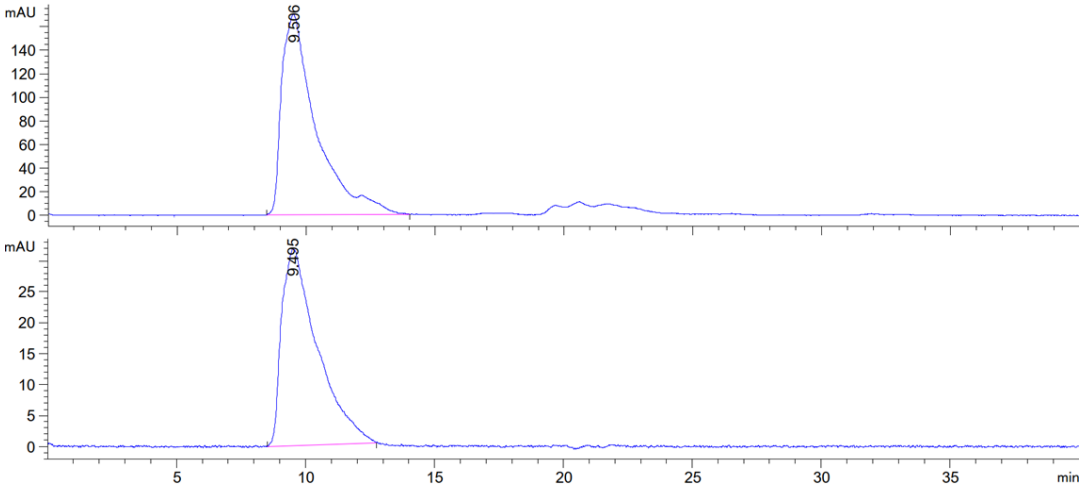

Figure S 71| Analytical SEC chromatogram of purified TAMRA-dextran-L17E$_{K2}^{Alloc}$ **28**, isocrat. 30% B, 0.6 mL/min, 220 nm (top), 550 nm (bottom), t_R = 9.506 min.

7.2.36 TAMRA-dextran-L17E(5) 29

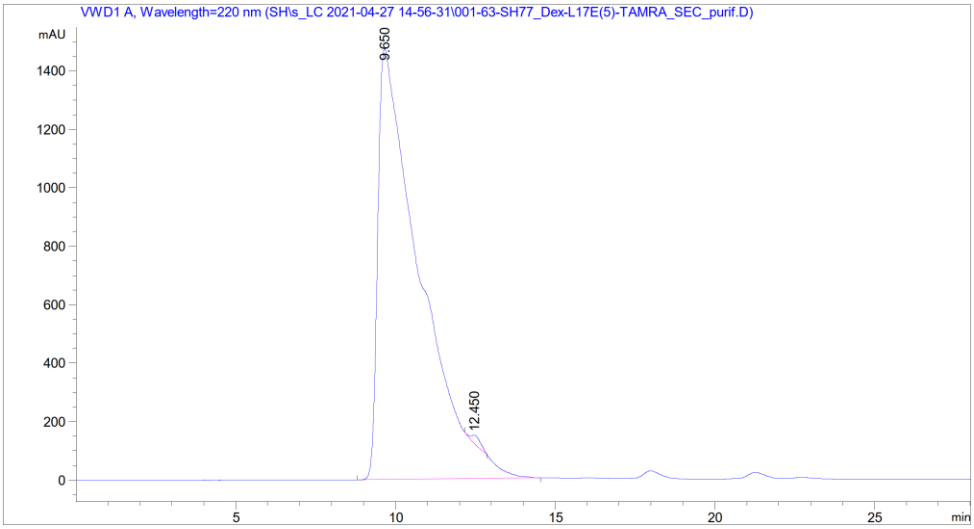

Figure S 72| Analytical SEC chromatogram of purified TAMRA-dextran-L17E **29**, isocrat. 30% B, 0.6 mL/min, 220 nm, t_R = 9.650 min.

7.2.37 L17E$_{K1+K2}^{Alloc}$-Pra 30

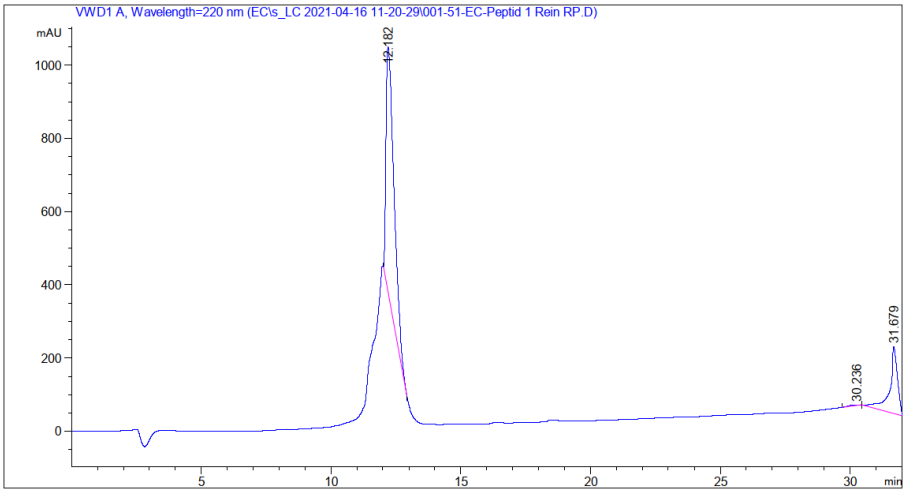

Figure S 73| Analytical RP-HPLC chromatogram of purified L17E$_{K1+K2}^{Alloc}$-Pra peptide **30**, 30 to 80% B (0.6 mL/min, 20 min gradient, 220 nm), t_R = 12.182 min.

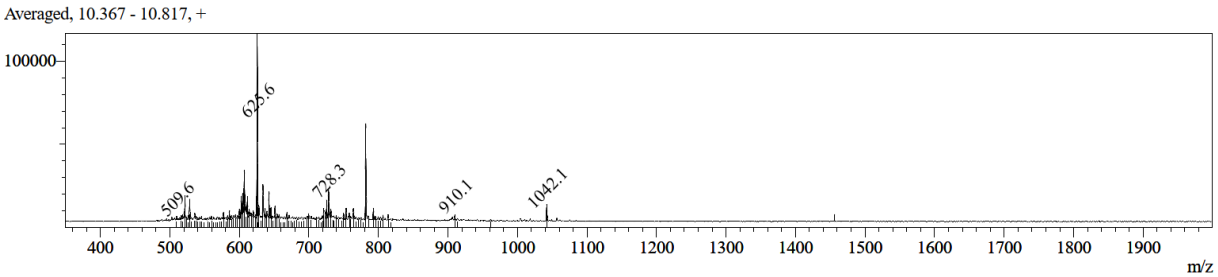

Figure S 74| MS (ESI) spectrum (positive mode) of L17E$_{K1+K2}^{Alloc}$-Pra peptide **30**. Calculated: $[M+H]^+$ = 3123.7; $[M+2H]^{2+}$ = 1562.3; $[M+3H]^{3+}$ = 1041.9; $[M+4H]^{4+}$ = 781.7; $[M+5H]^{5+}$ = 625.5; observed: $[M+3H]^{3+}$ = 1042.1; $[M+4H]^{4+}$ = 781.7; $[M+5H]^{5+}$ = 625.6.

7.2.38 L17E$_{K1+K3}^{Alloc}$-Pra 31

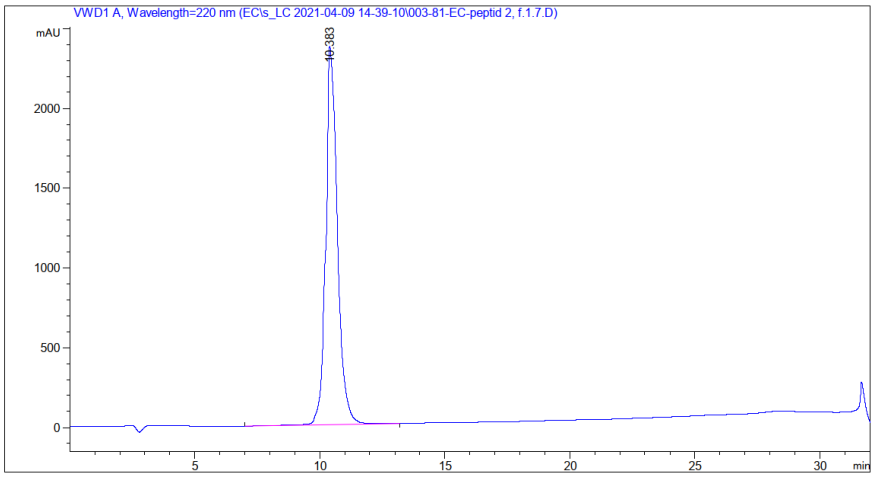

Figure S 75| Analytical RP-HPLC chromatogram of purified L17E$_{K1+K3}^{Alloc}$-Pra peptide **31**, 30 to 80% B (0.6 mL/min, 20 min gradient, 220 nm), t_R = 10.383 min.

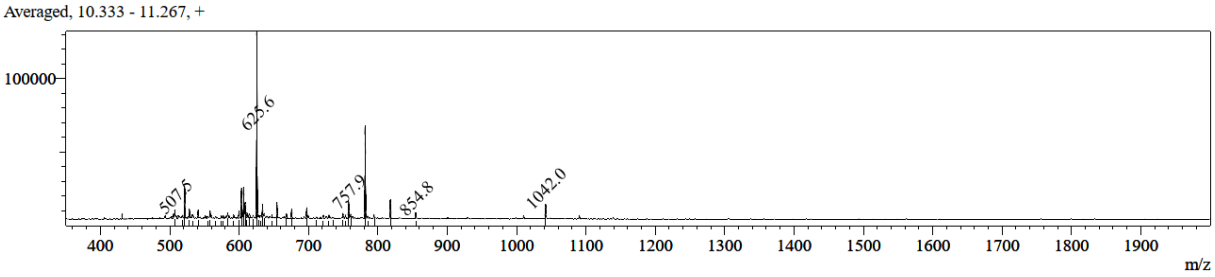

Figure S 76| MS (ESI) spectrum (positive mode) of L17E$_{K1+K3}^{Alloc}$-Pra peptide **31**. Calculated: $[M+H]^{+}$ = 3123.7; $[M+2H]^{2+}$ = 1562.3; $[M+3H]^{3+}$ = 1041.9; $[M+4H]^{4+}$ = 781.7; $[M+5H]^{5+}$ = 625.5; $[M+6H]^{6+}$ = 521.1; observed: $[M+3H]^{3+}$ = 1042.0; $[M+4H]^{4+}$ = 781.7; $[M+5H]^{5+}$ = 625.6.

7.2.39 L17E$_{K2+K4}^{Alloc}$-Pra 32

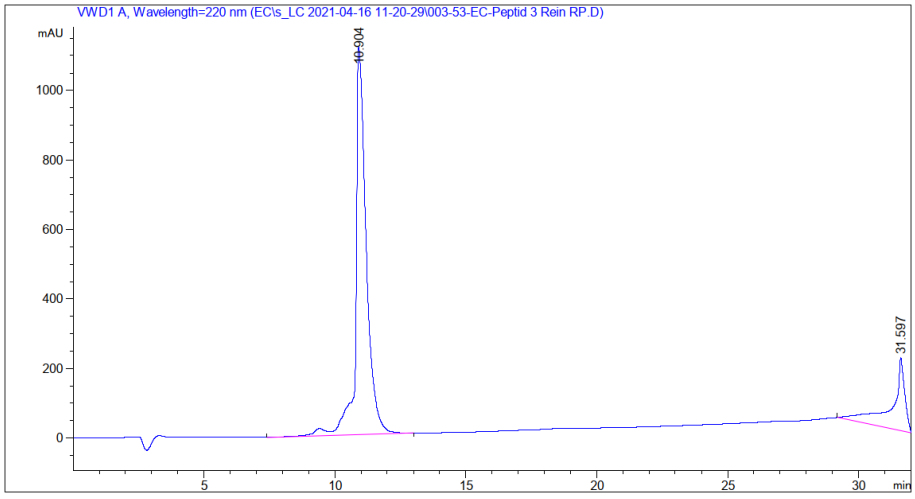

Figure S 77| Analytical RP-HPLC chromatogram of purified L17E$_{K2+K4}^{Alloc}$-Pra peptide **32**, 30 to 80% B (0.6 mL/min, 20 min gradient, 220 nm), t_R = 10.904 min.

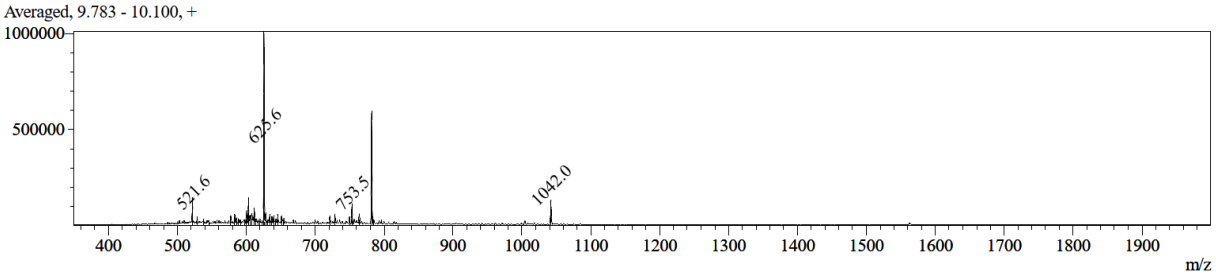

Figure S 78| MS (ESI) spectrum (positive mode) of L17E$_{K2+K4}^{Alloc}$-Pra peptide **32**. Calculated: $[M+H]^{+}$ = 3123.7; $[M+2H]^{2+}$ = 1562.3; $[M+3H]^{3+}$ = 1041.9; $[M+4H]^{4+}$ = 781.7; $[M+5H]^{5+}$ = 625.5; $[M+6H]^{6+}$ = 521.1; observed: $[M+3H]^{3+}$ = 1042.0; $[M+4H]^{4+}$ = 781.8; $[M+5H]^{5+}$ = 625.6; $[M+6H]^{6+}$ = 521.6.

7.2.40 L17E$_{K3+K5}^{Alloc}$-Pra 33

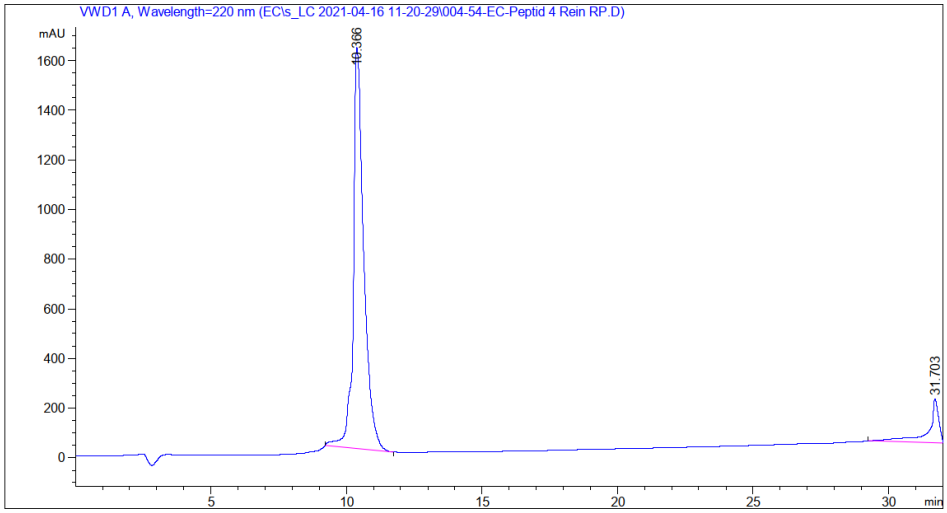

Figure S 79| Analytical RP-HPLC chromatogram of purified L17E$_{K3+K5}^{Alloc}$-Pra peptide **33**, 30 to 80% B (0.6 mL/min, 20 min gradient, 220 nm), t_R = 10.366 min.

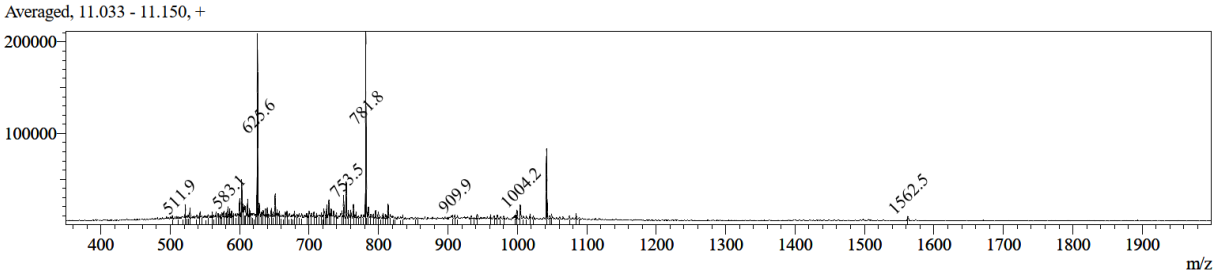

Figure S 80| MS (ESI) spectrum (positive mode) of L17E$_{K3+K5}^{Alloc}$-Pra peptide **33**. Calculated: $[M+H]^{+}$ = 3123.7; $[M+2H]^{2+}$ = 1562.3; $[M+3H]^{3+}$ = 1041.9; $[M+4H]^{4+}$ = 781.7; $[M+5H]^{5+}$ = 625.5; $[M+6H]^{6+}$ = 521.1; observed: $[M+2H]^{2+}$ = 1562.5; $[M+3H]^{3+}$ = 1041.9; $[M+4H]^{4+}$ = 781.8; $[M+5H]^{5+}$ = 625.6.

7.2.41 TAMRA-dextran-L17E$_{K1+K2}^{Alloc}$ 34

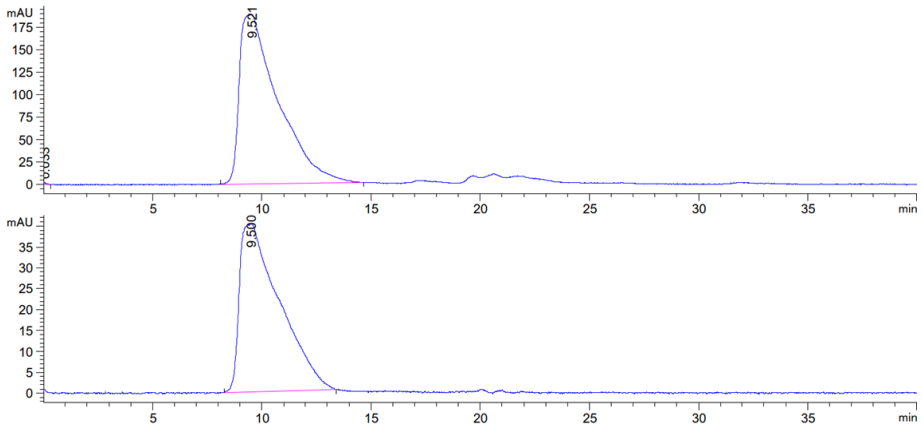

Figure S 81| Analytical SEC chromatogram of purified TAMRA-dextran-L17E$_{K1+K2}^{Alloc}$ **34**, isocrat. 30% B, 0.6 mL/min, 220 nm (top), 550 nm (bottom), t_R = 9.521 min.

7.2.42 TAMRA-dextran-L17E$_{K1+K3}^{Alloc}$ 35

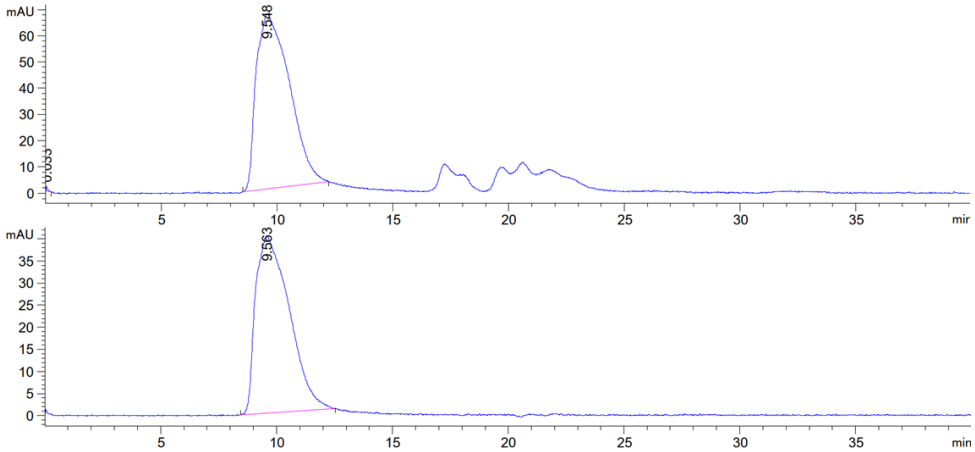

Figure S 82| Analytical SEC chromatogram of purified TAMRA-dextran-L17E$_{K1+K3}^{Alloc}$ **35**, isocrat. 30% B, 0.6 mL/min, 220 nm (top), 550 nm (bottom), t_R = 9.548 min.

7.2.43 TAMRA-dextran-L17E$_{K2+K4}^{Alloc}$ 36

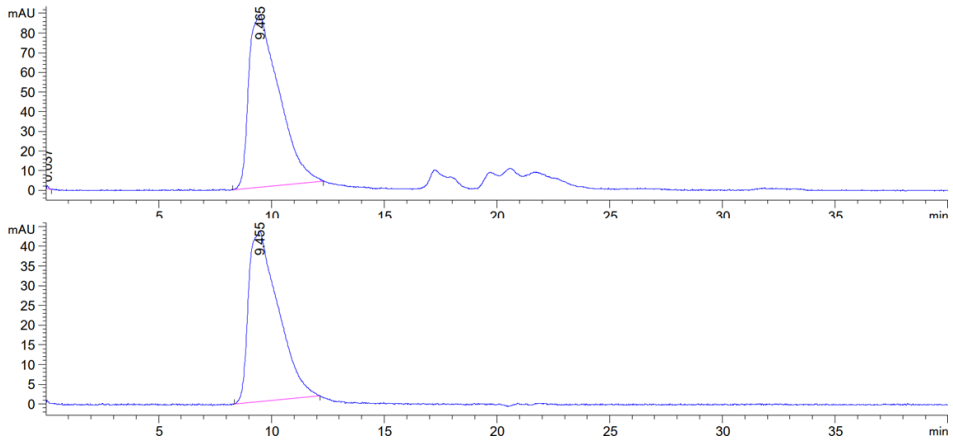

Figure S 83| Analytical SEC chromatogram of purified TAMRA-dextran-L17E$_{K2+K4}^{Alloc}$ **36**, isocrat. 30% B, 0.6 mL/min, 220 nm (top), 550 nm (bottom), t_R = 9.465 min.

7.2.44 TAMRA-dextran-L17E$_{K3+K5}^{Alloc}$ 37

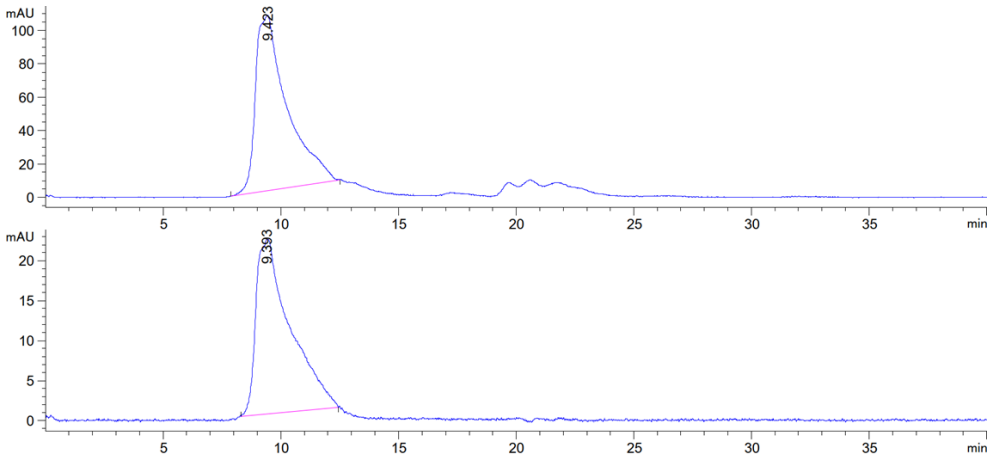

Figure S 84| Analytical SEC chromatogram of purified TAMRA-dextran-L17E$_{K3+K5}^{Alloc}$ **37**, isocrat. 30% B, 0.6 mL/min, 220 nm (top), 550 nm (bottom), t_R = 9.423 min.

7.2.45 L17E$_{K1}^{Ac}$-Pra 38

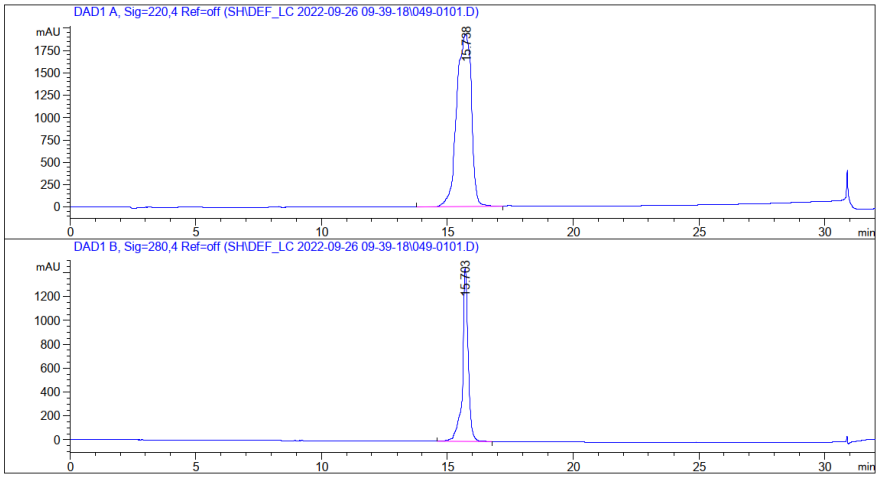

Figure S 85| Analytical RP-HPLC chromatogram of purified L17E$_{K1}^{Ac}$-Pra peptide **38**, 0 to 80% B (0.6 mL/min, 20 min gradient), 220 nm (top), 280 nm (bottom), t_R = 15.738 min.

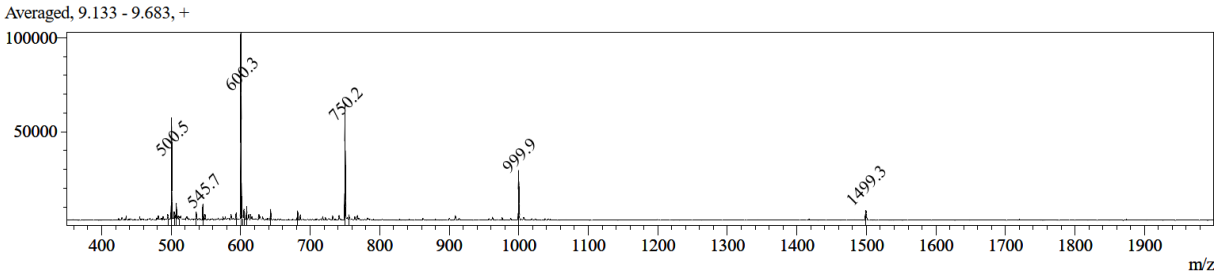

Figure S 86| MS (ESI) spectrum (positive mode) of L17E$_{K}^{Ac}$-Pra peptide **38**. Calculated: $[M+H]^{+}$ = 2997.6; $[M+2H]^{2+}$ = 1499.8; $[M+3H]^{3+}$ = 1000.2; $[M+4H]^{4+}$ = 750.4; $[M+5H]^{5+}$ = 600.5; $[M+6H]^{6+}$ = 500.6; observed: $[M+2H]^{2+}$ = 1499.3; $[M+3H]^{3+}$ = 999.9; $[M+4H]^{4+}$ = 750.2; $[M+5H]^{5+}$ = 600.3; $[M+6H]^{6+}$ = 500.5.

7.2.46 L17E$_{K2}^{Ac}$-Pra 39

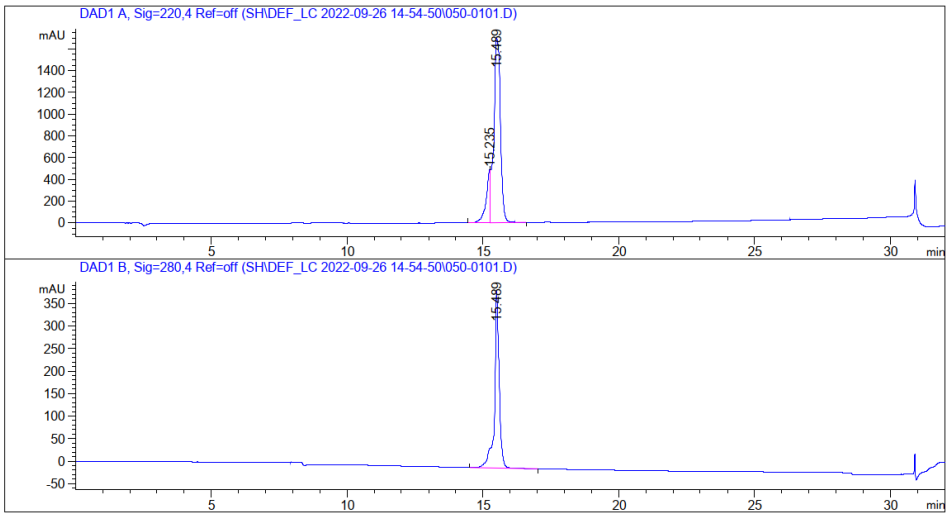

Figure S 87| Analytical RP-HPLC chromatogram of purified L17E$_{K2}^{Ac}$-Pra peptide **39**, 0 to 80% B (0.6 mL/min, 20 min gradient), 220 nm (top), 280 nm (bottom), t_R = 15.489 min.

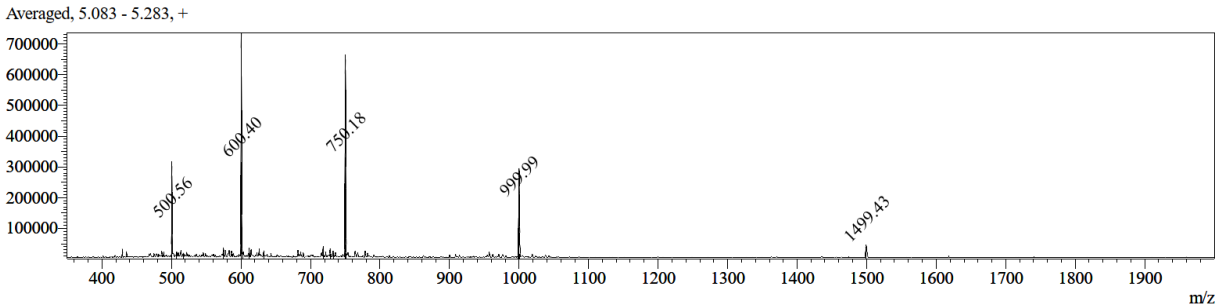

Figure S 88| MS (ESI) spectrum (positive mode) of L17E$_{K2}^{Ac}$-Pra peptide **39**. Calculated: $[M+H]^+$ = 2997.6; $[M+2H]^{2+}$ = 1499.8; $[M+3H]^{3+}$ = 1000.2; $[M+4H]^{4+}$ = 750.4; $[M+5H]^{5+}$ = 600.5; $[M+6H]^{6+}$ = 500.6; observed: $[M+2H]^{2+}$ = 1499.4; $[M+3H]^{3+}$ = 1000.0; $[M+4H]^{4+}$ = 750.2; $[M+5H]^{5+}$ = 600.4; $[M+6H]^{6+}$ = 500.6.

7.2.47 TAMRA-dextran-L17E$_{K1}^{Ac}$ 40

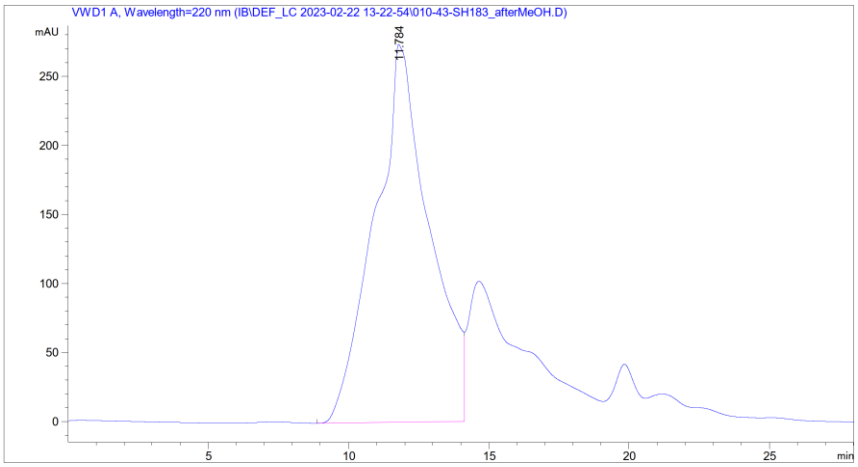

Figure S 89| Analytical SEC chromatogram of purified TAMRA-dextran-L17E$_{K1}^{Ac}$ **40**, isocrat. 30% B, 0.6 mL/min, 220 nm, t_R = 11.784 min.

7.2.48 TAMRA-dextran-L17E$_{K2}^{Ac}$ 41

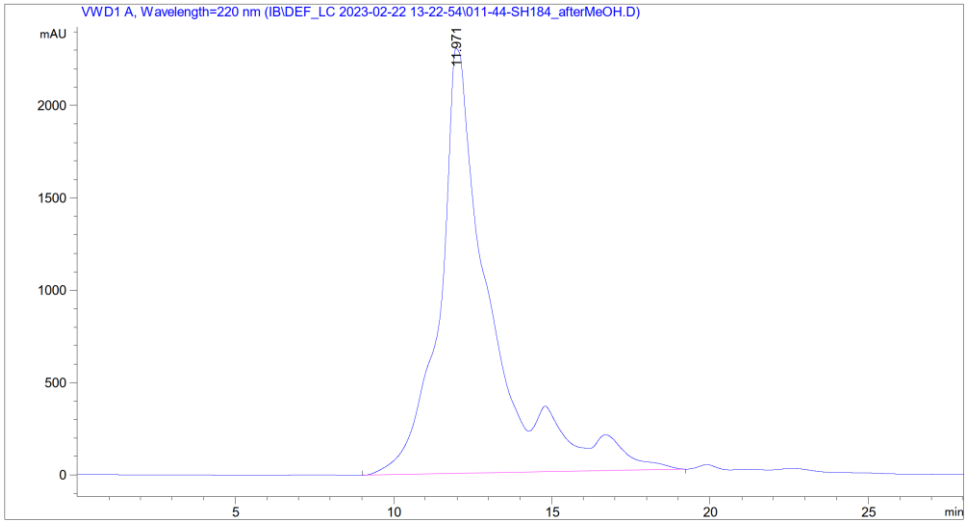

Figure S 90| Analytical SEC chromatogram of purified TAMRA-dextran-L17E$_{K2}^{Ac}$ **41**, isocrat. 30% B, 0.6 mL/min, 220 nm, t_R = 11.971 min.

7.2.49 L17E/Q21E-Pra 42

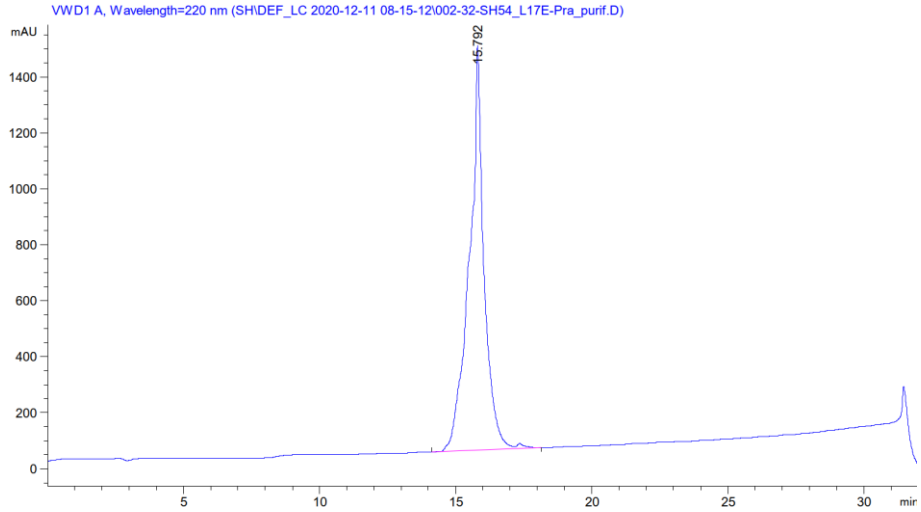

Figure S 91| Analytical RP-HPLC chromatogram of purified L17E/Q21E-Pra peptide **42**, 0 to 80% B (0.6 mL/min, 20 min gradient, 220 nm), t_R = 15.792 min.

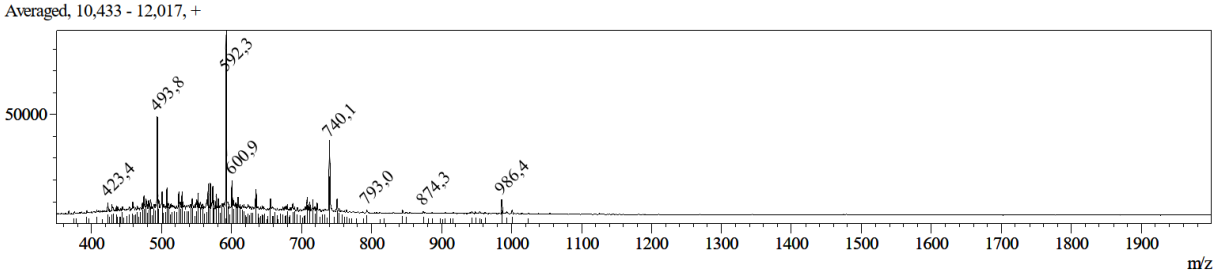

Figure S 92| MS (ESI) spectrum (positive mode) of L17E/Q21E-Pra peptide **42**. Calculated: $[M+H]^+$ = 2956.5; $[M+2H]^{2+}$ = 1478.8; $[M+3H]^{3+}$ = 986.2; $[M+4H]^{4+}$ = 739.9; $[M+5H]^{5+}$ = 592.1; $[M+6H]^{6+}$ = 493.5; observed: $[M+3H]^{3+}$ = 986.4; $[M+4H]^{4+}$ = 740.1; $[M+5H]^{5+}$ = 592.3; $[M+6H]^{6+}$ = 493.8.

7.2.50 HAad-Pra 43

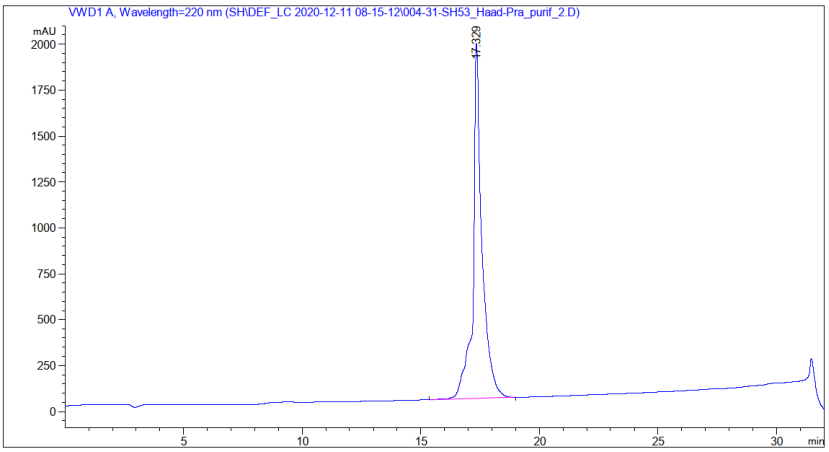

Figure S 93| Analytical RP-HPLC chromatogram of purified HAad-Pra peptide **43**, 0 to 80% B (0.6 mL/min, 20 min gradient, 220 nm), t_R = 17.329 min.

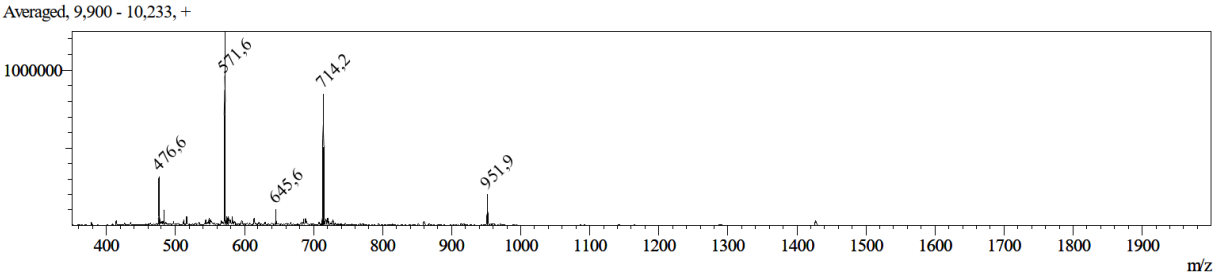

Figure S 94| MS (ESI) spectrum (positive mode) of HAad-Pra peptide **43**. Calculated: $[M+H]^{+}$ = 2851.4; $[M+2H]^{2+}$ = 1426.7; $[M+3H]^{3+}$ = 951.5; $[M+4H]^{4+}$ = 713.9; $[M+5H]^{5+}$ = 571.3; $[M+6H]^{6+}$ = 476.2; observed: $[M+3H]^{3+}$ = 951.9; $[M+4H]^{4+}$ = 714.2; $[M+5H]^{5+}$ = 571.6; $[M+6H]^{6+}$ = 476.6.

7.2.51 TAMRA-dextran-L17E/Q21E(5) 44

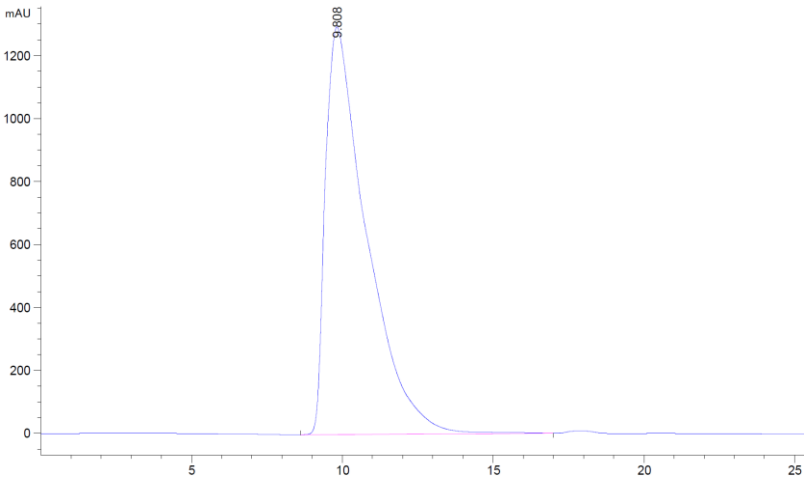

Figure S 95| Analytical SEC chromatogram of purified TAMRA-dextran-L17E/Q21E(5) **44**, isocrat. 30% B, 0.6 mL/min, 220 nm, t_R = 9.808 min.

7.2.52 TAMRA-dextran-HAad(5) 45

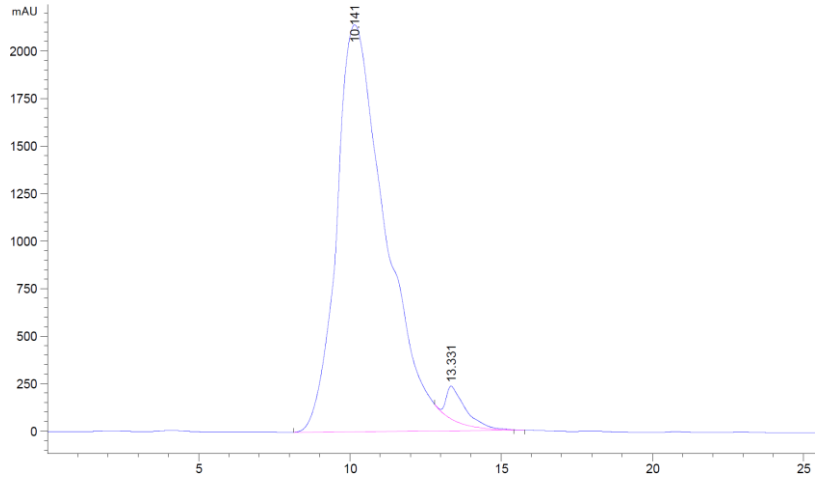

Figure S 96| Analytical SEC chromatogram of purified TAMRA-dextran-HAad(5) **45**, isocrat. 30% B, 0.6 mL/min, 220 nm, t_R = 10.141 min.

7.2.53 Biotin-dextran-N_3(3.7) 46

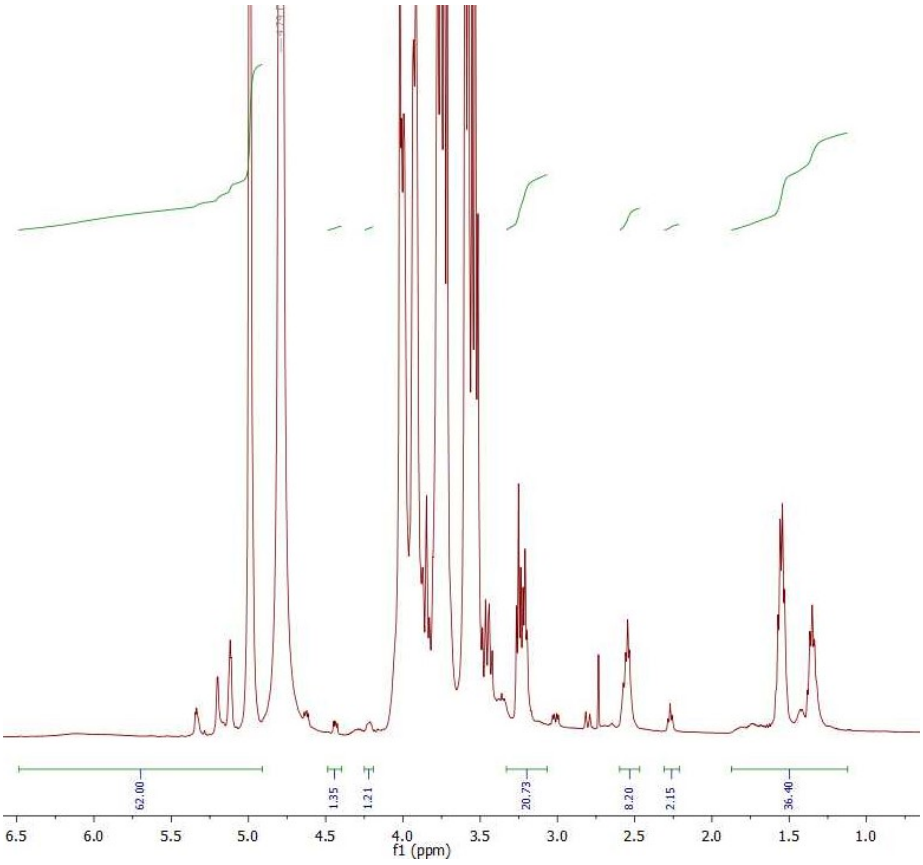

Figure S 97| ^{1}H-NMR spectrum (300 MHz, D_2O) of biotin-dextran-N_3(3.7) **46**.

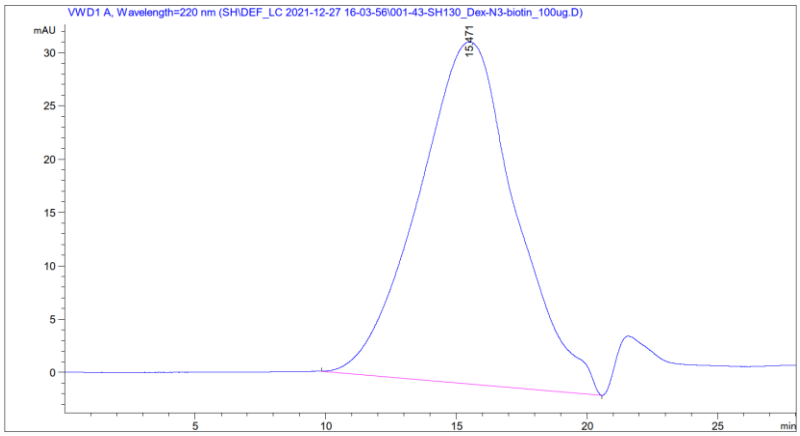

Figure S 98| Analytical SEC chromatogram of purified biotin-dextran-N_3(3.7) **46**, isocrat. 30% B, 0.6 mL/min, 220 nm, t_R = 15.471 min.

7.2.54 Biotin-dextran-N_3(6.3) 47

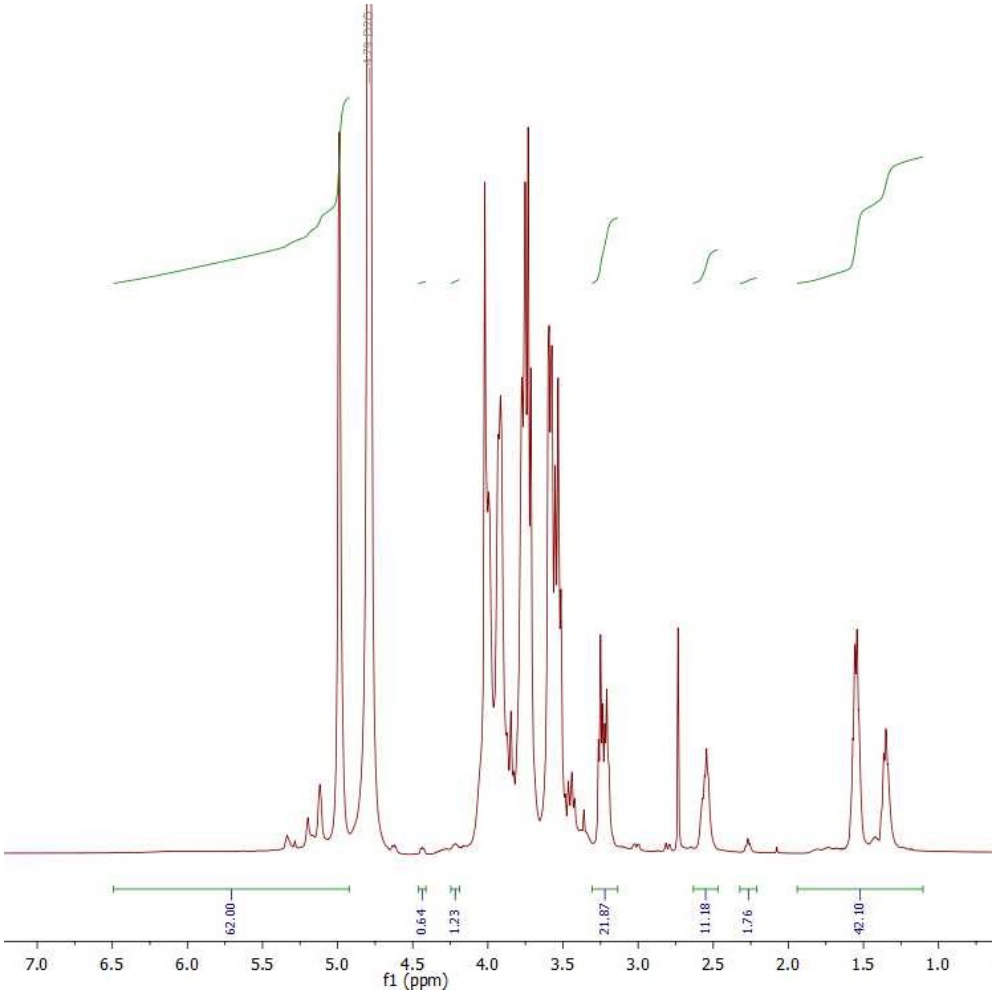

Figure S 99| ^{1}H-NMR spectrum (300 MHz, D_2O) of biotin-dextran-N_3(6.3) **47**.

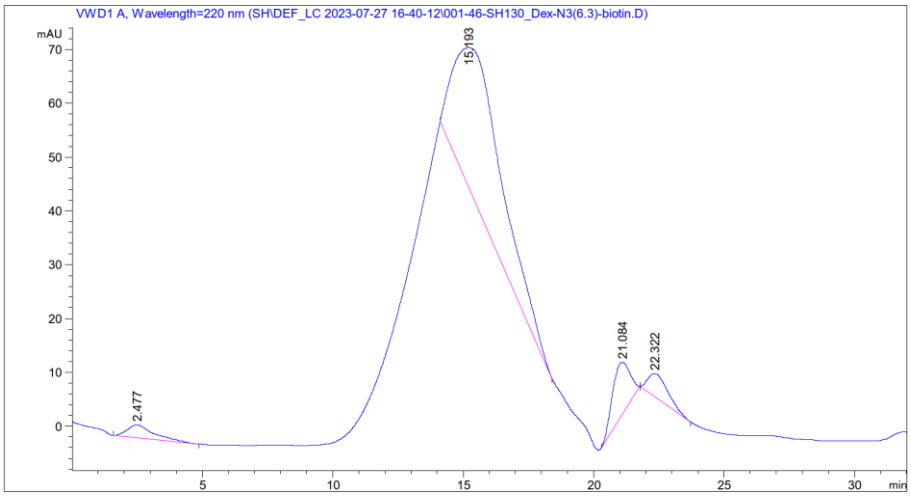

Figure S 100| Analytical SEC chromatogram of purified biotin-dextran-N_3(6.3) **47**, isocrat. 30% B, 0.6 mL/min, 220 nm, t_R = 15.193 min.

7.2.55 4-pentynoic acid-PEG$_2$-ATSP-7041 48

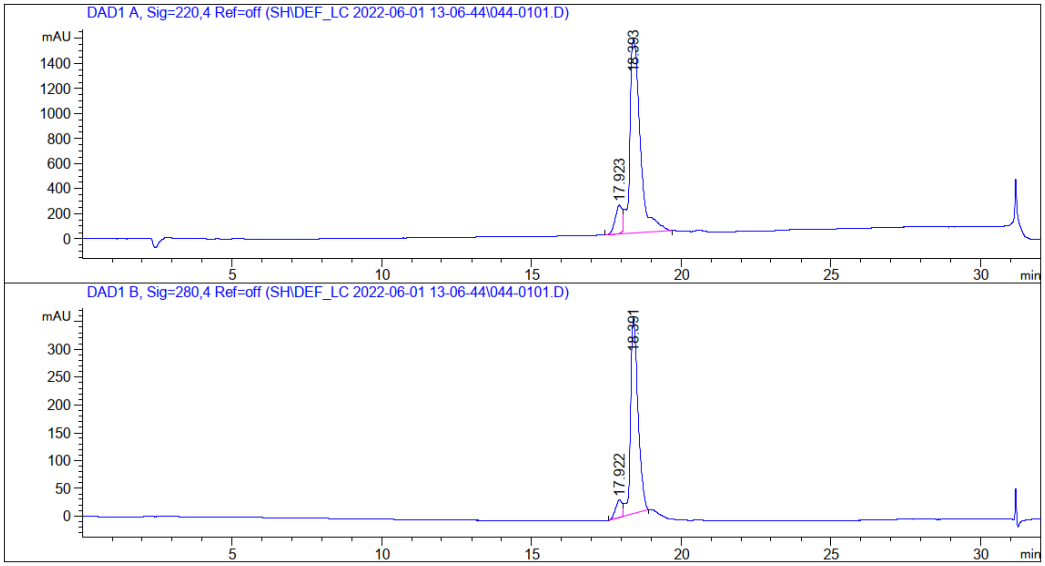

Figure S 101| Analytical RP-HPLC chromatogram of purified alkyne-ATSP-7041 peptide **48**, 40 to 100% B (0.6 mL/min, 20 min gradient), 220 nm (top), 280 nm (bottom), t_R = 18.393 min.

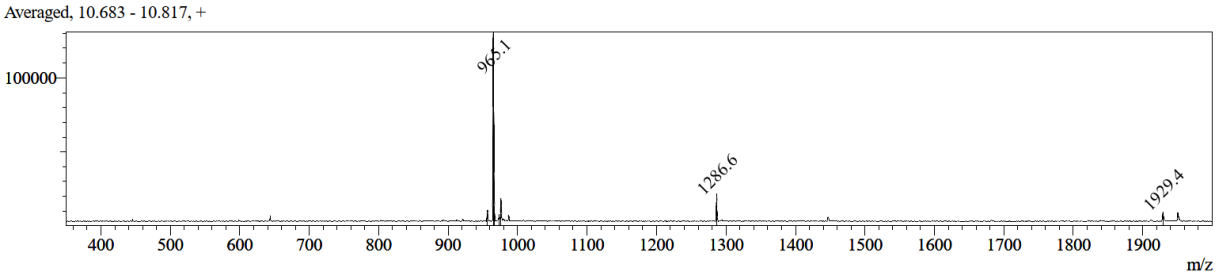

Figure S 102| MS (ESI) spectrum (positive mode) of alkyne-ATSP-7041 peptide **48**. Calculated: $[M+H]^+$ = 1929.2; $[M+2H]^{2+}$ = 965.1; $[M+3H]^{3+}$ = 643.7; observed: $[M+H]^+$ = 1929.4; $[M+2H]^{2+}$ = 965.1.

7.2.56 4-pentynoic acid-apCC-Di-B 49

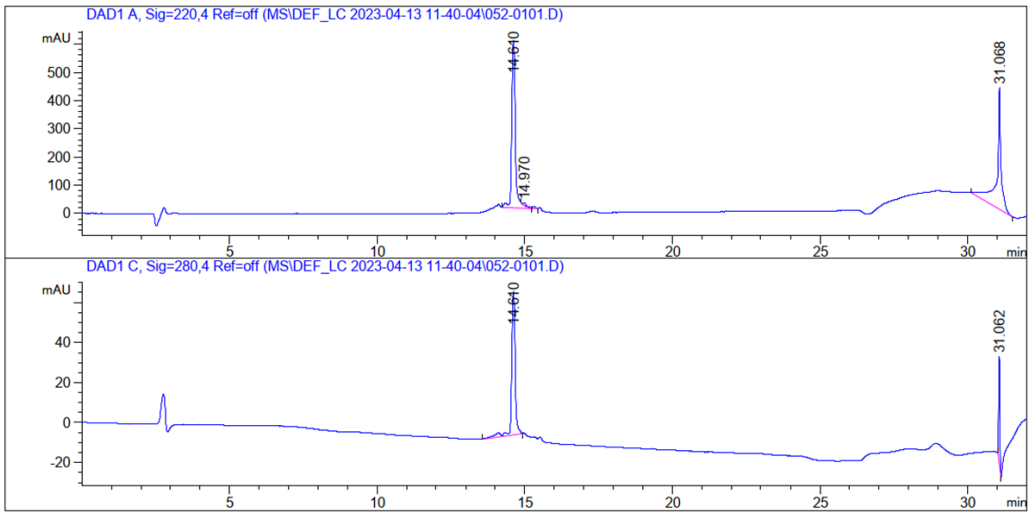

Figure S 103| Analytical RP-HPLC chromatogram of purified alkyne-ATSP-7041 peptide **48**, 40 to 100% B (0.6 mL/min, 20 min gradient), 220 nm (top), 280 nm (bottom), t_R = 14.610 min.

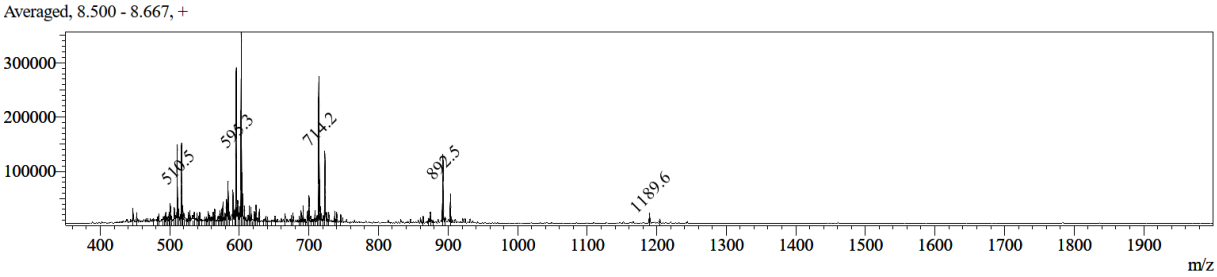

Figure S 104| MS (ESI) spectrum (positive mode) of alkyne-apCC-Di-B peptide **49**. Calculated: $[M+H]^{+}$ = 3566.2; $[M+2H]^{2+}$ = 1783.6; $[M+3H]^{3+}$ = 1189.4; $[M+4H]^{4+}$ = 892.3; $[M+5H]^{5+}$ = 714.0; $[M+6H]^{6+}$ = 595.2; $[M+7H]^{7+}$ = 510.5; observed: $[M+3H]^{3+}$ = 1189.6; $[M+4H]^{4+}$ = 892.5; $[M+5H]^{5+}$ = 714.2; $[M+6H]^{6+}$ = 595.3; $[M+7H]^{7+}$ = 510.5.

7.2.57 Biotin-dextran-L17E(3.7) 50

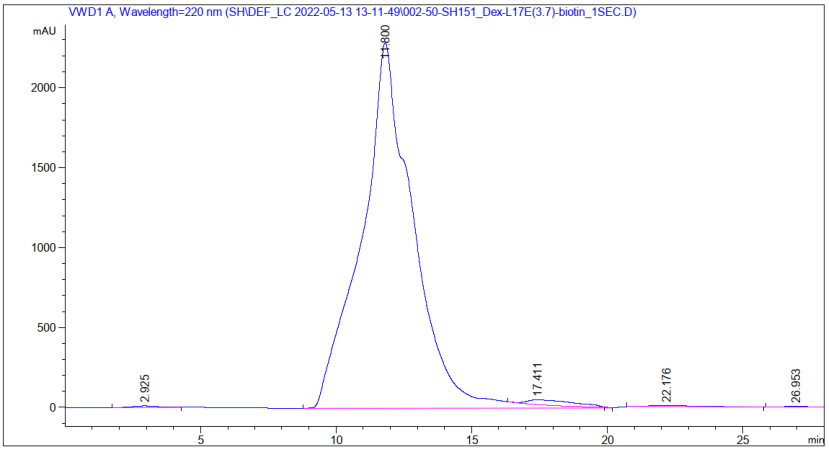

Figure S 105| Analytical SEC chromatogram of purified biotin-dextran-L17E(3.7) **50**, isocrat. 30% B, 0.6 mL/min, 220 nm, t_R = 11.800 min.

7.2.58 Biotin-dextran-ATSP-7041(3.7) 51

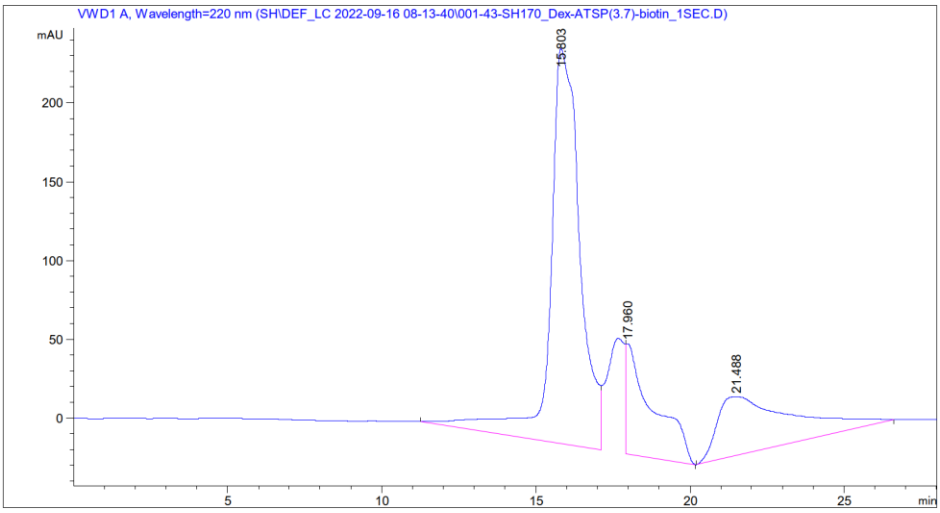

Figure S 106| Analytical SEC chromatogram of purified biotin-dextran-ATSP-7041(3.7) **51**, isocrat. 40% B, 0.6 mL/min, 220 nm, t_R = 15.803 min.

7.2.59 Biotin-dextran-apCC-Di-B(3.7) 52

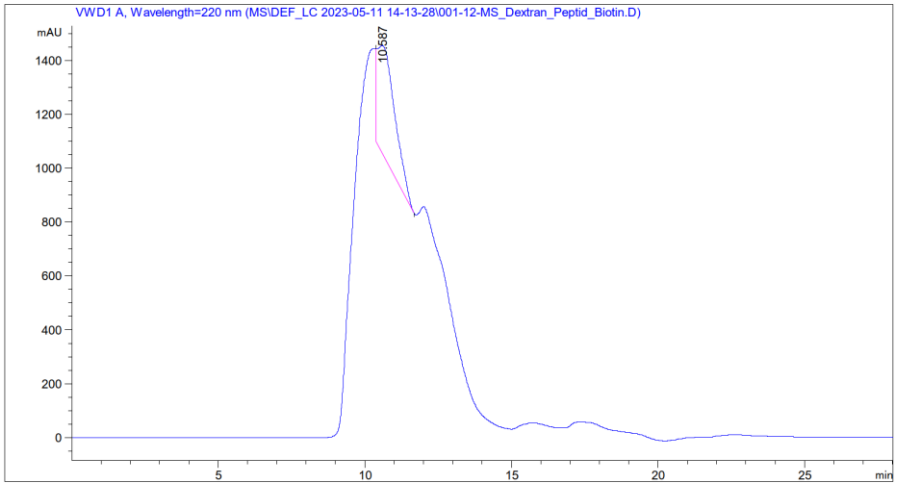

Figure S 107| Analytical SEC chromatogram of purified biotin-dextran-apCC-Di-B(3.7) **52**, isocrat. 30% B, 0.6 mL/min, 220 nm, t_R = 10.587 min.

7.2.60 Biotin-dextran-L17E/Q21E(6.3) 53

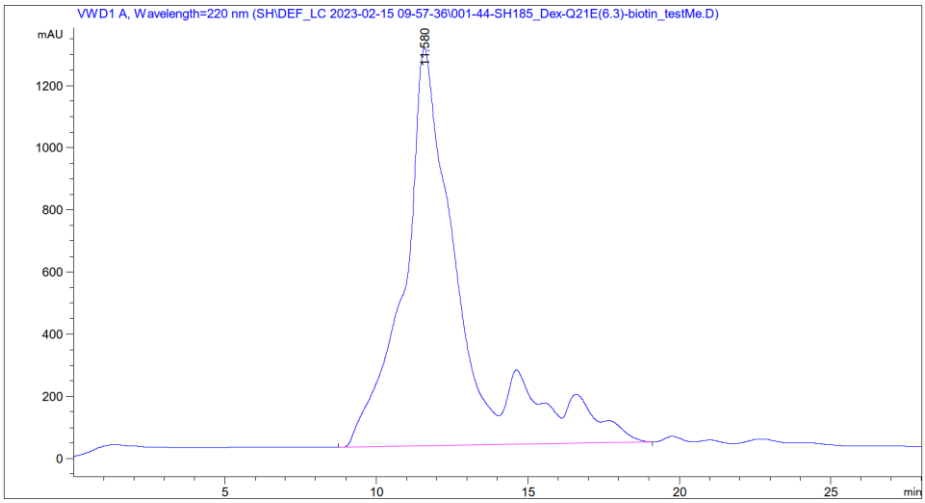

Figure S 108| Analytical SEC chromatogram of purified biotin-dextran-L17E/Q21E(6.3) **53**, isocrat. 30% B, 0.6 mL/min, 220 nm, t_R = 11.580 min.

7.2.61 Biotin-eGFP 54

MSGHHHHHHGSVSKGEELFTGVVPILVELDGDVNGHKFSVRGEGEGDATNGKLTLKFICTTGKLPV
PWPTLVTTLTYGVQCFSRYPDHMKQHDFFKSAMPEGYVQERTISFKDDGTYKTRAEVKFEGDTLVN
RIELKGIDFKEDGNILGHKLEYNFNSHNVYITADKQKNGIKANFKIRHNVEGFEIDKVWYDLDADGS
VQLADHYQQNTPIGDGPVLLPDNHYLSTQSKLSKDPNEKRDHMVLLEFVTAAGITLGMDELYKGLN
DIFEAQKIEWHE

Molecular weight: 31332.14

Theoretical pI: 5.70

Extinction coefficient: 31400, assuming all Cys residues are reduced

7.2.62 Pra-GSSG-GFP11 55

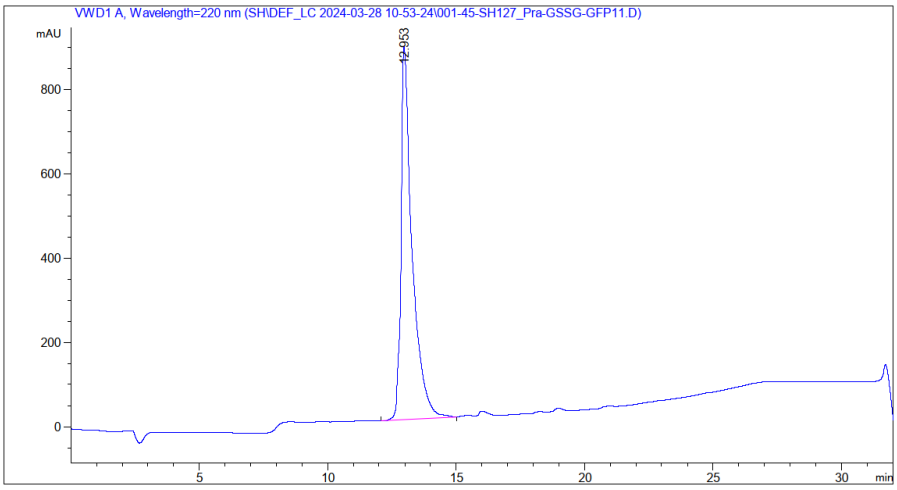

Figure S 109| Analytical RP-HPLC chromatogram of purified Pra-GSSG-GFP11 peptide **55**, 0 to 100% B (0.6 mL/min, 20 min gradient), 220 nm, t_R = 12.053 min.

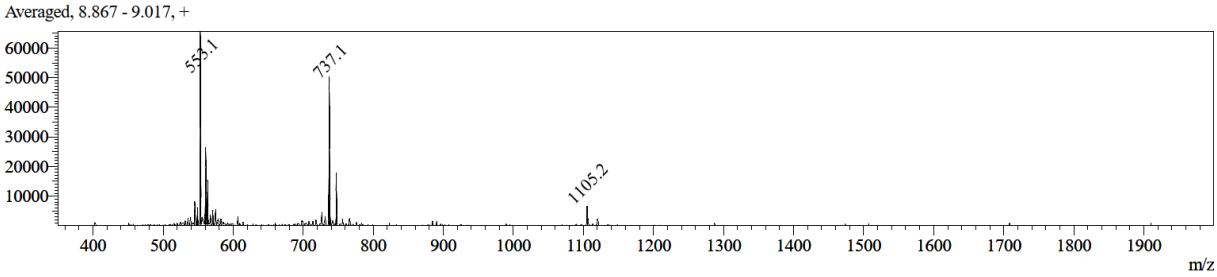

Figure S 110| MS (ESI) spectrum (positive mode) of Pra-GSSG-GFP11 peptide **55**. Calculated: $[M+H]^{+}$ = 2209.4; $[M+2H]^{2+}$ = 1105.2; $[M+3H]^{3+}$ = 737.1; $[M+4H]^{4+}$ = 553.1; observed: $[M+2H]^{2+}$ = 1105.2; $[M+3H]^{3+}$ = 737.1; $[M+4H]^{4+}$ = 553.1.

7.2.63 Biotin-dextran-GFP11(6.3) 56

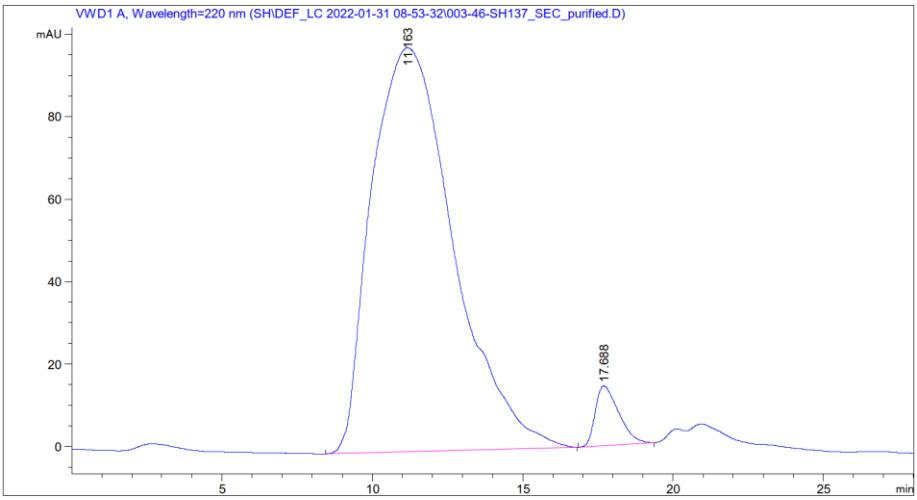

Figure S 111| Analytical SEC chromatogram of purified biotin-dextran-GFP11(6.3) **56**, isocrat. 30% B, 0.6 mL/min, 220 nm, t_R = 11.163 min.

7.2.64 4-pentynoic acid-PEG$_2$-KD3 57

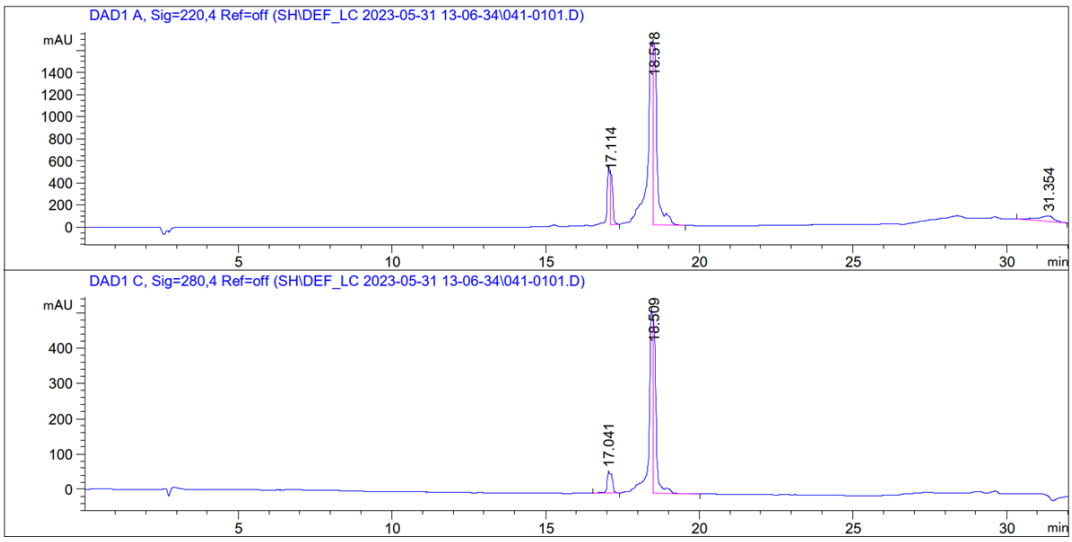

Figure S 112| Analytical RP-HPLC chromatogram of purified alkyne-KD3 peptide **57**, 10 to 80% B (0.6 mL/min, 20 min gradient), 220 nm (top), 280 nm (bottom), t_R = 18.518 min.

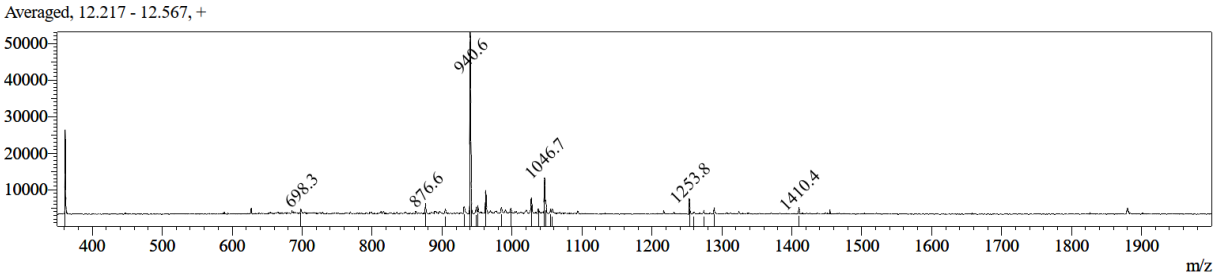

Figure S 113| MS (ESI) spectrum (positive mode) of alkyne-KD3 peptide **57**. Calculated: $[M+H]^+$ = 1881.1; $[M+2H]^{2+}$ = 941.0; $[M+3H]^{3+}$ = 627.7; $[M+4H]^{4+}$ = 471.0; observed: $[M+H]^+$ = 1881.0; $[M+2H]^{2+}$ = 940.6.

7.2.65 Biotin-dextran-KD3(6.3) 58

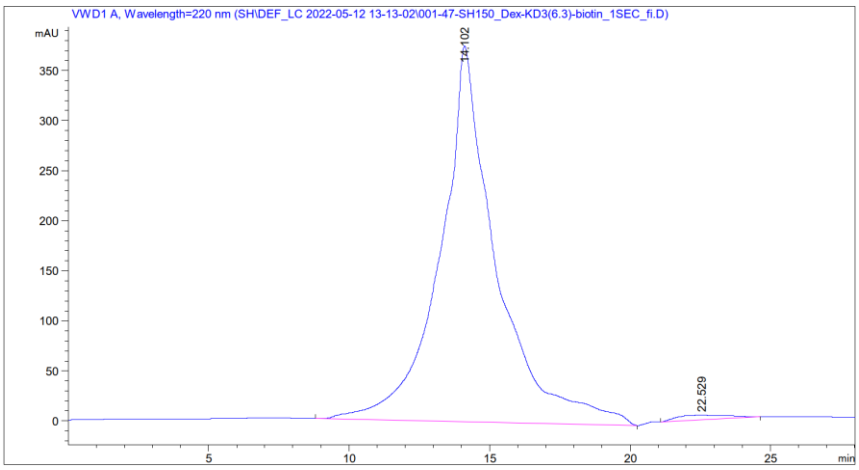

Figure S 114| Analytical SEC chromatogram of purified biotin-dextran-GFP11(6.3) **58**, isocrat. 30% B, 0.6 mL/min, 220 nm, t_R = 14.102 min.

7.2.66 4-pentynoic acid-GSSG-HiBiT 59

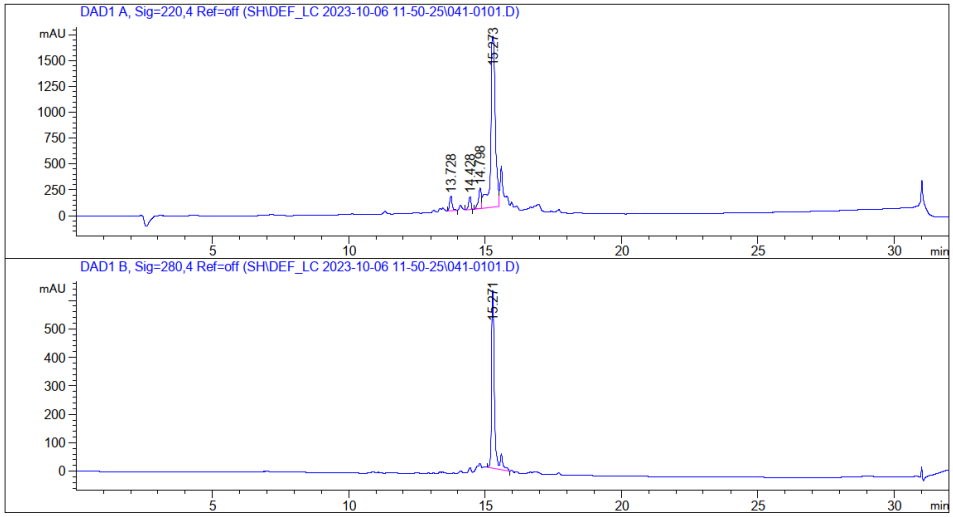

Figure S 115| Analytical RP-HPLC chromatogram of purified alkyne-HiBiT peptide **59**, 00 to 80% B (0.6 mL/min, 20 min gradient), 220 nm (top), 280 nm (bottom), t_R = 15.273 min.

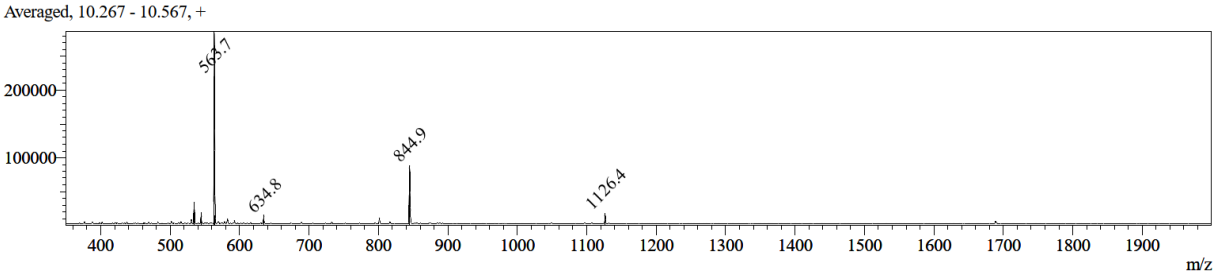

Figure S 116| MS (ESI) spectrum (positive mode) of alkyne-HiBiT peptide **60**. Calculated: $[M+H]^{+}$ = 1688.9; $[M+2H]^{2+}$ = 845.0; $[M+3H]^{3+}$ = 563.7; $[M+4H]^{4+}$ = 423.0; observed: $[M+H]^{+}$ = 1688.8; $[M+2H]^{2+}$ = 844.9; $[M+3H]^{3+}$ = 563.7.

7.2.67 Biotin-dextran-HiBiT(6.3) 60

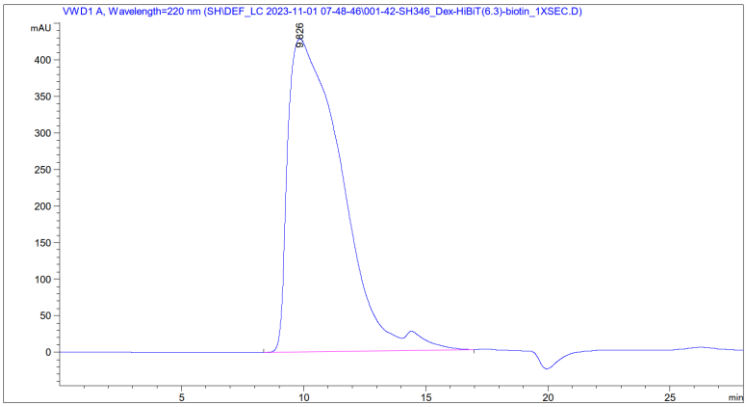

Figure S 117| Analytical SEC chromatogram of purified biotin-dextran-HiBiT(6.3) **60**, isocrat. 30% B, 0.6 mL/min, 220 nm, t_R = 9.826 min.

7.3 Abbreviations

2-CTC	2-chlorotrityl chloride
Aad	2-aminoadipic acid
Ac	acetyl
ACPPs	activatable cell penetrating peptides
ADC	antibody drug conjugates
ADEPT	antibody dependent enzyme prodrug therapy
ADP	adenosine diphosphate
alloc	allyloxy carbonyl
AMP	adenosine monophosphate
apCC	anti-parallel coiled-coil
API	active pharmaceutical ingredient
ATP	adenosine triphosphate
BirA	biotin ligase A
BIT	binary technology
Boc	*tert*-butyloxycarbonyl
CAGR	compound annual growth rate
Cba	cyclobutyl alanine
CE	carboxyethyl
CLSM	confocal laser scanning microscopy
CMDA	4-([2-chloroethyl][2-mesyloxyethyl]amino)benzoyl-L-glutamic acid
CPP	cell penetrating peptide
cry	cryptophycin
CuAAC	copper(I)-catalyzed azide-alkyne cycloaddition
Cy5	cyanine 5
DARPins	designed ankyrin repeat proteins
DAXI	DaxibotulinumtoxinA for Injection
DCE	dichloroethane
DCM	dichloromethane
Dde	N-[1-(4,4-dimethyl-2,6-dioxocyclohex-1-ylidene)ethyl]
DEACM	diethylaminocoumarin
Dex	dextran
DIC	*N,N*-diisopropyl carbodiimide
DIPEA	*N,N*-diisopropylethylamine
DMEM	Dulbecco's Modified Eagle Medium
DMF	*N,N*-dimethylformamide
DNA	deoxyribonucleic acid
DOX	doxorubicin
DTT	dithiothreitol
E. coli	*Escherichia coli*
EC_{50}	effective concentration 50
E_{max}	maximum cell killing
EEDQ	N-ethoxycarbonyl-2-ethoxy-1,2-dihydroquinoline
eGFP	enhanced green fluorescent protein
ESI	electrospray ionization
FACS	fluorescence-activated cell sorting

FBS	fetal bovine serum
FDA	food and drug administration
FRET	fluorescence resonance energy transfer
GFP	green fluorescent protein
GTP	guanosine triphosphate
HATU	1-[bis(dimethylamino)methylene]-1H-1,2,3-triazolo[4,5-b]pyridinium 3-oxide hexafluorophosphate
HBTU	3-[bis(dimethylamino)methyliumyl]-3H-benzotriazol-1-oxide hexafluorophosphate
HCl	hydrochloric acid
HDACs	histone deacetylases
HeLa	Henrietta Lacks
HER2	human epidermal growth factor receptor 2
HiBiT	high affinity BiT
HIV	human immunodeficiency virus
HPLC	high performance liquid chromatography
HSPG	heparan surface proteoglycan
IgG	immunoglobulin G
IR	infrared
KDAC	lysine deacetylase
LC	liquid chromatography
LgBiT	large BiT
NAD	nicotinamide adenine dinucleotide
NHS	N-hydroxysuccinimide
NMR	nuclear magnetic resonance
NSCLC	non/small cell lung cancer
mAb	monoclonal antibody
MDM	mouse double minute
MMAE	monomethyl auristatin E
MMP	matrix-metalloprotease
MS	mass spectrometry
mTG	microbial transglutaminase
Oxyma	ethyl cyanohydroxyiminoacetate
pHLIP	low pH insertion peptide
PTM	post translational modification
PTX	paclitaxel
KBr	potassium bromide
PAGE	polyacrylamide gel electrophoresis
PBS	phosphate-buffered saline
PDB	protein data bank
PE-channel	phycoerythrin-channel
PEG	polyethylene glycol
PEGF	platelet derived growth factor
PFA	paraformaldehyde
PPG	photo-removable protecting group
PPI	protein-protein interaction
Pra	propargylglycine

PS	penicillin/streptomycin
RAM	rink amide
RCM	ring closing metathesis
RNA	ribonucleic acid
ROS	reactive oxygen species
RP	reversed phase
Sav	streptavidin
SDS	sodium dodecyl sulfate
SEM	standard error of mean
Sir	silent information regulator
siRNa	small interfering RNA
SirT	sirtuin
Succ	succinyl
TAMRA	5(6)-carboxytetramethylrhodamine
TAT	trans activator of transcription
TES	triethyl silane
TIDES	peptides and oligonucleotides
TNBS	N-(2,4,6-trinitrophenyl)amine
TFA	trifluoro acetic acid
TRIS	tris(2-carboxyethyl)phosphine
UV	ultraviolet
VEGF	vascular endothelial growth factor

7.4 List of Figures

7.5 List of Tables

7.6 Danksagung

An dieser Stelle möchte ich mich bei allen bedanken, die mich während meiner Promotionszeit begleitet und unterstützt haben.

Mein ganz herzlicher Dank gilt **Prof. Dr. Harald Kolmar**, der es mir ermöglicht hat die Promotion in seinem Arbeitskreis durchzuführen. Während der vielen Gespräche, vor allem im letzten Promotionsjahr, sind durch die stetigen Diskussionen neue Ideen entstanden, die mir bei meiner Arbeit sehr geholfen haben.

Bei **Dr. Olga Avrutina** möchte ich mich für ihre Tipps, die sie stets parat hatte, und ihre immer positive, motivierende Einstellung sehr bedanken. Weiterhin danke ich **Dr. Andreas Christmann** für die technische Unterstützung im Labor sowie die Organisation der Lehre.

Dr. Simon Englert und **Dr. Bastian Becker**, die mich betreut haben und von denen ich so viel lernen konnte, danke ich für ihre Unterstützung seit meinem Beginn im Arbeitskreis Kolmar.

Ebenfalls danke ich **Barbara Diestelmann** für die netten Gespräche, die hellgelbe Kaffeetasse und ihre Hilfe im organisatorischem Bereich.

Ein großer Dank geht an **Dana Schmidt** und **Janine Becker**, die mir bei unterschiedlichen Laborarbeiten geholfen haben und für ihre unkomplizierte und zuvorkommende Art. Dank euch bleibt das Labor am Laufen!

Cicilie Gorus danke ich für die täglichen netten Begegnungen am frühen Morgen und ihrer Arbeit, welche vieles erleichtert hat.

Bei **Carolin Dombrowsky** möchte ich mich ganz herzlich für die tolle Zusammenarbeit an unseren gemeinsamen Projekten, das gemeinsame Durchstehen von Tiefen und Feiern von Höhen sowie ihre sachliche Art bedanken, die auf mich übergegangen ist.

Ingo Bork möchte ich besonders bedanken, der immer bereit war mit mir Ideen auszutauschen oder einfach zu reden! Auch **Peter Bitsch** und **Alessandro Emmanuello** danke ich für die fachliche und persönliche Unterstützung. Auf euch ist Verlass. Die Zeit mit euch im Labor hat mir immer Spaß gemacht!

Ebenso bedanke ich mich bei **Dominic Happel**, **Dr. Sebastian Bitsch**, **Felix Meiser**, **Felix Geyer**, **Katrin Schönfeld**, **Dr. Julia Harwardt**, **Michael Ulitzka**, **Dr. Jan Habermann**, **Adrian Bloch**, **Lieke van Gijzel**, **Yifei Li**, **Dr. Jorge Lerma** und **Dr. Stefania Carrara** für die

angenehme Arbeitsatmosphäre, Hilfsbereitschaft und vielen netten Gespräche, die den Alltag zusätzlich verschönert haben.

Auch geht ein großer Dank an **Yannick Burgdorf**, **Jan Queste**, **Thomas Stipp**, **Egzon Cermjani**, **Matijas Cica**, **Lorenzo Favier**, **Danna de Boer**, **Viktoria Höfling**, **Paul Pasda**, **Hue Tran**, **Lara Korth**, **David Rivic**, **Lisa Reinbold**, **Jasmin von Krogh** und **Barbara Geiger** für die schöne Zeit im Labor und auch im Privaten.

All meinen Praktis danke ich für die Unterstützung im Labor und die vielen hilfreichen Diskussionen.

Zusätzlich möchte ich unsere Sport-Montage mit dem gesamten Arbeitskreis erwähnen, die mir viel Spaß bereitet haben und auch immer noch bereiten. Ich kann mir keine besseren Kollegen vorstellen mit denen ich auch außerhalb der Uni viel unternommen hatte. Danke! Ich hoffe wir behalten unsere Kochabende bei.

Weiterhin möchte ich meinen Eltern, meinem Bruder und meinem Freund danken, die immer für mich da sind.

7.7 Erklärungen

Erklärungen laut Promotionsordnung

§8 Abs. 1 lit. c der Promotionsordnung der TU Darmstadt

Ich versichere hiermit, dass die elektronsiche Version meiner Dissertation mit der schriftlichen Version übereinstimmt und für die Durchführung des Promotionsverfahrens vorliegt.

§8 Abs. 1 lit. d der Promotionsordnung der TU Darmstadt

Ich versichere hiermit, dass zu einem vorherigen Zeitpunkt noch keine Promotion versucht wurde und zu keinem früheren Zeitpunkt an einer in- oder ausländischen Hochschule eingereicht wurde. In diesem Fall sind nähere Angaben über Zeitpunkt, Hochschule, Dissertationsthema und Ergebnis dieses Versuchs mitzuteilen.

§9 Abs. 1 der Promotionsordnung der TU Darmstadt

Ich versichere hiermit, dass die vorliegende Dissertation selbstständig und nur unter Verwendung der angegebenen Quellen verfasst wurde.

§9 Abs. 2 der Promotionsordnung der TU Darmstadt

Die Arbeit hat bisher noch nicht zu Prüfungszwecken gedient.

Darmstadt, den .....

_____

Sarah Hofmann